Stabilizing Highly Dynamic Locomotion in Planar Bipedal Robots with Dimension Reducing Control

by

Benjamin J. Morris

A dissertation submitted in partial fulfillment
of the requirements for the degree of
Doctor of Philosophy
(Electrical Engineering: Systems)
in The University of Michigan
2008

Doctoral Committee:
Professor Jessy W. Grizzle, Chair
Professor N. Harris McClamroch
Associate Professor Daniel P. Ferris
Associate Professor Richard B. Gillespie

With love and thanks to my parents, Jim and Annette, for their endless support

ACKNOWLEDGMENTS

As my time at Michigan draws to a close, I would like to thank a number of individuals, without whom the work of this thesis could not have been completed. First and foremost, I would like to wholeheartedly thank my advisor, Jessy Grizzle, for his continual inspiration and intellectual support throughout my time at the University of Michigan. In our conversations he has consistently valued theoretical insight and mathematical curiosity over the status quo of meetings, reports, and paperwork. In my time as a graduate student, I have been allowed the freedom to explore a number of research paths, many of which are contained in this thesis, but many more of which were dead ends. For Jessy's patience as a teacher, for his invitation to participate in the running experiments on RABBIT in France, and for his selfless interest in my career development, I am grateful. Secondly, and with equal enthusiasm I would like to thank Eric Westervelt for his roles as collaborator, co-author, travel companion, and friend throughout my years at the university, especially during the 2005-2006 academic year that produced the conference and journal papers addressing the control of passive dynamics within the framework of hybrid zero dynamics. With the many drafts of our coauthored papers, Eric has helped shape the style of my professional writing. I am indebted to my fellow coauthors Eric Westervelt, Jessy Grizzle, Christine Chevallereau, and Jun Ho Choi for the recently published book "Feedback Control of Dynamic Bipedal Robot Locomotion" to which I am truly honored to have contributed. I would like to thank Jonathan Hurst, Al Rizzi, and Matt Mason of Carnegie Mellon University for their contributions in the construction of the series compliant robotic prototypes that have helped shape the direction of our theoretical research here at Michigan. For graciously tutoring me in RHexLib and Ubuntu Linux and for setting up our initial computational framework for realtime control, Joel Chestnutt deserves special thanks. In addition, the willing and capable programming expertise of Koushil Sreenath at the University of Michigan has been invaluable throughout the last semester. Lastly, I would like to thank my family and close friends, who through a combination of encouragement and prodding have helped bring this document to completion.

Benjamin Morris

December 2007

TABLE OF CONTENTS

LIST OF TABLES

Table

LIST OF FIGURES

Figure

CHAPTER 1

Introduction

> "The employment of machinery forms an item of great importance in the general mass of national industry. 'Tis an artificial force brought in aid of the natural force of man; and, to all the purposes of labour, is an increase of hands, an accession of strength, unencumbered too by the expense of maintaining the laborer." Alexander Hamilton, to the US House of Representatives December 5, 1791.[1]

1.1 Why Study Bipedal Locomotion?

The field of legged locomotion is the branch of robotics that focuses on the study of machines that move from place to place using legs rather than wheels. Classical motivation for studying legged locomotion is that wheels require a continuous navigable surface such as a road, whereas legged machines only require intermittent support such as stepping stones.[2] More recent sources of motivation are the potential applications of legged robots in entertainment, recreation, rehabilitation, prosthesis development, human rescue, and health care. But, perhaps the strongest motivation for studying bipedal robots (in particular) is the potential for automated labor in environments that are much better suited for people than for traditional stationary or wheeled machines. Compared with industrial pick-and-place manipulators, humanoid robots could operate with relative ease in multi-level homes or offices, construction sites, or rescue environments.

Unfortunately, at the current time, no legged robots—let alone bipedal robots—have been mass

[1] Cited in [18].

[2] Raibert cites this motivation in his influential book [114].

produced for purposes other than entertainment, advertising, or education. The tasks of walking and running, which are elegant and simple for humans, are difficult and unnatural for most legged machines, so much so that dynamic legged locomotion is a limiting factor in what could be the next frontier of automation: the adaptation of machines to human environments.

A glimpse through the history of automation shows a technological shift from machines that assisted men in the Industrial Revolution, to machines that are merely supervised by men in the age of Industrial Automation. Starting in the mid 17th century, the use of highly specialized mechanical tools helped to increase the productivity of human labor when the task to be performed was especially simple.[3] Through the 19th and mid 20th centuries, the appearance of mechanized factories, interchangeable parts, assembly lines, and changes in organizational techniques showed manual labor adapting to better suit the environment of high-volume mechanized production.[4] In the late 20th century, the technology of robotics and automatic control brought about a period of Industrial Automation, characterized by automated factory lines of self-operating, self-regulating machines that are supervised and maintained by humans.

The success of automation in manufacturing suggests another potential venue for mechanized efficiency: the automation of services. In the present day, service makes up about 80% of the United States GDP[5], but robotic automation has only a minimal impact in service-oriented industries. Activities in auto repair, carpentry, construction, exploration, forestry, health care, hospitality, human rescue, shipping, and surveying represent a new domain of application of robotic labor. Tasks in these fields are difficult to automate not only because of cognitive requirements (successful robots would require high-level decision making skills and reliable operation in an unpredictable environment) but also because of fundamental physical challenges (dextrous operation must be done by mobile machines in areas not easily reachable by wheels). Those robots able to perform the fundamentally dynamic tasks of high speed walking, running, and dynamic balancing would be better suited to execute high-level tasks such as navigating in a crowd or transporting goods or people in a hostile environment.

Two hundred years from the onset of the Industrial Revolution, innovations in mobile robotics continue to occur. To name a few, a robot called the M2 “Mighty Mouse” has been used to clean

[3]The spinning jenny and mill works are examples of machines that assisted workers without replacing them [18].
[4]See Taylor’s “Principles of Scientific Management” [138].
[5]U.S. Department of Commerce Statistics [35]

up nuclear waste at White Sands Missle range in the US [127]; a company called Yobotics [3] is conducting research on a powered orthodic brace for those with lower leg injuries; the Japanese robot MARIE could provide robot-assisted health care for an aging population [1]; and researchers in METI's Humanoid Robotics Project (HRP) [68] are developing humanoid robots fit for operating a backhoe and forklift—machines that can operate other machines. The American military is funding research on a bipedal robot called BEAR for use in battlefield injury rescue scenarios [13]. Specializing in robotics and simulation, a company called Boston Dynamics [2] continues DARPA-supported research on hexapods such as RHex [122] and RiSE [125] and quadrupeds such as BigDog [113] and LittleDog [116]. Exoskeletons such as Bleex [86] and HAL [85] can be used to enhance certain aspects of human locomotion, rather than replacing them.

The idea of a robotic workforce has international appeal, with research groups working toward similar goals worldwide. An explicit goal of Honda's humanoid project [65] is to "develop technologies so that the humanoid robot can function not only as a machine, but blend in our social environment and interact with people, and play more important roles in our society". The Japanese Robot Association (JARA) also envisions the creation of a robotic society [79] with robots assisting people in everything from livestock farming to nuclear power.

If these distant frontiers of automation are to be explored, then machines must work not only in factories, but alongside people in their homes helping with day-to-day activities. With such a diversity of applications it's unlikely that a single "one size fits all" solution will be appropriate for every robot and for every application. Much more likely, a continuum of methods of locomotion are needed. What is clear is that the current state-of-the-art techniques are not yet sufficient for future needs. Before our robotic workforce is to be built, advances are needed in both the hardware design of legged machines and in the control algorithms that provide stable, coordinated movements.

1.2 Bottom-up Techniques of Control

Legged locomotion crosses traditional borders separating academic fields of study, leading to a rich diversity of methods and motivations of research. For example, a better understanding of the relationships between human and robotic walking would directly benefit those in kinesiology and rehabilitation. An understanding of the *first principles* of human and robot morphology would aid

those in mechanics, mechatronics, and machine design. Abstractions of gait planning and stabilization would interest those in computer science, applied mathematics, machine learning, dynamical systems, and control theory.

As part of this diversity, the primary purpose of this thesis is to develop nonlinear control theory that is appropriate to stabilize highly dynamic walking and running behaviors in underactuated planar bipedal robots. In order to focus on this task, other worthy aspects of locomotion—underlying biological principles, issues of mechanical and electrical efficiency, and design principles for legged machines—will be set aside. Results in this thesis are proven mathematically and illustrated using numerical simulation. The language of control theory will be used throughout this thesis, in which terms such as "stability", "proof", and "analysis" have specific mathematical interpretations.

Although potentially disconcerting at first, focusing on mathematical aspects of walking (rather than relying heavily on experimentation) is an accepted technique of study with a number of benefits that often go unspoken. Instead of starting anew with each new robot prototype, mathematical theory builds solidly on itself, largely independent of the robot on which it is applied. Once a theorem is proven to be true, it remains true for all time. In addition, the conclusions of mathematical analysis are generalizeable and falsifiable—both characteristics of solid research.

As hardware technologies for building legged robots become ever more sophisticated, the mathematical control techniques for coordinating and stabilizing their gaits must grow as well. While hardware aspects of legged locomotion tend to get the most attention, it is arguably the hidden technology of control that will enable practical uses of robots for day-to-day activities.[6] Without the bottom-up techniques of theorem and proof, sophisticated robot prototypes are doomed to remain pieces of animatronic sculpture, pacing slowly onstage and pleasantly waving for their human creators, unable to help them with any meaningful or profitable task.

1.3 Context and Motivation

This thesis is intended to be read in the context of the mathematical framework of hybrid zero dynamics (HZD), a methodology spanning everything from modeling and control to optimization and experimentation on walking and running in bipedal robots. A brief summary of key publications

[6] The idea of control as a "hidden technology" is due to Karl Åström [11].

in hybrid zero dynamics is given here, with a more thorough review of relevant literature to be presented in Chapter 2.

Four papers form the backbone of the method of hybrid zero dynamics. Early work on constraint-based walking was given by Grizzle, Abba, and Plestan in [60], using the method of Poincaré as an essential tool in the tractable stability analysis of underactuated planar bipedal walking. The HZD theory of walking was officially coined by Westervelt, Grizzle, and Koditschek in [153] where virtual constraints and hybrid invariance led to an elegant low dimensional test for evaluating the stability of a planar bipedal walking gait. Walking experiments on the French robot RABBIT were presented by Westervelt, Buche, and Grizzle in [149] in which RABBIT exhibited outstanding stability and robustness properties when walking under an HZD-based controller. The final milestone relevant to this thesis is the HZD theory of running presented by Chevallereau, Westervelt, and Grizzle in [31] where stable running is predicted for robots similar to RABBIT.

The research topic of this thesis is motivated by the tests that took place in September 2004 to experimentally validate the HZD control of running presented in [31]. A writeup of these experiments is available in the book chapter [101] by Morris, et al. Although experimental implementations of HZD walking controllers worked essentially "right out of the box," experimental implementations of HZD running controllers did not. In a number of experiments RABBIT was able to achieve five or six consecutive running steps, but no more than six were ever observed. The writeup of the experiments in [101] points to unmodeled boom dynamics, a walking surface with inconsistent stiffness, and the limited joint space of the robot as unforseen reasons that stable running did not occur in the two weeks allotted for experiments. Perhaps more significant than all of these, though, is the simple fact that the performance requirements for running using the constraint-based controllers of [31] were simply too near to the physical limitations of what RABBIT is capable of achieving. This conclusion is something of a double-edged sword. Is RABBIT incapable of running, or are the demands of the controllers presented in [31] unreasonably high? Neither explanation is satisfying, but both contain some element of truth. As a participant in the running experiments, it is the opinion of this author that in all likelihood RABBIT is capable of stable running under the constraint-based controllers of Chevallereau, Westervelt, and Grizzle. However, it is also the opinion of this author that if (or when) stable running is achieved on RABBIT the robust stability to model perturbations and external disturbances observed in planar walking will not be present in running. The relatively large

vertical deviations of the center of mass and high velocities typically seen in running in animals are difficult to achieve for robots such as RABBIT. Without springs to store energy or favorable natural dynamics, energy losses at toe strikes and actuator effort wasted doing negative work will hinder the robot's ability to run stably and gracefully.

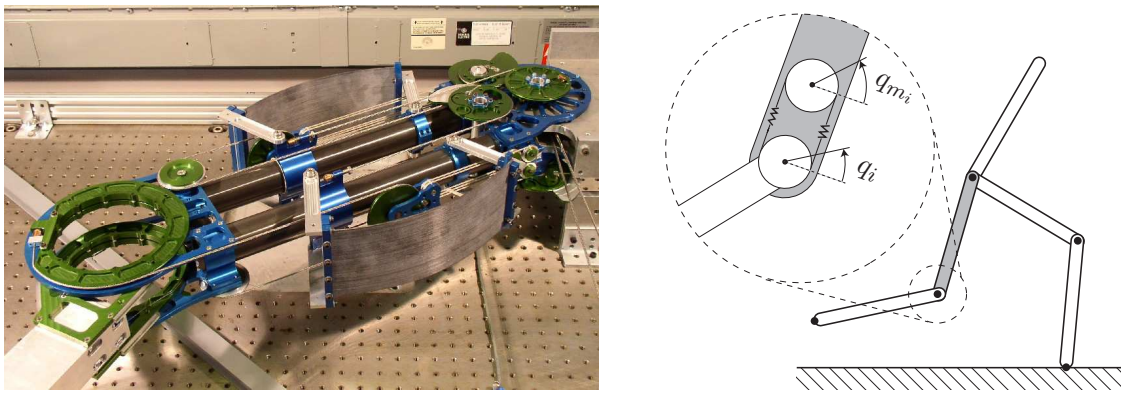

Figure 1.1: A picture of the AMASC actuator and a diagram of its potential use in a biped. Pictured at left is the AMASC actuator [76], designed by Jonathan Hurst at Carnegie Mellon University. The purpose of the AMASC is to mechanically store significant amounts of energy and to introduce compliance into an otherwise rigid mechanism. At right is a schematic diagram showing how such an actuator might be included into the design of a biped. While based on similar principles, the compliance mechanism of MABEL is significantly more complex than shown here.

In response to the experiments in Grenoble, a collaborative effort was begun between researchers at the University of Michigan and Carnegie Mellon University. With their expertise in robotics, contributors from Carnegie Mellon University would improve upon RABBIT's design, building a new planar bipedal robot that was more well-suited for the highly dynamic task of running. With hardware aspects of the projects in good hands, contributors from the University of Michigan would continue to research new methods in gait and controller design for bipedal running. The biped MABEL, designed by Jonathan Hurst at Carnegie Mellon, features series compliant actuators, in which a motor is separated from the joint it actuates by a large series spring. See Figure 1.1 for a graphical illustration.

1.4 Organization of Dissertation

In light of experiments on RABBIT and in preparation for the new robot MABEL, this thesis develops extensive new design tools that address the performance limiting aspects of previous HZD controllers. To this end, the remainder of this dissertation is organized into ten chapters and one appendix.

To provide the appropriate background from which to view the current work, Chapter 2 gives an overview of relevant literature in legged locomotion, highlighting philosophies and tools of research used by three major schools of thought. Setting the stage for theorem and proof, Chapter 3 establishes the technical background relevant to the method of hybrid zero dynamics. The formalism of systems with impulse effects, the definition of a solution, and rigorous descriptions of stability are summarized with original sources cited. Following earlier derivations in [153] and [31], Chapter 4 derives models of walking and running in N-link rigid planar bipeds with one degree of underactuation. These models will be used extensively through Chapter 9 where a model with compliance is developed.

Original work of this thesis begins in Chapter 5 where results are reported for the September 2004 constraint-based running experiments conducted on the French biped RABBIT housed in Grenoble, France.[7] The conclusion of this chapter sets the tone for the remainder of the document: performance limiting aspects of both RABBIT's hardware and the control methodology of HZD running need to be addressed before stable human-like running will be observed under constraint-based control. Of particular interest are the transition-on-landing controllers used in the reported running experiment. More formal versions of these controllers are seen in Chapter 6, Chapter 7, Chapter 8, and ultimately provide a rigorous controller for the capstone example in Chapter 9.

Original work continues with connections between passive dynamic walking and HZD controllers being explored in Chapter 6.[8] This chapter also analyzes the general case of walking on a slope, gives the closed-form inverse of the decoupling matrix of walking, and investigates a type of dynamic singularity that results from conservation properties of angular momentum.

[7] The contents of this Chapter 5 are taken, with minimal modification, from the book chapter [101] entitled "Achieving Bipedal Running with RABBIT: Six Steps toward Infinity" by B. Morris, E.R. Westervelt, C. Chevallereau, G. Buche, and J. W. Grizzle. Co-authored material used by permission.

[8] The contents of Chapter 6 are taken, with minimal modification, from the journal article [154] entitled "Analysis Results and Tools for the Control of Planar Bipedal Gaits using Hybrid Zero Dynamics" by E. R. Westervelt, B. Morris, and K. D. Farrell. Co-authored material used by permission.

In conjunction with deriving smooth stabilizing controllers, Chapter 7 presents two new sets of hypotheses under which reduced dimensional Poincaré maps can be used for low dimensional stability tests. The method of hybrid zero dynamics, as presented in [153] for the control of planar walking, assumed that any actuator dynamics were sufficiently fast that they could be neglected in the controller design process. Finite-time controllers were used to stabilize the associated transverse dynamics, resulting in a non-Lipshitz closed-loop system. Under the controller of Chapter 7, the stabilized transverse dynamics are not only Lipschitz continuous, but arbitrarily smooth. Accompanying stability tests are presented under two sets of hypotheses: one dependent on the existence of a special set of coordinates, the other coordinate-free.

Chapter 8 presents a new, constructive method for achieving the property of impact invariance on which the controllers of Chapter 7 depend. A set of sufficient conditions and a detailed procedure are provided for the construction of a suitable set of output functions that lead to the creation of an impact invariant manifold. In previous work on the HZD of running, nonconstructive methods were used to achieve impact invariance. In a scheme based on transition polynomials, the new method of achieving impact invariance significantly reduces the computational burden otherwise faced by a control designer searching for invariant manifolds.

Chapter 9 contains a capstone example of walking in a biped with series compliance, tying together virtually every result developed in previous chapters: the need for springs as motivated by Chapter 5, the transition polynomials of Chapter 6, the stability tests of Chapter 7, and the parameterization of Chapter 8. Conclusions and final remarks are given in Chapter 10, with Appendix A containing relevant proofs of the theorems and corollaries presented in Chapter 3, Chapter 7, and Chapter 8.

CHAPTER 2

Survey of Related Literature

To compare and contrast existing literature with the contents of this thesis, a few of the more dominant trends in bipedal locomotion will now be examined. This survey is not intended to be exhaustive, but rather to provide a representative cross section showing both the breadth and the depth of ongoing projects in bipedal locomotion, emphasizing a correlation between robot morphologies and control tools. For more complete histories of legged locomotion, see [142, 114, 89, 119, 14, 148, 73].

Three classes of research in bipedal locomotion will be briefly reviewed: analytical approaches to locomotion, the ZMP (zero moment point) criterion, and passive dynamic walkers. Boundaries between these groups are often blurred, but they nevertheless represent a few of the dominant approaches driving research in robotic locomotion. The first group, the camp of formal stability theory, focuses on the use of rigorous mathematical methods in the procedures of gait design, controller derivation, and stability proof. Analytically proving the stability of dynamic walking and running motions can be relatively difficult, stemming from the multi-phase, hybrid nature of the problem and the mathematical precision involved in the formulation of relevant theorems and proofs. For this reason many researchers choose to study static or quasi-static walking using the ZMP criterion, forming a second major trend in bipedal locomotion research. Here trajectory tracking controllers are coupled with online gait modification schemes to achieve quasi-static walking gaits that keep the robot upright, but often at the cost of producing a slow, crouching motion. A third group of researchers follows in the footsteps of Tad McGeer, studying robots that require no actuation other than gravity to walk stably down a slope. With no active control whatsoever, passive dynamic

walkers produce elegant, human-like gaits with maximal efficiency, but with minimal versatility of locomotion behavior.

The following sections examine these three methodologies in greater detail, highlighting research philosophies, common tools, and explaining a few of the notable experimental successes of each group. Because the work of this thesis is so closely tied to the context of hybrid zero dynamics and provable stability, more emphasis will be placed on reviewing this area than the other two.

2.1 Formal Stability Analysis

The body of work on formal stability analysis of bipedal locomotion is characterized primarily by an emphasis on mathematical rigor and by the use of a common set of mathematical tools including the modeling formalism of systems with impulse effects and the method of Poincaré sections.

Systems with impulse effects are a commonly used modeling formalism [12], consisting of a continuous portion modeled by the flow of a differential equation and a discrete portion modeled by a state reset map. In the context of legged locomotion, steady-state walking or running gaits are modeled as periodic orbits occurring in systems with impulse effects. For the rigorous definition of a solution in the presence of nonsmooth impacts, see [21]. Continuous phase dynamics are typically modeled in the canonical form presented in [102] and [134], with rigid collisions often treated using the impact map of [74]. See [73] for a literature review addressing systems with impulse effects and other common frameworks of modeling bipedal walking.

Essential to the formal stability analysis of legged locomotion is the method of Poincaré sections, as it is nearly the only way to establish the property of provable stability of a walking or running motion. Parker and Chua have authored an introductory reference to the method of Poincaré in the context of chaotic systems [106], and Hiskens provides a general development of hybrid trajectory sensitivities for systems with impulse effects [70]. Numerical studies using the method of Poincaré are common and too numerous to list. In contrast, *analysis* on the Poincaré map is much more limited. Koditschek and Buehler examine an idealized model of Raibert's hopper [88], simplifying analysis by examining the regulation of energy. Using the method of Poincaré sections, Espiau and Goswami study the stability of the two-link walker in [45] and together with Thuilot, identify chaos in [57]. A three-link planar biped with one degree of underactuation is analyzed

by Grizzle, Abba, and Plestan in [60] and extended to planar models with N links by Westervelt, Grizzle, and Koditschek in [153].

To accompany hybrid modeling formalisms and the method of Poincaré sections, several control tools are used to simplify the subsequent analysis. Some of the more commonly used methods are partial feedback linearization [131], sliding mode and finite time controllers [143, 16], continuous phase zero dynamics (or abstractions thereof) [23, 77, 22, 123, 47], virtual constraints [29, 25], passivity-based control and energy shaping [136, 5, 104], numerical optimization [99, 151], immersion and invariance [10], controlled symmetries [133], Routhian reductions [8], port Hamiltonians [42, 64], and linear matrix inequalities [128].

Because the work of this thesis is so closely tied to previous results in hybrid zero dynamics, an extended review of HZD-specific results is now provided. In the notable work of [60] by Grizzle, Abba, and Plestan a three-link planar biped with one degree of underactuation was analyzed in detail. Using techniques of zero dynamics in conjunction with a finite-time controller [16], a 1D restricted Poincaré map was derived to check the stability of walking over flat ground. The biped model, written as a system with impulse effects, was developed using standard continuous-phase dynamics [102] and Hürmüzlü's rigid body impact map [74]. Ideas of this work are extended further in [153], where Westervelt, Grizzle, and Koditschek develop the notion of a *hybrid zero dynamics* (HZD): a powerful analytical tool resulting in a restricted, lower dimensional *system* and not just a restricted *Poincaré map*. Techniques of optimization of HZD's were published by Westervelt and Grizzle in [151], where SQP optimization was used to choose virtual constraint parameters that resulted in stable gaits. Conditions such as joint limitations, gait stability, and boundary conditions were represented as constraints of optimization. One of the major benefits of using hybrid zero dynamics is that optimization can be performed directly on the parameters of the controller to simultaneously determine a periodic walking or running motion and a controller that achieves it. In this sense, the optimizer searches directly over parameterized closed-loop systems to find one that exhibits a desired behavior and is approximately optimal with respect to some criterion.

Initial work in hybrid zero dynamics has been extended to a much broader domain of robot models. The method was extended to encompass walking in robots with rotating feet in [34] and impulsive feet in [33], both by Choi and Grizzle. It is shown that the dimension reduction techniques of hybrid zero dynamics are also valid in systems having full actuation, specifically walkers with

actuated ankles. The hybrid zero dynamics theory of running was presented in [31] by Chevallereau, Westervelt, and Grizzle, in which an HZD of running was constructed by generating a deadbeat parameter update scheme that regulated the robot so that it would land in a desired configuration. Finite time controllers were used in the stance phase to ensure that the stability analysis performed on the hybrid zero dynamics would extend to the full model. In both theory and practice, running was found to be more difficult than walking. Running was attempted on RABBIT in 2004 using a variant of hybrid zero dynamics control. Although numerous consecutive steps were observed, a stable gait was not achieved; see the experimental results reported in [101]. Recently, principles of hybrid zero dynamics have been used in conjunction with passive dynamic gaits and Routhian reductions to achieve quasi-3D walking by Ames and Gregg in [8].

The utility of mathematically rigorous methods is not limited to just theorem and proof. Demonstrations of provably stable walking controllers have been observed on RABBIT and ERNIE. Designed and constructed by the French group ROBEA, the planar robot RABBIT was designed with point feet (and without ankles) to encourage advances in control theory. At rest RABBIT stands 1.5 m tall, has two symmetric legs with knees and hips actuated by electric motors through harmonic gear reducers. The most popular method of controlling such a robot would ordinarily be to use the ZMP, which relies on ankle torque to effect changes in the distribution of ground reaction forces on the stance foot. Without ankles, this technique cannot be applied. Sill, RABBIT has walked successfully under controllers that are fundamentally different from control of the ZMP. Stable walking at 1.0 m/s was achieved in March 2003 using hybrid zero dynamics and virtual constraints [149, 29]. Other robots designed and built without ankles are BIRT and ERNIE constructed at the Ohio State University. BIRT [126, 19] is a freestanding three-legged robot with the outer two legs coordinated by feedback control. ERNIE has a similar mass distribution as BIRT but with only two legs. Like RABBIT it is attached to a boom. Both BIRT and ERNIE were designed without ankles to encourage innovation in control.

2.2 The Zero Moment Point Criterion

The ZMP criterion is an intuitive argument that was proposed in the late 1960's by Vukobratović et al. [148, 146]. It states that as long as the zero moment point[1] of a robot remains strictly within the interior of the support polygon formed by the robot's foot (feet), then the robot cannot fall by tipping over the edges of its foot (feet). When the robot does not tip, the contact of the robot with the ground can be idealized as a rigid connection to the global frame, and various tracking techniques can be applied to provide joint coordination [115, 4, 58]. See the anniversary paper [146] by Vukobratović and Borovac for an overview of the method.

Owing to its simplicity and potential for application in high DOF freestanding robots, the ZMP has inspired several variants. A related notion is the FRI (Foot Rotation Index) by Goswami [54], and the CoP (center of pressure) explored by Sardain and Bessonnet in [124]. Such connections are sometimes highly contested as in the confrontational work of [147]. Experimental results of Erbatur et al. [44] examine the validity of the ZMP by taking data from human walking. A frequency domain representation of the ZMP has also been developed [24].

One benefit of using the ZMP is that it provides a simple, physically oriented metric to evaluate how close a robot is to tipping over. Researchers more interested in human-robot interaction, the design of anthropomorphic hardware, or online gait synthesis can conduct experiments without having to acquire an expertise in nonlinear control theory as well. But, a distinct drawback of the ZMP is that many trials are often required before success, and successes on one robot are often only weakly transferrable to another. Furthermore, from the standpoint of formal control theory, satisfaction of the ZMP criterion is neither necessary nor sufficient for stability as described in Chapter 3 of this thesis. Analysis and experiment on RABBIT [150] have proven non-necessity, and a computational example in Choi's thesis [32] proves nonsufficiency in the absence of a higher-level supervising controller.

Formal theory aside, ZMP-based control has been successfully used in a number of robots worldwide. One of the most well-known biped robots is ASIMO, Honda's signature humanoid. To date, ASIMO has made public appearances opening the New York Stock exchange[2], danced for

[1] The zero moment point is a point on the walking surface about which the net moment of the forces on the robot is zero, including inertial forces due to acceleration.

[2] "Adding the Android Touch" The New York Times, February 15, 2002.

US daytime television[3], and visited children worldwide[4]. ASIMO itself is the result of two decades of research by Honda into humanoid robotics. Work began with the E0 in 1986, continued through E1-E6, P1-P3, and finally to ASIMO in 2000; see [72]. As remarked in [71], the world's first self-regulating biped was Honda's P2. In the P2 biped a supervised ZMP-based scheme was implemented where three types of controllers interacted to achieve posture stabilization [67]: ground reaction force control, model ZMP control, and foot landing position control. Controllers were developed by idealizing the robot as an inverted pendulum and using trajectory tracking on the individually actuated joints. Improvements made from the P2 to the P3 are discussed in [66]. System specifications[5] for ASIMO are available in [121] with high level footstep planning algorithms available at [98]. In December 2004, ASIMO achieved running at 3 km/h (0.8 m/s) with a 50 ms flight phase using a controller based on posture control. A year later, in December 2005, ASIMO ran at 6 km/h (1.6 m/s) with a flight phase of 80 ms. Stable walking has been achieved at 2.7 km/h (0.75 m/s) [72].

Originally sponsored by Honda, and later by Japan's METI (Ministry of Economy, Trade and Industry) and NEDO, the Humanoid Robotics Project (HRP) has the stated goal of "investigating the applications of a humanoid robot for the maintenance tasks of industrial plants and security services of home and office" [68]. The project has produced a number of bipeds including HRP-1, HRP-1S [161], HRP-2L [81, 83], HRP-2A, HRP-2P [84], and HRP-2, with hardware descriptions and control software architecture described in [68]. Detailed descriptions of HRP-1S are available in [161] including the experimental success of walking at 0.25 m/s over uneven ground. Experiments relating to HRP-2 stepping over obstacles are in [145] and simulations of complex collision avoidance are in [162]. In early 2004, running was announced for HRP-2LR [82] using a controller based on a technique of resolved momentum.

Sony's QRIO is an example of a bipedal entertainment robot that utilizes ZMP control for walking [51]. At 58 cm tall, QRIO features 38 flexible joints and 4 pressure sensors on each of its feet. In addition to using the ZMP for walking and balance, neural oscillator CPG control has been successfully applied on QRIO [43].

[3]The Ellen DeGeneres show, February 10, 2006

[4]See http://world.honda.com/ASIMO/event/

[5]For the level of sophistication to which Honda's humanoid robot project has grown, relatively few details have been officially published of the control algorithms governing walking and running.

In addition to these popular humanoid walkers of the private sector, the biped JOHNNIE at TUM is an example of an academic biped using the ZMP as its primary method of control. For an overview of the hardware design and controller objectives of Johnnie see [52, 107]. For experimental demonstrations of walking at speeds up to 0.67 m/s, see [94].

2.3 Passive Dynamics and Minimal Actuation

Strongly influenced by the pioneering work of McGeer [96, 95] in the 1990's, researchers that study passive dynamic walking build or simulate robots that walk on gentle slopes without active feedback control or energy input aside from gravity. In simulation studies, candidate walking gaits are found using numerical optimization or root finding techniques, with stability determined numerically by estimating the eigenvalues of the Jacobian linearization of the Poincaré map. Typically, this is a testing-only procedure whereby walking motions are deemed either stable or unstable—the stability test is not a procedure for generating stable motions.

A thorough analysis of passive bipedal walking is given by Garia et al. in [50], where simulation shows stable period-one gaits doubling to period-two gaits in the presence of increased slopes, with continued period doubling until the onset of chaos. Hürmüzlü and Moskowitz study a similar model in [75], examining the role of impacts in achieving stable motions. In a separate effort, Goswami et al. also demonstrate period doubling to bifurcation with extensive analysis and simulation of a two-link walker with prismatic knees [57]. Experimental successes include that of Collins, Wisse, and Ruina where a 3D fully passive walker was able to walk stably down a slope of 3.1 degrees [39].

Extensions have been made to add minimal actuation to the paradigm of passive dynamic walking, allowing walking on flat ground. A biped similar to the 3D walker of [39] was later constructed by Collins [37] and featured minimal actuation in the form of a winding and releasing toe-off spring. The biped was able to walk stably on flat ground at a rate of 0.44 m/s with an energetic cost of transport similar to that of a human. In a similar effort, Wisse has produced a number of minimally actuated bipeds, many with small pneumatically powered actuators called McKibben muscles [144]. A 3D biped with yaw and roll compensation was simulated in [157] stably walking at 0.5 m/s on flat ground. A key conclusion of passive planar walking is given in [156] by the simple rule "You

will never fall forward if you put your swing leg fast enough in front of your stance leg. In order to prevent falling backward the next step, the swing leg shouldn't be too far in front." The concept was tested on a planarized walker called Mike, showing this simple control law to dramatically enlarge the basin of attraction over that of a passive walker. See [155] by Wisse and [38] by Collins, Ruina, Tedrake, and Wisse for additional examples of walkers that utilize minimalist control and actuation for walking on flat ground.

Passive dynamics can also be used as a point of departure for further investigations. Elements of passive dynamics are tied with learning control in Tedrake's 3D biped Toddler [139, 140]. In a similar marriage of fields, Kuo et al. examine the energetics of bipedal walking in relation to the metabolic cost of human walking [91, 93]. A recent article by Kuo highlights the tradeoffs between performance and versatility in legged locomotion [92].

2.4 Marc Raibert

No review of locomotion literature would be complete without mentioning Raibert's fundamental contributions. First at the CMU Leg Lab and then at the MIT Leg Lab, Marc Raibert was a pioneer in the use of natural dynamics in the design and control of legged machines. Raibert designed machines with light legs, prismatic knees, and a majority of body mass concentrated at the hips. His controllers focused on the regulation of physically motivated, intuitive quantities such as hopping height, touchdown angle, and body angle. With this philosophy of design and control, Raibert successfully demonstrated running on his 2D and 3D hopper prototypes. The top recorded speed of the 3D hopper was an impressive 2.2 m/s. His widely cited 1986 book [114] is a cornerstone of legged locomotion.

When robots have favorable natural dynamics and an appropriate morphology, use of Raibert's controllers (or a variant thereof) could be applied to achieve stable running. However, in the case that a robot's natural dynamics or its morphology are slightly different (either by the use of electric motors for actuation or the introduction of massive legs, for instance) Raibert's controllers are no longer sufficient to provide stability. In many ways they have no *obvious* extensions to bipeds with more general mass distributions or link morphologies. Despite what is claimed in [110], the problem of running was not "mostly solved" by Raibert. While their usefulness is remarkable,

Raibert's methods have their limitations, as do all approaches to bipedal locomotion. As a whole, the field of legged locomotion is relatively new, largely open, always ripe for new results.

CHAPTER 3

Technical Background

The development of provably stable controllers requires proficiency in a basic set of mathematical tools. In preparation for the analysis of later chapters, this chapter reviews technical material in five areas: the formalism of systems with impulse effects, periodic orbits within such systems, the definition of the Poincaré return map, principles of hybrid invariance, and notions of relative degree.

3.1 Systems with Impulse Effects

Systems with impulse effects will be used to model the inherently hybrid nature of walking and running in legged machines. Systems with impulse effects have a continuous phase, described by the flow of a differential equation, and a discrete phase, described by an instantaneous state reset event. See [12] for a more detailed description. To define a C^1 control system with impulse effects, consider a nonlinear affine control system

$$\dot{x} = f(x) + g(x)u, \tag{3.1}$$

where the state manifold $\mathcal{X}$ is an open connected subset of $\mathbb{R}^n$, the control input u takes values in $\mathcal{U} \subset \mathbb{R}^m$, and f and the columns of g are C^1 vector fields on $\mathcal{X}$. An impact (or switching) surface, $\mathcal{S}$, is a codimension one C^1 submanifold with $\mathcal{S} = \{x \in \mathcal{X} \mid H(x) = 0,\ H_0(x) > 0\}$ where $H_0 : \mathcal{X} \to \mathbb{R}$ is continuous, $H : \mathcal{X} \to \mathbb{R}$ is C^1, $\mathcal{S} \neq \emptyset$, and $\forall x \in \mathcal{S}$, $\frac{\partial H}{\partial x}(x) \neq 0$. An impact (or reset) map is a C^1 function $\Delta : \mathcal{S} \times \mathcal{V} \to \mathcal{X}$, $\mathcal{V} \subset \mathbb{R}^p$, $p \geq 0$ where $\mathcal{S} \cap \Delta(\mathcal{S} \times \mathcal{V}) = \emptyset$, that is, where the image of the impact map is disjoint from its domain. A C^1 *control system with impulse*

effects has the form

$$\Sigma : \begin{cases} \dot{x} &= f(x) + g(x)u & x^- \notin \mathcal{S} \\ x^+ &= \Delta(x^-, v) & x^- \in \mathcal{S}, \end{cases} \tag{3.2}$$

where $v \in \mathcal{V}$ is a control input for the impact map, and x^- and x^+ are the left and right limits of the solution of the system. A system with inputs into the vector field but not into the impact map,

$$\Sigma : \begin{cases} \dot{x} &= f(x) + g(x)u & x^- \notin \mathcal{S} \\ x^+ &= \Delta(x^-) & x^- \in \mathcal{S}, \end{cases}$$

can be written as a special case of (3.2) with $\mathcal{V} = \emptyset$. Replacing the control system (3.1) with an autonomous system

$$\dot{x} = f(x) \tag{3.3}$$

and taking $\mathcal{V} = \emptyset$ leads to a C^1 *autonomous system with impulse effects*,

$$\bar{\Sigma} : \begin{cases} \dot{x} &= f(x) & x^- \notin \mathcal{S} \\ x^+ &= \Delta(x^-) & x^- \in \mathcal{S}. \end{cases} \tag{3.4}$$

For compactness of notation, an autonomous system with impulse effects (3.4) will be denoted as a 4-tuple, $\bar{\Sigma} = (\mathcal{X}, \mathcal{S}, \Delta, f)$, while a control system with impulse effects (3.2) will be denoted as a 7-tuple, $\Sigma = (\mathcal{X}, \mathcal{S}, \mathcal{V}, \mathcal{U}, \Delta, f, g)$.

Denote the solution of a system with impulse effects (3.2) or (3.4) as[1] $\varphi(t, t_0, x_0)$, for $t > t_0$ and $x_0 \in \mathcal{X}$. The solution is specified by the flow of the differential equation (3.1) or (3.3) until its state intersects the hypersurface $\mathcal{S}$ at some time t_I. At t_I, application of the impact model Δ results in a discontinuity in the state trajectory. The impact model provides the new initial condition from which the differential equation evolves until the next impact with $\mathcal{S}$. In order to avoid the state having to take on two values at the impact time, the impact event is, roughly speaking, described in terms of the state just prior to impact $x^- = \lim_{\tau \nearrow t_I} \varphi(\tau, t_0, x_0)$ and the state just after impact $x^+ = \lim_{\tau \searrow t_I} \varphi(\tau, t_0, x_0)$. From this description, a formal definition of a solution is written down by piecing together appropriately initialized solutions of (3.1) or (3.3); see [160, 60, 103, 27]. A choice must be made whether a solution is a left- or a right-continuous function of time at each impact event; here, solutions are assumed to be right continuous.

[1]The solution will sometimes be denoted $\varphi(t, x_0)$ where it is implicitly assumed that $t_0 = 0$.

3.2 Periodic Orbits

Cyclic behaviors such as walking and running are represented as periodic orbits of systems with impulse effects. A solution $\varphi(t, t_0, x_0)$ of is *periodic* if there exists a finite $T > 0$ such that $\varphi(t + T, t_0, x_0) = \varphi(t, t_0, x_0)$ for all $t \in [t_0, \infty)$. A set $\mathcal{O} \subset \mathcal{X}$ is a *periodic orbit* if $\mathcal{O} = \{\varphi(t, t_0, x_0) \mid t \geq t_0\}$ for some periodic solution $\varphi(t, t_0, x_0)$. While a system with impulse effects can certainly have periodic solutions that do not involve impact events, they are not of interest here because they could be studied more simply as solutions of (3.3) or (3.1). If a periodic solution has an impact event, then the corresponding periodic orbit $\mathcal{O}$ is not closed; see [60, 100]. Let $\bar{\mathcal{O}}$ denote the set closure of $\mathcal{O}$. A periodic orbit $\mathcal{O}$ is *transversal* to $\mathcal{S}$ if its closure intersects $\mathcal{S}$ in exactly one point, and for $x^* = \bar{\mathcal{O}} \cap S$, $L_f H(x^*) = \frac{\partial H}{\partial x}(x^*) f(x^*) \neq 0$ (in words, at the intersection, $\bar{\mathcal{O}}$ is not tangent to $\mathcal{S}$).

Notions of stability in the sense of Lyapunov, asymptotic stability, and exponential stability of orbits follow the standard definitions; see [87, p. 302], [60, 103]. For convenience, these definitions are reviewed here. Given a norm $\|\cdot\|$ on $\mathcal{X}$, define the distance between a point x and a set $\mathcal{C}$ to be $\text{dist}(x, \mathcal{C}) = \inf_{y \in \mathcal{C}} \|x - y\|$. A periodic orbit $\mathcal{O}$ is *stable in the sense of Lyapunov (i.s.L)* if for every $\epsilon > 0$ there exists $\delta > 0$ such that such that, $\forall\, t \geq 0$,

$$\text{dist}(\varphi(t, x_0), \mathcal{O}) \leq \epsilon,$$

whenever $\text{dist}(x_0, \mathcal{O}) < \delta$. A periodic orbit is *asymptotically stable* if it is stable i.s.L and

$$\lim_{t \to \infty} \text{dist}(\varphi(t, x_0), \mathcal{O}) = 0,$$

whenever $\text{dist}(x_0, \mathcal{O}) < \delta$. A periodic orbit is *exponentially stable* if there exists $\delta > 0$, $N > 0$, and $\gamma > 0$ such that $\forall\, t \geq 0$,

$$\text{dist}(\varphi(t, x_0), \mathcal{O}) \leq N e^{-\gamma t}\, \text{dist}(x_0, \mathcal{O}),$$

whenever $\text{dist}(x_0, \mathcal{O}) < \delta$.

3.3 Poincaré Return Map

The method of Poincaré sections and return maps is widely used to determine the existence and stability of periodic orbits in a broad range of system models, such as time-invariant and

periodically-time-varying ordinary differential equations [106, 62], hybrid systems consisting of several time-invariant ordinary differential equations linked by event-based switching mechanisms and re-initialization rules [60, 103, 120], differential algebraic equations [69], and relay systems with hysteresis [53], to name just a few. While the analytical details can vary significantly from one class of models to another, on a conceptual level, the method of Poincaré is consistent and straightforward: sample the solution of a system according to an event-based or time-based rule, and then evaluate the stability properties of equilibrium points (also called fixed points) of the sampled system, which is called the Poincaré return map. To define an event-based sampling rule, a Poincaré section $\mathcal{S}$ is chosen, and the value of the Poincaré return map is defined as subsequent intersections of the system solution with the Poincaré section; see Figure 3.1 and Figure 3.2. Fixed points of the Poincaré map correspond[2] to *periodic orbits* of the underlying system.

The advantage of the method of Poincaré is that it reduces the study of periodic orbits to the study of equilibrium points, with the latter being a more extensively studied problem. The analytical challenge when applying the method of Poincaré lies in calculating the return map, which, for a typical system, is impossible to do in closed form because it requires the solution of a differential equation. Certainly, numerical schemes can be used to compute the return map, find its fixed points, and estimate eigenvalues for determining exponential stability. However, the numerical computations are usually time intensive, and performing them iteratively as part of a system design process can be cumbersome. A more important drawback is that the numerical computations are not insightful, in the sense that it is often difficult[3] to establish a direct relationship between the parameters that a designer can vary in a system and the existence or stability properties of a fixed point of the Poincaré map.

In the study of periodic orbits in systems with impulse effects, it is natural to select the impact surface as the Poincaré section. To define the return map, let $\phi(t, x_0)$ denote the maximal solution of (3.3) with initial condition x_0 at time $t_0 = 0$. The *time-to-impact* function, $T_I : \mathcal{X} \to \mathbb{R} \cup \{\infty\}$,

[2]Fixed points of $P^k = P \circ \cdots \circ P$ k-times also correspond to periodic orbits. The associated analysis problems for $k > 1$ are essentially the same as for $k = 1$ and are not discussed further.

[3]Of course, "difficult" does not mean "impossible". There have been success with numerical implementations of Poincaré methods in the passive-robot community in terms of finding parameter values—masses, inertias, link lengths—for a given robot that yield asymptotically stable periodic orbits [54, 141, 90, 39].

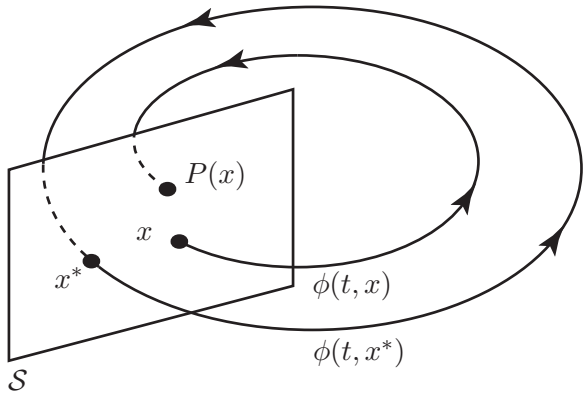

Figure 3.1: Geometric interpretation of a Poincaré return map for an ODE (non-hybrid) system. The return map is an event-based sampling of the solution near a periodic orbit. The Poincaré section, $\mathcal{S}$, can be any codimension one C^1 hypersurface that is transversal to the periodic orbit.

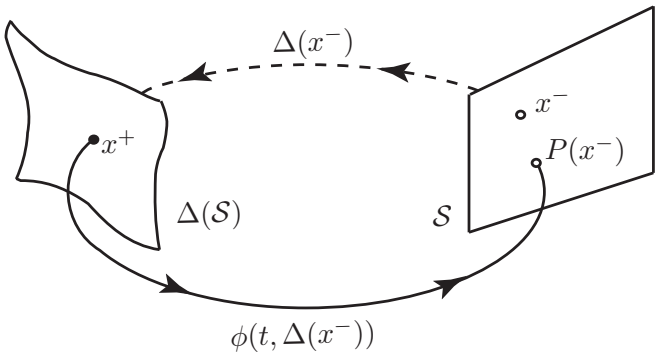

Figure 3.2: Geometric interpretation of a Poincaré return map for a system with impulse effects. The Poincaré section is selected as the switching surface, $\mathcal{S}$. A periodic orbit exists when $P(x^-) = x^-$. Due to right-continuity of the solutions, x^- is not an element of the orbit. With left-continuous solutions, $\Delta(x^-)$ would not be an element of the orbit.

is defined by

$$T_I(x_0) = \begin{cases} \inf\{t \geq 0 | \phi(t, x_0) \in \mathcal{S}\} & \text{if } \exists\, t \text{ such that } \phi(t, x_0) \in \mathcal{S} \\ \infty & \text{otherwise.} \end{cases}$$

The Poincaré return map, $P : \mathcal{S} \to \mathcal{S}$, is then given as the partial map

$$P(x) = \phi(T_I \circ \Delta(x), \Delta(x)). \tag{3.5}$$

For convenience, define the partial mapping

$$\phi_{T_I}(x) = \phi(T_I(x), x)$$

so that the Poincaré return map can be written as

$$P(x) = \phi_{T_I} \circ \Delta(x).$$

For a C^1 system with impulse effects, P is differentiable at x^*, so long as the orbit is transversal to the impact surface. Indeed, the differentiability of T_I is proven in [106, App. D] at each point of $\tilde{\mathcal{S}} = \{x \in \mathcal{S} \mid T_I(x) < \infty \text{ and } L_f H(P(x)) \neq 0\}$. From this, the differentiability of Δ and f prove that P is differentiable on $\tilde{\mathcal{S}}$. Hence, exponential stability of orbits can be checked by linearizing P at x^* and computing eigenvalues. The following theorem, different versions of which appear in [106, 60, 103, 100], relates the stability of fixed points of the return map (3.5) to the stability of periodic orbits in systems with impulse effects.

Theorem 3.1 (Method of Poincaré Sections for Systems with Impulse Effects)**.** *If the C^1 autonomous system with impulse effects $\bar{\Sigma} = (\mathcal{X}, \mathcal{S}, \Delta, f)$ has a periodic orbit $\mathcal{O}$ that is transversal to $\mathcal{S}$, then the following are equivalent:*

i) x^* is an exponentially stable (resp., asymp. stable, or stable i.s.L.) fixed point of P;

ii) $\mathcal{O}$ is an exponentially stable (resp., asymp. stable, or stable i.s.L.) periodic orbit.

3.4 Hybrid Invariance and Restriction Dynamics

The notion of continuous phase zero dynamics, forward invariant manifolds, and functional equivalents thereof are relatively common in the locomotion literature [23, 77, 22, 123, 47]. A

novel contribution of the work of Westervelt, Grizzle, and Koditschek in [153] is the coupling of this idea with the concept of *impact invariance* to form the principle of *hybrid invariance*. Types of invariance (for autonomous systems with impulse effects) and controlled invariance (for control systems with impulse effects) will now be reviewed.

For an autonomous system with impulse effects $\bar{\Sigma} = (\mathcal{X}, \mathcal{S}, \Delta, f)$, a submanifold $\mathcal{Z} \subset \mathcal{X}$ is *forward invariant* if for each point x in $\mathcal{Z}$, $f(x) \in T_x\mathcal{Z}$. A submanifold $\mathcal{Z}$ is *impact invariant* in an autonomous system with impulse effects $\bar{\Sigma} = (\mathcal{X}, \mathcal{S}, \Delta, f)$ or in a control system with impulse effects $\Sigma = (\mathcal{X}, \mathcal{S}, \emptyset, \mathcal{U}, \Delta, f, g)$, if for each point x in $\mathcal{S} \cap \mathcal{Z}$, $\Delta(x) \in \mathcal{Z}$. A submanifold $\mathcal{Z}$ is *hybrid invariant* if it is both forward invariant and impact invariant. In a control system with impulse effects $\Sigma = (\mathcal{X}, \mathcal{S}, \mathcal{V}, \mathcal{U}, \Delta, f, g)$, a submanifold $\mathcal{Z}$ is *controlled forward invariant* if there exists a C^1 mapping $u : \mathcal{X} \to \mathcal{U}$ such that for each point x in $\mathcal{Z}$, $f(x) + g(x)u(x) \in T_x\mathcal{Z}$. A submanifold $\mathcal{Z}$ is *controlled impact invariant* if there exists a C^1 mapping $v : \mathcal{S} \to \mathcal{V}$ such that for each point x in $\mathcal{S} \cap \mathcal{Z}$, $\Delta(x, v(x)) \in \mathcal{Z}$. A submanifold $\mathcal{Z}$ is *controlled hybrid invariant* if it is both controlled forward invariant and controlled impact invariant.

If a C^1 embedded submanifold $\mathcal{Z}$ is hybrid invariant in an autonomous system with impulse effects $\bar{\Sigma}$ and $\mathcal{S} \cap \mathcal{Z}$ is C^1 with dimension one less than that of $\mathcal{Z}$, then

$$\bar{\Sigma}|_{\mathcal{Z}} : \begin{cases} \dot{z} &= f|_{\mathcal{Z}}(z) & z^- \notin \mathcal{S} \cap \mathcal{Z} \\ z^+ &= \Delta|_{\mathcal{S}\cap\mathcal{Z}}(z^-) & z^- \in \mathcal{S} \cap \mathcal{Z} \end{cases} \tag{3.6}$$

is called a *hybrid restriction dynamics* of the autonomous system $\bar{\Sigma}$, where $f|_{\mathcal{Z}}$ and $\Delta|_{\mathcal{S}\cap\mathcal{Z}}$ are the restrictions of f and Δ to $\mathcal{Z}$ and $\mathcal{S} \cap \mathcal{Z}$, respectively. If, in addition, the system $\bar{\Sigma}$ has a periodic orbit $\mathcal{O} \subset \mathcal{Z}$, then $\mathcal{O}$ is a periodic orbit of the hybrid restriction dynamics. The system (3.6) will sometimes be denoted as $\bar{\Sigma}|_{\mathcal{Z}} = (\mathcal{Z}, \mathcal{S} \cap \mathcal{Z}, \Delta|_{\mathcal{S}\cap\mathcal{Z}}, f|_{\mathcal{Z}})$. Hybrid invariance of $\mathcal{Z}$ implies that the Poincaré return map has the property that

$$P(\mathcal{S} \cap \mathcal{Z}) \subset \mathcal{S} \cap \mathcal{Z}. \tag{3.7}$$

On the basis of (3.7), the *restricted Poincaré map*, $\rho : \mathcal{S} \cap \mathcal{Z} \to \mathcal{S} \cap \mathcal{Z}$, is defined as $\rho = P|_{\mathcal{Z}}$, or equivalently,

$$\rho(z) = \phi|_{\mathcal{Z}}(T_I|_{\mathcal{Z}} \circ \Delta|_{\mathcal{S}\cap\mathcal{Z}}(z), \Delta|_{\mathcal{S}\cap\mathcal{Z}}(z)) = \phi_{T_I}|_{\mathcal{Z}} \circ \Delta|_{\mathcal{S}\cap\mathcal{Z}}(z). \tag{3.8}$$

3.5 Notions of Relative Degree

The differential geometric concept of relative degree [78] will be important for the derivation of a manifold $\mathcal{Z}$ having appropriate invariance properties. Associate an output with a given system with impulse effects

$$\Sigma : \begin{cases} \dot{x} &= f(x) + g(x)u \quad x^- \notin \mathcal{S} \\ x^+ &= \Delta(x^-, v) \qquad x^- \in \mathcal{S} \\ y &= h(x) \end{cases} \tag{3.9}$$

where $h : \mathcal{X} \to \mathbb{R}^q$. Recall that u takes values in $\mathcal{U} \subset \mathbb{R}^m$. A system with impulse effects is *square* if the number of inputs equals the number of outputs. For the following definition, let $h_i : \mathcal{X} \to \mathbb{R}$ with $1 \leq i \leq q$ refer to the individual scalar entries of the vector-valued function h, and let $g_i : \mathcal{X} \to \mathbb{R}^n$ refer to the columns of g.

Definition 3.2. *(Modified from [78]) The output h of a square system* (3.9) *has relative degree $\{r_1, \ldots, r_m\}$ at a point $x^\circ \in \mathcal{X}$ if $L_{g_j} L_f^k h_i(x) = 0$ for all $1 \leq j \leq m$, for all $k \leq r_i - 1$, for all $1 \leq i \leq m$, and for all x in a neighborhood of $\mathcal{X}$ containing x°. Define the decoupling matrix as*

$$\begin{pmatrix} L_{g_1} L_f^{r_1 - 1} h_1(x) & \ldots & L_{g_m} L_f^{r_1 - 1} h_1(x) \\ L_{g_1} L_f^{r_2 - 1} h_2(x) & \ldots & L_{g_m} L_f^{r_2 - 1} h_2(x) \\ \ldots & \ldots & \ldots \\ L_{g_1} L_f^{r_m - 1} h_m(x) & \ldots & L_{g_m} L_f^{r_m - 1} h_m(x) \end{pmatrix}.$$

If the decoupling matrix is invertible, then the output h is said to have vector relative degree $\{r_1, \ldots, r_m\}$ at the point x°. If in addition all values r_i are equal to a single value r, then the output h is said to have uniform vector relative degree r at the point x° and the decoupling matrix is equal to $L_g L_f^{r-1} h(x)$.

Unless otherwise stated it is assumed in the following chapters that the relative degree is the same for each output component. The developed results can be extended to systems with general vector relative degree, or to systems for which a vector relative degree is achievable by dynamic feedback; see [78]. If desired, the Lie derivatives used in the above definition can be expanded to a more familiar notation using the relationships $L_f h(x) = \left(\frac{\partial}{\partial x} h(x)\right) f(x)$, $L_f^2 h(x) = \left(\frac{\partial}{\partial x} L_f h(x)\right) f(x)$, $L_g L_f h(x) = \left(\frac{\partial}{\partial x} L_f h(x)\right) g(x)$, etc.

Notation Introduced in Chapter 3

Symbol	Meaning	Defined
x	state of a system with impulse effects	Section 3.1
$\mathcal{X}$	state manifold of a system with impulse effects	Section 3.1
u	vector of control inputs to the continuous flow	Section 3.1
$\mathcal{U}$	set of valid control inputs to the continuous flow	Section 3.1
f	drift vector field of a system with impulse effects	Section 3.1
g	control vector fields of a control system with impulse effects	Section 3.1
$\mathcal{S}$	switching surface of a system with impulse effects	Section 3.1
H, H_0	functions used in the definition of a switching surface	Section 3.1
Δ	impact map of a system with impulse effects	Section 3.1
v	vector input to the impact map	Section 3.1
$\mathcal{V}$	set of valid control inputs to the impact map	Section 3.1
Σ	a control system with impulse effects	Section 3.1
$\bar{\Sigma}$	an autonomous system with impulse effects	Section 3.1
t_I	time until the next impact event	Section 3.1
x^-	state of a system with impulse effects “just prior to impact”	Section 3.1
x^+	state of a system with impulse effects “just after impact”	Section 3.1

Symbol	Meaning	Defined
$\varphi(t, t_0, x_0)$	the solution of a system with impulse effects	Section 3.2
$\mathcal{O}$	a periodic orbit of a system with impulse effects	Section 3.2
$\bar{\mathcal{O}}$	set closure of a periodic orbit $\mathcal{O}$	Section 3.2
dist$(x_0, \mathcal{C})$	distance between a point $x_0 \in \mathcal{X}$ and a set $\mathcal{C} \subset \mathcal{X}$	Section 3.2
$\phi(t, x_0)$	solution of the autonomous system $\dot{x} = f(x)$ initialized at $t_0 = 0$ with initial state x_0	Section 3.3
T_I	the time to impact function (a partial mapping)	Section 3.3
ϕ_{T_I}	function returning the system state at the next impact (a partial mapping)	Section 3.3
P	the Poincaré return map (a partial mapping)	Section 3.3
$\mathcal{Z}$	A manifold potentially having invariance properties	Section 3.4
$f\|_{\mathcal{Z}}$	the drift vector restricted to the domain of $\mathcal{Z}$	Section 3.4
$\Delta\|_{\mathcal{S}\cap\mathcal{Z}}$	the impact map restricted to the domain of $\mathcal{Z}$	Section 3.4
$\bar{\Sigma}\|_{\mathcal{Z}}$	the autonomous system with impulse effects $\bar{\Sigma}$ restricted to the domain of $\mathcal{Z}$	Section 3.4
ρ	the Poincaré map restricted to $\mathcal{Z}$ (a partial mapping)	Section 3.4
$y = h(x)$	output vector of a system with impulse effects	Section 3.5
$h_i(x)$	reference to the i^{th} entry of $h(x)$	Section 3.5
$g_j(x)$	reference to the j^{th} column of $g(x)$	Section 3.5
$L_f h(x)$	Lie derivative of $h(x)$ w.r.t. the drift vector field	Section 3.5
$L_f^2 h(x)$	Lie derivative of $L_f h(x)$ w.r.t. the drift vector field	Section 3.5
$L_g L_f h(x)$	Lie derivative of $L_f h(x)$ w.r.t. the control vector fields	Section 3.5

CHAPTER 4

Models of Walking and Running in Planar Bipeds with Rigid Links

Following earlier derivations in [153] and [31], this chapter derives models of walking and running in N-link rigid planar bipeds with one degree of underactuation. Further assumptions are made as to the biped's morphology, the type and location of actuators, the ground model, and definitions of what it means to walk and run. The biped RABBIT (pictured in Figure 5.1(a)), is one real-world example of the models of this chapter. Housed in Grenoble France, RABBIT has been used to experimentally verify the hybrid zero dynamics framework for the systematic design, analysis, and optimization of provably stable walking controllers [60, 153]. Although the class of models considered here have pivot feet, understanding them is a relevant first step in achieving anthropomorphic walking motions in robots with non-trivial feet and actuated ankles [33, 34, 41]. Similarly, the models of this chapter are a necessary precursor to controller development for the compliant model of Chapter 9.

Guided by a set of detailed modeling hypotheses, the following sections derive the differential equations of stance and flight and the algebraic maps of liftoff, landing, and double support. Coordinate relabeling, although counterintuitive at first, simplifies the stability analysis of later chapters. The chapter concludes by assembling the stance and flight phases into control systems with impulse effects—open-loop plant models of walking and running for rigid planar bipeds.

4.1 Model Hypotheses

The bipeds under consideration consist of N links connected in a planar tree structure to form two identical legs with knees, but without feet[1], with the legs connected at a common point called the hips. Other limbs such as a torso or arms can be connected in any configuration at or above the hips. All links have mass, are rigid, and are connected by revolute joints. The careful choice of a measurement convention will simplify subsequent analysis—the joint angles, $q_{\mathrm{b}} = (q_1, q_2, \ldots, q_{N-1})$, are to be measured relative to other links and a single global angle, q_N, is to be measured against a fixed global frame. The position of the center of mass will be referenced by the vector $p_{\mathrm{cm}} = (x_{\mathrm{cm}}, y_{\mathrm{cm}})$.

Actuation is provided by ideal motors (that is, ideal torque sources) connected to the relative joint angles either directly or through rigid, lossless transmissions. The body coordinates q_{b} are actuated but the global angle q_N and the position of the COM are unactuated. Hence, for an N-link biped there are $(N-1)$ torque inputs. The vector of generalized coordinates $q_{\mathrm{f}} = (q_{\mathrm{b}}, q_N, p_{\mathrm{cm}})$ will be used to represent the full configuration of the robot in flight. In stance, the location of the center of mass is given as a function $p_{\mathrm{cm}} = \Upsilon_{\mathrm{cm}}(q_{\mathrm{b}}, q_N)$, meaning that the stance phase will have two fewer degrees of freedom. The vector of generalized coordinates $q_{\mathrm{s}} = (q_{\mathrm{b}}, q_N)$ will be used to represent the full configuration of the robot in stance. See Figure 4.1 for examples of robot morphology and coordinate conventions.

The robot is said to be in the *flight phase* when neither leg is in contact with the ground, and in the *stance phase* when one leg is in stationary contact with the ground and the other swings freely under the influence of gravity and the actuators. If both feet are on the ground, the robot is in *double support*. During stance, the leg contacting the ground is called the *stance leg* and the other is called the *swing leg*. The transition from stance to flight is called *takeoff* or *liftoff* and the transition from flight to stance is called *landing*. In this context, steady-state *running* is defined as a sequence of alternating stance and flight phases that is symmetric with respect to the left and right legs stride-to-stride.[2] Steady-state *walking* is a sequence of alternating phases of stance and double support that is symmetric with respect to the left and right legs stride-to-stride.

[1] Although the models described here do not have feet per se, each leg terminates in a single pivot point that will informally be called a foot.

[2] The chosen definition of running is fundamental to subsequent model and controller development. Other authors have defined running based on the motion of the center of mass or the reaction force profile on the stance leg, for example see [97].

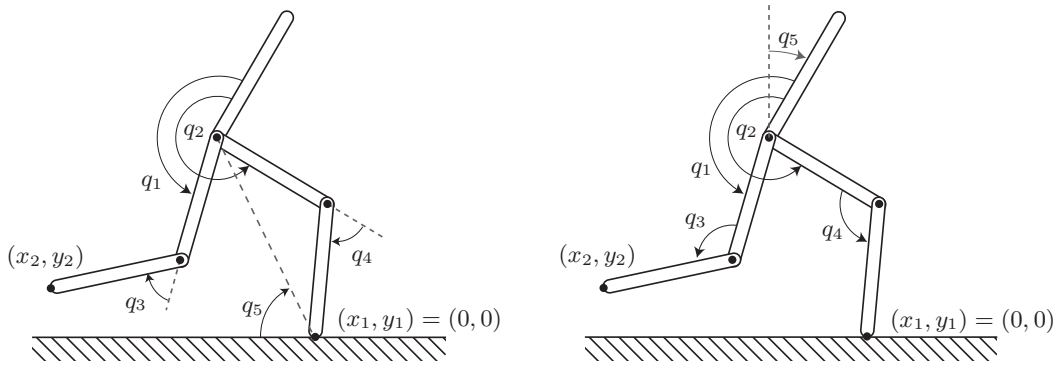

Figure 4.1: A simplifying coordinate convention. All but one of the generalized coordinates of stance are measured as the relative angles between two links. Exactly one coordinate is measured globally.

4.2 Phases of Motion

4.2.1 Flight Dynamics

In the flight phase, the robot has $(N+2)$ DOF with generalized coordinates $q_{\rm f} = (q_{\rm b}, q_N, p_{\rm cm})$. The equations of motion for flight can be written as

$$D_{\rm f}(q_{\rm f})\ddot{q}_{\rm f} + C_{\rm f}(q_{\rm f}, \dot{q}_{\rm f})\dot{q}_{\rm f} + G_{\rm f}(q_{\rm f}) = B_{\rm f}u, \tag{4.1}$$

where $D_{\rm f}$ is the inertia matrix, the matrix $C_{\rm f}$ contains Coriolis and centrifugal terms, and $G_{\rm f}$ is a vector of conservative forces. Let the configuration space $\mathcal{Q}_{\rm f}$ of the robot in flight be a simply connected open subset of $I\!R^{N+2}$ corresponding to physically reasonable configurations of the robot. Introducing the state vector

$$x_{\rm f} = (q_{\rm f}, \dot{q}_{\rm f}) \in \mathcal{X}_{\rm f} = \mathcal{Q}_{\rm f} \times I\!R^{N+2}$$

the flight model is easily expressed as

$$\dot{x}_{\rm f} = f_{\rm f}(x_{\rm f}) + g_{\rm f}(x_{\rm f})u,$$

with $f_{\rm f}$ and columns of $g_{\rm f}$ being C^1 vector fields on $\mathcal{X}_{\rm f}$.

4.2.2 Stance Dynamics

In the stance phase the stance leg end is fixed, and therefore the location of the center of mass is given as a function $p_{\rm cm} = \Upsilon_{\rm cm}(q_{\rm b}, q_N)$. As a result, the robot in stance phase has N DOF with

generalized coordinates $q_{\rm s} = (q_{\rm b}, q_N)$. Similar to the flight phase, the equations of motion can be written as

$$D_{\rm s}(q_{\rm s})\ddot{q}_{\rm s} + C_{\rm s}(q_{\rm s}, \dot{q}_{\rm s})\dot{q}_{\rm s} + G_{\rm s}(q_{\rm s}) = B_{\rm s}u. \tag{4.2}$$

Note that (4.2) can be obtained by subjecting (4.1) to the constraint that one leg end is in contact with the ground. Let the configuration space $\mathcal{Q}_{\rm s}$ be a simply-connected, open subset of $I\!R^N$ corresponding to physically reasonable configurations of the robot. Introducing the state vector

$$x_{\rm s} = (q_{\rm s}, \dot{q}_{\rm s}) \in \mathcal{X}_{\rm s} = \mathcal{Q}_{\rm s} \times I\!R^N$$

the stance model is written as

$$\dot{x}_{\rm s} = f_{\rm s}(x_{\rm s}) + g_{\rm s}(x_{\rm s})u,$$

with $f_{\rm s}$ and the columns of $g_{\rm s}$ being C^1 vector fields on $\mathcal{X}_{\rm s}$.

4.2.3 Landing Map

During running the transition from the flight phase to the stance phase is called *landing* and is modeled as an inelastic collision between the robot and the ground. During this instantaneous event impulsive reaction forces from the ground bring the velocity of the tip of the advancing leg to zero without causing it to rebound or slip. In addition, at the moment of landing, the robot's configuration remains unchanged, but joint velocities change instantaneously [74]. The post-impact joint velocities[3] are given by a function [31, Eq. (21)] that is based on the rigid body collision results of [74].

Let $\Upsilon_{F2}(q_{\rm f})$ be the function that gives the in-flight location of (x_2, y_2). At landing, impulsive reaction forces δf at the end of the swing leg induce impulsive torques $\delta\tau$ at each of the joints by a relationship found using the method of virtual work

$$\delta\tau = \left(\frac{\partial \Upsilon_{F2}(q_{\rm f})}{\partial q_{\rm f}}\right)' \delta f.$$

A momentum balance illustrates the effect of the impact on joint angular velocities

$$D_{\rm f}(q_{\rm f})\hat{\dot{q}}_{\rm s}^{\,+} - D_{\rm f}(q_{\rm f})\dot{q}_{\rm f}^{-} = \delta\tau.$$

[3]The terms $x_{\rm f}^- = (q_{\rm f}^-, \dot{q}_{\rm f}^-)$ and $x_{\rm s}^+ = (q_{\rm s}^+, \dot{q}_{\rm s}^+)$ refer to the system state just before and just after the landing event. The terms $x_{\rm s}^- = (q_{\rm s}^-, \dot{q}_{\rm s}^-)$ and $x_{\rm f}^+ = (q_{\rm f}^+, \dot{q}_{\rm f}^+)$ refer to the system state just before and just after the takeoff event. The addition of the superscript " *" (such as $x_{\rm f}^{+*}$) indicates reference to the value *at steady-state*, i.e., on the periodic orbit.

By definition of the impact event, the end of the swing leg must be at rest after the impact, and therefore

$$(\dot{x}_2, \dot{y}_2) = \frac{\partial \Upsilon_{F2}(q_{\rm f})}{\partial q_{\rm f}} \hat{\dot{q}}_{\rm s}^{\,+} = (0, 0).$$

Together these can be written as a single matrix equation

$$\begin{bmatrix} D_{\rm f}(q_{\rm f}) & -\frac{\partial \Upsilon_{F2}(q_{\rm f})}{\partial q_{\rm f}}' \\ \frac{\partial \Upsilon_{F2}(q_{\rm f})}{\partial q_{\rm f}} & 0 \end{bmatrix} \begin{bmatrix} \hat{\dot{q}}_{\rm s}^{\,+} \\ \delta f \end{bmatrix} = \begin{bmatrix} D_{\rm f}(q_{\rm f}) \dot{q}_{\rm f}^{-} \\ 0 \end{bmatrix}.$$

When the required matrix inverse exists, solving for the post-impact angular velocities is straightforward:

$$\hat{\dot{q}}_{\rm s}^{\,+} = \left(\begin{bmatrix} I & 0 \end{bmatrix} \begin{bmatrix} D_{\rm f}(q_{\rm f}) & -\frac{\partial \Upsilon_{F2}(q_{\rm f})}{\partial q_{\rm f}}' \\ \frac{\partial \Upsilon_{F2}(q_{\rm f})}{\partial q_{\rm f}} & 0 \end{bmatrix}^{-1} \begin{bmatrix} I \\ 0 \end{bmatrix} \right) D_{\rm f}(q_{\rm f}) \dot{q}_{\rm f}^{-}.$$

Recall that the generalized coordinates of flight $q_{\rm f} = (q_{\rm b}, q_N, p_{\rm cm})$ are a superset of the generalized coordinates of stance $q_{\rm s} = (q_{\rm b}, q_N)$. As a result, the angular velocities at the beginning of the stance phase $\dot{q}_{\rm s}^{+}$ can be found by simply choosing the appropriate elements of $\hat{\dot{q}}_{\rm s}^{\,+}$ as found above.

With this in mind, the overall flight-to-stance transition map can be put into the form

$$x_{\rm s}^{+} = \Delta_{({\rm f}\to{\rm s})}(x_{\rm f}^{-}).$$

This transition operator is applied when the end of the advancing leg touches the ground, that is, when $y_2 = 0$ (see Figure 4.1). Define the function, $H_{({\rm f}\to{\rm s})} : \mathcal{X}_{\rm f} \to I\!R$ by $H_{({\rm f}\to{\rm s})}(x_{\rm f}) = y_2$, so that $H_{({\rm f}\to{\rm s})}(x_{\rm f}) = 0$ characterizes the transition hypersurface surface $\mathcal{S}_{({\rm f}\to{\rm s})}$ within $\mathcal{X}_{\rm f}$.

4.2.4 Liftoff Map

During running the transition from stance to flight is called *liftoff* and is modeled as an instantaneous event on which joint angles and angular velocities are unchanged. Recall that when the robot is in the stance phase $p_{\rm cm} = \Upsilon_{\rm cm}(q_{\rm s})$. In this case, the pre-transition velocity of the center of mass $(\dot{x}_{\rm cm}^{-}, \dot{y}_{\rm cm}^{-})$ is easily found as

$$(\dot{x}_{\rm cm}^{-}, \dot{y}_{\rm cm}^{-}) = \frac{\partial}{\partial q_{\rm s}} \Upsilon_{\rm cm}(q_{\rm s}) \dot{q}_{\rm s}^{-}.$$

By hypothesis, all positions and velocities of the robot are continuous across the liftoff event, making the post-liftoff values of the generalized coordinates and velocities trivial to find. The transition

model for takeoff will be written as

$$x_{\mathrm{f}}^{+} = \Delta_{(\mathrm{s}\to\mathrm{f})}(x_{\mathrm{s}}^{-}).$$

The transition from stance to flight occurs when the vertical reaction force on the stance leg goes to zero. This force is a function of the generalized coordinates of stance, their angular velocities, and (potentially) the torque vector u. In the case that the vertical toe force is dependent on the torque vector, a feedback law for the stance phase must be known before a transition hypersurface can be defined for the liftoff event.

Let $H_{(\mathrm{s}\to\mathrm{f})}(x_{\mathrm{s}}) : \mathcal{X}_{\mathrm{s}} \to I\!R$ represent the (perhaps closed-loop) expression for the vertical component of the stance leg reaction force as a function of the stance state vector so that $H_{(\mathrm{s}\to\mathrm{f})}(x_{\mathrm{s}}) = 0$ characterizes the transition hypersurface surface $\mathcal{S}_{(\mathrm{s}\to\mathrm{f})}$ within $\mathcal{X}_{\mathrm{s}}$. If the vertical component of the reaction force is dependent on the control law, then the transition surface $\mathcal{S}_{(\mathrm{s}\to\mathrm{f})}$ must also be dependent on the control law.

4.2.5 Double Support Phase

During walking, the robot progresses from stance, to double support, to stance, etc. without going through an intermediate flight phase. Although no flight phase is present, the impact map for the double support phase of walking can be written as a composition of the liftoff and landing events,

$$\Delta_{\mathrm{s}}(x_{\mathrm{s}}) = \Delta_{(\mathrm{f}\to\mathrm{s})} \circ \Delta_{(\mathrm{s}\to\mathrm{f})}(x_{\mathrm{s}}).$$

This transition operator is applied when the end of the swing leg touches the ground, that is, when $y_2 = 0$. Define the function $H_{\mathrm{s}} : \mathcal{X}_{\mathrm{s}} \to I\!R$ by $H_{\mathrm{s}}(x_{\mathrm{s}}) = y_2$ so that $H_{\mathrm{s}}(x_{\mathrm{s}}) = 0$ characterizes the transition hypersurface surface $\mathcal{S}_{\mathrm{s}}$ within $\mathcal{X}_{\mathrm{s}}$. An occasionally useful property of the impact map of the double support phase is that

$$\begin{aligned} q_{\mathrm{s}}^{+} &= \Delta_{q_{\mathrm{s}}}(q_{\mathrm{s}}^{-}) \\ \dot{q}_{\mathrm{s}}^{+} &= \Delta_{\dot{q}_{\mathrm{s}}}(q_{\mathrm{s}}^{-})\dot{q}_{\mathrm{s}}^{-}, \end{aligned}$$

where $\Delta_{q_{\mathrm{s}}}$ and $\Delta_{\dot{q}_{\mathrm{s}}}$ are implicitly defined.

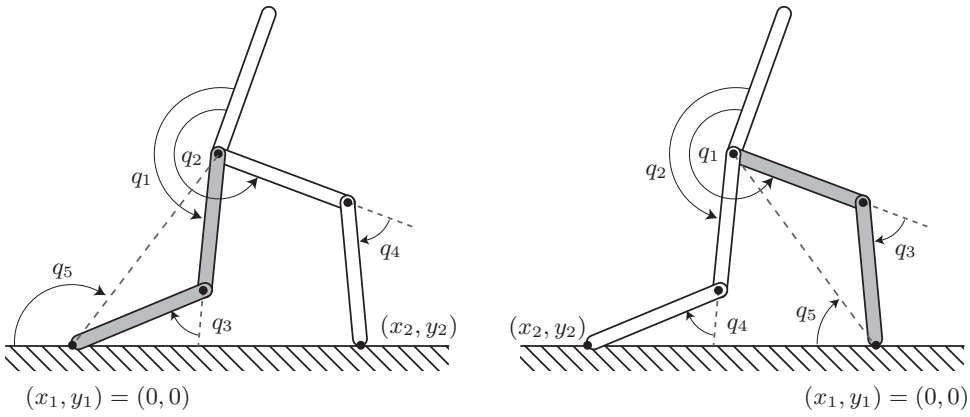

Figure 4.2: An illustration of leg swapping. The model at left is pictured at the end of a stance phase. The greyed leg is the stance leg of the recently completed stance phase. The model at right is in the same configuration, but the roles of the legs have been swapped. The greyed leg is now the stance leg of the upcoming stance phase.

4.2.6 Coordinate Relabeling

As a result of previous assumptions on symmetry, the biped will have quantitatively the same behavior whether the "left" leg is acting as the stance leg or the "right" leg is acting as the stance leg. At the moment of impact, the roles of the legs are swapped: the old stance leg becomes the new swing leg and vice versa. To mathematically account for this change in roles, a coordinate relabeling operator is used. Such a construction allows normal, left-right symmetric walking or running to be analyzed as a period-one gait, rather than a period-two gait. See Figure 4.2 for a graphical illustration of the leg swapping operator. Rather than account for the coordinate relabeling operation explicitly (which would lead to cumbersome notation and add little insight) we will assume that coordinate relabeling has been implicitly carried out in the derivation of the landing event of running and the double support phase of walking.

4.3 Open-Loop Models of Walking and Running

Having derived the stance and flight phases, the open-loop model of walking is written as a system with impulse effects

$$\Sigma_{\mathrm{s}} : \begin{cases} \dot{x_{\mathrm{s}}} &= f_{\mathrm{s}}(x_{\mathrm{s}}) + g_{\mathrm{s}}(x_{\mathrm{s}})u & {x_{\mathrm{s}}}^{-} \notin \mathcal{S}_{\mathrm{s}} \\ {x_{\mathrm{s}}}^{+} &= \Delta_{\mathrm{s}}({x_{\mathrm{s}}}^{-}) & {x_{\mathrm{s}}}^{-} \in \mathcal{S}_{\mathrm{s}} \end{cases} \tag{4.3}$$

or, in an alternative notation as

$$\Sigma_{\mathrm{s}} = \left(\mathcal{X}_{\mathrm{s}}, \mathcal{S}_{\mathrm{s}}, \emptyset, I\!R^{(N-1)}, \Delta_{\mathrm{s}}, f_{\mathrm{s}}, g_{\mathrm{s}}\right).$$

The open-loop[4] model of running is written as a discrete event system with two charts (terminology taken from [63])

$$\begin{aligned} \Sigma_{\mathrm{f}} : \begin{cases} \dot{x}_{\mathrm{f}} &= f_{\mathrm{f}}(x_{\mathrm{f}}) + g_{\mathrm{f}}(x_{\mathrm{f}})u & x_{\mathrm{f}}^{-} \notin \mathcal{S}_{(\mathrm{f}\to\mathrm{s})} \\ x_{\mathrm{s}}^{+} &= \Delta_{(\mathrm{f}\to\mathrm{s})}(x_{\mathrm{f}}^{-}) & x_{\mathrm{f}}^{-} \in \mathcal{S}_{(\mathrm{f}\to\mathrm{s})} \end{cases} \\ \Sigma_{\mathrm{s}} : \begin{cases} \dot{x}_{\mathrm{s}} &= f_{\mathrm{s}}(x_{\mathrm{s}}) + g_{\mathrm{s}}(x_{\mathrm{s}})u & x_{\mathrm{s}}^{-} \notin \mathcal{S}_{(\mathrm{s}\to\mathrm{f})} \\ x_{\mathrm{f}}^{+} &= \Delta_{(\mathrm{s}\to\mathrm{f})}(x_{\mathrm{s}}^{-}) & x_{\mathrm{s}}^{-} \in \mathcal{S}_{(\mathrm{s}\to\mathrm{f})} \end{cases} \end{aligned} \tag{4.4}$$

or, in an alternative notation as

$$\Sigma_{\mathrm{f}} = \left(\mathcal{X}_{\mathrm{f}}, \mathcal{S}_{(\mathrm{f}\to\mathrm{s})}, \emptyset, I\!R^{(N-1)}, \Delta_{(\mathrm{f}\to\mathrm{s})}, f_{\mathrm{f}}, g_{\mathrm{f}}\right)$$

$$\Sigma_{\mathrm{s}} = \left(\mathcal{X}_{\mathrm{s}}, \mathcal{S}_{(\mathrm{s}\to\mathrm{f})}, \emptyset, I\!R^{(N-1)}, \Delta_{(\mathrm{s}\to\mathrm{f})}, f_{\mathrm{s}}, g_{\mathrm{s}}\right).$$

Walking and running motions are modeled as periodic orbits occurring in the state manifolds of (4.3) or (4.4). Having rigorously derived models of walking and running, attention is turned toward the derivation of stabilizing model based controllers. By the definitions presented in Chapter 3, asymptotic stability is interpreted as the property of a closed-loop walker or runner to asymptotically reject arbitrarily small disturbances and converge over time to a periodic gait. Note that stability is not to be confused with robustness, which is the ability to reject large disturbances. Although robustness implies stability, stability does not imply robustness. Furthermore, neither stability nor robustness in the given sense should be confused with the property of "not falling down", which is a more general concept addressed by Yang, et al. in [159].

[4]Recall that the definition of the liftoff surface $\mathcal{S}_{(\mathrm{s}\to\mathrm{f})}$ may require a priori knowledge of control law. We prefer this slight abuse of notation in favor of a more involved model derivation that would provide little additional insight.

The derivations of this chapter have produced open-loop walking and running models for a class of rigid planar bipeds with one degree of underactuation. The following chapters present additional results for bipeds in this class. Chapter 5 contains experimental results from the control of model based running in RABBIT, and Chapter 6 analytically explores relationships between HZD control and passive walkers. And, chapters 7 and 8 derive controllers and stability tests that are applicable either to the models of this chapter, or to the model of compliant walking in Chapter 9.

Notation Introduced in Chapter 4

Symbol	Meaning	Defined
N	number of (rigid) links in a planar biped	Section 4.1
q_{b}	vector of actuated body coordinates	Section 4.1
q_N	the unactuated absolute coordinate	Section 4.1
p_{cm}	location of the center of mass	Section 4.1
q_{f}	generalized coordinates of flight	Section 4.1
q_{s}	generalized coordinates of stance	Section 4.1
D_{f}	inertia matrix of flight	Section 4.2.1
C_{f}	matrix of centrifugal and Coriolis terms of flight	Section 4.2.1
G_{f}	conservative forces of flight	Section 4.2.1
$\mathcal{Q}_{\mathrm{f}}$	configuration space of the flight phase	Section 4.2.1
x_{f}	state of the robot in flight	Section 4.2.1
$\mathcal{X}_{\mathrm{f}}$	state manifold for the flight phase	Section 4.2.1
f_{f}	drift vector of the robot in flight	Section 4.2.1
g_{f}	control vectors of the robot in flight	Section 4.2.1
D_{s}	inertia matrix of stance	Section 4.2.2
C_{s}	matrix of centrifugal and Coriolis terms of stance	Section 4.2.2
G_{s}	conservative forces of stance	Section 4.2.2
$\mathcal{Q}_{\mathrm{s}}$	configuration space of the stance phase	Section 4.2.2
x_{s}	state of the robot in stance	Section 4.2.2
$\mathcal{X}_{\mathrm{s}}$	state manifold for the stance phase	Section 4.2.2
f_{s}	drift vector of the robot in stance	Section 4.2.2
g_{s}	control vectors of the robot in stance	Section 4.2.2
Υ_{cm}	function returning the position of the center of mass	Section 4.2.2

Symbol	Meaning	Defined
x_{f}^{-}	state of the robot in flight, just before landing	Section 4.2.3
x_{f}^{+}	state of the robot in flight, just after takeoff	Section 4.2.3
x_{s}^{-}	state of the robot in stance, just before liftoff (or just before double support)	Section 4.2.3
x_{s}^{+}	state of the robot in stance, just after landing (or just after double support)	Section 4.2.3
Υ_{F2}	flight phase function returning the location of the swing foot	Section 4.2.3
$\mathcal{S}_{(\mathrm{f}\to\mathrm{s})}$	transition surface of landing	Section 4.2.3
$\Delta_{(\mathrm{f}\to\mathrm{s})}$	landing map of flight	Section 4.2.3
$\mathcal{S}_{(\mathrm{s}\to\mathrm{f})}$	transition surface of liftoff	Section 4.2.4
$\Delta_{(\mathrm{s}\to\mathrm{f})}$	liftoff map of stance	Section 4.2.4
$\mathcal{S}_{\mathrm{s}}$	transition surface of double support	Section 4.2.5
Δ_{s}	impact map of the double support phase	Section 4.2.5
Σ_{s}	open-loop model of the stance phase of flight (or the open-loop model of walking, depending on context)	Section 4.3
Σ_{f}	open-loop model of the flight phase of running	Section 4.3

CHAPTER 5

Running Experiments with RABBIT: Six Steps toward Infinity*

In March 2003, the French robot RABBIT achieved robust walking under a provably stable hybrid zero dynamics controller [149]. Walking controllers for RABBIT acted by enforcing *virtual constraints*, which are holonomic constraints used to coordinate link movements throughout a gait. The stability properties of such walking motions were analyzed on the basis of the *hybrid zero dynamics of walking*, with the conclusions of theory supported by experimental results.

In September 2004, similar experiments were conducted to validate the hybrid zero dynamics theory of running presented in [31]. In a number of experiments, RABBIT achieved five or six running steps before tracking errors exceeded software bounds, but stable running (that is, an experiment resulting in a potentially unbounded number of steps) was never observed. One experiment where RABBIT took six steps is examined in detail. The observed gait was remarkably human-like, having long stride lengths (approx. 50 cm or 36% of body length), flight phases of significant duration (approx. 100 ms or 25% of step duration), an upright posture, and an average forward rate of 0.6 m/s. A video is available at [59]. Details of the online controller and the offline gait optimizer are discussed along with hardware modifications leading up to the sample experiment in which RABBIT took six consecutive running steps. An additional discussion about some unmodeled dynamic and geometric effects that contributed to implementation difficulties is given.

*The contents of this chapter are taken, with minimal modification, from the book chapter [101] entitled "Achieving Bipedal Running with RABBIT: Six Steps toward Infinity" by B. Morris, E.R. Westervelt, C. Chevallereau, G. Buche, and J. W. Grizzle. Co-authored material used by permission.

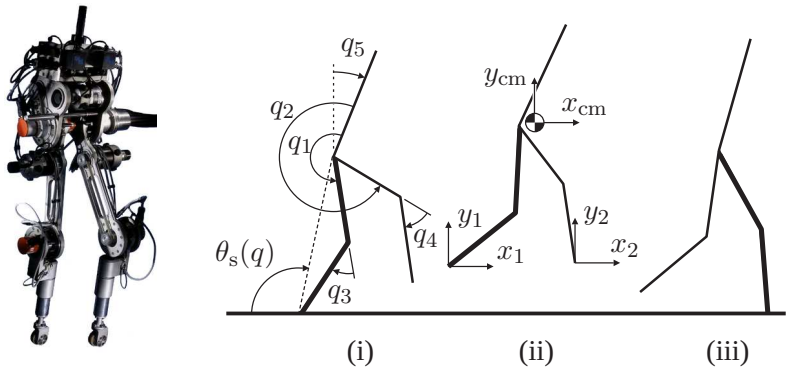

(a) RABBIT (b) Phases of running and coordinate conventions.

Figure 5.1: Phases of running and coordinate conventions. A stick figure of RABBIT is shown (i) at the end of the stance phase with the stance leg in bold; (ii) during flight with the previous stance leg in bold; and (iii) at the beginning of the stance phase just after landing and coordinate swap, with the stance leg of the upcoming stance phase in bold. To avoid clutter, the coordinate conventions have been spread out over the stance and flight phases. Angles are positive in the *counterclockwise* direction.

The remainder of this chapter is a self-contained description of the theoretical development and hardware modifications leading up to one example of an experiment in which RABBIT took six consecutive running steps. To facilitate implementation, the controller hypotheses of [31] are slightly relaxed, leading to controllers that are easier to design than those proposed in [31] but which still lend the closed-loop system to a reduced dimensionality stability test. Philosophy and motivation of the modified control law are given in Section 5.1.1 with a detailed development of the hybrid controller in Sections 5.1.3 to 5.1.7. The resulting closed-loop model of RABBIT and its stability properties are discussed in Sections 5.1.8 and 5.1.9. Beyond this, Section 5.2 outlines a method for the design of stable gaits using constrained nonlinear optimization and includes a numerical example. Section 5.3 presents results from the first experimental implementation of running on RABBIT and a discussion outlining a number of possible reasons why stable running was not observed. Conclusions are drawn in Section 5.4. Supplemental material not appearing in [101] is provided in Section 5.5.

5.1 Controller Derivation

5.1.1 Summary and Philosophy

The overall philosophy of HZD control is to use the freedom available in feedback design to achieve a parameterized family of closed-loop systems whose stability analysis is analytically tractable. This allows the use of numerical optimization to search among the family of closed-loop systems to find those that yield a desired behavior, such as stable running at a pre-determined speed with upper bounds on peak actuator power and the coefficient of static friction between the leg end and the ground.

Parameterization is achieved through the use of virtual constraints in both the stance and flight phases. Perfect enforcement of virtual constraints results in low dimensional surfaces that are invariant under the differential equations of the closed-loop model and are also invariant under the transition maps. To achieve the invariance at landing, a deadbeat action is incorporated in the flight phase controller that steers the robot to land in a pre-determined configuration, while respecting conservation of angular momentum about the robot's center of mass. This hybrid controller creates a 1DOF HZD that allows the stability of a running motion to be analyzed in closed form on the basis of a one-dimensional Poincaré map.

5.1.2 Parameterized Control with Impact Updated Parameters

In the first running experiment attempted on RABBIT, there was not sufficient time[1] to implement completely the controller of [31]. The controller that was implemented used virtual constraints in both the stance and flight phases, but the deadbeat action of the flight phase controller was not implemented to regulate the final configuration of the robot at touchdown. Instead, to account for the changing configuration of the robot at touchdown, the transition controller of [152] was adopted[2]. Key points of the related analysis are highlighted in Section 5.1.9.

[1] A total of two weeks were available to perform the experiments.

[2] The transition controller of this chapter takes into account the joint angles of the robot at touchdown but not the joint angular velocities. As a result a true HZD of running is not created, and the resulting analysis of Section 5.1.9 (based on [60]) is modified accordingly.

5.1.3 Parameterized Virtual Constraints

For notational convenience, the stance phase and flight phase virtual constraints will be parameterized separately by a_{s} and a_{f}, respectively. These parameter sets, which lie in the parameter spaces $\mathcal{A}_{\mathrm{s}} = \mathbb{R}^{n_{\mathrm{s}}}$ and $\mathcal{A}_{\mathrm{f}} = \mathbb{R}^{n_{\mathrm{f}}}$, can be updated at takeoff and landing events but are otherwise constant. With this notation, the virtual constraints for stance and flight are, respectively,[3]

$$y = q_{\mathrm{b}} - h_{d,\mathrm{s}}(\theta_{\mathrm{s}}(q_{\mathrm{s}}), a_{\mathrm{s}}) \tag{5.1a}$$

$$y = q_{\mathrm{b}} - h_{d,\mathrm{f}}(\theta_{\mathrm{f}}(q_{\mathrm{f}}, a_{\mathrm{f}}), a_{\mathrm{f}}). \tag{5.1b}$$

5.1.4 Stance Phase Control

The controller for the stance phase acts by updating the parameters a_{s} and by enforcing the virtual constraints (5.1a). As a result of enforcing the virtual constraints, in stance phase, the robot behaves as an unactuated 1 DOF system whose properties can be tuned by choosing different constraint parameters. Apart from different boundary conditions on the virtual constraints, this control is identical to the walking controllers developed in [153, 149]. The stance phase parameter vector, a_{s}, can be expressed as

$$a_{\mathrm{s}} = (a_{\mathrm{s},0},\ a_{\mathrm{s},1}, \ldots,\ a_{\mathrm{s},m_{\mathrm{s}}-1},\ a_{\mathrm{s},m_{\mathrm{s}}},\ \theta_{\mathrm{s}}^{-},\ \theta_{\mathrm{s}}^{+}), \tag{5.2}$$

where $m_{\mathrm{s}} \geq 3$, $a_{\mathrm{s},i} \in \mathbb{R}^4$ for $i \in \{0, 1, \ldots, m_{\mathrm{s}} - 1, m_{\mathrm{s}}\}$, and $\theta_{\mathrm{s}}^{-}, \theta_{\mathrm{s}}^{+} \in \mathbb{R}$. Note that $n_{\mathrm{s}} = 4\,(m_{\mathrm{s}} + 1) + 2$. The terms θ_{s}^{-} and θ_{s}^{+} are the values of the function $\theta_{\mathrm{s}}(q_{\mathrm{s}})$ evaluated at the end and the beginning of the stance phase. In [153, 149], h_d is expressed in terms of Bézier polynomials. Here, a slightly different class of polynomials[4] is used that satisfy the following:

$$\begin{aligned} h_{d,\mathrm{s}}(\theta_{\mathrm{s}}^{+}, a_{\mathrm{s}}) &= a_{\mathrm{s},0} & \tfrac{d}{d\theta_{\mathrm{s}}} h_{d,\mathrm{s}}(\theta_{\mathrm{s}}^{-}, a_{\mathrm{s}}) &= a_{\mathrm{s},m_{\mathrm{s}}-1} \\ \tfrac{d}{d\theta_{\mathrm{s}}} h_{d,\mathrm{s}}(\theta_{\mathrm{s}}^{+}, a_{\mathrm{s}}) &= a_{\mathrm{s},1} & h_{d,\mathrm{s}}(\theta_{\mathrm{s}}^{-}, a_{\mathrm{s}}) &= a_{\mathrm{s},m_{\mathrm{s}}}. \end{aligned} \tag{5.3}$$

The stance phase virtual constraints are imposed on the dynamics by using a control $u_{\mathrm{s}} : \mathcal{X}_{\mathrm{s}} \times \mathcal{A}_{\mathrm{s}} \to \mathbb{R}^4$ that drives (5.1a) to zero *in finite time*. The specific assumptions are as in [60, 153].

[3] Terms that are constant during the continuous phases of motion, and potentially updated at phase transitions, will be considered *parameters*.

[4] Any class of smooth functions satisfying these properties can be used to define virtual constraints.

5.1.5 Flight Phase Control

The development of the flight phase controller is similar to that of the stance phase controller. The key difference is the choice of $\theta_{\rm f}$ in (5.1b) to be a function of the position of the center of mass. The flight phase parameter vector, $a_{\rm f}$, is defined as

$$a_{\rm f} = (a_{{\rm f},0},\ a_{{\rm f},1},\ldots,\ a_{{\rm f},m_{\rm f}-1},\ a_{{\rm f},m_{\rm f}},\ x^+_{\rm cm,f},\ \dot{x}^+_{\rm cm,f},\ T_{\rm f}), \tag{5.4}$$

where $m_{\rm f} \geq 3$, $a_{{\rm f},i} \in I\!R^4$ for $i \in \{0,1,\ldots,m_{\rm f}-1,m_{\rm f}\}$, and $x^+_{\rm cm,f}, \dot{x}^+_{\rm cm,f}, T_{\rm f} \in I\!R$. Note that $n_{\rm f} = 4\,(m_{\rm f}+1)+3$. The terms $x^+_{\rm cm,f}$, $\dot{x}^+_{\rm cm,f}$, and $T_{\rm f}$ are, respectively, the horizontal position of the center of mass at the beginning of the flight phase, the horizontal velocity of the center of mass at the beginning of the flight phase, and the estimated[5] duration of the flight phase. The flight phase virtual constraints (5.1b) are given by

$$\theta_{\rm f}(q_{\rm f}, a_{\rm f}) = \frac{1}{T_{\rm f}}\left(\frac{x_{\rm cm} - x^+_{\rm cm,f}}{\dot{x}^+_{\rm cm,f}}\right), \tag{5.5}$$

and $h_{d,{\rm f}}$, which, as in the stance phase, is a smooth, vector-valued function that satisfies

$$\begin{aligned} h_{d,{\rm f}}(0,a_{\rm f}) &= a_{{\rm f},0} & \tfrac{d}{d\theta_{\rm f}} h_{d,{\rm f}}(1,a_{\rm f}) &= a_{{\rm f},m_{\rm f}-1} \\ \tfrac{d}{d\theta_{\rm f}} h_{d,{\rm f}}(0,a_{\rm f}) &= a_{{\rm f},1} & h_{d,{\rm f}}(1,a_{\rm f}) &= a_{{\rm f},m_{\rm f}}. \end{aligned} \tag{5.6}$$

For a given stride, let $t_{\rm f}$ denote the elapsed time within the flight phase. By conservation of linear momentum, $\dot{x}^+_{\rm cm,f}$ is constant during flight, which implies that $t_{\rm f} = (x_{\rm cm} - x^+_{\rm cm,f})/\dot{x}^+_{\rm cm,f}$. As a result, $\theta_{\rm f} = t_{\rm f}/T_{\rm f}$ is a valid substitute for (5.5), and for this reason, the given flight phase virtual constraints are said to be *time scaled*. Flight phase virtual constraints are enforced using any smooth state feedback controller $u_{\rm f} : \mathcal{X}_{\rm f} \times \mathcal{A}_{\rm f} \to I\!R^4$ that drives (5.1b) to zero exponentially quickly.

Note that finite time convergence is not used in the flight phase. A finite time controller is used in the stance phase to render the stance phase constraint surface finite time attractive so that the analysis of running will be similar to that of walking [60]. For further discussion of this point, refer to Section 5.1.9.

[5] Calculation of $T_{\rm f}$ requires the height of the center of mass at landing, $y^-_{\rm cm,f}$, to be known *a priori*, which is only possible if the virtual constraints are exactly enforced throughout the flight phase.

5.1.6 Transition Control: Landing

In the event that landing occurs with the state of the robot not satisfying the virtual constraints, the control parameters of the subsequent stance phase, a_{s}, are updated to ensure that the configuration of the robot satisfies $q_b - h_{d,\mathrm{s}}(\theta_{\mathrm{s}}^+, a_{\mathrm{s}}) = 0$.[6] The parameter updates are governed by the differentiable function $w_{(\mathrm{f}\to\mathrm{s})} : \mathcal{S}_{(\mathrm{f}\to\mathrm{s})} \to \mathcal{A}_{\mathrm{s}}$, such that for $a_{\mathrm{s}} = w_{(\mathrm{f}\to\mathrm{s})}(x_{\mathrm{f}}^-)$,

$$\begin{aligned} a_{\mathrm{s},0} &= q_b^+ & & \\ a_{\mathrm{s},1} &= a_{\mathrm{s},1}^* & \theta_{\mathrm{s}}^+ &= \theta_{\mathrm{s}}(q_{\mathrm{s}}^+) \\ &\vdots & & \\ & & \theta_{\mathrm{s}}^- &= \theta_{\mathrm{s}}^{-*} \\ a_{\mathrm{s},m_{\mathrm{s}}-1} &= a_{\mathrm{s},m_{\mathrm{s}}-1}^* & & \\ a_{\mathrm{s},m_{\mathrm{s}}} &= a_{\mathrm{s},m_{\mathrm{s}}}^*. & & \end{aligned} \tag{5.7}$$

In the above, q_{s}^+ is calculated using $\Delta_{(\mathrm{f}\to\mathrm{s})}(x_{\mathrm{f}}^-)$, and the terms θ_{s}^{-*} and $a_{\mathrm{s},i}^* \in I\!R^4$, $i \in \{1, \ldots, m_{\mathrm{s}} - 1, m_{\mathrm{s}}\}$ are constant parameters chosen during design.

If the stance phase finite time controller can satisfy the virtual constraints (5.1a) before the liftoff event occurs, and the parameter updates obey (5.7), then the stance phase will terminate with $q_b - h_{d,\mathrm{s}}(\theta_{\mathrm{s}}^-, a_{\mathrm{s}}) = 0$, or equivalently, with $q^- = q^{-*}$.

5.1.7 Transition Control: Takeoff

At takeoff, the parameters of the flight phase virtual constraints, a_{f}, are updated so that the duration of the planned motion of the robot is equal to the estimated flight time. Parameter updates are governed by a continuously differentiable function $w_{(\mathrm{s}\to\mathrm{f})} : \mathcal{S}_{(\mathrm{s}\to\mathrm{f})} \to \mathcal{A}_{\mathrm{f}}$, such that for $a_{\mathrm{f}} = w_{(\mathrm{s}\to\mathrm{f})}(x_{\mathrm{s}}^-)$,

[6] Our velocity estimates were rather noisy, so we did not update $a_{\mathrm{s},1}$. Updating $a_{\mathrm{s},0}$ and $a_{\mathrm{s},1}$ would allow that just after landing, the full state satisfied the virtual constraints.

$$
\begin{aligned}
a_{\mathrm{f},0} &= a^*_{\mathrm{f},0} \\
a_{\mathrm{f},1} &= a^*_{\mathrm{f},1} \qquad\qquad x_{\mathrm{cm_f}}^{+} = \Upsilon_{x_{\mathrm{cm}}}(q_{\mathrm{s}}^{-}) \\
&\vdots \qquad\qquad \dot{x}^{+}_{\mathrm{cm,f}} = \frac{\partial \Upsilon_{x_{\mathrm{cm}}}}{\partial q_{\mathrm{s}}}(q_{\mathrm{s}}^{-})\,\dot{q}_{\mathrm{s}}^{-} \\
a_{\mathrm{f},m_{\mathrm{f}}-1} &= a^*_{\mathrm{f},m_{\mathrm{f}}-1} \\
a_{\mathrm{f},m_{\mathrm{f}}} &= a^*_{\mathrm{f},m_{\mathrm{f}}} \\
T_{\mathrm{f}} &= \frac{\dot{y}^{+}_{\mathrm{cm,f}}}{g} + \frac{\sqrt{(\dot{y}^{+}_{\mathrm{cm,f}})^2 - 2g(y^{-*}_{\mathrm{cm,f}} - y^{+}_{\mathrm{cm,f}})}}{g}.
\end{aligned}
\tag{5.8}
$$

where, g is the magnitude of the acceleration of gravity and $y^{-*}_{\mathrm{cm,f}}$ is the height of the center of mass at the end of the flight phase, on the limit cycle. The terms $a^*_{\mathrm{f},i} \in I\!R^4, i \in \{0, 1, \ldots, m_{\mathrm{f}} - 1, m_{\mathrm{f}}\}$ are parameters chosen during design. Initiation of the takeoff event is a control decision, designated to occur when $\theta_{\mathrm{s}}(q) = \theta_{\mathrm{s}}^{-}$. In the closed-loop model the switching hypersurface is $\mathcal{S}_{(\mathrm{s}\to\mathrm{f})} = \{(x_{\mathrm{s}}, a_{\mathrm{s}}) \in \mathcal{X}_{\mathrm{s}} \times \mathcal{A}_{\mathrm{s}} \mid H_{(\mathrm{s}\to\mathrm{f})}(x_{\mathrm{s}}, a_{\mathrm{s}}) = 0\}$ where $H_{(\mathrm{s}\to\mathrm{f})}(x_{\mathrm{s}}, a_{\mathrm{s}}) = \theta_{\mathrm{s}}(q_{\mathrm{s}}) - \theta_{\mathrm{s}}^{-}$.

5.1.8 Resulting Closed-Loop Model of Running

To form the closed-loop model of running, the state space of the open-loop model, (4.4), is enlarged to include the parameters of the flight and stance phases. Define the augmented state spaces

$$
\begin{aligned}
\mathcal{X}_{\mathrm{f}\mathbf{e}} &= \mathcal{X}_{\mathrm{f}} \times \mathcal{A}_{\mathrm{f}} \\
\mathcal{X}_{\mathrm{s}\mathbf{e}} &= \mathcal{X}_{\mathrm{s}} \times \mathcal{A}_{\mathrm{s}}
\end{aligned}
$$

with elements given by

$$
\begin{aligned}
x_{\mathrm{f}\mathbf{e}} &= (q_{\mathrm{f}}, \dot{q}_{\mathrm{f}}, a_{\mathrm{f}}) \\
x_{\mathrm{s}\mathbf{e}} &= (q_{\mathrm{s}}, \dot{q}_{\mathrm{s}}, a_{\mathrm{s}}).
\end{aligned}
$$

The closed-loop dynamics can then be written as

$$
\begin{aligned}
\bar{f}_{\mathrm{f}\mathbf{e}}(x_{\mathrm{f}\mathbf{e}}) &= \begin{bmatrix} f_{\mathrm{f}}(x_{\mathrm{f}}) + g_{\mathrm{f}}(x_{\mathrm{f}})u(x_{\mathrm{f}}, a_{\mathrm{f}}) \\ 0_{N_{\mathrm{f}}\times 1} \end{bmatrix} \\
\bar{f}_{\mathrm{s}\mathbf{e}}(x_{\mathrm{s}\mathbf{e}}) &= \begin{bmatrix} f_{\mathrm{s}}(x_{\mathrm{s}}) + g_{\mathrm{s}}(x_{\mathrm{s}})u(x_{\mathrm{s}}, a_{\mathrm{s}}) \\ 0_{N_{\mathrm{s}}\times 1} \end{bmatrix}.
\end{aligned}
$$

The zero vectors reflect that the virtual constraint parameters do not change during the continuous phases of running. The closed-loop impact maps include the parameter update laws,

$$\begin{aligned}\overline{\Delta}_{(\mathrm{f}\to\mathrm{s})_{\mathbf{e}}}(x_{\mathrm{f}\mathbf{e}}^-) &= \begin{bmatrix} \Delta_{(\mathrm{f}\to\mathrm{s})}(x_{\mathrm{f}}^-) \\ w_{(\mathrm{f}\to\mathrm{s})}(x_{\mathrm{f}}^-) \end{bmatrix} \\ \overline{\Delta}_{(\mathrm{s}\to\mathrm{f})_{\mathbf{e}}}(x_{\mathrm{s}\mathbf{e}}^-) &= \begin{bmatrix} \Delta_{(\mathrm{s}\to\mathrm{f})}(x_{\mathrm{s}}^-) \\ w_{(\mathrm{s}\to\mathrm{f})}(x_{\mathrm{s}}^-) \end{bmatrix}.\end{aligned}$$

The closed-loop hybrid model is then

$$\bar{\Sigma}_{\mathrm{f}\mathbf{e}}: \begin{cases} \dot{x}_{\mathrm{f}\mathbf{e}} = \bar{f}_{\mathrm{f}\mathbf{e}}(x_{\mathrm{f}\mathbf{e}}) & x_{\mathrm{f}\mathbf{e}}^- \notin \mathcal{S}_{(\mathrm{f}\to\mathrm{s})_{\mathbf{e}}} \\ x_{\mathrm{s}\mathbf{e}}^+ = \overline{\Delta}_{(\mathrm{f}\to\mathrm{s})_{\mathbf{e}}}(x_{\mathrm{f}\mathbf{e}}) & x_{\mathrm{f}\mathbf{e}}^- \in \mathcal{S}_{(\mathrm{f}\to\mathrm{s})_{\mathbf{e}}} \end{cases} \tag{5.9a}$$

$$\bar{\Sigma}_{\mathrm{s}\mathbf{e}}: \begin{cases} \dot{x}_{\mathrm{s}\mathbf{e}} = \bar{f}_{\mathrm{s}\mathbf{e}}(x_{\mathrm{s}\mathbf{e}}) & x_{\mathrm{s}\mathbf{e}}^- \notin \mathcal{S}_{(\mathrm{s}\to\mathrm{f})_{\mathbf{e}}} \\ x_{\mathrm{f}\mathbf{e}}^+ = \overline{\Delta}_{(\mathrm{s}\to\mathrm{f})_{\mathbf{e}}}(x_{\mathrm{s}\mathbf{e}}) & x_{\mathrm{s}\mathbf{e}}^- \in \mathcal{S}_{(\mathrm{s}\to\mathrm{f})_{\mathbf{e}}}, \end{cases} \tag{5.9b}$$

which may be written as

$$\begin{aligned}\bar{\Sigma}_{\mathrm{f}\mathbf{e}} &= \left(\mathcal{X}_{\mathrm{f}\mathbf{e}}, \mathcal{S}_{(\mathrm{f}\to\mathrm{s})_{\mathbf{e}}}, \overline{\Delta}_{(\mathrm{f}\to\mathrm{s})_{\mathbf{e}}}, \bar{f}_{\mathrm{f}\mathbf{e}}\right) \\ \bar{\Sigma}_{\mathrm{s}\mathbf{e}} &= \left(\mathcal{X}_{\mathrm{s}\mathbf{e}}, \mathcal{S}_{(\mathrm{s}\to\mathrm{f})_{\mathbf{e}}}, \overline{\Delta}_{(\mathrm{s}\to\mathrm{f})_{\mathbf{e}}}, \bar{f}_{\mathrm{s}\mathbf{e}}\right).\end{aligned}$$

5.1.9 Existence and Stability of Periodic Orbits

The first step to evaluate the stability of a running gait using the method of Poincaré is to construct a system with impulse effects (that is, a single-chart hybrid model) that has the same Poincaré map as (5.9). Following [31, Eq. (62)], define

$$\bar{\Sigma}: \begin{cases} \dot{\bar{x}} = \bar{f}(\bar{x}) & x^- \notin \bar{\mathcal{S}} \\ \bar{x}^+ = \bar{\Delta}(\bar{x}^-) & \bar{x}^- \in \bar{\mathcal{S}}, \end{cases}$$

where $\bar{x} = x_{\mathrm{s}\mathbf{e}}$, $\bar{f} = \bar{f}_{\mathrm{s}\mathbf{e}}$, $\bar{\Delta} = \overline{\Delta}_{(\mathrm{f}\to\mathrm{s})_{\mathbf{e}}} \circ \phi_{T_I,\mathrm{f}} \circ \overline{\Delta}_{(\mathrm{s}\to\mathrm{f})_{\mathbf{e}}}$, and $\bar{\mathcal{S}} = \mathcal{S}_{(\mathrm{s}\to\mathrm{f})_{\mathbf{e}}}$. In words, this system consists of the differential equation of the closed-loop stance phase model of (5.9) and a generalized impact map $\bar{\Delta}$ that includes the transition map from stance to flight, the flight phase dynamics, and the impact map from flight to stance. The generalized impact map is the result of event-based sampling of the solution of (5.9) at takeoff events.

Because the virtual constraints in the stance phase are enforced using a continuous finite time controller [17], the reduction technique of [60, Thm. 2] is applicable. Because the parameter updates

in the stance phase can be computed in terms of the state of the robot at takeoff, the analysis of periodic orbits can be reduced to the computation of a one-dimensional restricted Poincaré map, ρ, having $\mathcal{S}_{(\mathrm{s}\to\mathrm{f})_{\mathbf{e}}}$ as a Poincaré section.

5.2 Design of Running Motions with Optimization

5.2.1 Optimization Parameters

To design a running motion, a numerical routine is used to search the parameter spaces $\mathcal{A}_{\mathrm{s}}$ and $\mathcal{A}_{\mathrm{f}}$ for a set of parameters that results in a desirable gait (periodic orbit of (5.9)). Common requirements on the gait are achieved by incorporating constraints into the numerical search. Such constraints address actuator limits, allowable joint space, and unilateral ground contact forces. For the experiments reported here, the gait was designed using an optimization approach that combined the ideas of [30] and [153]; the optimization was performed directly on the parameters of the virtual constraints in order to *simultaneously* determine a periodic running motion and a controller that achieves it. This is in contrast with the approach of [31] where virtual constraints are designed by regression against optimal, pre-computed, periodic trajectories.

Virtual constraints are assumed to be satisfied on the periodic orbit, which has two consequences: first, the integration of the closed-loop system dynamics can be performed using the stance and flight phase zero dynamics (see [31] for details), resulting in short computation times; and second, the virtual constraint parameters, a_{s} and a_{f}, are not independent. Once the independent parameters have been identified, standard numerical optimization routines can be used to search for desirable gaits. The implementation of such a procedure is outlined in the following subsections.

5.2.2 Boundary Conditions of the Virtual Constraints

The transition maps of takeoff and landing can be used to identify redundancies between the virtual constraint parameter vectors a_{s} and a_{f}. Given the state corresponding to the end of the limit cycle stance phase, $x_{\mathrm{s}}^{-*} = (q_{\mathrm{s}}^{-*}, \dot{q}_{\mathrm{s}}^{-*})$, the state at the beginning of the subsequent flight phase can be computed as $x_{\mathrm{f}}^{+*} = (q_{\mathrm{f}}^{+*}, \dot{q}_{\mathrm{f}}^{+*}) = \Delta_{(\mathrm{s}\to\mathrm{f})}(x_{\mathrm{s}}^{-*})$. For both x_{s}^{-*} and x_{f}^{+*} to satisfy the virtual

constraints of their respective phases, the following relations must hold,

$$\begin{aligned} a^*_{\mathrm{s},m_\mathrm{s}-1} &= \dot{q}^{-*}_{b,\mathrm{s}}/\dot{\theta}^{-*}_{\mathrm{s}} & a^*_{\mathrm{f},0} &= q^{+*}_{b,\mathrm{f}} \\ a^*_{\mathrm{s},m_\mathrm{s}} &= q^{-*}_{b,\mathrm{s}} & a^*_{\mathrm{f},1} &= \dot{q}^{+*}_{b,\mathrm{f}}\, T^*_{\mathrm{f}}, \end{aligned} \tag{5.10}$$

which are derived by applying (5.3), (5.5), (5.6), and (5.8) to (5.1). These are the boundary conditions associated with the liftoff event of the periodic orbit. The state of the robot at the beginning of the stance phase, $x^{+*}_{\mathrm{s}} = (q^{+*}_{\mathrm{s}}, \dot{q}^{+*}_{\mathrm{s}})$, can be related to the state at the end of the previous flight phase, $x^{-*}_{\mathrm{f}} = (q^{-*}_{\mathrm{f}}, \dot{q}^{-*}_{\mathrm{f}})$, by the landing map, $x^{+*}_{\mathrm{s}} = \Delta_{(\mathrm{f}\to\mathrm{s})}(x^{-*}_{\mathrm{f}})$, to yield the following additional design constraints,

$$\begin{aligned} a^*_{\mathrm{s},0} &= q^{+*}_{b,\mathrm{s}} & a^*_{\mathrm{f},m_\mathrm{f}-1} &= \dot{q}^{-*}_{b,\mathrm{f}}\, T^*_{\mathrm{f}} \\ a^*_{\mathrm{s},1} &= \dot{q}^{+*}_{b,\mathrm{s}}/\dot{\theta}^{+*}_{\mathrm{s}} & a^*_{\mathrm{f},m_\mathrm{f}} &= q^{-*}_{b,\mathrm{f}}. \end{aligned} \tag{5.11}$$

The update law presented here enforces fewer boundary conditions than the update law of [31]. The extra boundary conditions associated with takeoff are already satisfied by (5.10), but those of landing are not met by (5.11); they are more difficult to satisfy due to conservation of angular momentum in the flight phase. The main theoretical result of this chapter is that invariance of the flight and stance phase constraint surfaces over the landing event is not a necessary condition for achieving provably stable running. As noted earlier, relaxing this condition makes running motions significantly easier to design.

5.2.3 Optimization Algorithm Details

Trial gaits for the running experiments were generated using the constrained nonlinear optimization routine `fmincon` of MATLAB's Optimization Toolbox. Three quantities are involved in optimization: *J*, a scalar cost function to be minimized on the periodic orbit, *EQ*, a vector of equality constraints, and $INEQ$, a vector of inequality constraints. The following is a description of the optimization procedure that was implemented. The independent and dependent terms[7] of optimization are given in Table 5.1. Note that when the optimizer terminates with the constraints satisfied, x^{+*}_{s} will be a point located on a closed-loop periodic orbit and the virtual constraints will be given by (5.2) and (5.4).

[7] "Terms" is used to describe those variables used in optimization; these are different from the "parameters" of the virtual constraints.

Algorithm

1. Select $x_{\mathrm{f}}^{-*} = (q_{\mathrm{f}}^{-*}, \dot{q}_{\mathrm{f}}^{-*})$, the state corresponding to the end of the flight phase.

2. Using the flight-to-stance transition function, $\Delta_{(\mathrm{f}\to\mathrm{s})}$, calculate $x_{\mathrm{s}}^{+*} = (q_{\mathrm{s}}^{+*}, \dot{q}_{\mathrm{s}}^{+*})$, the state corresponding to the beginning of the subsequent stance phase.

3. Calculate θ_{s}^{+*} by (5.7) and $a_{\mathrm{s},0}^{*}$, $a_{\mathrm{s},1}^{*}$ by (5.11).

4. Select $a_{\mathrm{s},2}^{*}, \ldots, a_{\mathrm{s},m_{\mathrm{s}}}^{*}$, and θ_{s}^{-*} to complete the stance phase parameter vector a_{s}.

5. Using parameters a_{s} and the initial condition x_{s}^{+*}, integrate the equations of motion of stance and apply the stance-to-flight transition operator, $\Delta_{(\mathrm{s}\to\mathrm{f})}$, to obtain $x_{\mathrm{f}}^{+*} = (q_{\mathrm{f}}^{+*}, \dot{q}_{\mathrm{f}}^{+*})$.

6. Calculate $a_{\mathrm{f},0}^{*}$, $a_{\mathrm{f},1}^{*}$ by (5.10); $a_{\mathrm{f},m_{\mathrm{f}}-1}^{*}$, $a_{\mathrm{f},m_{\mathrm{f}}}^{*}$ by (5.11); and $x_{\mathrm{cm,f}}^{+*}$, $\dot{x}_{\mathrm{cm,f}}^{+*}$, and T_{f}^{*} by (5.8).

7. Select $a_{\mathrm{f},2}^{*}, \ldots, a_{\mathrm{f},m_{\mathrm{f}}-2}^{*}$ to complete the flight phase parameter vector a_{f}.

8. Using parameters a_{f}, and initial condition x_{f}^{+*}, integrate the equations of motion of flight to obtain x_{f}^{-}.

9. Evaluate *J*, *EQ*, and $INEQ$.

10. Iterate Steps 1 to 9 until *J* is (approximately) minimized, each entry of *EQ* is zero, and each entry of $INEQ$ is less than zero.

5.2.4 An Example Running Motion

A sample running gait designed by the above algorithm is now presented. A stick diagram of this motion is given in Figure 5.2(a). The stability analysis outlined in Section 5.1.9 was applied to the resulting running motion. Figure 5.2(b) gives the restricted Poincaré map, which indicates that the motion is locally exponentially stable. The gait was designed to minimize the integral of torque squared per distance traveled, with the following constraints:

Equality constraints, *EQ*

- error associated with finding a fixed point $||x_{\mathrm{f}}^{-} - x_{\mathrm{f}}^{-*}||$

Terms of Optimization	
Independent	**Dependent**
$x_{\mathrm{f}}^{-*} \in I\!R^{14}$	$\theta_{\mathrm{s}}^{+*} \in I\!R$
$a_{\mathrm{s},2}^*, \ldots, a_{\mathrm{s},m_{\mathrm{s}}}^* \in I\!R^4$	$a_{\mathrm{s},0}^*, a_{\mathrm{s},1}^* \in I\!R^4$
$\theta_{\mathrm{s}}^{-*} \in I\!R$	$x_{\mathrm{s}}^{+*} \in I\!R^{10}$
$a_{\mathrm{f},2}^*, \ldots, a_{\mathrm{f},m_{\mathrm{f}}-2}^* \in I\!R^4$	$a_{\mathrm{f},0}^*, a_{\mathrm{f},1}^* \in I\!R^4$
	$a_{\mathrm{f},m_{\mathrm{f}}-1}^*, a_{\mathrm{f},m_{\mathrm{f}}}^* \in I\!R^4$
	$x_{\mathrm{cm,f}}^{+*}, \dot{x}_{\mathrm{cm,f}}^{+*}, T_{\mathrm{f}}^* \in I\!R$
	$x_{\mathrm{f}}^{-} \in I\!R^{14}$

Table 5.1: Independent and dependent terms used in optimization. The choice of the independent terms is non-unique and depends on the specific optimization procedure. The parameters below correspond to the algorithm in Section 5.2.3, which is one straightforward method to ensure the boundary conditions of the virtual constraints are met.

- deviation from the desired running rate
- required frictional forces at the leg ends are zero just before takeoff and just after landing (to prevent slipping at these transitions)

Inequality constraints, *INEQ*

- magnitude of the required torque at each joint less than 100 Nm
- knee angles to lie in $(0^\circ, -70^\circ)$ and hip angles to lie in $(130^\circ, 250^\circ)$ (see Figure 5.1(b) for measurement conventions)
- minimum height of the swing foot during stance greater than 7 cm
- required coefficient of friction of the stance phase less than 0.7
- flight time greater than or equal to 25% of total gait duration
- landing foot impacts the ground at an angle of approach less than 45° from vertical
- joint angular velocities less than 5 rad/s

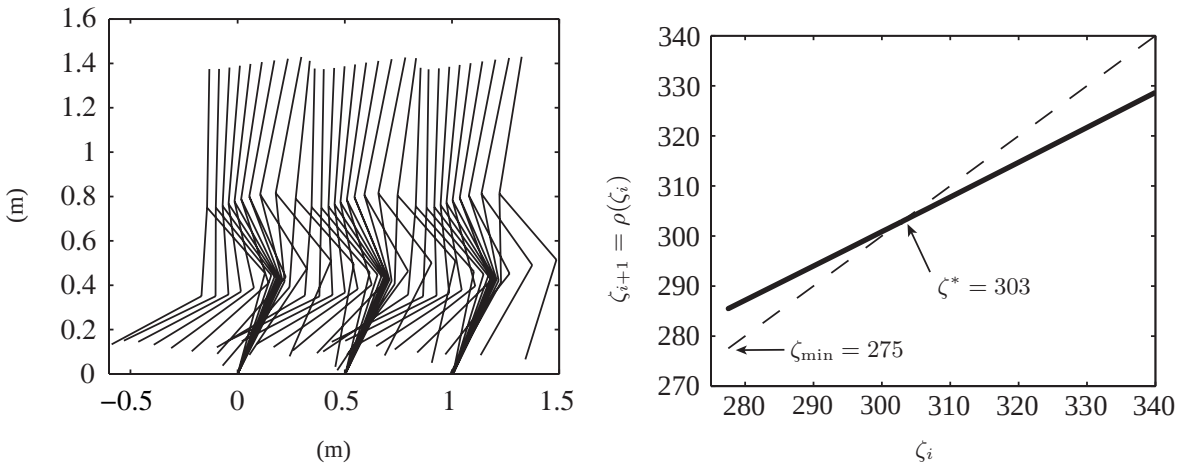

(a) Stick diagram

(b) Poincaré map

Figure 5.2: Stick diagram and Poincaré map for the example running motion (rate 0.58 m/s). Poincaré map constructed by evaluating $\zeta = (\sigma_{s,1}^-)^2/2$ at the end of successive stance phases, where $\sigma_{s,1}^-$ is the angular momentum about the stance leg end just before liftoff. The fixed point, $\zeta^* = 303$, is located at the intersection of ρ and the identity map $\zeta_i = \zeta_{i+1}$, and corresponds to an equilibrium running rate of 0.58 m/s. The slope of the graph at ζ^* is $d\rho/d\zeta \approx 0.67$, indicating exponential stability.

5.3 Experiment

5.3.1 Hardware Modifications to RABBIT

Prior to the experiment reported here, only walking experiments had been performed with RABBIT. To prepare for the task of running, four hardware modifications were made.

The first modification was the inclusion of prosthetic shock absorbers in the shanks. It was speculated that with shock absorbers the landing would cause less wear and tear on the harmonic drive gear reducers that form RABBIT's hip and knee joints. The inclusion of shock absorbers added approximately 5 cm to each shank.

The second modification was the installation of force sensitive resistors into RABBIT's point feet. These devices allowed for more accurate measurement of the touchdown time than did the previously installed mechanical contact switches. Since these sensors suffer from significant drift, their signals were numerically differentiated to make easier the detection of impact events.

The last two modifications were the bolting of aluminum u-channel stock along each thigh and

the widening of the hips. Both of these changes were made to help prevent flexing of the legs in the frontal plane. Significant flexing was witnessed during the first several experimental trials of running. This problem was more pronounced in running than in walking because of the greater impact forces associated with landing. On several occasions RABBIT "tripped itself" during a stance phase of running when the swing leg passed by the stance leg (the legs knocked against each other). This came about because RABBIT was designed to have its legs close together to better approximate a planar biped.

5.3.2 Result: Six Running Steps

After completing hardware modifications and successfully reproducing previous walking experiments, running experiments were conducted. A number of experimental trials resulted in RABBIT taking several human-like[8] running steps. One such trial, which was an implementation of the example running motion of Section 5.2.4, will be discussed here.

For this experiment, motion was initiated by an experimenter who pushed the robot forward, into the basin of attraction of a walking controller that induced walking with an average forward walking rate of 0.8 m/s. RABBIT then achieved stable walking, followed by a transition to running in a single step, followed by six running steps. After the sixth step, the experiment was terminated by the control software when the tracking error limit of 0.3 radians was exceeded for the stance knee angle. Examination of collected data suggests that tracking error resulted from actuator saturation.[9] Data also show the swing leg extremely close to the ground at the moment the experiment was terminated, suggesting the swing leg may have, in fact, struck the ground contributing additional tracking error.

A plot of estimated[10] foot height is given in Figure 5.3. Average stride duration for the steps was 431 ms. Flight times, observed as those portions of Figure 5.3 where neither leg is at zero height, lasted an average of 107 ms (25% of the stride). Videos of the experiment and many additional data plots are available at [59].

[8] A human-like gait is considered to be characterized by an upright posture, a torso leaning slightly forward, and a long step length.

[9] See [149] for a description of the PD controllers used to enforce the virtual constraints.

[10] When RABBIT is in flight, there is no accurate way to determine hip height. A sensor was mounted to record boom pitch angle, but due to flexing of the boom, these data were inaccurate. During the stance phase this lack of sensing is not a problem because the end of the stance leg is always at zero height.

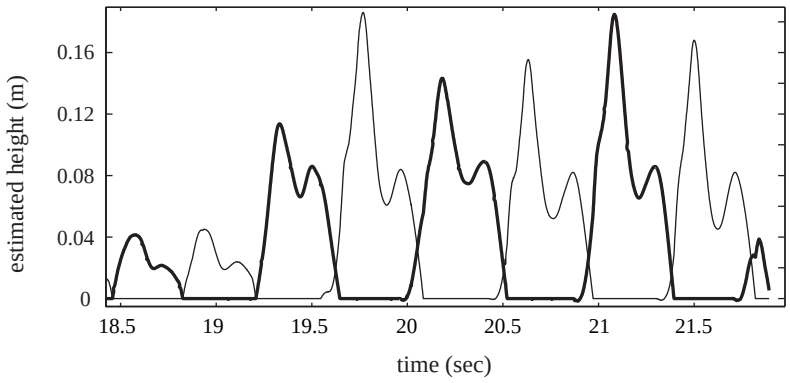

Figure 5.3: Estimated height of RABBIT's point feet during the reported running experiment. RABBIT's left foot is indicated in bold. Flight phases occur when neither foot is at zero height.

Several problematic issues related to RABBIT's hardware did not appear until running was attempted. (For a discussion of general implementation issues of walking including unmodeled effects of the boom, gear reducers, and an uneven walking surface see [149].) Future running experiments—whether on RABBIT or another, similar mechanism—should take into account the following issues.

Boom dynamics

The perturbing effects of the boom were found to be much more significant during flight phases than during stance phases. When RABBIT is modeled as a planar system, an analysis of the three-dimensional mechanics shows that the contribution of the boom to the center of mass dynamics is significant. Specifically, q_5 is no longer, in general, a cyclic variable during flight. However, if boom masses are appropriately distributed, the parabolic motion of the center of mass, as modeled in a planar system, is recovered. Unfortunately, this special mass distribution was impossible because RABBIT does not have a counterweight system.

Walking surface

The walking surface was also a source of problems. This surface—consisting of rubber over elevated plywood supported on the edges by a wood frame—was originally built to provide a uniform, level surface. Although the surface appears uniform, walking experiments demonstrated otherwise. It was found that the surface has "fast" and "slow" areas corresponding to varying floor stiffness

and coefficient of friction.

Limited joint space

For safety, RABBIT's joints have hard stops that limit its joint space, which, for example, prevent the shank from contacting the thigh. Although the available joint space was sufficient for walking, it became a significantly limiting factor in the design of running gaits. These hard stops prevented the swing leg from being folded close to the hip, which is a natural and desirable motion that minimizes the leg's rotational inertia.

5.4 Conclusion

A novel approach to the control of running in planar bipeds and its first experimental implementation on RABBIT have been presented. The control law is hybrid, consisting of continuous actions in the stance and flight phases and discrete actions at the transitions between these phases. In the stance and flight phases, the controller coordinates the relative motions of the robot's links by imposing virtual constraints at the actuated joints. At the transition from stance to flight, the controller adjusts the virtual constraints for the flight phase as a function of estimated flight duration to ensure that the former swing leg is advanced properly to take up its role as the next stance leg. At the transition from flight to stance, the controller updates the virtual constraints of the stance phase to account for the orientation of the robot at landing. For the nominal periodic running motion, the parameters of the virtual constraints are determined by numerical optimization in order to meet actuator power limits, friction bounds, joint limits, etc. For running experiments, RABBIT's mechanical and electrical systems were modified: shock absorbers were added to the shanks; the ground contact sensors were improved; the stiffnesses of legs in the frontal plane were increased; and the hips were widened.

The main theoretical result of this chapter was the development of a running controller that is based on the HZD methodology, but easier to design and implement while still resulting in a reduced dimensionality stability test. The main experimental result of this chapter was the physical realization of six consecutive running steps with a human-like gait and identification of hardware difficulties of running with RABBIT that were not present in walking.

Takeoff Time	Landing Time	Flight Phase Duration
$19.5465\ s$	$19.6470\ s$	$0.1005\ s$
$19.9545\ s$	$20.0835\ s$	$0.1290\ s$
$20.4255\ s$	$20.5215\ s$	$0.0960\ s$
$20.8695\ s$	$20.9715\ s$	$0.1020\ s$
$21.3045\ s$	$21.3945\ s$	$0.0900\ s$
$21.6990\ s$	$21.8205\ s$	$0.1215\ s$

Table 5.2: Flight phase durations for the six running steps. Time t = 0 s corresponds to the initiation of the experiment.

5.5 Supplemental Material

To support the conclusions of this chapter, several additional data plots are provided here that did not appear in [101]. Figure 5.4 shows the value of a normalized gait parameter as a function of time. Values from 0 to 1 indicate the completed fraction of the planned stance phase, and values from 1 to 2 indicate the completed fraction of the planned flight phase. Power was automatically cut after the sixth step due to high joint tracking error. Corresponding takeoff times, landing times, and flight phase durations are given in Table 5.2. Plots of actuator saturation are shown in Figure 5.5 where the provided torque and the commanded torque level are shown in fractions of motor capacity. Flattened peaks at 1 and -1 indicate the controller commanded more torque than the motors could output. Data suggests that torque saturation during the flight phase caused a buildup of tracking error across the six running steps. The tracking plots of Figure 5.6 show how closely the local PD joint controllers enforced the virtual constraints at each joint, indicating that actual joint trajectories were ordinarily very close to their desired values. The experiment was terminated by the accumulation of tracking error in the right knee joint as shown in Figure 5.7.

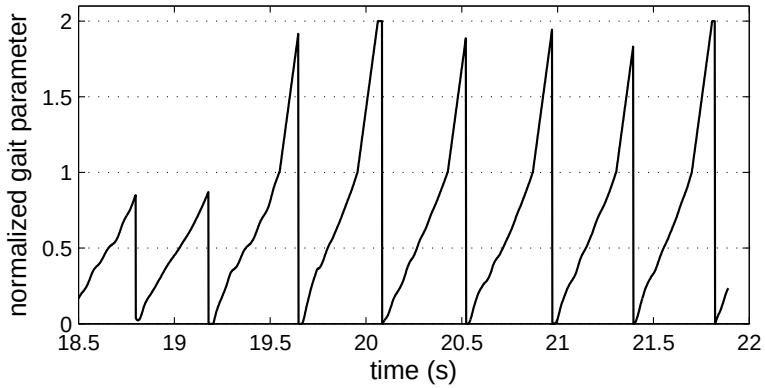

Figure 5.4: Normalized gait parameter showing the existence of six running steps. Values from 0 to 1 indicate the completed fraction of the planned stance phase, and values from 1 to 2 indicate the completed fraction of the planned flight phase.

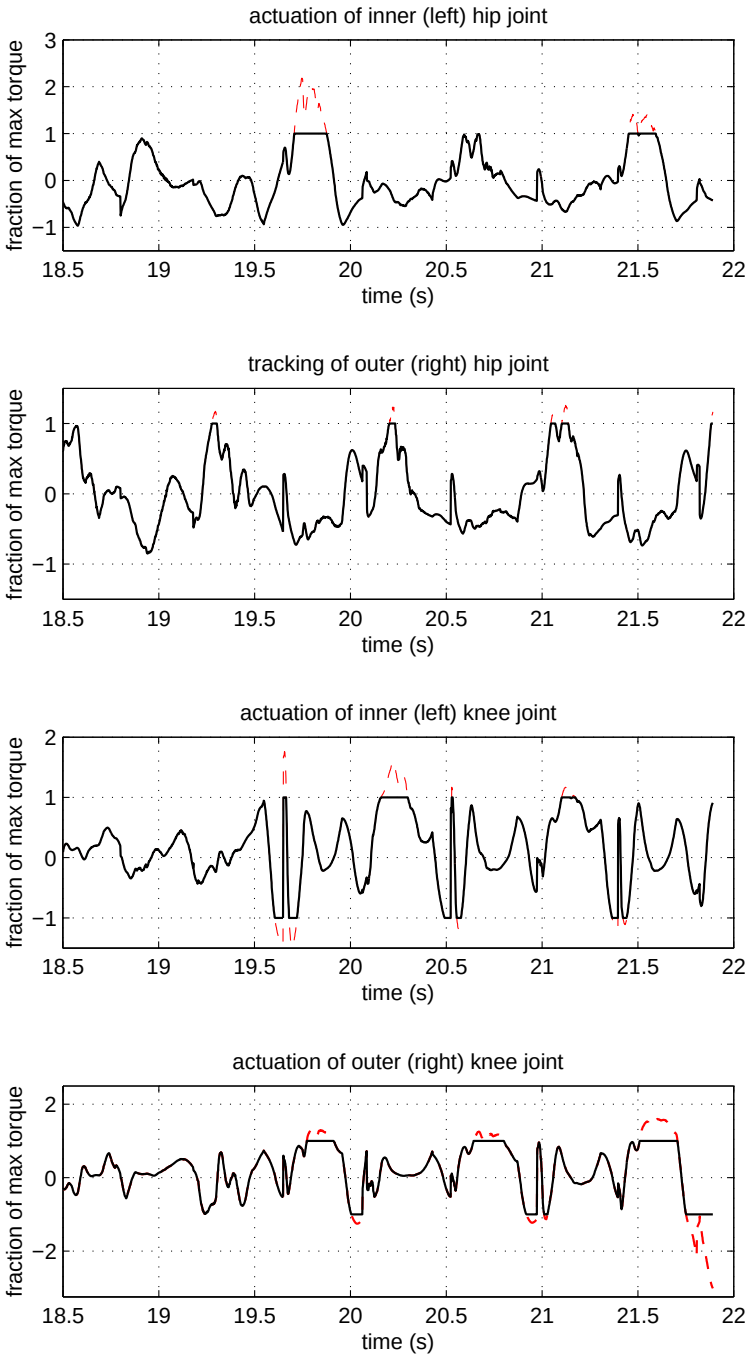

Figure 5.5: Actuator saturation during running. The provided actuation is shown as a solid line. The actuation requested by the controller is shown by a lighter, dashed line. Flat peaks at 1 and -1 indicate the controller required more torque than the motors could safely provide.

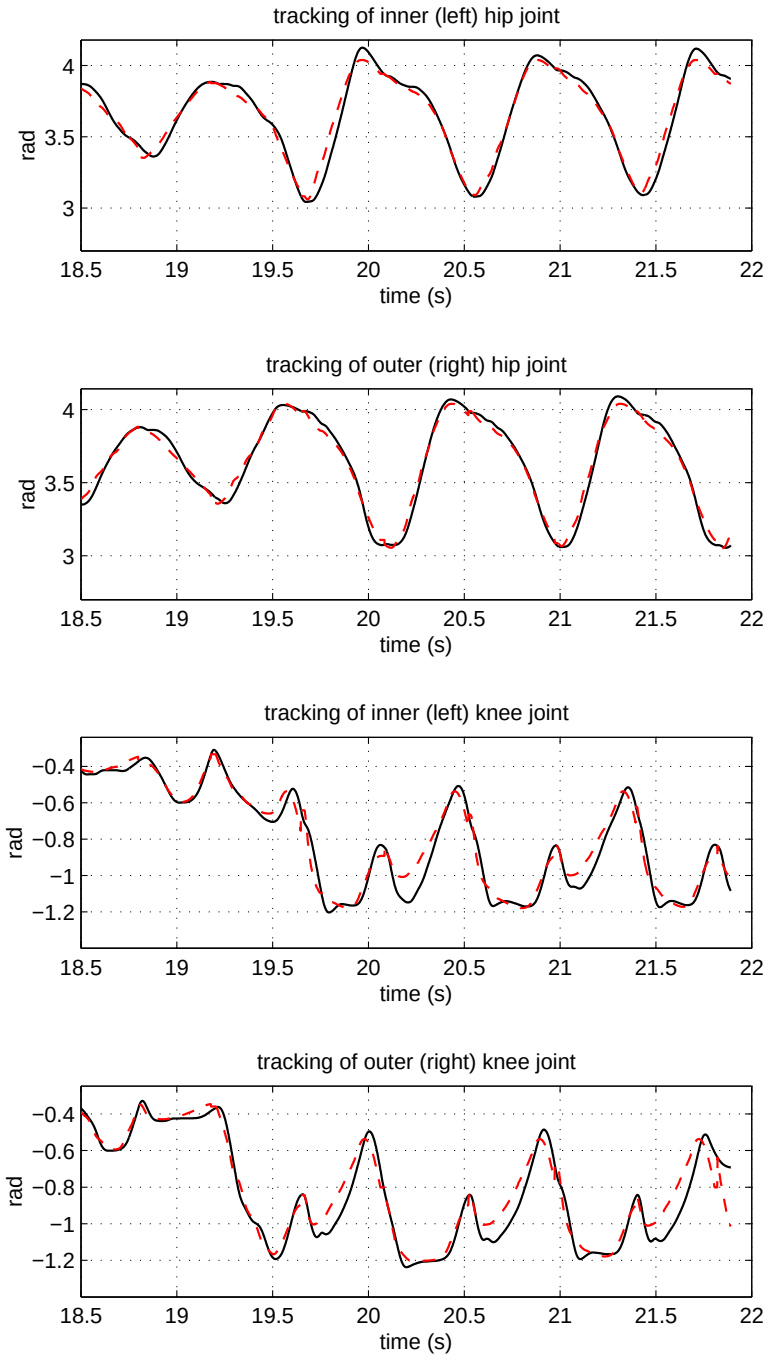

Figure 5.6: Joint tracking performance during running. The observed trajectory is shown as a solid line, the reference trajectory, by a lighter, dashed line.

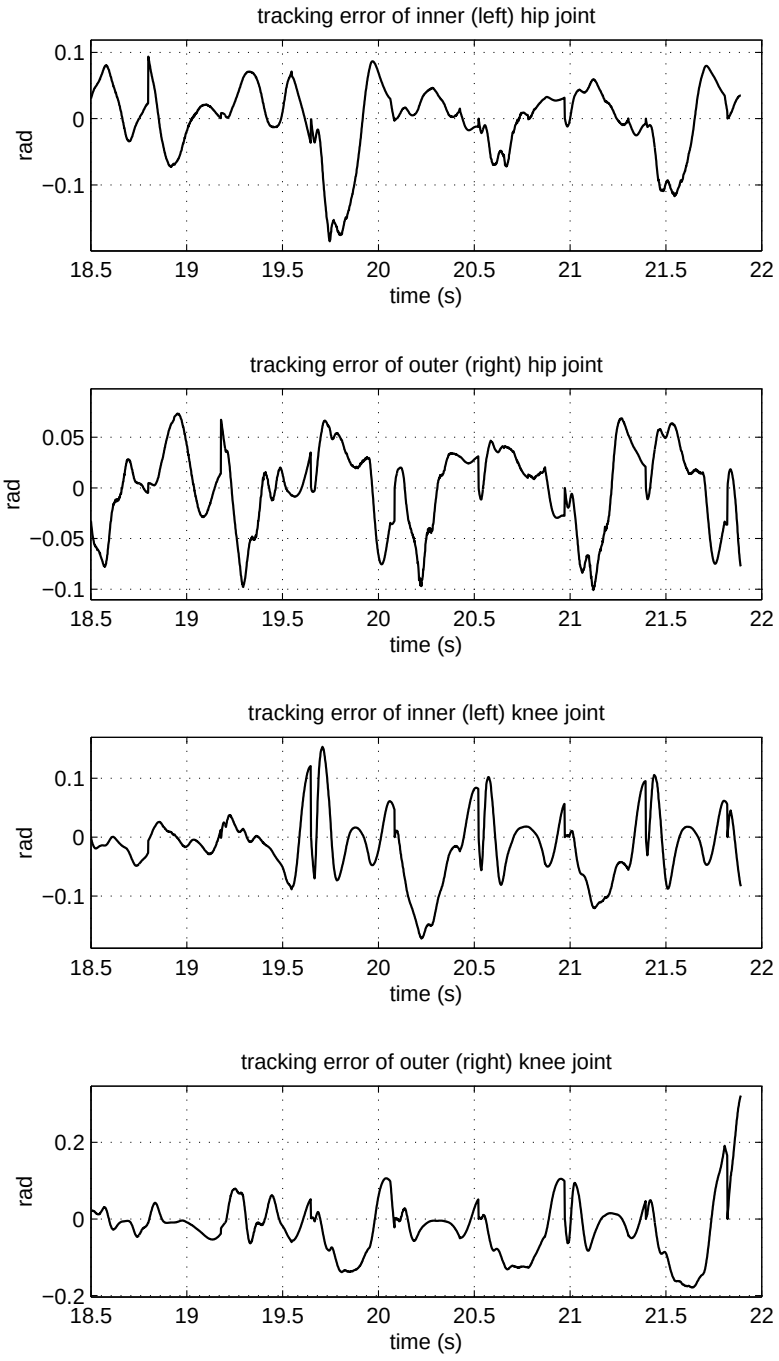

Figure 5.7: Joint tracking error during running. An accumulation of error in the outer knee triggered safety conditions that automatically terminated the experiment.

Notation Introduced in Chapter 5

Symbol	Meaning	Defined
$\mathcal{A}_{\mathrm{s}}$	parameter space of the virtual constraints of stance	Section 5.1.3
$\mathcal{A}_{\mathrm{f}}$	parameter space of the virtual constraints of flight	Section 5.1.3
$h_{d,\mathrm{s}}, \theta_{\mathrm{s}}$	functions defining the virtual constraints of stance	Section 5.1.3
$h_{d,\mathrm{f}}, \theta_{\mathrm{f}}$	functions defining the virtual constraints of flight	Section 5.1.3
$w_{(\mathrm{f}\to\mathrm{s})}$	parameter updates at landing	Section 5.1.6
$w_{(\mathrm{s}\to\mathrm{f})}$	parameter updates at liftoff	Section 5.1.7
$\mathcal{X}_{\mathrm{s}_{\mathbf{e}}}$	state manifold of the closed-loop stance phase	Section 5.1.8
$\mathcal{X}_{\mathrm{f}_{\mathbf{e}}}$	state manifold of the closed-loop flight phase	Section 5.1.8
$x_{\mathrm{s}_{\mathbf{e}}}$	state of the robot in closed-loop stance	Section 5.1.8
$x_{\mathrm{f}_{\mathbf{e}}}$	state of the robot in closed-loop flight	Section 5.1.8
$\bar{f}_{\mathrm{s}_{\mathbf{e}}}$	vector field of the closed-loop stance phase	Section 5.1.8
$\bar{f}_{\mathrm{f}_{\mathbf{e}}}$	vector field of the closed-loop flight phase	Section 5.1.8
$\overline{\Delta}_{(\mathrm{s}\to\mathrm{f})_{\mathbf{e}}}$	closed-loop liftoff map	Section 5.1.8
$\overline{\Delta}_{(\mathrm{f}\to\mathrm{s})_{\mathbf{e}}}$	closed-loop landing map	Section 5.1.8
$\bar{\Sigma}_{\mathrm{s}_{\mathbf{e}}}$	model of the closed-loop stance phase	Section 5.1.8
$\bar{\Sigma}_{\mathrm{f}_{\mathbf{e}}}$	model of the closed-loop flight phase	Section 5.1.8

CHAPTER 6

Sample-Based HZD Control for Robustness and Slope Invariance of Planar Passive Bipedal Gaits*

To explore potential connections between passive dynamic walkers and hybrid zero dynamics controllers, this chapter presents new analysis results and tools for the HZD framework. These include (i) analysis of the effects of walking on a slope, (ii) analysis of dynamic singularities resulting from enforcing virtual constraints, and (iii) an alternative method for designing virtual constraints. Extensions are motivated by a desire to make the gaits of passive walkers robust to disturbances. As noted in Chapter 2, passive bipedal walkers have the ability to walk stably down a slope without the use of actuation [96] and typically suffer from sensitivity to initial conditions and to external disturbances. The new results and tools facilitate the design of controllers to make such passive gaits robust.

The first result, analysis of walking on a slope, is an extension of [153, 149] in which components of the closed-loop system dynamics are examined to determine the overall effects of changing ground slope. Results make indirect use of observations given in [133] regarding the fact that planar rotations of the robot are a group symmetry of the robot's kinetic energy but not of its potential energy.

The second result sheds light onto the condition of decoupling matrix invertibility. For an HZD controller to be valid, the decoupling matrix associated with performing input-output linearization of

*The contents of this chapter are taken, with minimal modification, from the journal article [154] entitled "Analysis Results and Tools for the Control of Planar Bipedal Gaits using Hybrid Zero Dynamics" by E. R. Westervelt, B. Morris, and K. D. Farrell. Co-authored material used by permission.

the robot's dynamics must be invertible [78, Chp. 5]. The closed-loop system is said to encounter a *dynamic singularity* at points where the decoupling matrix is noninvertible. This definition is used to parallel the notion of a kinematic singularity[1]. Dynamic singularities, like kinematic singularities, represent configurations of the robot at which there is a reduction in the number of DOFs. But, unlike kinematic singularities—which arise from the mechanism's kinematics and involve only its kinematic parameters—dynamic singularities involve both kinematic and inertial parameters. One type of dynamic singularity related to bipedal walking involves the decoupling matrix used in HZD feedback controllers. Other types of dynamic singularities will not be considered. It is shown that decoupling matrix singularities can be computed with a relatively simple, closed form expression. Interpretations of dynamic singularities are given as well as analysis of the effects of approaching a singularity.

The third result, an alternative method for designing virtual constraints, expands the set of reference gaits controllable within the HZD framework, separating gait design and controller design into two distinct steps. In previous work, the virtual constraints were chosen using numerical optimization over a pre-chosen, finitely parameterized family of constraints. This technique is acceptable when the objective of controller design is to find a gait with certain stability and energetic properties. However, when the goal is to exactly achieve a given gait, existing techniques can do no better than to project the motion onto the closest member of the parameterized family of constraints. The alternative method, termed *sample-based HZD control*, does not use a pre-chosen family of virtual constraints. In essence, a given (period-one) gait is sampled to obtain full state information at chosen instants of time. Certain normalized quantities are computed from this full state information and are used to define the virtual constraints of an HZD controller. The sampled gait can be obtained from, for example, a gait induced by a potentially unknown control strategy, or a gait whose corresponding control strategy is not equivalent to imposing holonomic constraints. An example of the latter is the work of [30] where joint motions were designed to be polynomial functions of *time*, rather than of state. By using this approach, it is usually not possible to *explicitly* represent the motions as following holonomic constraints [28].[2]

With regard to passive gaits, sample-based HZD control enables the design of controllers that

[1] For other definitions of dynamic singularities relating to spacecraft manipulators, see [105, 158].

[2] What this section provides is a computationally tractable *implicit* representation of the holonomic constraints that correspond to such motions.

can (i) render a stable, passive gait robust and (ii) systematically modify a given gait's characteristics. The sample-based HZD controller method combines the provable stability properties and large basins of attraction of HZD controllers with the energy efficiency of passive or nearly passive gaits. The theory differs from the work of [133], [9], and [137] in that full actuation[3] is not assumed and a means to systematically modify the gait is given. The theory also differs from the work of [56] in that a given passive gait is enforced (with arbitrary accuracy), rather than inducing a gait that does not correspond to one that is passive.

The theoretical results of the chapter are illustrated via five examples. Although the developed theory applies to N-link planar bipeds with point feet, for presentation simplicity all examples use the two-link walker depicted in Figure 6.1. The dynamics of the biped during the single support phase is that of the Acrobot [132].

The content of the remainder of the chapter is as follows. Section 6.1 presents the model for walking on sloped ground. Section 6.2 reviews the concepts of virtual constraints and HZD control in the context of walking on a sloped surface. Section 6.3 gives the analysis of dynamic singularities followed by an example. Section 6.4 develops sample-based virtual constraints and augmentation functions, and includes an application to the design of controllers for torque specified gaits. Section 6.5 contains three examples that apply the tools of Section 6.4 to the design of controllers that make passive gaits robust. Conclusions are drawn in Section 6.6.

6.1 Model of Walking on Sloped Ground

6.1.1 A System with Impulse Effects

The biped is assumed to be comprised of N rigid links connected by revolute joints such that (i) there are no closed kinematic chains; (ii) there are two symmetric legs and, possibly, a torso; and (iii) the leg ends contact the ground at a single point. The robot is said to be in single support (or in the swing phase) when exactly one leg is in contact with the ground. The leg contacting the ground is called the stance leg and the other is called the swing leg. It is assumed that all of the biped's

[3] In the HZD framework, the biped is assumed to have point contact with the ground and is therefore underactuated. With this assumption, the effective underactuation that exists between the biped and the ground—because of unilateral constraints due to finite foot size—is made explicit. If a biped in question is, in fact, fully actuated, the HZD framework still applies. First an HZD controller is designed, and then an outer-loop control is designed that makes use of the ankle torque [34].

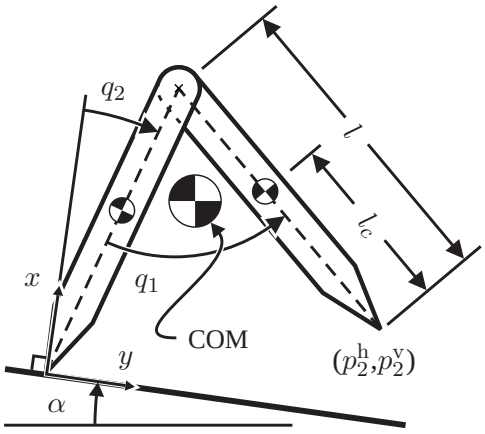

Figure 6.1: Diagram of a two-link planar biped walking down a slope. The dynamics during the single support phase is that of the Acrobot [132].

internal degrees of freedom (DOFs) are actuated, but that the degree of freedom associated with the robot's absolute orientation is unactuated (i.e., no torque can be supplied between the robot and the ground). The swing phase model is therefore underactuated.

The generalized coordinates of the biped are $q = (q_a, q_u) \in \mathrm{Q}$, where Q is an appropriate subset of $\mathbb{R}^N$, q_a is the column vector of the relative, actuated coordinates, and q_u is the unactuated coordinate. It is assumed that the unactuated coordinate is measured relative to the walking surface. The swing phase equation of motion of the biped is

$$D(q)\ddot{q} + F[\alpha](q, \dot{q}) = Bu, \tag{6.1}$$

with $B = [\, I \;\; 0 \,]'$ and where[4] α is the ground slope; for example, see Figure 6.1. Let the state of the biped be $x = (q, \dot{q}) \in T\mathrm{Q}$. Then, (6.1) can be written as

$$\dot{x} = f[\alpha](x) + g(x)u. \tag{6.2}$$

The walking gait is assumed to be symmetric with respect to the two legs so that, in particular, the same swing phase model can be used irrespective of which leg is the stance leg.

Swing phases are separated by phases of double support, occurring when both feet are in contact with the ground. This transition is modeled as an instantaneous, rigid body collision [74] that occurs when $x \in \mathcal{S} = \{x \in T\mathrm{Q} \mid p_2^{\mathrm{v}}(x) = 0\}$, where p_2^{v} is the vertical height of the swing leg end. The

[4]Throughout this chapter, dependence on the ground slope parameter is emphasized by the use of square brackets.

transition model, which includes a permutation of the coordinates to account for the swapping of the legs' roles, is algebraic and can be written as

$$x^+ = \Delta(x^-), \tag{6.3}$$

where the superscript "$+$" (resp. "$-$") refers to the value at the beginning (resp. end) of a step.

The overall model is expressed as a single-charted system with impulse effects:

$$\Sigma : \begin{cases} \dot{x} = f[\alpha](x) + g(x)u, & x^- \notin \mathcal{S} \\ x^+ = \Delta(x^-), & x^- \in \mathcal{S}. \end{cases} \tag{6.4}$$

Walking gaits will be analyzed as periodic orbits of (6.4), with stability of a walking gait referring to stability of the corresponding periodic orbit. For formal definitions of solutions, orbits, and stability relating to (6.4), see [60].

6.1.2 Example Model: A Two-Link Walker

For presentation simplicity, the results of this chapter will be illustrated on a two-link biped walker—a biped with the fewest number of links to which the results apply. The biped is depicted in Figure 6.1, and its parameters are given in Table 6.1. The terms of the equations of motion for the walker are as follows. The (symmetric) mass inertia matrix is

$$D_{11}(q_1) = (l - l_c)^2\, m + J \tag{6.5a}$$

$$D_{12}(q_1) = m\, l(l - l_c)\cos(q_1) - (l - l_c)^2\, m - J \tag{6.5b}$$

$$D_{22}(q_1) = -2\, m\, l(l - l_c)\cos(q_1) + \left(2(l_c^2 + l^2) - 2\, l_c\, l\right)\, m + 2\, J. \tag{6.5c}$$

The vector of Coriolis, centrifugal, and gravity terms is

$$F_1[\alpha](q, \dot{q}) = -m\, l \sin(q_1)(l - l_c)\dot{q}_2^2 + m\, g_0 \sin(q_1 - q_2 - \alpha)(l - l_c) \tag{6.6a}$$

$$\begin{aligned} F_2[\alpha](q, \dot{q}) = {} & -m\, l \sin(q_1)(l - l_c)(\dot{q}_1 - \dot{q}_2)\dot{q}_1 + m\, l \sin(q_1)(l - l_c)\dot{q}_1\dot{q}_2 \\ & + m\, g_0\big((l_c - l)\sin(q_1 - q_2 - \alpha) - \sin(q_2 + \alpha)(l_c + l)\big). \end{aligned} \tag{6.6b}$$

Leg scuffing that necessarily occurs during the swing phase of the two-link walker is ignored.

Parameter	Units	Value
Leg length, l	m	1.0
Leg COM location, l_c	m	0.8
Leg mass, m	kg	0.3
Leg inertia about leg COM, J	kg·m^2	0.03
Acceleration due to gravity, g_0	m/s^2	9.81

Table 6.1: Parameters of the two-link model. (Parameters taken from [48, Tab. 4.1].)

6.2 HZD Framework for the Control of Walking on Sloped Ground

6.2.1 Defining Virtual Constraints

Virtual constraints are holonomic constraints that are imposed on the robot's configuration by feedback. These constraints are parameterized by a scalar function of the robot's configuration, and, when enforced by feedback, effectively reduce the closed-loop DOFs of the robot. When virtual constraints satisfying certain invariance properties are exactly enforced, the HZD of walking results.

To formally define virtual constraints, consider the following output on (6.2),

$$\theta(q) : \mathrm{Q} \to R_\theta \subset \mathbb{R} \tag{6.7a}$$

$$s(\theta) : R_\theta \to [\,0, 1\,] \tag{6.7b}$$

$$h_d(s) : [\,0, 1\,] \to \mathbb{R}^{N-1} \tag{6.7c}$$

$$y = h(q) = q_a - h_d \circ s \circ \theta(q) \tag{6.7d}$$

where $\theta(q)$ is a function that is monotonic over a step and has a compact image R_θ, $s(\theta)$ is a bijection with respect to R_θ and normalizes θ to the unit interval, and $h_d(s)$ is a twice continuously differentiable function that gives the actuated coordinates of the robot. For notational simplicity, define $\bar{h}_d(\theta) = h_d \circ s(\theta)$ so that (6.7d) can be written

$$y = q_a - \bar{h}_d \circ \theta(q)\,. \tag{6.8}$$

Let θ^+ and θ^- denote, respectively, the values of $\theta(q)$ at the beginning and the end of a step. Then,

a valid choice for s, is $s(\theta) = (\theta - \theta^+)/(\theta^- - \theta^+)$ with

$$\theta = c\,q, \tag{6.9}$$

where $c = (c_1,\, c_2)$, $c_1 \in \mathbb{R}^{N-1}$ and $c_2 \in \mathbb{R}$ with c_2 nonzero. This choice will be assumed for the remainder of the chapter. Virtual constraints are said to be satisfied or enforced when $y \equiv 0$. The constraint surface $\mathcal{Z}$ is defined as the subset of $T\mathrm{Q}$ where the virtual constraints are satisfied,

$$\mathcal{Z} = \{x \in T\mathrm{Q} \mid h(x) = 0, L_f h(x) = 0\}. \tag{6.10}$$

Note that it can be easily verified that $L_g h(x) = 0$ for all $x \in T\mathrm{Q}$.

When viewed within the context of the hybrid model (6.4), the virtual constraints are required to have two types of invariance: forward invariance (or continuous phase invariance) and impact invariance (or invariance across the impact event). Continuous phase invariance refers to the property that once a solution of (6.4) is within the constraint surface, the solution remains in the constraint surface until the end of the single support phase. This type of invariance is achieved by the appropriate design of a feedback controller. The virtual constraints are invariant across the impact event if lying within the constraint surface before impact guarantees that the solution will lie within the constraint surface after impact. This type of invariance is a property of virtual constraints themselves and is independent of the feedback controller.

6.2.2 A Feedback yielding Continuous Phase Invariance

Assume a constraint of the form (6.7), which may or may not be impact invariant. The controller given in this subsection will render it continuous phase invariant. The controller's development begins by taking the first two derivatives of the constraint,

$$\dot{y} = \dot{q}_a - \frac{\partial \bar{h}_d(\theta)}{\partial \theta}\,\dot{\theta}, \tag{6.11a}$$

$$\ddot{y} = \Upsilon(\theta)\,\ddot{q} - \frac{\partial^2 \bar{h}_d(\theta)}{\partial \theta^2}\,\dot{\theta}^2, \tag{6.11b}$$

$$\Upsilon(\theta) = \left[H - \frac{\partial \bar{h}_d(\theta)}{\partial \theta}\,c\right], \tag{6.12}$$

$$H = \begin{bmatrix} \mathrm{I}_{(N-1)\times(N-1)} & 0_{(N-1)\times 1} \end{bmatrix}. \tag{6.13}$$

With (6.1), (6.11b) can be expressed as

$$\ddot{y} = L_f^2 h[\alpha](q, \dot{q}) + L_g L_f h(q) u. \tag{6.14}$$

where

$$L_f^2 h[\alpha](q, \dot{q}) = -\Upsilon(\theta) D^{-1}(q) F[\alpha](q, \dot{q}) - \frac{\partial^2 \bar{h}_d(\theta)}{\partial \theta^2} \dot{\theta}^2 \tag{6.15}$$

$$L_g L_f h(q) = \Upsilon(\theta) D^{-1}(q) B. \tag{6.16}$$

The term $L_g L_f h(q)$ is known as the decoupling matrix from the input u to the output y. See Section 6.3 for explicit calculation and interpretation of the decoupling matrix's singularities as well as an example. With the application of the input-output linearizing pre-feedback

$$u = (L_g L_f h(q))^{-1} \left(v - L_f^2 h[\alpha](q, \dot{q}) \right), \tag{6.17}$$

the error dynamics (6.14) becomes $\ddot{y} = v$. Thus, choosing v to be a PD controller,

$$v = -K_p \, y - K_d \, \dot{y} \tag{6.18}$$

with poles sufficiently fast [100], the virtual constraints (6.8) will be asymptotically enforced and continuous phase invariant.

Remark 6.1. *The control law, (6.17) and (6.18), requires measurement of $(q, \dot{q})$ and computation of $L_g L_f h(q)$ and $L_f^2 h[\alpha](q, \dot{q})$. While $D(q)$, $F[\alpha](q, \dot{q})$, and B can be readily obtained from the system dynamics, the functions $\bar{h}_d(\theta)$, $\partial \bar{h}_d(\theta)/\partial \theta$, and $\partial^2 \bar{h}_d(\theta)/\partial \theta^2$ depend upon the choice of virtual constraints.*

6.2.3 The HZD of Walking

The HZD of walking is a subdynamic of the full hybrid walking model (6.4) that corresponds to the dynamics that are "left over" once the virtual constraints have been imposed. Like the full hybrid model, the HZD of walking is also a single-charted system with impulse effects, but of lower dimension. The HZD resulting from virtual constraints based on (6.7) are developed next.

The angular momentum about the stance leg end contact point with the ground is

$$\sigma = d_n(q) \, \dot{q}, \tag{6.19}$$

where d_n is the last row of D. In a neighborhood of any point where the decoupling matrix is invertible, $(y, \dot{y}, \theta, \sigma)$ is a valid change of coordinates[5] on $T\mathrm{Q}$. Furthermore, the inverse of the coordinate change is given by

$$q = \Phi_q(\theta, y) \tag{6.20a}$$

$$\dot{q} = \Phi_{\dot{q}}(\theta, \sigma, y, \dot{y}), \tag{6.20b}$$

where

$$\Phi_q(\theta, y) = \begin{bmatrix} H \\ c \end{bmatrix}^{-1} \begin{bmatrix} \bar{h}_d(\theta) + y \\ \theta \end{bmatrix} \tag{6.21a}$$

$$\Phi_{\dot{q}}(\theta, \sigma, y, \dot{y}) = \begin{bmatrix} \Upsilon(\theta) \\ d_n(q) \end{bmatrix}^{-1} \Bigg|_{q=\Phi_q(\theta,y)} \begin{bmatrix} \dot{y} \\ \sigma \end{bmatrix}. \tag{6.21b}$$

Assuming that the decoupling matrix is invertible, the zero dynamics manifold can be written as

$$\mathcal{Z} = \left\{ (q, \dot{q}) \in T\mathrm{Q} \;\middle|\; \begin{array}{l} q = \Phi_q(\theta, 0),\ \dot{q} = \Phi_{\dot{q}}(\theta, \sigma, 0, 0), \\ \theta \in [\theta^+, \theta^-], \sigma \in \mathbb{R} \end{array} \right\}. \tag{6.22}$$

With the output given by (6.7), and a few additional technical assumptions (see [153, Thm. 1]), the swing phase zero dynamics—the maximum dynamics that are compatible with $y \equiv 0$—are

$$\dot{\theta} = \frac{1}{I(\theta, 0)}\, \sigma, \tag{6.23a}$$

$$\dot{\sigma} = M_t\, g_0\, x_{\mathrm{cm}}[\alpha](\theta, 0), \tag{6.23b}$$

where

$$I(\theta, y) = \left(c\, \Phi_{\dot{q}}(\theta, 1, y, 0)\right)^{-1} \tag{6.24}$$

and where M_t is the total mass of the biped, g_0 is the magnitude of the acceleration of gravity, and $x_{\mathrm{cm}}[\alpha](\theta, y)$ is the horizontal position of the center of mass measured with respect to the stance leg end [29, Eq. (15)]. It can be shown that if the virtual constraints are impact invariant, then at an impact,

$$\sigma^+ = \delta_{\mathrm{zero}}\, \sigma^-, \tag{6.25}$$

[5] Note that a valid change of coordinates on $\mathcal{Q}$ is (θ, y), regardless of decoupling matrix invertibility. This fact is used in Theorem 6.7.

where δ_{zero} is a constant readily computed using the definition of σ, (6.3), (6.20), and (6.21). Taking $z = (\theta, \sigma)$ as a state vector, the single-charted HZD is,

$$\Sigma_{\text{zero}} : \begin{cases} \dot{z} = f_{\text{zero}}[\alpha](z), & z^- \notin \mathcal{S} \cap \mathcal{Z} \\ z^+ = \Delta_{\text{zero}}(z^-), & z^- \in \mathcal{S} \cap \mathcal{Z}. \end{cases} \tag{6.26}$$

The HZD is said to be *well-defined* if the virtual constraints are both forward and impact invariant. Forward invariance means that solutions of the HZD are also solutions of the full system (6.4), which, in the context of this chapter, is equivalent to the decoupling matrix, $L_g L_f h(q)$, being invertible along solutions of the HZD. If an HZD is well-defined, then θ will be a monotonic quantity, either increasing or decreasing along the continuous portions of a walking gait [153, Prop. 1]. For the remainder of the chapter it will be assumed that $\theta^+ < \theta^-$, or equivalently, that θ is monotonically increasing along the continuous phase of the orbit.

6.2.4 Gait Stability

A primary benefit of the HZD approach to the control of bipedal walking is the simple stability metric that it affords: the stability of a walking gait (periodic orbit of (6.4)) can be verified by checking two inequality constraints. Assume that the HZD is well-defined and that the virtual constraints are perfectly enforced. Since $\theta(t)$ is monotonic over a step, the coordinate change

$$\zeta = \frac{1}{2}\sigma^2 \tag{6.27}$$

allows (6.23) to be integrated and rewritten as

$$\zeta(\theta) = \zeta^+ - V_{\text{zero}}[\alpha](\theta) \tag{6.28a}$$

$$\sigma(\theta) = \text{signum}(\sigma^+)\sqrt{2\,\zeta(\theta)} \tag{6.28b}$$

where

$$V_{\text{zero}}[\alpha](\theta) = -\int_{\theta^+}^{\theta} I(\vartheta, 0) M_t\, g_0\, x_{\text{cm}}[\alpha](\vartheta, 0) d\vartheta \tag{6.29}$$

[153, Thm. 3]. With the impact map, ζ^- is related to ζ^+ by

$$\zeta^+ = \delta_{\text{zero}}^2 \zeta^-. \tag{6.30}$$

The step-to-step evolution of ζ^-—the restricted Poincaré map—is therefore given by

$$\zeta^-(k+1) = \delta_{\text{zero}}^2 \zeta^-(k) - V_{\text{zero}}[\alpha](\theta^-). \tag{6.31}$$

The fixed point of this map is

$$\zeta^{-*} = -\frac{V_{\text{zero}}[\alpha](\theta^-)}{1 - \delta_{\text{zero}}^2} \tag{6.32}$$

as long as

$$\zeta^{-*} \geq \frac{V_{\text{zero}}^{\max}[\alpha]}{\delta_{\text{zero}}^2} \tag{6.33}$$

where $V_{\text{zero}}^{\max} = \max_{\theta^+ \leq \theta \leq \theta^-} V_{\text{zero}}(\theta)$. The fixed point is exponentially stable if

$$\delta_{\text{zero}}^2 < 1. \tag{6.34}$$

Hence, a stable gait will exist in the full model (6.4) if the HZD is well-defined, if (6.33) and (6.34) hold, and if the virtual constraints are enforced by a sufficiently fast controller (6.18).

6.2.5 Effects of Varying Ground Slope

The effects of varying the ground slope on the existence of (stable) gaits are now presented. The presentation begins with two propositions summarizing several important facts.

Proposition 6.2. *Under the assumption that the unactuated coordinate is measured relative to the walking surface, the following functions and surfaces are independent of ground slope, α:*

i) the transition model, $\Delta(x)$,

ii) the restricted switching surface, $\mathcal{S} \cap \mathcal{Z}$,

iii) the restricted impact coefficient, δ_{zero}, and

iv) the decoupling matrix, $L_g L_f h(q)$.

Proof. Proof of part (i) is trivial by inspection of [153, Eqns. 6 and 7]. Condition (ii) holds since $\mathcal{S}$ is independent of α, which is trivial by inspection, and because the output (6.7) is independent of α. Condition (iii) holds by (i) and because σ and (6.20) are independent of α. Part (iv) is trivial. □

Proposition 6.3. *Under the assumption that the unactuated coordinate is measured relative to the walking surface, if the HZD is well-defined for a given ground slope α, then it will be well-defined for an arbitrary α.*

Proof. Invariance of the virtual constraints with respect to impacts and α holds by Proposition 6.2 parts (i) and (ii). Invariance of the decoupling matrix with respect to α holds by Proposition 6.2 part (iv). □

By Proposition 6.3, the minimum ground slope required for stable walking can be determined by finding the smallest α such that

$$-\frac{V_{\text{zero}}[\alpha](\theta^-)}{V_{\text{zero}}^{\max}[\alpha]} = \frac{1-\delta_{\text{zero}}^2}{\delta_{\text{zero}}^2}\,. \tag{6.35}$$

Note that the loss of stability amounts to the fixed point moving outside the restricted Poincaré map's domain of definition and not a change in the map's eigenvalue. Calculation of the maximum ground slope is more tedious and involves consideration of the ground reaction forces and actuator limits. The next proposition gives an interesting observation regarding the loss of stability due to ground slope decrease.

Proposition 6.4. *The effects of ground slope on (6.35) are due to the change in the relative horizontal distance between the COM and the contact point over a step.*

Proof. Consider (6.29). Since the function $I(\theta, 0)$ is independent of the absolute coordinate it is also independent of the ground slope, leaving $x_{\text{cm}}[\alpha](\theta, 0)$ as the only term dependent on α. □

This result makes indirect use of observations given in [133]. Namely, the results hold in part due to the fact that planar rotations of the robot are a group symmetry of the robot's kinetic energy but not of its potential energy.

6.3 Analysis of a Dynamic Singularity

By definition, a manipulator encounters a kinematic singularity at a configuration where its manipulator Jacobian is rank deficient. At a kinematic singularity, end effector motion in one or more directions cannot be achieved—not because of inertial considerations or actuator limits—but because of the geometry of the manipulator itself. Dynamic singularities, which are less common and defined in a variety of ways, are states of a robot that are impossible to attain for causes related to the robot's dynamics, and not the robot's kinematics alone.

As an example of a dynamic singularity, consider an idealized figure skater, viewed from above, that is rotating in place. Assume that the skater is massless except for point mass hands, and that the point of rotation is frictionless. For any nonzero rate of rotation the skater will be unable to bring both of their hands to the axis of rotation, due to conservation of angular momentum. Having both hands on the axis of rotation—resulting in the skater's inertia being zero—is a type of dynamic singularity. For other notions of dynamic singularities, see [105, 158].

The remainder of this section develops mathematical and physical explanations for one type of dynamic singularity that is encountered in the control of bipedal walking. The dynamic singularity occurs when the effective moment of inertia about the stance leg end is zero. The condition is characterized by rank deficiency of the decoupling matrix, whose inverse is required in the computation of the feedback controller (6.17). A numerical example is given in which the two-link walker encounters such a dynamic singularity.

6.3.1 Singularity in the Decoupling Matrix

Independent of slope, implementation of the HZD controller (6.17) requires inversion of the decoupling matrix (6.16), which is not necessarily full rank over the entire state space. At points where the decoupling matrix is rank deficient, the closed-loop system is said to encounter a dynamic singularity. At a point of singularity, the controller (6.17) is no longer valid and so the zero dynamics (6.23) and all associated analysis are meaningless. This section develops a means of identifying dynamic singularities so that they may be avoided in controller design. Physical interpretation of a dynamic singularity is also developed as it applies to bipedal walking.

The development begins by noting that the decoupling matrix (6.16) is a continuous function of the configuration q. As a result, as long as the decoupling matrix is invertible along the periodic orbit, it will be invertible on the constraint surface $\mathcal{Z}$ and also in some open region containing the constraint surface[6]; see [108, Section V.B]. In this case, keeping the solution of the closed-loop system sufficiently close to the constraint surface will ensure that dynamic singularities are avoided. However, ensuring that the solution remains close to the constraint surface requires careful initial-

[6]The decoupling matrix is invertible along the orbit if, and only if, it is invertible for all $q = \Phi_q(\theta, 0)$ for $\theta \in [\theta^+, \theta^-]$. This same set of configurations appears in the description of zero dynamics manifold (6.22). So, invertibility along the orbit implies invertibility along the entire zero dynamics manifold. By continuity arguments, the decoupling matrix is invertible in some open region of TQ containing the zero dynamics manifold $\mathcal{Z}$.

ization of the system's state and, possibly, the use of large control gains. Although singularities are avoided with this approach, no insight is provided into their origin.

6.3.2 A Closed Form Inverse

Finding the region of invertibility of the decoupling matrix is a nontrivial task in general. For the class of output functions given by (6.7), however, both the decoupling matrix's inverse and its region of invertibility can be computed in closed form. These results are developed next.

Application of the partial linearizing feedback,

$$u = \bar{D}(q)v + \bar{F}[\alpha](q, \dot{q}), \tag{6.36}$$

where

$$\bar{D}(q) = D_{11}(q) - D_{12}(q)D_{22}^{-1}(q)D_{21}(q) \tag{6.37a}$$

$$\bar{F}[\alpha](q, \dot{q}) = F_1[\alpha](q, \dot{q}) - D_{12}(q)D_{22}^{-1}(q)F_2[\alpha](q, \dot{q}), \tag{6.37b}$$

to the swing phase equations of motion (6.1) results in

$$\begin{bmatrix} \ddot{q}_a \\ \ddot{q}_u \end{bmatrix} = \underbrace{\begin{bmatrix} 0_{(N-1)\times 1} \\ -D_{22}^{-1}(q)F_2[\alpha](q, \dot{q}) \end{bmatrix}}_{\bar{f}} + \underbrace{\begin{bmatrix} \mathrm{I}_{(N-1)\times(N-1)} \\ -D_{22}^{-1}(q)D_{21}(q) \end{bmatrix}}_{\bar{g}} v. \tag{6.38}$$

The decoupling matrix relating the input v and output y, (6.16), can then be expressed as

$$L_{\bar{g}}L_{\bar{f}}h(q) = \mathrm{I}_{(N-1)\times(N-1)} - \frac{\partial \bar{h}_d(\theta)}{\partial \theta} c \begin{bmatrix} \mathrm{I}_{(N-1)\times(N-1)} \\ -D_{22}^{-1}(q)D_{21}(q) \end{bmatrix}. \tag{6.39}$$

Proposition 6.5 (Decoupling matrix inverse in closed form)**.** *The decoupling matrix (6.39) is invertible everywhere that $S(q) \neq 0$, with $S(q)$ given by*

$$S(q) = 1 - c \begin{bmatrix} \mathrm{I}_{(N-1)\times(N-1)} \\ -D_{22}^{-1}(q)D_{21}(q) \end{bmatrix} \frac{\partial \bar{h}_d(\theta(q))}{\partial \theta}. \tag{6.40}$$

The inverse of the decoupling matrix, when defined, is

$$L_{\bar{g}}L_{\bar{f}}h(q)^{-1} = \mathrm{I}_{(N-1)\times(N-1)} + S(q)^{-1} \frac{\partial \bar{h}_d(\theta(q))}{\partial \theta} c \begin{bmatrix} \mathrm{I}_{(N-1)\times(N-1)} \\ -D_{22}^{-1}(q)D_{21}(q) \end{bmatrix}. \tag{6.41}$$

Proof. The proof follows from direct application of the Sherman-Morrison formula.[7] In this case, the matrices involved are

$$\frac{\partial h_d(\theta(q))}{\partial \theta} \quad \text{and} \quad c \begin{bmatrix} \mathrm{I}_{(N-1)\times(N-1)} \\ -D_{22}^{-1}(q)D_{21}(q) \end{bmatrix}. \tag{6.42}$$

□

Although Proposition 6.5 gives a simplified means of finding dynamic singularities—by finding zeros of $S(q)$—it does not provide physical insight into the origin of the singularities. Such interpretations are developed next.

6.3.3 Interpretations

Development of physical interpretations of dynamic singularities involves analysis of the coordinates of the zero dynamics, (6.19) and (6.9). First, (6.19) is expanded to obtain

$$\sigma = D_{21}(q)\dot{q}_a + D_{22}(q)\dot{q}_u, \tag{6.43}$$

and (6.9) is manipulated to yield

$$\dot{q}_u = c_2^{-1}\dot{\theta} - c_2^{-1}c_1\dot{q}_a. \tag{6.44}$$

Use of (6.8), (6.11a), (6.43), and (6.44), results in

$$\sigma = D_{21}(\theta, y)\left(\frac{\partial \bar{h}_d(\theta)}{\partial \theta}\,\dot{\theta} + \dot{y}\right) + D_{22}(\theta, y)\left(c_2^{-1}\dot{\theta} - c_2^{-1}c_1\left(\frac{\partial \bar{h}_d(\theta)}{\partial \theta}\,\dot{\theta} + \dot{y}\right)\right), \tag{6.45}$$

$$= I(\theta, y)\dot{\theta} + I_y(\theta, y)\dot{y} \tag{6.46}$$

where

$$I_y(\theta, y) = D_{21}(\theta, y) - c_2^{-1}D_{22}(\theta, y)c_1 \tag{6.47a}$$

$$I(\theta, y) = {c_2}^{-1}D_{22}(\theta, y)S(\theta, y) \tag{6.47b}$$

$$= I_{RB}(\theta, y) + I_{AB}(\theta, y) \tag{6.47c}$$

and

$$I_{RB}(\theta, y) = c_2^{-1}D_{22}(\theta, y) \tag{6.48a}$$

$$I_{AB}(\theta, y) = \left(D_{21}(\theta, y) - c_2^{-1}c_1D_{22}(\theta, y)\right)\frac{\partial \bar{h}_d(\theta)}{\partial \theta} \tag{6.48b}$$

[7] The *Sherman-Morrison formula* states that the matrix $(\mathrm{I}_{n\times n} - PQ)$, $P \in \mathbb{R}^{n\times m}$, $Q \in \mathbb{R}^{m\times n}$ is invertible if, and only if, $(\mathrm{I}_{m\times m} - QP)$ is invertible, in which case $(\mathrm{I}_{n\times n} - PQ)^{-1} = \mathrm{I}_{n\times n} + P(\mathrm{I}_{m\times m} - QP)^{-1}Q$.

Here, the terms I and I_{RB} are named the *virtual inertia* and the *rigid body inertia*. The rigid body inertia is the mass inertia of the robot (assuming q_a is constant) about the ground contact point, and, hence, $I_{RB}(\theta, y)\dot{\theta}$ is the rigid body angular momentum about this same point. The terms $I_{AB}(\theta, y)\dot{\theta}$ and $I_y(\theta, y)\dot{y}$ are *articulated body angular momenta*[8], contributions to the angular momentum about the ground contact point due to internal motions of the robot (variations of q_a). Note that while $I_{AB}(\theta, y)\dot{\theta}$ participates in the zero dynamics, $I_y(\theta, y)\dot{y}$ does not since $\dot{y} = 0$ on the zero dynamics manifold by definition.

In the context of (6.46), dynamic singularities have physical interpretations as given in the following theorem.

Theorem 6.6. *The following are equivalent:*

(i) *The decoupling matrix, $L_g L_f h(q)$, is singular.*

(ii) $S(q) = 0$.

(iii) *The virtual inertia $I(\theta, y)$ is zero.*

(iv) $I_{RB}(\theta, y) + I_{AB}(\theta, y) = 0$

Proof. *(i) $\Leftrightarrow$ (ii)* Since the rank properties and singularities of the decoupling matrix $L_g L_f h(q)$, are not altered by pre-feedback (6.36), singularities of $L_g L_f h(q)$ are the same as those of $L_{\bar{g}} L_{\bar{f}} h(q)$. The invertibility condition of $L_{\bar{g}} L_{\bar{f}} h(q)$ is given by Proposition 6.5.

(ii) $\Leftrightarrow$ (iii) Using (6.47b), since the scalar c_2 is nonzero by hypothesis and the scalar $D_{22}(q)$ is nonzero by positive definiteness of $D(q)$, $I(\theta, y) = 0$ if, and only if, $S(q) = 0$.

(iii) $\Leftrightarrow$ (iv) The result follows from (6.47c) and (6.48). □

Regarding the physical interpretation of condition *(iv)*, the planned motion (constraint) will result in a dynamic singularity if, and only if, the motion (constraint) is such that the rigid body inertia I_{RB} is equal and opposite in sign to the inertial term associated with the articulated body angular momentum, I_{AB}.

[8] Note that the inertial term associated with the articulated body angular momentum, I_{AB}, does not correspond to the usual notion of the articulated body inertia, as defined, for example, by [46].

6.3.4 Approaching a Dynamic Singularity

Although the HZD controller is not well-defined at a dynamic singularity, when approaching such a point the closed loop system will exhibit the following behaviors:

Theorem 6.7. *Suppose that within the state space of the zero dynamics (6.23) there exists a unique value $\theta_s \in [\theta^+, \theta^-]$ whose associated configuration $q_s = \Phi_q(\theta_s, 0)$ corresponds to a singularity of the decoupling matrix, i.e., $S(q_s) = 0$. If a solution of the zero dynamics approaches θ_s with nonzero angular momentum, i.e., $\lim_{\theta \nearrow \theta_s} \sigma(\theta) \neq 0$ with $\sigma(\theta)$ as in (6.28b), then*

(i) the time from step start to singularity is finite,

(ii) the magnitudes of $\dot{\theta}$, $\ddot{\theta}$, $\theta^{(3)}$, etc. grow without bound, and

(iii) the angular velocity, acceleration, etc. of at least one joint grow without bound.

Proof. (i) The time to singularity from initialization is (see [153, Eqn. 81])

$$T_s = \int_{\theta^+}^{\theta_s} \frac{I(\theta, 0)}{\sigma(\theta)} \, d\theta, \tag{6.49}$$

where $I(\theta, y)$ and $\sigma(\theta)$ are given by (6.24) and (6.28b). T_s is finite since the integrand is a bounded function on the bounded interval $[\theta^+, \ \theta_s]$.

(ii) Using (6.23a), $\dot{\theta}$ can be parameterized by θ, i.e., for $\theta \in [\theta^+, \theta_s)$,

$$\dot{\theta}(\theta) = \frac{1}{I(\theta, 0)} \, \sigma(\theta). \tag{6.50}$$

Observe that $I(\theta, y)$ and $\sigma(\theta)$ are continuous functions, that $I(\theta_s, 0) = 0$ by Theorem 6.6, and that $\lim_{\theta \nearrow \theta_s} \sigma(\theta) \neq 0$ by assumption. As a result, $\lim_{\theta \nearrow \theta_s} \dot{\theta}(\theta) = \infty$. Proof of unboundedness of $\ddot{\theta}$, $\theta^{(3)}$, etc. can be formalized by contradiction against $\dot{\theta}$ unbounded in finite time.

(iii) Because θ is a linear combination of the joint angles (see (6.9)), the above implies that as $\dot{\theta}$ and $\ddot{\theta}$ grow without bound, so must the magnitudes of angular velocity and acceleration of at least one joint. □

It is worth emphasizing that Theorem 6.7 (iii) shows that near a singularity, angular velocities $\dot{q}$ can become unbounded while angular momentum about the contact point, σ, remains finite. In

addition to the predictions of Theorem 6.7, an obvious behavior associated with approaching a dynamic singularity is that the HZD controller (6.17) will typically command extremely large torques, which will quickly result in actuator saturation—yet another motivation for avoiding singularities.

6.3.5 Example 1: A Singularity for the Two-Link Walker

For the two-link walking model of Section 6.1.2 with parameters given in Table 6.1, assume that the robot is walking on level ground, i.e., $\alpha = 0$, and choose $c_1 = 0$ and $c_2 = 1$. Condition (iv) of Theorem 6.6 states that at a singularity, $I_{RB} = -I_{AB}$, or in this case,

$$-2\left(ml(l-l_c)\cos(q_1) - \left(l^2 - l_c\, l + l_c^2\right) m - J\right) \\ = \left(ml(l-l_c)\cos(q_1) - (l-l_c)^2\, m - J\right) \frac{\partial \bar{h}_d}{\partial \theta}. \quad (6.51)$$

Recall that when the state is in the constraint surface $y \equiv 0$, which implies $q_1 = h_d(\theta)$. Therefore, the singularity condition (6.51) implies that a singularity will occur when the state is in the constraint surface if, and only if,

$$\frac{\partial \bar{h}_d}{\partial \theta} = 2\frac{ml(l-l_c)\cos(q_1) - \left(l^2 - l_c\, l + l_c^2\right) m - J}{ml(l-l_c)\cos(q_1) - (l-l_c)^2\, m - J}. \quad (6.52)$$

Suppose that the singularity occurs for some $\theta = \theta_s$ where $h_d(\theta_s) = 0$, i.e., when the legs are together. Then, the condition for singularity is that when $q = (0, \theta_s) = q_s$,

$$\dot{q} = \begin{bmatrix} -\frac{74}{3} \\ 1 \end{bmatrix} \dot{\theta} = \dot{q}_s(\dot{\theta}). \quad (6.53)$$

Note that $\sigma = d_n(q_s)\dot{q}_s(\dot{\theta}) = 0$ for all $\dot{\theta} \in \mathbb{R}$. As a result, at the instant of singularity only $\dot{\theta} = 0$ is compatible with (6.23). And so, the only motion compatible with the constraint is one in which the robot is at rest at $\theta = \theta_s$.

A motion was designed such that condition (6.52) is satisfied at $\theta = \theta_s = 0$ and $q_1 = \bar{h}_d = 0$. Figure 6.2 gives plots of the joint angles, joint velocities, and joint torque for a simulation in which $\dot{\theta} \neq 0$. Note that the control effort becomes unbounded as the singularity is approached, at approximately 1.19 seconds, resulting in unbounded joint velocities as predicted by Theorem 6.7.

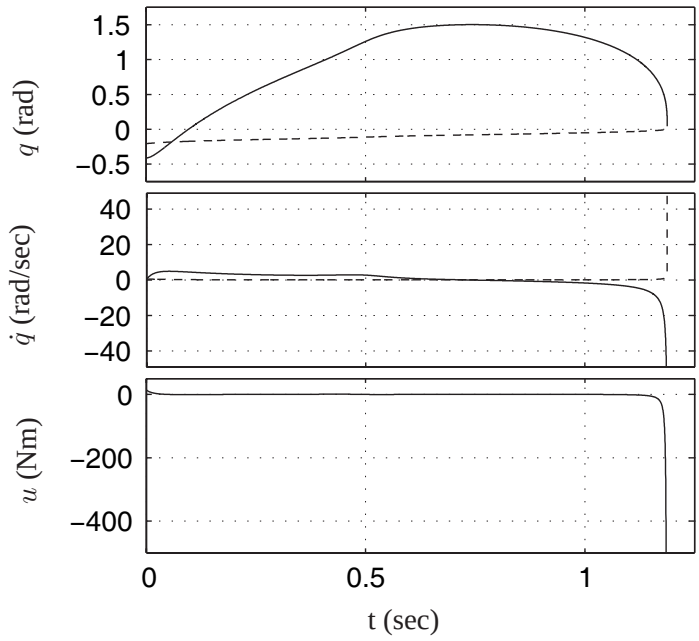

Figure 6.2: Illustrations of the effect of a decoupling matrix singularity. The singularity occurs at approximately 1.19 seconds. Curves corresponding to q_1 and q_2 are solid and dashed, respectively.

6.4 Development of Additional Tools for the HZD Framework

In a typical HZD controller design procedure, the output function $\bar{h}_d(\theta)$ is selected by numerical optimization from a pre-chosen, finitely parameterized family of constraints. The first and second derivatives required by the controller, $\partial\bar{h}_d(\theta)/\partial\theta$ and $\partial^2\bar{h}_d(\theta)/\partial\theta^2$, are found by differentiating the output function itself. Using the typical design method, controllers cannot be designed around a given, arbitrary gait since it is unlikely that the associated holonomic constraints will lie within the family chosen for optimization.

6.4.1 Sample-Based Virtual Constraints

The following method can be used to design an HZD controller around an arbitrary, period-one gait. Define $\mathbf{q}(t)$ as the time evolution of the coordinates q on the limit cycle. Similarly, define $\dot{\mathbf{q}}(t)$, $\ddot{\mathbf{q}}(t)$, $\mathbf{\Theta}(t)$, $\dot{\mathbf{\Theta}}(t)$, $\ddot{\mathbf{\Theta}}(t)$ as the time evolution of $\dot{q}$, $\ddot{q}$, θ, $\dot{\theta}$, and $\ddot{\theta}$, on the limit cycle. By monotonicity, $\theta = \mathbf{\Theta}(t)$ has a well-defined inverse, $t = \mathbf{\Theta}^{-1}(\theta)$.

Proposition 6.8. *Assume an output of the form (6.7). Given a period-one periodic orbit of (6.4),*

the associated controller functions $\bar{h}_d(\theta)$, $\partial\bar{h}_d(\theta)/\partial\theta$, and $\partial^2\bar{h}_d(\theta)/\partial\theta^2$ are

$$\bar{h}_d(\theta) \equiv \mathbf{q}_a(t)|_{t=\mathbf{\Theta}^{-1}(\theta)} \tag{6.54a}$$

$$\frac{\partial\bar{h}_d}{\partial\theta}(\theta) \equiv \left.\frac{\dot{\mathbf{q}}_a(t)}{\dot{\mathbf{\Theta}}(t)}\right|_{t=\mathbf{\Theta}^{-1}(\theta)} \tag{6.54b}$$

$$\frac{\partial^2\bar{h}_d}{\partial\theta^2}(\theta) \equiv \left(\frac{\ddot{\mathbf{q}}_a(t)}{\dot{\mathbf{\Theta}}^2(t)} - \frac{\dot{\mathbf{q}}_a(t)\ddot{\mathbf{\Theta}}(t)}{\dot{\mathbf{\Theta}}^3(t)}\right)_{t=\mathbf{\Theta}^{-1}(\theta)}. \tag{6.54c}$$

Proof. On the periodic orbit $y \equiv 0$ by assumption. Successive differentiation of (6.8) and (6.11) show that on the periodic orbit,

$$0 = q_a(t) - \bar{h}_d(\theta(t)) \tag{6.55a}$$

$$0 = \dot{q}_a(t) - \frac{\partial\bar{h}_d(\theta(t))}{\partial\theta}\,\dot{\theta}(t) \tag{6.55b}$$

$$0 = \ddot{q}_a(t) - \frac{\partial^2\bar{h}_d(\theta(t))}{\partial\theta^2}\,\dot{\theta}(t)^2 - \frac{\partial\bar{h}_d(\theta(t))}{\partial\theta}\,\ddot{\theta}(t). \tag{6.55c}$$

Evaluate (6.55) at $t = \mathbf{\Theta}^{-1}(\theta)$ and manipulate to complete the derivation. □

Because the controller (6.17) and (6.18) is being used, the implicitly defined virtual constraints (6.54) will be continuous phase invariant. It can be shown that such virtual constraints are automatically invariant over the impact event. Thus, the outputs produced by Proposition 6.8 result in a valid HZD, and so the analysis of Sections 6.2.4 and 6.2.5 holds.

When given full state information about the periodic orbit, the above proposition shows how to compute the output function and its derivatives in closed form. By Remark 6.1, knowledge of the model and the terms of Proposition 6.8 are enough information to compute the feedback law $u(x)$ of (6.17). Note that in practice it may be impossible to solve for $t = \mathbf{\Theta}^{-1}(\theta)$ in closed form. Cubic spline interpolation can be used to circumvent this problem, as well as improve the efficiency of computing the control law $u(x)$.

Proposition 6.9. *The term $\bar{h}_d(\theta)$ and its derivatives can be reproduced with arbitrary accuracy by sampling full state information of the periodic orbit and applying cubic spline interpolation between sample points.*

Proof. First, sample the full state information associated with the periodic orbit: $\mathbf{q}(t)$, $\dot{\mathbf{q}}(t)$, $\ddot{\mathbf{q}}(t)$, $\mathbf{\Theta}(t)$, $\dot{\mathbf{\Theta}}(t)$, $\ddot{\mathbf{\Theta}}(t)$. Calculate the quantities of Proposition 6.8 for each unique value of θ. Cubic spline interpolation between sample points will result in estimates of $\bar{h}_d(\theta)$, $\partial\bar{h}_d(\theta)/\partial\theta$, and $\partial^2\bar{h}_d(\theta)/\partial\theta^2$ each having an accuracy of $\mathcal{O}(|\tau^4|)$, where τ is the distance to the nearest sample point [40, Ch. 5]. □

Thus, given an existing limit cycle the associated HZD controller terms $\bar{h}_d(\theta)$, $\partial\bar{h}_d(\theta)/\partial\theta$, and $\partial^2\bar{h}_d(\theta)/\partial\theta^2$ can be approximated arbitrarily accurately using sample-based virtual constraints, without a closed-form representation of $\bar{h}_d(\theta)$. For computational efficiency, the sampled functions $\bar{h}_d(\theta)$, $\partial\bar{h}_d(\theta)/\partial\theta$, and $\partial^2\bar{h}_d(\theta)/\partial\theta^2$ may be pre-computed and stored in a lookup table. By the contrapositive of (iii) of Theorem 6.7, these sample-based virtual constraints cannot lead to a dynamic singularity on the periodic orbit—if a dynamic singularity were encountered, at least one joint velocity $\dot{q}_i$ would be unbounded.

Note that the method of Proposition 6.9 is not equivalent to fitting $\bar{h}_d(\theta)$ to a set of splines and then differentiating the splines to obtain $\partial\bar{h}_d(\theta)/\partial\theta$ and $\partial^2\bar{h}_d(\theta)/\partial\theta^2$. Differentiation techniques would leave $\bar{h}_d(\theta)$ with an accuracy of $\mathcal{O}(|\tau^4|)$, $\partial\bar{h}_d(\theta)/\partial\theta$ an accuracy of $\mathcal{O}(|\tau^3|)$, and $\partial^2\bar{h}_d(\theta)/\partial\theta^2$ an accuracy of $\mathcal{O}(|\tau^2|)$ [40, Ch. 5]. Another alternative method of obtaining $\bar{h}_d(\theta)$ would be to regress joint trajectories against a single polynomial of θ and differentiate the fit. In practice the authors have observed that polynomial degrees high enough to obtain sufficiently accurate fits to joint motion result in poor fits to the motion's derivatives.

6.4.2 Augmentation Functions

A constraint augmentation function is a finitely parameterized function, such as a polynomial, that gives a means to systematically modify a set of sample-based virtual constraints. As in previous work, the parameters of the augmentation function can be chosen via optimization. Augmentation functions can be used to make passive gaits zero slope capable, as will be demonstrated in Section 6.5.4, or to modify any other kinematic or dynamic property of the induced motion, while retaining, as much as possible, the robot's original unactuated dynamic behavior.

Consider the decomposition of h_d, into

$$h_d(s) = h_{d,0}(s) + h_{d,\delta}(s), \tag{6.56}$$

where $s \in [0, 1]$, $h_{d,0}$ is a nominal desired motion, and $h_{d,\delta}$ is an augmentation function. The function $h_{d,\delta}$ will be finitely parameterized and used to change the properties of the nominal motion associated with $h_{d,0}$. So that the analysis of Section 6.2 can be applied, the function $h_{d,\delta}$ is required to be such that the virtual constraint h_d is impact invariant.

Let the augmentation function's parameters be denoted by a. Then, augmenting the nominal motion with $h_{d,\delta}$, will result in the function V_{zero} and the constant δ_{zero} being parameterized by a. The parameters a can therefore be used to tune the restricted Poincaré map (6.31) to select its fixed point, the fixed point's stability properties, and the lower bound of the map. The use of augmentation functions is illustrated in Example 5 in Section 6.5.4.

6.4.3 Example 2: Sampling a Torque Specified Gait

This example illustrates how the technique of sample-based constraints can be used to design controllers[9] for gaits found by direct optimization of the steady-state torque profile. In the first part of the example a periodic orbit is found from which virtual constraints are calculated in the second part of the example. With this approach, the joint motions are not slaved to finitely parameterized functions, but rather to the motions they naturally achieve on the limit cycle with a finitely parameterized torque profile.

Consider again the two-link walking model of Section 6.1.2 with parameters given in Table 6.1 and assume that the robot is walking on level ground, i.e., $\alpha = 0$. The pre-chosen family of steady-state torque profiles is chosen to be

$$u(t) = A \cos\left(\left(\frac{2\pi}{T}\right)(t - t^+) + \phi\right), \tag{6.57}$$

where A, T, and ϕ are to be chosen and t^+ is the time of the most recent initialization of the swing phase. To fully describe the gait, the initial condition x_0 and values for the parameters A, T, and ϕ must be found such the corresponding trajectory is a periodic orbit of the hybrid model, (6.4). Using numerical optimization valid parameters were found to be $A = 0.445$, $T = 0.728$, $\phi = -1.22$, with initial condition $x_0 = (-0.356,\ -0.178,\ 0.135,\ 0.756)$.

To design a controller for the torque parameterized gait, the periodic orbit is densely sampled to obtain the output function and its derivatives (see Figure 6.3). A plot of $S(q)$ verifies, as expected,

[9] The resulting HZD controller will not necessarily stabilize the gait, although in the authors' experience this is usually the case. The test for stability is discussed in Section 6.2.4.

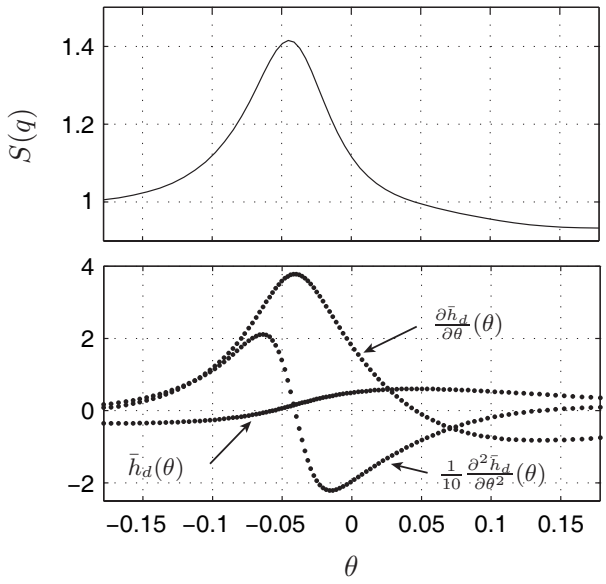

Figure 6.3: Verification that the decoupling matrix is non-singular along the periodic orbit. Non-singularity is indicated by the function $S(q)$ being bounded away from zero, and the sample-based virtual constraints relations given in Propositions 6.8 and 6.9.

that the decoupling matrix is not singular on the periodic orbit (again, see Figure 6.3). Figure 6.4 gives the response of the closed-loop system to a perturbation in initial condition. As the robot approaches steady-state, commanded torque converges to the designed sinusoidal profile (6.57).

6.5 Applications to the Control of Passive Bipedal Gaits

This section applies the tools developed in Sections 6.4.1 and 6.4.2 to the robust enforcement of passive bipedal gaits in three illustrative examples. Before presenting the examples, a brief overview of passive bipedal walking is given.

6.5.1 Control of Passive Walking

A passive bipedal walker is a two-legged mechanism that is able to walk stably down a slope without active feedback control or energy input aside from gravity. Since McGeer first simulated and built such a mechanism in the 1980's [96], passive bipedal walkers have had continued interest, primarily as a point of departure for building energetically efficient, actuated biped robots [38]. Such

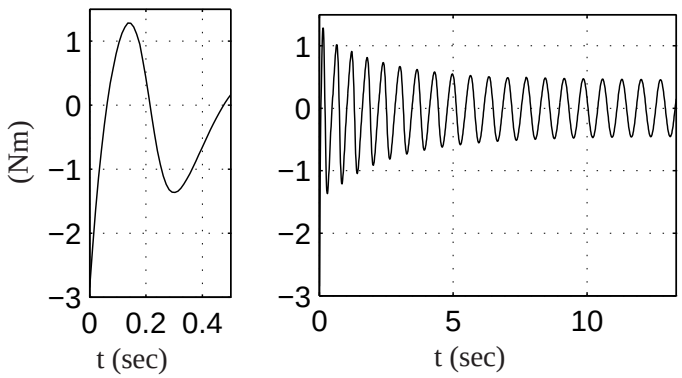

Figure 6.4: Torque evolution for a torque specified gait initialized off the orbit. Simulation is of twenty (20) steps on level ground for the torque specified gait of Example 2. The initial error is $\delta x_0 = (0.025,\, 0.0125,\, 3,\, 0)$. Note that the torque requirements converge rapidly to the steady-state sinusoidal profile.

walkers, however, have two fundamentally limiting features. The first is that the basins of attraction associated with their orbits are small—meaning passive bipedal walkers are easily toppled. The second is a lack of variety of available walking motions; a gait's features can only be changed by robot redesign or by ground slope change.

Actuation can remedy both of these shortcomings. Ideal actuation[10] under active feedback control can be used to increase robustness and to change a gait's characteristics, such as the minimum slope on which the biped is able to walk.[11] Since the energetic cost of passive dynamic walking is, in fact, nonzero—work must be done to lift the mechanism to the top of the slope—the loss of stable passive gaits does not preclude the use of energetic efficiency as a metric in achieving a given objective, such as walking at a certain rate, walking on flat ground, or walking with increased robustness.

Although the basin of attraction of the biped with the sample-based HZD controller may be larger, the closed-loop system will, in general, not be capable of achieving a variety of different gaits. To address this shortcoming, a constraint augmentation function can be used.

[10]The addition of non-ideal actuation often results in the loss of all stable, passive gaits. This is because the usual means of actuating a biped is with actuators that are collocated with the biped's joints. In such a configuration, the actuator's dynamics are coupled with the biped's. An example where this does not occur is Collins's powered 3D biped [38], which is powered by impulsive foot action.

[11]Although there do theoretically exist stable gaits for passive bipeds at arbitrarily small slopes, the basins of attractions can be impractically small [49].

The recent work of [133] gives a means to change the ground slope capabilities of passive walkers by the introduction of *full* actuation in conjunction with a potential energy shaping controller. The results given here are conceptually similar but are in the context of the hybrid zero dynamics (HZD) framework, which is for the control of walking in *underactuated* planar bipeds, specifically those not having actuated ankles.

The remainder of the section is organized into three examples. In the first, a sample-based HZD controller is designed that increases the robustness of a passive gait and is such that control effort is used only to increase the basin of attraction—*zero controller effort is required at steady-state*. When using non-ideal actuators, zero control effort is achieved in the sense that actuators perform no *mechanical work* on the system. With electrical motors, for example, electrical energy will be consumed to prevent the motor's frictional and inertial forces from doing work on the system. The second example demonstrates the robustness of the sample-based HZD control approach to external force perturbations and parameter variations. The third illustrates how various features of an existing gait can be modified using sampled-based HZD control with an augmentation function.

6.5.2 Example 3: Enlarging the Basin of Attraction of a Stable, Passive Gait of a Two-link Biped

The basin of attraction for the two-link passive biped depicted in Figure 6.1 with parameters given in Table 6.1 walking on a ground slope of 0.02 rad (1.15 deg) is given in Figure 6.5. The maximum coefficient of static friction at the stance leg end is assumed to be 0.6.

The steady-state passive gait, with the biped walking on a 0.02 rad slope, was enforced using a sample-based HZD controller with $K_P = 200$ and $K_D = 25$. The basin of attraction of the biped in closed loop with this controller is given in Figure 6.5. Although the basin of attraction of the controlled walker is significantly larger than that of the passive walker, the basin of attraction of the controlled walker is missing a small region that is present in the passive basin corresponding to extreme combinations of velocity and configuration.

As an illustration, the closed-loop system was simulated for thirty steps with an initial condition $x_0 = x_{0,\mathrm{nom}} + \delta x_0$, where $x_{0,\mathrm{nom}}$ is the state of the biped at the start of step on the periodic orbit of the passive gait and $\delta x_0 = (0.2,\, 0.1,\, -1,\, 0)$. Figure 6.6 gives the evolution of the applied torque

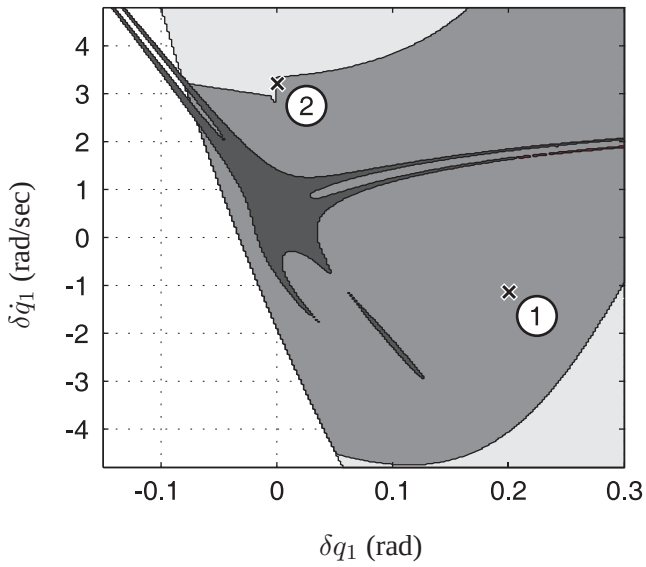

Figure 6.5: Basins of attraction: passive walker vs. HZD stabilized walker. Two-dimensional slices of the initial condition basin of attraction for walking on a 0.02 rad slope. The basin for the passive walker is dark gray, the basin for the controlled walker with $K_P = 200$ and $K_D = 25$ is light gray, and the basin for the controlled walker with a magnitude torque limit of 3 Nm and a coefficient of static friction at the stance leg end of 0.6 is medium gray. Other slices of the basins of attraction are similarly proportioned. Here $\delta\dot{q}_2 = 0$. The initial conditions for Examples 3 and 5 are indicated.

u. Note that the peak control effort is relatively small and that the control effort goes to zero as the state approaches the passive orbit.

An interesting observation is that, for this example, increased controller gains (the proportional and derivative control gains K_P and K_D) result in a smaller basin of attraction. This effect is more pronounced for increases in K_D, as can be seen in Figure 6.7. An increase in the control gains results in larger transient control signals, and, potentially, larger ground reaction force magnitudes. The former may result in actuator saturation, and the latter may result in the coefficient of static friction being exceeded.

6.5.3 Example 4: Demonstration of Robustness to External Force Perturbations and Mass and Inertia Variations

As a test of robustness, the controlled two-link biped of Example 3 was simulated with horizontal, aperiodic forces acting on its hip and swing leg end and mismatch between the model and

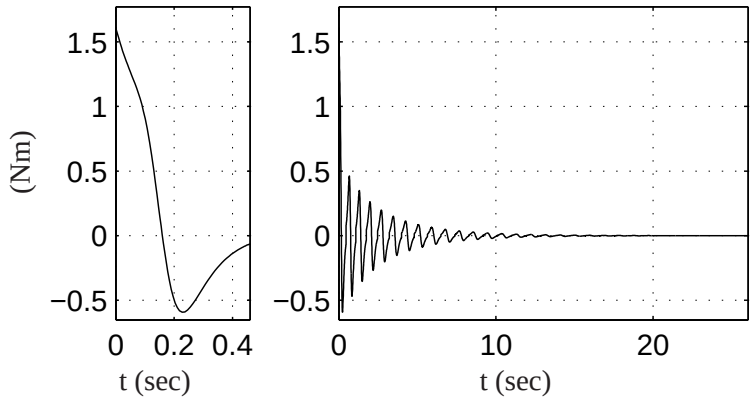

Figure 6.6: Torque evolution of walking on a slope for thirty steps. Simulation is done assuming a ground slope of $\alpha = 0.02$ rad using a sample-based HZD controller. Torque evolution over first step is left and the torque evolution over all steps is right. Note that the applied torque approaches zero as the state converges to the limit cycle. The peak torque is 1.6 Nm.

controller in leg mass, m, and leg inertia, J. Between 4.6 and 4.75 seconds, a horizonal force of 15 Nm acted at the hips opposite to the direction of forward progression, and between 6.1 and 6.3 seconds a horizontal force of 9.25 Nm acted at the swing leg end in the same direction as the first. The controller's values for the leg mass and leg inertia were set to 80% and 120%, respectively, of the parameters given in Table 6.1. Figure 6.8 gives plots of the joint angles, joint velocities, and joint torque. Note that because of the parameter mismatch, the steady-state control effort is no longer zero. Also note the rather modest control effort required to reject these force perturbations.

6.5.4 Example 5: Changing the Minimum Slope Capability of a Motion

For the two-link biped of Example 3, the minimum ground slope required for stable walking was found numerically (using (6.35)) to be 0.0171 rad (0.980 deg). With numerical optimization, the augmentation function depicted in Figure 6.9 was found such that the resulting closed-loop system was capable of walking uphill on a slope of -0.01 rad (-0.523 deg). As an illustration, the closed-loop system was simulated on zero slope, i.e., $\alpha = 0$, for an initial condition $x_0 = x_{0,\mathrm{nom}} + \delta x_0$, where $x_{0,\mathrm{nom}}$ is the state of the biped at the start of step on the periodic orbit of the passive gait on the nominal slope, $\alpha = 0.02$ rad, and $\delta x_0 = (0.025,\ 0.0125,\ 3,\ 0)$. Figure 6.10 gives the evolution of the applied torque u. Note that peak control effort is relatively small.

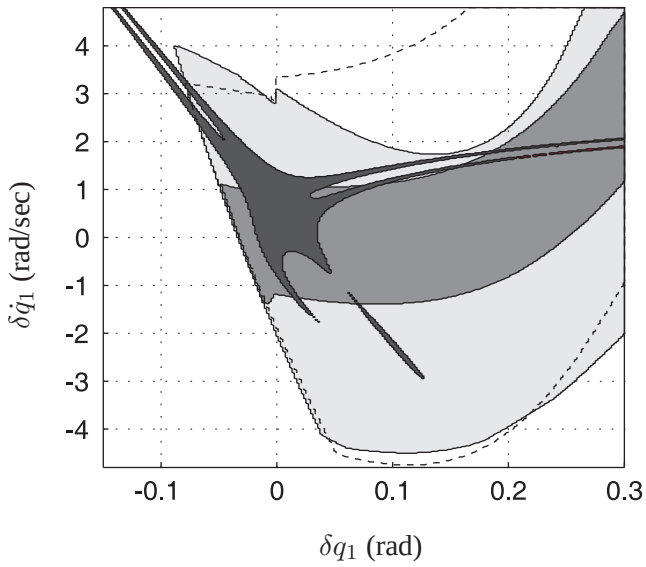

Figure 6.7: Basins of attraction for walking on a slope with different controller gains. Two-dimensional slices of the initial condition basin of attraction slices for walking on a 0.02 rad slope for three different sets of controller gains. The basin for the passive walker is dark gray. The basin with $K_P = 200$ and $K_D = 25$ is outlined in with a dashed line, the basin with $K_P = 700$ and $K_D = 25$ is light gray, and the basin with $K_P = 500$ and $K_D = 75$ is medium gray. A maximum torque limit of 3 Nm and a coefficient of static friction at the stance leg end of 0.6 were assumed. Here $\delta\dot{q}_2 = 0$.

6.6 Conclusions

This chapter presented new analysis and control tools for the control of planar bipedal walking using hybrid zero dynamics (HZD) based control. HZD control acts by imposing virtual constraints on the biped's configuration as a function of forward progression. The benefits of the HZD approach include explicit (analytical) calculation of the induced gait's stability properties and robust performance.

The new analysis results include analysis of the effects of walking on a slope and analysis of dynamic (decoupling matrix) singularities. The former was used in the design of controllers that render passive gaits zero slope capable. The latter provides insights into the nature of constraints that require infinite control effort to enforce, yet impose motions that are otherwise kinematically feasible (i.e., the mechanism does not encounter a kinematic singularity).

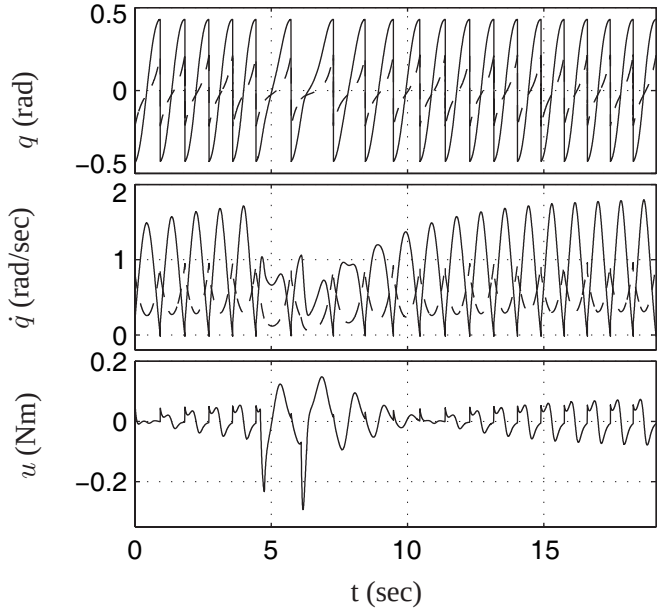

Figure 6.8: Effects of external perturbations. Curves corresponding to q_1 and q_2 are solid and dashed, respectively.

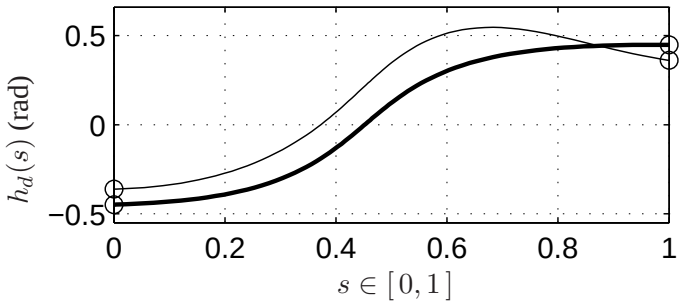

Figure 6.9: Augmeted motion as a function of normalized forward progression. Passive motion (bold line) and augmented passive motion (normal weight line) as a function of normalized forward progression. Enforcement of the augmented motion results in a closed-loop system that is capable of walking on a ground slope of zero.

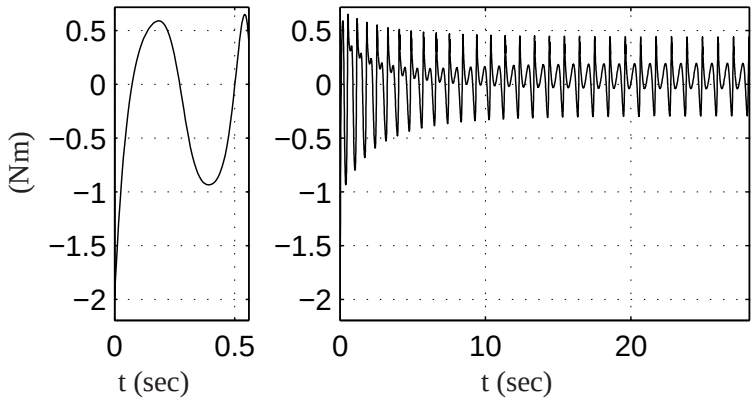

Figure 6.10: A zero slope capable motion. Torque evolution for a simulation of thirty (30) steps on zero slope using a sample-based HZD controller. Torque evolution over first step is left and the torque evolution over all steps is right. The peak torque is 2.0 Nm.

The new control tools provide an alternative method for choosing virtual constraints via sampling and interpolation. The technique was used to enlarge the basin of attraction of the gait of a passive dynamic walker. Unlike other approaches to the robust enforcement of passive bipedal gaits, the control acts without the need for full actuation—no actuation is assumed between the robot and the ground. The new control tools were also used to design controllers for torque specified gaits. Constraint augmentation functions were introduced, defined as finitely parameterized functions added to the nominal, sample-based constraints that enable the kinematic and dynamic properties of the gait to be modified.

Notation Introduced in Chapter 6

Symbol	Meaning	Defined
l, l_c, m, J, g_0	parameters of the two-link model	Table 6.1
α	ground slope	Figure 6.1
$\mathcal{S}$	switching surface; Poincaré section	Section 6.1.1
Σ	full dynamics walking model	Section 6.1.1
u	control input	Section 6.1.1
$x = (q, \dot{q})$	state vector of the full dynamics	Section 6.1.1
$[\alpha]$	functional dependence on α; emphasized with square brackets	Section 6.1.1
q_a	vector of actuated coordinates	Section 6.1.1
q_u	unactuated coordinate (scalar)	Section 6.1.1
$D(q)$	inertial matrix of the full dynamics	Section 6.1.2
$F[\alpha](q, \dot{q})$	Coriolis, centrifugal, gravitational terms of the full dynamics	Section 6.1.2
$h_d(s)$, $\bar{h}_d(\theta)$	desired joint angles of the actuated joints	Section 6.2.1
$\theta(q)$	scalar function that is a surrogate for time; monotonic over a step	Section 6.2.1
θ^+, θ^-	values of θ at the beginning and ending of a gait	Section 6.2.1
$y = h(q)$	output defining virtual constraints	Section 6.2.1
$s(\theta)$	normalization function for θ	Section 6.2.1
$\mathcal{Z}$	zero dynamics manifold; constraint surface	Section 6.2.1
K_p, K_d	PD controller gains	Section 6.2.2
$L_g L_f h(q)$	decoupling matrix from input u to output y	Section 6.2.2

Symbol	Meaning	Defined
Σ_{zero}	HZD model of walking	Section 6.2.3
σ	angular momentum about pivot foot	Section 6.2.3
$z = (\theta, \sigma)$	state vector of the restricted (zero) dynamics	Section 6.2.3
$L_{\bar{g}} L_{\bar{f}} h(q)$	decoupling matrix from input v to output y	Section 6.3.2
$S(q)$	function used to determine invertibility of decoupling matrix	Section 6.3.2
$I(\theta, y)$	closed-loop virtual inertia	Section 6.3.3
$I_y(\theta, y)$	virtual inertia of transverse dynamics	Section 6.3.3
$I_{RB}(\theta, y)$	rigid body inertia	Section 6.3.3
$I_{AB}(\theta, y)$	inertia associated with the articulated body angular momentum	Section 6.3.3
θ_s	value of θ corresponding to a singularity	Section 6.3.4
T_s	time from step start to singularity	Section 6.3.4
a	augmentation function parameter vector	Section 6.4.2

CHAPTER 7

A Restricted Poincaré Map for Determining Exponentially Stable Periodic Orbits in the Presence of Smooth Transverse Dynamics

When the method of Poincaré sections is applied in practical problems, it is very common to see the Jacobian linearization of the Poincaré map estimated numerically and the exponential stability of a fixed point (i.e., a periodic orbit) deduced on the basis of the eigenvalues. Although straightforward in principle, this process can become computationally unwieldy when the dimension of the system under study is large or when stability needs to be evaluated repeatedly as part of an iterative procedure to design a feedback controller. In order to simplify its application to nonlinear systems with impulse effects, this chapter develops reduced dimensionality stability tests based on the method of Poincaré sections, emphasizing the role played by *(hybrid) invariance*, *attractivity*, and *timescale separation*. Simple properties are identified that govern the stability of periodic orbits that lie within hybrid zero dynamics manifolds—when the transverse dynamics of a given system is rendered exponentially stable with a sufficiently fast convergence rate, the stability of the periodic orbit can be evaluated on the basis of the zero dynamics alone.

The work presented in this chapter is primarily an extension of the work on restricted Poincaré maps by Grizzle, Abba, and Plestan in [60] in which a set of hypotheses required that an invariant manifold be rendered finite time[1] attractive through a feedback that was continuous but not Lipschitz continuous. Hybrid invariance was introduced by Westervelt, Grizzle, and Koditschek in [153], but the requirement of a finite time converging transverse dynamics remained. The results presented here relax this requirement to exponential convergence at a "sufficiently rapid" rate, enabling the

[1] See [17] for an introduction to finite time controllers.

use of smooth feedback controllers and the stability analysis of periodic orbits in C^1 systems with impulse effects.

If the task of weakening controller hypotheses seems mundane, consider this: as observed in the running experiments on RABBIT in Chapter 5, the presence of strong hypotheses on controller properties can complicate the procedure of controller design. The property of "configuration determinism" at landing, required by the HZD running controllers of [31] could not be met in the time alloted for experiments. A failure to meet this condition necessitated the use of transition controllers—a much simpler way of arriving at a similar stability test. The stability theorems of this chapter are designed to have weaker hypotheses so that they are compatible with a broader range of potentially stabilizing controllers. The strongest hypothesis of this chapter, a reliance on impact invariance, can be achieved by the methods of Chapter 8.

The remainder of this chapter is organized as follows: Section 7.1 presents a reduced dimensionality stability test for periodic orbits in systems with impulse effects. Use of the theorem requires the existence of special coordinates, a hybrid invariant manifold, and a restricted Poincaré map. A similar result is derived in Section 7.2 where these hypotheses are weakened to eliminate the requirement of the existence of a particular set of coordinates. The benefits of these stability tests are demonstrated in a case study in Section 7.4. Both sets of hypotheses are verified, and both reduced dimensional tests are used to evaluate the stability a periodic orbit corresponding to RABBIT walking on flat ground.

7.1 Coordinate Dependent Hypotheses and Stability Test

The first set of hypotheses is coordinate dependent and pertains to a family of systems with impulse effects that depends on a real parameter $\epsilon > 0$, where for each fixed value of ϵ

$$\bar{\Sigma}^\epsilon : \begin{cases} \dot{x} &= \bar{f}^\epsilon(x) \quad x^- \notin \mathcal{S} \\ x^+ &= \Delta(x^-) \quad x^- \in \mathcal{S} \end{cases} \tag{7.1}$$

is a C^1 system with impulse effects. Following the convention established in Chapter 3, the solution of the autonomous system $\dot{x} = \bar{f}^\epsilon(x)$ is written as $\phi^\epsilon(t, x_0)$, the time-to-impact function is T_I^ϵ, and the Poincaré map is $P^\epsilon : \mathcal{S} \to \mathcal{S}$. In addition, assume that this family of systems has a periodic orbit, coordinate transform, and invariant manifold meeting the following hypotheses:

Hypotheses 7.1:

i) There exist global coordinates $x = (z, \eta)$ for $\mathcal{X} \subset \mathbb{R}^n$, such that $z \in \mathbb{R}^k$, and $\eta \in \mathbb{R}^{n-k}$, $1 < k < n$, in which $\bar{f}^\epsilon$ has the form

$$\bar{f}^\epsilon(x) = \bar{f}^\epsilon(z, \eta) = \begin{bmatrix} \bar{f}_{1:k}(z, \eta) \\ \bar{f}^\epsilon_{k+1:n}(\eta) \end{bmatrix};$$

ii) the set $\mathcal{Z} = \{(z, \eta) \in \mathcal{X} \mid \eta = 0\}$ is such that $\mathcal{S} \cap \mathcal{Z}$ is a $(k-1)$-dimensional, C^1-embedded submanifold satisfying the property that

$$\Delta(\mathcal{S} \cap \mathcal{Z}) \subset \mathcal{Z}; \tag{7.2}$$

iii) the autonomous system $\bar{\Sigma}^\epsilon$ has a periodic orbit $\mathcal{O}$ that is contained in $\mathcal{Z}$, and hence the orbit is independent of ϵ;

iv) $x^* = \bar{\mathcal{O}} \cap \mathcal{S} \cap \mathcal{Z}$ is a singleton;

v) $L_{\bar{f}^\epsilon} H(x^*) \neq 0$; and

vi) $\bar{f}^\epsilon_{k+1:n}(\eta) = A(\epsilon)\eta$ with $\lim_{\epsilon \searrow 0} e^{A(\epsilon)} = 0$.

The above conditions can be interpreted as follows: Hypotheses H7.1-i and H7.1-vi imply that the set $\mathcal{Z}$ is invariant under the continuous part of the model, $\dot{x} = \bar{f}^\epsilon(x)$, so that if $x_0 \in \mathcal{Z}$ then for all t in its maximal domain of existence, $\phi^\epsilon(t, x_0) \in \mathcal{Z}$. Hypothesis H7.1-ii implies that $\mathcal{Z}$ remains invariant across the impact event. Together, H7.1-i and H7.1-ii show that the restriction of $\bar{\Sigma}^\epsilon$ to the manifold $\mathcal{Z}$ is a well-defined system with impulse effects, which will be called the *restriction dynamics*,

$$\bar{\Sigma}^\epsilon|_{\mathcal{Z}} : \begin{cases} \dot{z} &= \bar{f}^\epsilon|_{\mathcal{Z}}(z) \quad z^- \notin \mathcal{S} \cap \mathcal{Z} \\ z^+ &= \Delta|_{\mathcal{Z}}(z^-) \quad z^- \in \mathcal{S} \cap \mathcal{Z}. \end{cases} \tag{7.3}$$

Hybrid invariance of $\mathcal{Z}$ further implies that

$$P^\epsilon(\mathcal{S} \cap \mathcal{Z}) \subset \mathcal{S} \cap Z. \tag{7.4}$$

From H7.1-iii, $\mathcal{O}$ is a periodic orbit of the restriction dynamics that is period-one by H7.1-iv. The restriction of $\bar{f}^\epsilon$ to $\mathcal{Z}$ removes any dependence on ϵ. This fact can be used to show that $\phi_{\mathcal{Z}} = \phi^\epsilon|_{\mathcal{Z}}$, $T_{I,\mathcal{Z}} = T^\epsilon_I|_{\mathcal{Z}}$, and $P^\epsilon|_{\mathcal{Z}}$ are also independent of ϵ, and hence,

$$t^* = T^\epsilon_I(\Delta(x^*)) \tag{7.5}$$

$$= T_{I,\mathcal{Z}}(\Delta_{\mathcal{Z}}(x^*)), \tag{7.6}$$

is independent of ϵ. On the basis of (7.4), the *restricted Poincaré map*, $\rho : \mathcal{S} \cap \mathcal{Z} \to \mathcal{S} \cap \mathcal{Z}$, can be defined as $\rho = P^\epsilon|_{\mathcal{Z}}$, or equivalently,

$$\rho(z) = \phi_{\mathcal{Z}}(T_{I,\mathcal{Z}} \circ \Delta_{\mathcal{Z}}(z), \Delta_{\mathcal{Z}}(z)), \tag{7.7}$$

and is independent of ϵ. From H7.1-iv, it follows that x^* is a fixed point of P^ϵ and ρ, and from H7.1-v, the orbit is transversal to $\mathcal{S}$, and hence also to $\mathcal{S} \cap \mathcal{Z}$. Hypothesis H7.1-vi says that the dynamics transversal to $\mathcal{Z}$ is "strongly" exponentially contracting with the rate of convergence becoming arbitrarily fast as ϵ decreases to zero. When the solution of (7.1) is not on the periodic orbit, $\eta(t) \neq 0$. In many situations, such as bipedal walking, the impact map increases the norm of η at each impact; see Figure 7.5. Hypothesis H7.1-vi provides control over the speed with which $\eta(t)$ converges to zero during the continuous phase, so that, over a cycle consisting of an impact event followed by continuous flow, the solution may converge to the orbit. Based on these hypotheses, a reduced dimensional stability test is given by the following theorem:

Theorem 7.2 (**Coordinate Dependent Reduced Dimensional Stability Test).** *Under Hypotheses H7.1, there exists $\bar{\epsilon} > 0$ such that for $0 < \epsilon < \bar{\epsilon}$, the following are equivalent:*

i. *x^* is an exponentially stable fixed point of ρ;*

ii. *x^* is an exponentially stable fixed point of P^ϵ.*

In other words, for $\epsilon > 0$ sufficiently small, an exponentially stable periodic orbit of the restriction dynamics is also an exponentially stable periodic orbit of the full order model. The proof is based on evaluating $\mathcal{D}P^\epsilon(x^*)$, the linearization of the Poincaré map about the fixed point, in a set of local coordinates. This is a commonly employed technique even for systems with impulse effects [55, 141, 90, 39]. The usual approach to finding the eigenvalues of $\mathcal{D}P^\epsilon(x^*)$ is to smoothly extend the domain of P^ϵ from $\mathcal{S}$ to $\mathcal{X}$ and then to evaluate the linearization of the resulting $n \times n$ Jacobian linearization. It must subsequently be shown that one of the eigenvalues of this matrix is always equal to unity and the remaining $n-1$ eigenvalues are those of $\mathcal{D}P^\epsilon(x^*) : T_{x^*}\mathcal{S} \to T_{x^*}\mathcal{S}$; see [106, 70]. Here, local coordinates on $\mathcal{S}$ will be used so that $\mathcal{D}P^\epsilon(x^*)$ is computed directly as an $(n-1) \times (n-1)$ matrix. This method will give an expression for $\mathcal{D}P^\epsilon(x^*)$ that brings out its structure due to Hypotheses H7.1.

7.2 Coordinate-Free Hypotheses and Stability Test

A stability test similar to the one above can be achieved under a much weaker set of hypotheses. In this case assume there exists a system

$$\bar{\Sigma}: \begin{cases} \dot{x} &= \bar{f}(x) \quad x^- \notin \mathcal{S} \\ x^+ &= \Delta(x^-) \quad x^- \in \mathcal{S}, \end{cases} \tag{7.8}$$

for which there are sets $\mathcal{O} \subset \mathcal{X}$ and $\mathcal{Z} \subset \mathcal{X}$ such that

Hypotheses 7.3:

i) $\mathcal{Z}$ is hybrid invariant;

ii) $\mathcal{S} \cap \mathcal{Z}$ is a C^1 embedded submanifold and has dimension one less than $\mathcal{Z}$; and

iii) $\mathcal{O}$ is a periodic orbit that is transversal to $\mathcal{S}$ and is contained in $\mathcal{Z}$.

The list in H7.3 is a weaker set of hypotheses than H7.1. Condition H7.3-i is implied by H7.1-i, H7.1-ii, and H7.1-vi. Condition H7.3-ii is implied by H7.1-ii, and H7.3-iii is implied by H7.1-iii. The benefit of these weaker hypotheses is that they are easier to meet in practice. The drawback is that the following theorem and its proof are somewhat more abstract.

Theorem 7.4 (Structure of the Linearized Return Map). *Consider a C^1 autonomous system with impulse effects $\bar{\Sigma} = (\mathcal{X}, \mathcal{S}, \Delta, f)$ and assume there exists a C^1 embedded k-dimensional submanifold $\mathcal{Z}$ such that H7.3 are satisfied. Then, there exist local changes of coordinates $\Gamma : U \to \mathbb{R}^{k-1} \times \mathbb{R}^{n-k}$ and $\Psi : V \to \mathbb{R}^k \times \mathbb{R}^{n-k}$, about $x^* = \bar{\mathcal{O}} \cap \mathcal{S}$ and $\Delta(x^*)$, respectively, such that when the Poincaré map of the system $\bar{\Sigma}$ is represented in the new coordinates, its Jacobian[2] about the fixed point x^* is*

$$\mathcal{D}\hat{P}(z^*, \eta^*) = \left[\begin{array}{c|c} \mathcal{D}\rho(z^*) & \star \\ \hline 0 & S_{\phi_{T_I}}(\bar{z}^*, \bar{\eta}^*) S_\Delta(z^*, \eta^*) \end{array}\right], \tag{7.9}$$

where[3] $\hat{P} = \Gamma \circ P \circ \Gamma^{-1}$, ρ is the restricted map of (7.7)*, $S_{\phi_{T_I}}(\bar{z}^*, \bar{\eta}^*) = \mathcal{D}_2(\Gamma_2 \circ \phi_{T_I} \circ \Psi^{-1})(\bar{z}^*, \bar{\eta}^*)$, and $S_\Delta(z^*, \eta^*) = \mathcal{D}_2(\Psi_2 \circ \Delta \circ \Gamma^{-1})(z^*, \eta^*)$, for $(z^*, \eta^*) = (\Gamma_1(x^*), \Gamma_2(x^*)) = \Gamma(x^*)$ and $(\bar{z}^*, \bar{\eta}^*) = \Psi \circ \Delta(x^*) = (\Psi_1 \circ \Delta(x^*), \Psi_2 \circ \Delta(x^*))$.*

[2] For a differentiable function $g(x_1, x_2, ..., x_p)$, the notation $\mathcal{D}_i g(y_1, y_2, ..., y_p)$ refers to $\partial g / \partial x_i$ evaluated at $(x_1, x_2, ..., x_p) = (y_1, y_2, ..., y_p)$. The argument x_i may be a vector. $\mathcal{D}g(y_1, ..., y_p)$ is $(\partial g/\partial x_1, \ldots, \partial g/\partial x_p)$ evaluated at $(x_1, ..., x_p) = (y_1, ..., y_p)$.

[3] $\Gamma_1(x)$ and $\Gamma_2(x)$ refer to the first $k-1$ and last $n-k$ coordinates of $\Gamma(x)$, and $\Psi_1(x)$ and $\Psi_2(x)$ refer to the first k and last $n-k$ coordinates of $\Psi(x)$, respectively.

The above theorem identifies two features present in the linearized Poincaré map when it is evaluated at a fixed point lying in a hybrid invariant manifold. The first is the upper triangular structure, which is immediate from the hybrid invariance of $\mathcal{Z}$; see (7.4). The second, more interesting result is that the bottom right block is the product of $S_{\phi_{T_I}}$ and S_Δ, which are the sensitivities of the transverse dynamics with respect to the continuous flow and impact map, respectively. If either of the sensitivities $S_{\phi_{T_I}}$ or S_Δ can be made sufficiently small, then the spectral radius of $\mathcal{D}\hat{P}$ will be determined solely by the restricted Poincaré map. Corollary 7.6 below is based on the observation that continuous flow sensitivity, $S_{\phi_{T_I}}$, can be made arbitrarily small through sufficiently rapid convergence of the transverse dynamics. Chapter 8 will address S_Δ by showing that this term can be made arbitrarily small by controlling the behavior of the impact map.

To develop a second reduced dimensional stability test, assume there exists a family of systems,

$$\bar{\Sigma}^\epsilon : \begin{cases} \dot{x} &= \bar{f}^\epsilon(x) \quad x^- \notin \mathcal{S} \\ x^+ &= \Delta(x^-) \quad x^- \in \mathcal{S}, \end{cases} \tag{7.10}$$

for which there exist sets $\mathcal{O} \subset \mathcal{X}$ and $\mathcal{Z} \subset \mathcal{X}$ satisfying H7.3 and also satisfying the following

Hypotheses 7.5:

i) the submanifold $\mathcal{Z}$ and fixed point x^* are independent of ϵ;

ii) $\bar{f}^\epsilon$ restricted to $\mathcal{Z}$ is independent of ϵ; and

iii) there exists a function $K : (0, \infty) \to [0, \infty)$ such that $\lim_{\epsilon \searrow 0} K(\epsilon) = 0$, and $\forall\ \epsilon > 0$, $\exists$ $\delta > 0$ such that[4]

$$\forall\ x_0 \in B_\delta(\Delta(x^*)),\ \text{dist}(\phi_{T_I}^\epsilon(x_0), \mathcal{Z}) \leq K(\epsilon)\, \text{dist}(x_0, \mathcal{Z}).$$

The fact that H7.5-i and H7.5-ii are implied by H7.1-i, H7.1-ii, and H7.1-iii is obvious. Less obvious is the connection between H7.5-iii and H7.1-vi. Hypothesis H7.5-iii can be interpreted as a Lipschitz bound describing the relationship between the distance to the manifold $\mathcal{Z}$ just after an impact and the distance to the manifold $\mathcal{Z}$ just before the next impact. This hypothesis is claiming that the flow of the system is attracted to the manifold $\mathcal{Z}$ in a way that is uniform with respect to the initial distance, but not necessarily uniformly with respect to time. Also notice that H7.5-iii is a statement about pre- and post-impact boundary conditions, whereas H7.1-vi is a statement about an

[4]Throughout this chapter, the notation $B_r(x)$ refers to an open ball of radius r about the point x.

entire transverse dynamics. The following corollary shows how these weaker hypotheses are used to achieve virtually the same stability test as developed in Theorem 7.2.

Corollary 7.6 (Coordinate Independent Reduced Dimensional Stability Test). *Consider a family of C^1 autonomous systems with impulse effects, $\bar{\Sigma}^\epsilon = \left(\mathcal{X}, \mathcal{S}, \Delta, \bar{f}^\epsilon\right)$, with the vector field of each member depending on a real parameter $\epsilon > 0$. Assume that for each value of $\epsilon \in (0, \infty)$, Hypotheses H7.3 and H7.5 are met. Then the restriction dynamics $\bar{\Sigma}^\epsilon|_{\mathcal{Z}} = \left(\mathcal{Z}, \mathcal{S} \cap \mathcal{Z}, \Delta|_{\mathcal{S}\cap\mathcal{Z}}, \bar{f}^\epsilon|_{\mathcal{Z}}\right)$ is independent of ϵ. In addition, there exists $\bar{\epsilon} > 0$ such that for $0 < \epsilon < \bar{\epsilon}$, the following are equivalent:*

i) x^* is an exponentially stable fixed point of ρ, and

ii) x^* is an exponentially stable fixed point of P^ϵ.

The proof of the corollary is given in the appendix and shows that H7.5-iii is sufficient for achieving $\lim_{\epsilon \searrow 0} S^\epsilon_{\phi_{T_I}} = 0$. In other words, for $\epsilon > 0$ sufficiently small, an exponentially stable periodic orbit of the restriction dynamics $\bar{\Sigma}^\epsilon|_{\mathcal{Z}} = \left(\mathcal{Z}, \mathcal{S} \cap \mathcal{Z}, \Delta|_{\mathcal{S}\cap\mathcal{Z}}, \bar{f}^\epsilon|_{\mathcal{Z}}\right)$ is an exponentially stable periodic orbit of the full model $\bar{\Sigma}^\epsilon = \left(\mathcal{X}, \mathcal{S}, \Delta, \bar{f}^\epsilon\right)$.

7.3 Feedback Design to Meet Stability Hypotheses

The next result shows how to construct a closed-loop system meeting the hypotheses of Corollary 7.6. Given a control system with impulse effects,

$$\Sigma : \begin{cases} \dot{x} &= f(x) + g(x)u \quad x^- \notin \mathcal{S} \\ x^+ &= \Delta(x^-) \qquad\quad x^- \in \mathcal{S}, \end{cases} \tag{7.11}$$

assume there exists an output function h such that the following are satisfied:

Hypotheses 7.7:

i) $h(x)$ has uniform vector relative degree k;

ii) there exists a point x such that $h(x) = 0, L_f h(x) = 0, \ldots, L_f^{k-1} h(x) = 0$; and

iii) the distribution $span\{g_1(x), \cdots, g_m(x)\}$ is involutive.

Corollary 7.8 (Feedback Design for Reduced Dimension Stability Testing). *Given a control system with impulse effects $\Sigma = (\mathcal{X}, \mathcal{S}, \emptyset, \mathcal{U}, \Delta, f, g)$ and a smooth output $h : \mathcal{X} \to \mathbb{R}^m$ satisfying Hypotheses H7.7 the following hold:*

i) the set $\mathcal{Z} = \{x \in \mathcal{X} \mid h(x) = 0, L_f h(x) = 0, \cdots, L_f^{k-1} h(x) = 0\}$ is a smooth embedded submanifold of $\mathcal{X}$,

ii) for any $\epsilon > 0$ and scalar constants $K_0, \ldots, K_{k-1}$ chosen so that $s^k + K_{k-1} s^{k-1} + \cdots + K_0$ is Hurwitz, the feedback

$$u^\epsilon(x) = -\left(L_g L_f^{k-1} h(x)\right)^{-1} \left(\begin{array}{c} L_f^k h(x) + \sum_{i=0}^{k-1} \frac{1}{\epsilon^{k-i}} K_i L_f^i h(x) \end{array} \right), \tag{7.12}$$

applied to Σ renders $\mathcal{Z}$ forward invariant in the family of closed-loop systems

$$\bar{\Sigma}^\epsilon = \left(\mathcal{X}, \mathcal{S}, \Delta, \bar{f}^\epsilon\right)$$

for $\bar{f}^\epsilon(x) = f(x) + g(x)u^\epsilon(x)$; and

iii) the family of systems $\bar{\Sigma}^\epsilon$ and the manifold $\mathcal{Z}$ satisfy conditions H7.5.

The most significant contribution of the corollary is the interpretation that for a broad class of feedbacks (7.12), Hypotheses H7.7 imply the satisfaction of Hypotheses H7.5. Corollaries 7.6 and 7.8 provide precise guidelines for designing a closed-loop system where the stability of a periodic orbit can be determined on the basis of a restriction dynamics. This result is similar to that of Theorem 7.2, but is stated without reference to a specific set of coordinates.

7.4 Case Study: RABBIT Walking on Flat Ground

The following example shows in detail how the theorems of this section can be used to design controllers to induce stable walking on flat ground in a 5 DOF bipedal model resembling the biped RABBIT. Both the coordinate dependent hypotheses of Theorem 7.2 and the coordinate independent hypotheses of Theorem 7.4 and its corollaries will be verified. This comparison will help to highlight the differences between the two proposed methods of reduced dimensionality stability testing.

7.4.1 Open-Loop Model

A model of RABBIT with coordinates $q = (q_1, \ldots, q_5) \in \mathcal{Q}$ as shown in Figure 7.1 is briefly summarized. Following [29], the method of Lagrange leads to the standard mechanical model

$$D(q)\ddot{q} + C(q,\dot{q})\dot{q} + G(q) = Bu, \text{ with } B = \begin{bmatrix} I \\ \\ 0 \end{bmatrix}. \tag{7.13}$$

The impact (i.e., switching) surface is $\mathcal{S} = \{(q,\dot{q}) \in \mathcal{X} \mid \mathbf{y}_2(q) = 0,\ \mathbf{x}_2(q) > 0\}$, the set of points where the swing leg height is zero and in front of the stance leg. When the swing leg contacts the ground an inelastic collision gives rise to a jump in the velocity coordinates[5]. An impact map $\Delta : \mathcal{S} \to \mathcal{X}$ can be computed as in [74, 60, 29]. Defining $x = (q,\dot{q})$, the mechanical model is expressed in state variable form as a controlled system with impulse effects:

$$\Sigma : \begin{cases} \dot{x} = & f(x) + g(x)u \quad x^- \notin \mathcal{S} \\ x^+ = & \Delta(x^-) \qquad\quad x^- \in \mathcal{S}, \end{cases} \tag{7.14}$$

where the vector of control torques is $u \in I\!R^4$.

In [153, Section V-VII], it is shown how to design output functions $y = h(x)$ using Bézier polynomials and (nonconstructive) numerical optimization to meet many of the assumptions made so far, as they relate to RABBIT: invertibility of the decoupling matrix $L_g L_f h$, impact invariance $\Delta(\mathcal{S} \cap \mathcal{Z}) \subset \mathcal{Z}$, the existence of a periodic orbit lying within $\mathcal{Z}$ that is transversal to $\mathcal{S} \cap \mathcal{Z}$. These conditions can often be met while simultaneously meeting other performance objectives involving walking speed, actuator power, and the contact forces at the leg ends. Since RABBIT has five degrees of freedom in the stance phase and four independent actuators, the restricted Poincaré map is scalar valued, and hence the Jacobian linearization of the restricted Poincaré map is a scalar. What remains is to design a feedback controller so that the resulting closed-loop system meets conditions on reduced dimensionality stability testing.

7.4.2 Feedback Design

The feedback designs developed in [153] are based on virtual constraints, which are holonomic constraints on the robot's configuration that are asymptotically imposed through feedback control.

[5] So that the same mechanical model can be used independent of which leg is the stance leg, the coordinates must also be relabeled, giving rise to a jump in the configuration variables as well; see[60, 153, 29]. The impact map satisfies $\Delta(\mathcal{S}) \cap \mathcal{S} = \emptyset$.

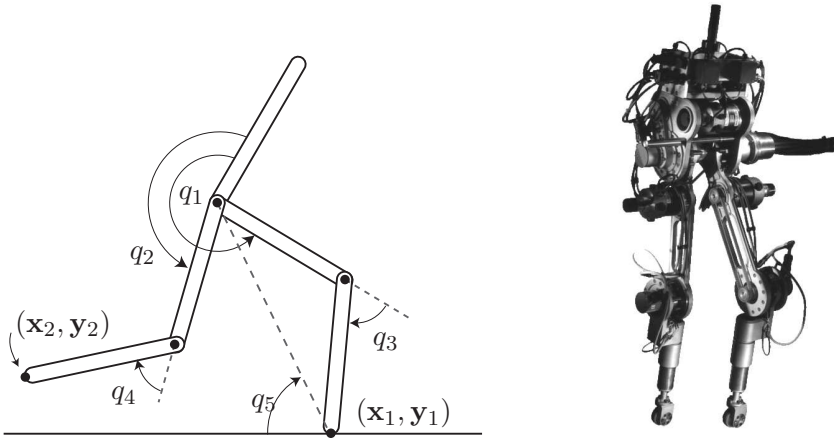

Figure 7.1: Coordinate system for RABBIT. The world frame is assumed to be attached to the base of the stance foot. There are four actuators, two at the knees at two at the hips. The contact point with the ground is unactuated, and angles are positive in the counterclockwise direction. RABBIT was developed as part of the French National Project, ROBEA, and is housed at LAG (Grenoble) [118].

Their function is to coordinate the evolution of the various links throughout a step. Since RABBIT has four independent actuators (two at the hips and two and the knees), four virtual constraints can be imposed. Following [153], since q_5 is naturally monotonic as the robot advances from left to right in a step, the four virtual constraints are written as

$$y = h(q) = q_{\mathrm{b}} - h_d(q_5), \tag{7.15}$$

where $q_b = (q_1, \ldots, q_4)$ is the vector of actuated (body) coordinates, and $h_d(q_5)$ gives the desired configuration of the actuated joints as the robot advances in a step. Here, h_d is chosen as in the example in [153, Sect. VII]. Because $y = h(q)$ depends only on the configuration variables, its relative degree is at least two. Differentiating the output twice gives

$$\ddot{y} = L_f^2 h(q, \dot{q}) + L_g L_f h(q) u. \tag{7.16}$$

Suppose for the moment that the decoupling matrix $L_g L_f h$ is invertible, which would imply that the output (7.15) has uniform vector relative degree two. The columns of g are involutive as in [78, p. 222]. If the constraints h_d are physically meaningful, then there will exist at least one point where they are satisfied, thus meeting all conditions of Hypotheses H7.7.

As described in Corollary 7.8, choose scalars K_D and K_P such that

$$s^2 + K_D s + K_P = 0 \tag{7.17}$$

has distinct roots with negative real parts, and let $\epsilon > 0$. Then the feedback law

$$u(x) = -(L_g L_f h(x))^{-1} \left(L_f^2 h(x) + \frac{1}{\epsilon} K_D L_f h(x) + \frac{1}{\epsilon^2} K_P h(x) \right) \tag{7.18}$$

applied to $\dot{x} = f(x) + g(x)u$ results in

$$\ddot{y} = -\frac{1}{\epsilon} K_D \dot{y} - \frac{1}{\epsilon^2} K_P y. \tag{7.19}$$

7.4.3 Closed-Loop Analysis

Having met the coordinate-free hypotheses of H7.7, Corollary 7.8 states that the set

$$\mathcal{Z} = \{x \in \mathcal{X} \mid h(x) = 0,\ L_f h(x) = 0\}$$

is a smooth two-dimensional submanifold of $\mathcal{X}$ and is invariant under the closed-loop dynamics

$$\bar{f}^\epsilon(x) = f(x) + g(x)u^\epsilon(x).$$

We now turn our attention to Corollary 7.6; assume that $\mathcal{Z}$ is impact invariant, that $\mathcal{S} \cap \mathcal{Z}$ has codimension one in $\mathcal{Z}$, and that there exists a periodic orbit within $\mathcal{Z}$ that is transversal to $\mathcal{S}$ (all common constraints used in choosing the output function (7.15)). With H7.5 satisfied by Corollary 7.8 and H7.3 satisfied by assumption, Corollary 7.6 shows that for sufficiently small $\epsilon > 0$, the periodic orbit is stable in the zero dynamics if and only if it is stable in the full dynamics.

When testing stability based on Theorem 7.2, our first objective will be to put $\bar{f}^\epsilon$ in the proper coordinates so that Hypotheses H7.1 can be checked. Note that because $h(q) = q_{\mathrm{b}} - h_d(q_5)$,

$$\Psi(q) = \begin{bmatrix} h(q) \\ q_5 \end{bmatrix} \tag{7.20}$$

is a global diffeomorphism on $\mathcal{Q}$. It follows that

$$\begin{bmatrix} z_1 \\ z_2 \\ \eta_{1:4} \\ \eta_{5:8} \end{bmatrix} = \begin{bmatrix} q_5 \\ d_5(q)\dot{q} \\ h(q) \\ \frac{\partial h}{\partial q}(q)\dot{q} \end{bmatrix} \tag{7.21}$$

is a global diffeomorphism on $\mathcal{X} = T\mathcal{Q}$, where d_5 is the last row of the inertia matrix D, and $\sigma = d_5(q)\dot{q}$ is the angular momentum of the biped about the end of the stance leg end [29]. In these coordinates [78, pp. 224],

$$\bar{f}^{\epsilon}(z,\eta) = \begin{bmatrix} \bar{f}_{1:2}(z,\eta) \\ A(\epsilon)\eta \end{bmatrix}, \tag{7.22}$$

where

$$A(\epsilon) = \begin{bmatrix} 0 & I_{4\times 4} \\ \frac{-k_P}{\epsilon^2} I_{4\times 4} & \frac{-k_D}{\epsilon} I_{4\times 4} \end{bmatrix}, \tag{7.23}$$

thus meeting H7.1-i. As mentioned earlier, conditions H7.1-ii, H7.1-iii, H7.1-iv, and H7.1-v (including impact invariance and the existence of a periodic orbit lying within $\mathcal{Z}$) are ensured by the correct selection of an output function. To verify the final hypotheses we will show that $\lim_{\epsilon \searrow 0} e^{A(\epsilon)} = 0$. Note that

$$A(\epsilon) = \Pi(\epsilon)\frac{1}{\epsilon}A_0\Pi^{-1}(\epsilon), \tag{7.24}$$

where

$$A_0 = \begin{bmatrix} 0 & I_{4\times 4} \\ -k_P I_{4\times 4} & -k_D I_{4\times 4} \end{bmatrix} \tag{7.25}$$

and

$$\Pi(\epsilon) = \begin{bmatrix} \epsilon I_{4\times 4} & 0 \\ 0 & I_{4\times 4} \end{bmatrix}. \tag{7.26}$$

Since (7.17) is a Hurwitz polynomial,

$$\lim_{\epsilon \searrow 0} e^{\frac{1}{\epsilon}A_0} = 0$$

and hence

$$\lim_{\epsilon \searrow 0} e^{A(\epsilon)} = 0,$$

thus fulfilling H7.1-vi. Applying Theorem 7.2, for $\epsilon > 0$ sufficiently small the feedback law (7.18) exponentially stabilizes in the full order model a periodic orbit that is exponentially stable in the restriction dynamics.

7.4.4 Numerical Simulation

In the previous subsection, two reduced dimensionality stability tests were applied to the problem of walking of walking on flat ground, with similar results. In the case where critical properties can be verified (invertibility of the decoupling matrix $L_g L_f h$, impact invariance $\Delta(\mathcal{S} \cap \mathcal{Z}) \subset \mathcal{Z}$, and the existence of a periodic orbit lying within $\mathcal{Z}$ that is transversal to $\mathcal{S} \cap \mathcal{Z}$), a periodic orbit that is exponentially stable in the hybrid zero dynamics will be exponentially stable in the full system. Claims of stability will now be investigated numerically.

For the choice of virtual constraints shown in Figure 7.2, the restricted Poincaré map will have a fixed point at $\sigma^- = -40.8$, corresponding to an average walking rate of exactly 2.0 m/s. A stick figure animation of the corresponding walking motion is shown in Figure 7.3. The eigenvalue associated with the restricted return map found numerically as 0.58. Stability of the orbit within the zero dynamics is illustrated in Figure 7.4. The eigenvalues of the full return map, $\mathcal{D}P^\epsilon$, were computed at the fixed point for various values of $\epsilon > 0$. Table 7.1 shows that the eigenvalue associated with the restricted Poincaré map (shown in bold) is indeed constant for varying values of ϵ. This table indicates that for $\epsilon \leq 0.17$, the periodic motion is exponentially stable in the full order model, but for $\epsilon = 0.20$, it is unstable. Figure 7.5 shows that decreasing ϵ causes $\|\eta(t)\|_2$ to converge to zero more quickly. Discontinuities in $\eta(t)$ occur at each impact event, with the impact tending to increase $\|\eta(t)\|_2$ rather than decrease it. From the proof of Theorem 7.2 it follows that $\log(\det(\mathcal{D}P^\epsilon))$ should be affine in $1/\epsilon$. This is confirmed in Figure 7.6, lending credibility to the numerical computations.

7.5 Discussion

This chapter has shown in two separate theorems that under certain conditions a periodic orbit is stable in a system with impulse effects if and only if the orbit is stable within a hybrid zero dynamics that is a subdynamic of the full model. The two theorems differ in the sets of hypotheses they require. The first stability test, given in Theorem 7.2, requires conditions that can only be verified in a particular set of coordinates. The second stability test, given in Theorem 7.4 and Corollary 7.6, requires hypotheses that can be verified without placing the system in any special set of coordinates, which typically makes their rigorous verification much easier.

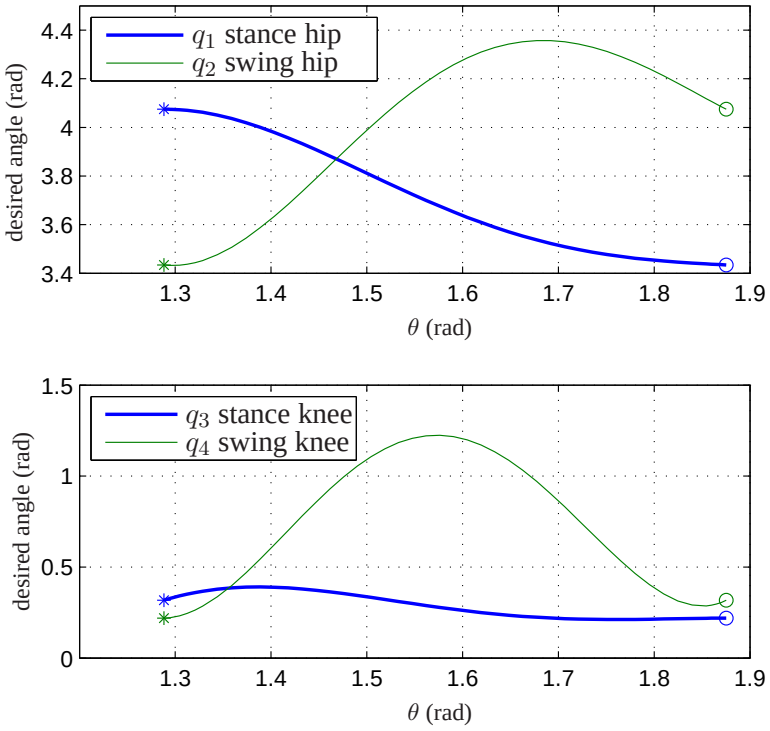

Figure 7.2: A graphical representation of the virtual constraints.

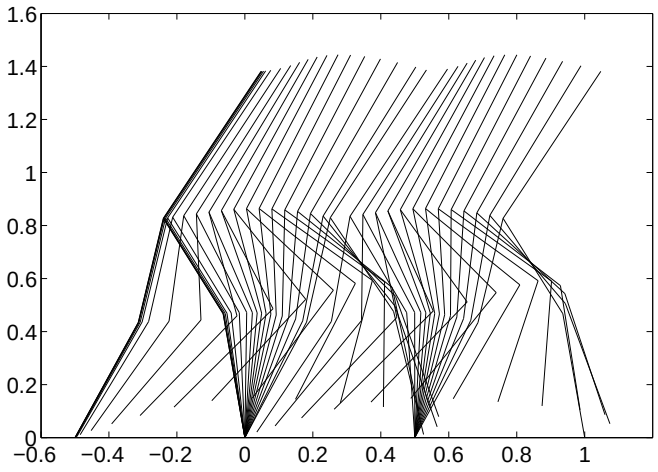

Figure 7.3: A stick figure animation of the walking motion used in the example.

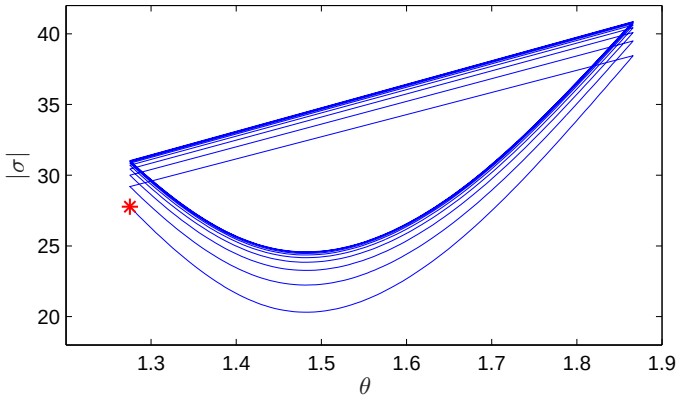

Figure 7.4: System response within the hybrid zero dynamics manifold. The initial condition (noted with an asterisk) lies within the hybrid zero dynamics manifold. Convergence to the orbit is rapid, with an estimated eigenvalue of 0.58. Stability of an orbit within the zero dynamics manifold is independent of the value of ϵ.

$\epsilon = 0.12$	$\epsilon = 0.17$	$\epsilon = 0.20$
0.58	-0.62	$\boxed{-1.91}$
0.48	**0.58**	**0.58**
$-0.12 + 4.4 \times 10^{-2}\, i$	$-0.19 + 0.14\, i$	$-0.12 + 0.27\, i$
$-0.12 - 4.4 \times 10^{-2}\, i$	$-0.19 - 0.14\, i$	$-0.12 - 0.27\, i$
$-0.11 + 5.4 \times 10^{-2}\, i$	$-0.17 + 0.16\, i$	$-0.15 + 0.25\, i$
$-0.11 - 5.4 \times 10^{-2}\, i$	$-0.17 - 0.16\, i$	$-0.15 - 0.25\, i$
2.5×10^{2}	0.14	0.21
$9.2 \times 10^{-3} - 1.8 \times 10^{-2}\, i$	-8.2×10^{-2}	-4.2×10^{-2}
$9.2 \times 10^{-3} + 1.8 \times 10^{-2}\, i$	8.0×10^{-3}	7.6×10^{-3}

Table 7.1: Eigenvalues of $\mathcal{D}P^{\epsilon}$ for three values of ϵ, ranked by magnitude. The eigenvalue of $\mathcal{D}\rho$ is shown in bold.

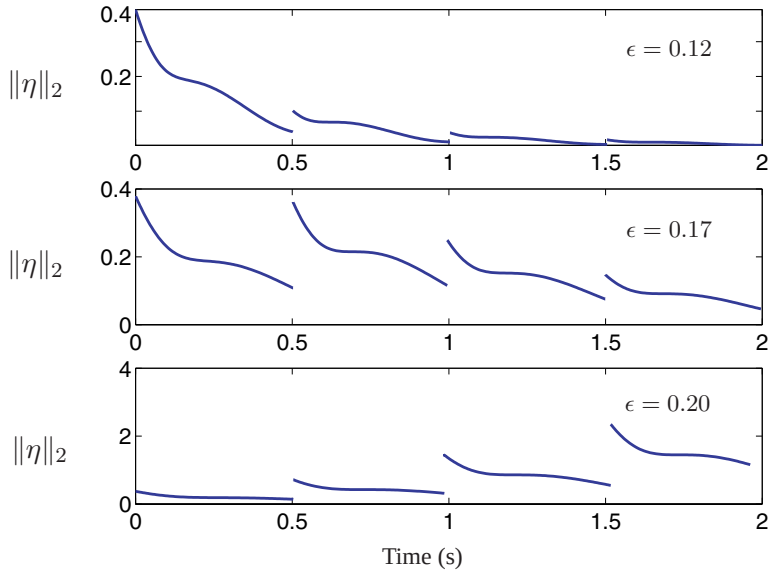

Figure 7.5: Error profiles for three values of ϵ. The restricted system corresponds to $\eta \equiv 0$. As ϵ decreases to zero, $\eta(t)$ converges more quickly to zero. Note that the orbit is unstable for $\epsilon = 0.2$ even though it is exponentially stable in the restricted dynamics and the "transversal part" of the closed-loop ODE is decoupled, linear, and exponentially stable.

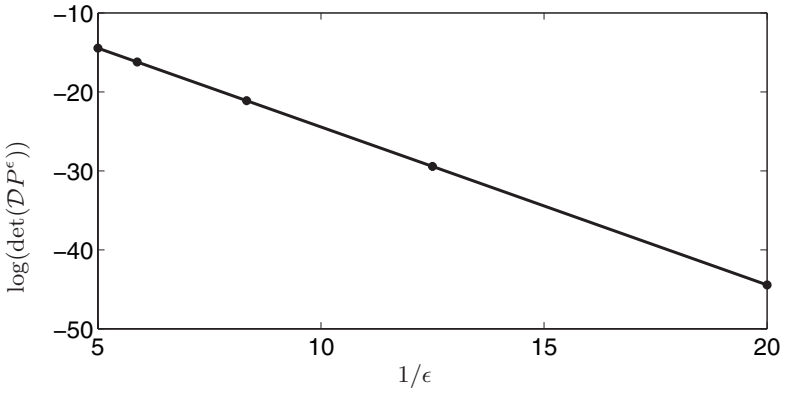

Figure 7.6: The graph of $\log(\det(\mathcal{D}P^\epsilon))$ versus $1/\epsilon$. The correlation should be affine when the controller (7.18) is used. The circles locate the numerically estimated values of $\log(\det(\mathcal{D}P^\epsilon))$ for five different values of ϵ. The solid line is an affine fit.

Both of these theorems improve upon the previous work by relaxing the requirement of finite time attractivity (previously used in theorems on restricted Poincaré stability testing) with a more general requirement for sufficiently fast exponential attractivity. This relaxation of requirements allows a wider class of feedback control laws to be considered for the task of stabilizing locomotion in bipedal robots. The utility of the two new theorems was highlighted in a case study. A periodic orbit whose design was carried out on the basis of a two-dimensional restriction dynamics (i.e., the hybrid zero dynamics of walking) could be systematically rendered exponentially stable in the full order model by using a smooth state variable feedback, as predicted by both the coordinate-based stability test of Theorem 7.2 and the coordinate-free stability test of Theorem 7.4 and its corollaries.

Notation Introduced in Chapter 7

Symbol	Meaning	Defined
ϵ	a strictly positive scalar parameter used for tuning the rate of convergence to a hybrid invariant manifold $\mathcal{Z}$	Section 7.1
$\bar{\Sigma}^\epsilon$	a family of systems with impulse effects, where for a fixed value of ϵ, each member is a C^1 system with impulse effects	Section 7.1
$\phi^\epsilon(t, x_0)$	solution of the autonomous system $\dot{x} = \bar{f}^\epsilon(x)$	Section 7.1
$T_I^\epsilon(x)$	the ϵ-dependant time-to-impact function for $\bar{\Sigma}^\epsilon$	Section 7.1
$P^\epsilon(x)$	the ϵ-dependant Poincaré return map for $\bar{\Sigma}^\epsilon$	Section 7.1
$\bar{\Sigma}^\epsilon\|_{\mathcal{Z}}$	the restriction of $\bar{\Sigma}^\epsilon$ to a hybrid invariant manifold $\mathcal{Z}$	Section 7.1
$DP^\epsilon(x^*)$	the Jacobian linearization of P^ϵ as evaluated at the fixed point x^*	Section 7.1
$T_{x^*}\mathcal{S}$	the tangent space of $\mathcal{S}$ at the point x^*	Section 7.1
η	coordinates of the transverse dynamics	Section 7.1
z	coordinates of the zero dynamics	Section 7.1
$D\hat{P}(z^*, \eta^*)$	the Jacobian linearization of a Poincaré map for an autonomous system with impulse effects, written in special coordinates	Section 7.2
Γ, Ψ	coordinate transforms proposed by Theorem 7.4	Section 7.2
$S_{\phi_{T_I}}$	sensitivity of the transverse dynamics to the continuous flow of an autonomous system with impulse effects	Section 7.2
S_Δ	sensitivity of the transverse dynamics to the impact map of an autonomous system with impulse effects	Section 7.2

CHAPTER 8

Parameter Updates for Achieving Impact Invariance

In the context of systems with impulse effects, hybrid invariance occurs when a manifold is invariant under both the continuous (ODE) portion and the discrete (impact) map of the model. Chapter 7 has shown that the property of hybrid invariance can significantly reduce the computational burden associated with testing the stability of a periodic orbit in a system with impulse effects. In the special case of models based on RABBIT, designing hybrid invariant manifolds is quite easy because of special structures that arise when the virtual constraints have uniform vector relative degree two, and previously published works in hybrid zero dynamics only address these types of outputs. In the case of robots with series springs, relevant outputs do not necessarily have uniform vector relative degree two, and achieving hybrid invariance is much more difficult.

Forward invariance in ODE models is a rich, well-studied subject. In particular the methods developed by Byrnes and Isidori in the area of *zero dynamics* can be used to design forward invariant manifolds, not necessarily resulting from outputs having uniform vector relative degree two. A less well-studied and hence more challenging problem is how to achieve impact invariance in more general classes of output functions than those previously considered. To address the problem, this chapter introduces the tool of *parameterized extensions*, a type of dynamic extension for systems with impulse effects. With the introduction of parameterized outputs, a discrete feedback element becomes available—the parameter update law. When used properly, a discrete feedback controller can provide impact invariance, with a separately designed continuous feedback controller providing forward invariance.

A valid concern when using parameter update schemes is the potential for introducing unstable

modes into the system. Albeit discrete, unstable parameter dynamics could destabilize an otherwise stable system control system. For this reason, the proposed hybrid extensions are *deadbeat*, or put differently, memoryless in the parameters. Deadbeat parameter extensions introduce no additional dynamics, discrete or continuous, stable or unstable.

The remainder of this chapter gives two solutions for achieving impact invariance of manifolds resulting from outputs having arbitrary uniform vector relative degree. Under the assumption that an appropriate parameter update function can be found, Section 8.2 presents a deadbeat hybrid extension for achieving impact invariance. Because derivation of this function is often difficult, the result of Section 8.3 provides an alternative solution for achieving impact invariance, one in which the original output function is modified so that the parameter update scheme is known in closed form. The closed-loop properties of both parameter update schemes are explored in Chapter 9 in a case study examining walking in a planar robot with compliance.

8.1 Definition and Properties of Parameter Extensions

Let $\Sigma = (\mathcal{X}, \mathcal{S}, \emptyset, \mathcal{U}, \Delta, f, g)$ be a control system with impulse effects[1] and let $\mathcal{A}$ be an open subset of $\mathbb{R}^q$, $q \geq 1$. Then, the system

$$\Sigma_{\mathbf{e}} : \begin{cases} (\dot{x}, \dot{\alpha}) &= (f(x) + g(x)u, 0) \quad (x^-, \alpha^-) \notin \mathcal{S} \times \mathcal{A} \\ (x^+, \alpha^+) &= (\Delta(x^-), v) \qquad\quad (x^-, \alpha^-) \in \mathcal{S} \times \mathcal{A} \end{cases} \tag{8.1}$$

is called a *parameterized extension* of Σ and can be denoted in alternative notation as

$$\Sigma_{\mathbf{e}} = (\mathcal{X}_{\mathbf{e}}, \mathcal{S}_{\mathbf{e}}, \mathcal{A}, \mathcal{U}, \Delta_{\mathbf{e}}, f_{\mathbf{e}}, g_{\mathbf{e}})$$

(with elements of the 7-tuple $\Sigma_{\mathbf{e}}$ defined in the obvious way). When a parameter update law is chosen to be independent of the parameter itself, that is, $\Delta_v : \mathcal{S} \to \mathcal{A}$, the resultant system

$$\Sigma_{\mathbf{e}} = \left(\mathcal{X}_{\mathbf{e}}, \mathcal{S}_{\mathbf{e}}, \emptyset, \mathcal{U}, \bar{\Delta}_{\mathbf{e}}, f_{\mathbf{e}}, g_{\mathbf{e}}\right)$$

with $\bar{\Delta}_{\mathbf{e}}(x_{\mathbf{e}}) = (\Delta(x), \Delta_v(x))$ and $x_{\mathbf{e}} = (x, \alpha)$, is called an *open-loop deadbeat hybrid extension*. A *closed-loop deadbeat hybrid extension* is an autonomous system denoted

$$\bar{\Sigma}_{\mathbf{e}} = \left(\mathcal{X}_{\mathbf{e}}, \mathcal{S}_{\mathbf{e}}, \bar{\Delta}_{\mathbf{e}}, \bar{f}_{\mathbf{e}}\right)$$

[1] Note that $\mathcal{V} = \emptyset$, indicating an absence of control authority over the impact map.

where $\bar{f}_{\mathbf{e}}(x_{\mathbf{e}}) = f_{\mathbf{e}}(x_{\mathbf{e}}) + g_{\mathbf{e}}(x_{\mathbf{e}})u(x_{\mathbf{e}})$ for some state feedback law $u : \mathcal{X}_{\mathbf{e}} \to \mathcal{U}$.

8.2 Nonconstructive Parameter Extensions for Hybrid Invariance

One critical aspect of applying Theorems 7.2 or 7.4 in the context of bipedal locomotion is the selection of an output $h(x)$ that leads to a hybrid invariant manifold. Appropriately choosing an output so that its zeroing manifold is impact invariant is a nontrivial task, in general. In previous work, [153, Section V, Thm. 4] identified a class of holonomic[2], uniform vector relative degree two outputs for which it is straightforward to meet the impact invariance condition. The reasoning employed in [153] relied heavily on the fact that both the impact map Δ and $L_f h$ were linear in the generalized velocity coordinate. This linearity property breaks down already for $L_f^2 h$ (equivalently, for outputs with uniform vector relative degree, which are relevant in the context of compliant actuation). Without linearity of both the boundary conditions of the virtual constraints and the impact map itself, giving verifiable conditions for impact invariance can become hard. The following remark gives a restatement of the condition of impact invariance that is more amenable to the development of a parameter update law leading to impact invariance.

Remark 8.1. *When a system with impulse effects*

$$\Sigma : \begin{cases} \dot{x} &= f(x) + g(x)u \quad x^- \notin \mathcal{S} \\ x^+ &= \Delta(x^-) \qquad\quad x^- \in \mathcal{S}, \end{cases} \tag{8.2}$$

has an output $h(x)$ with uniform vector relative degree k, with

$$\mathcal{Z} = \{x \in \mathcal{X} \mid h(x) = 0, L_f h(x) = 0, \cdots, L_f^{k-1} h(x) = 0\},$$

then the following are equivalent:

a) $\Delta(\mathcal{S} \cap \mathcal{Z}) \subset \mathcal{Z}$*;*

b) $\forall x \in \Delta(\mathcal{S} \cap \mathcal{Z})$ *and* $\forall 0 \leq i \leq k-1$, $L_f^i h(x) = 0$.

If the output function $h(x)$ is dependent on a vector of reals $\alpha \in \mathcal{A} \subset \mathbb{R}^q$ and the set $\mathcal{S} \cap \mathcal{Z}$ is independent of α, then condition $b)$ above can be restated as a condition on controlled impact

[2]The output function h depended only on the configuration variables of the robot, hence the terminology "holonomic".

invariance:

$$\forall x \in \Delta(\mathcal{S} \cap \mathcal{Z})\ \exists \alpha \in \mathcal{A} \text{ such that } L_f^i h(x,\alpha) = 0\ \ \forall 0 \leq i \leq k-1. \tag{8.3}$$

The following theorem illustrates the use of a parameter update law to achieve the controlled invariance described above. Under the given conditions, the extra dimensionality associated with the parameters does not significantly complicate the Poincaré return map. The theorem is labeled as "nonconstructive" because no closed form parameter update scheme is given.

Theorem 8.2 (Invariance by Nonconstructive Deadbeat Hybrid Extension). *Consider a C^1 system with impulse effects*

$$\Sigma : \begin{cases} \dot{x} &= f(x) + g(x)u & x^- \notin \mathcal{S} \\ x^+ &= \Delta(x^-) & x^- \in \mathcal{S} \end{cases} \tag{8.4}$$

with an n-dimensional state manifold $\mathcal{X}$ and m-dimensional inputs u. Let $\mathcal{A}$ be an open subset of $\mathbb{R}^q$, for some $q \geq 1$, and let $h : \mathcal{X} \times \mathcal{A} \to \mathbb{R}^m$ be an output function. Suppose furthermore that

Hypotheses 8.3:

i) $\forall \alpha \in \mathcal{A}$, *the output $y = h(x,\alpha)$ has uniform vector relative degree k;*

ii) there exists a non-empty C^1 submanifold $\mathcal{Z}$ such that $\forall \alpha \in \mathcal{A}$,

$$\mathcal{Z}_\alpha = \{x \in \mathcal{X} \mid h(x,\alpha) = 0, \cdots, L_f^{k-1} h(x,\alpha) = 0\}$$

is diffeomorphic to $\mathcal{Z}$;

iii) $\mathcal{S} \cap \mathcal{Z}_\alpha$ is independent of α and equals $\mathcal{S} \cap \mathcal{Z}$;

iv) $\mathcal{S} \cap \mathcal{Z}$ is C^1 and has dimension one less than $\mathcal{Z}$; and

v) there exits a C^1 function $\Delta_v : \mathcal{S} \to \mathcal{A}$ such that, $\forall x \in \mathcal{S} \cap \mathcal{Z}$, the values $\xi = \Delta(x)$, $\alpha = \Delta_v(x)$ result in

$$\begin{aligned} h(\xi,\alpha) &= 0 \\ L_f h(\xi,\alpha) &= 0 \\ &\cdots \\ L_f^{k-1} h(\xi,\alpha) &= 0. \end{aligned}$$

Then for any $\epsilon > 0$ the closed-loop deadbeat hybrid extension,

$$\bar{\Sigma}^{\epsilon}_{\mathbf{e}} : \begin{cases} (\dot{x}, \dot{\alpha}) &= (f(x) + g(x)u^{\epsilon}(x,\alpha), 0) & (x^-, \alpha^-) \notin \mathcal{S} \times \mathcal{A} \\ (x^+, \alpha^+) &= (\Delta(x^-), \Delta_v(x^-)) & (x^-, \alpha^-) \in \mathcal{S} \times \mathcal{A} \end{cases} \tag{8.5}$$

with feedback $u^{\epsilon}(x,\alpha)$ modified from (7.12)

$$u^{\epsilon}(x,\alpha) = -\left(L_g L_f^{k-1} h(x,\alpha)\right)^{-1} \left(\begin{array}{c} L_f^k h(x,\alpha) + \sum_{i=0}^{k-1} \frac{1}{\epsilon^{k-i}} K_i L_f^i h(x,\alpha) \end{array} \right), \tag{8.6}$$

has a hybrid zero dynamics $\bar{\Sigma}^{\epsilon}_{\mathbf{e}}|_{\mathcal{Z}_{\mathbf{e}}}$. Moreover,

a) the hybrid zero dynamics manifold of (8.5) *is $\mathcal{Z}_{\mathbf{e}} = \cup_{\alpha \in \mathcal{A}} (\mathcal{Z}_{\alpha}, \alpha)$,*

b) $\mathcal{Z}_{\mathbf{e}} \cap (\mathcal{S} \times \mathcal{A}) = (\mathcal{S} \cap \mathcal{Z}) \times \mathcal{A}$, and

c) the Poincaré map $P^{\epsilon}_{\mathbf{e}}|_{\mathcal{Z}_{\mathbf{e}}} : (\mathcal{S} \cap \mathcal{Z}) \times \mathcal{A} \to (\mathcal{S} \cap \mathcal{Z}) \times \mathcal{A}$ for the restriction dynamics is

$$P^{\epsilon}_{\mathbf{e}}|_{\mathcal{Z}_{\mathbf{e}}}(z,\alpha) = (\rho_{\mathbf{e}}(z), \Delta_v(z)), \tag{8.7}$$

where $\rho_{\mathbf{e}} : \mathcal{S} \cap \mathcal{Z} \to \mathcal{S} \cap \mathcal{Z}$ is independent of ϵ.

Remark 8.4. *Suppose that $\Sigma = (\mathcal{X}, \mathcal{S}, \emptyset, \mathcal{U}, \Delta, f, g)$ has a periodic orbit $\mathcal{O}$. Define the parameter vector $\alpha^* = \Delta_v(x^*)$ for $x^* = \bar{\mathcal{O}} \cap \mathcal{S}$. Then the set $\mathcal{O}_{\mathbf{e}} = \mathcal{O} \times \alpha^*$ is a periodic orbit of the open-loop deadbeat hybrid extension $\Sigma_{\mathbf{e}}$. The orbit $\mathcal{O}_{\mathbf{e}}$ will be called the trivial lift of $\mathcal{O}$ into $\Sigma_{\mathbf{e}}$.*

Given an appropriate parameter update function Δ_v, the above theorem shows how to construct a deadbeat hybrid extension to produce a hybrid invariant manifold. The restricted Poincaré map $P^{\epsilon}_{\mathbf{e}}|_{\mathcal{Z}_{\mathbf{e}}}(z,\alpha)$ has the additional property that its spectral radius is determined solely by the properties of $\rho(z,a)$. Using Theorem 8.2, observe that

$$\frac{\partial\, P^{\epsilon}_{\mathbf{e}}|_{\mathcal{Z}_{\mathbf{e}}}(z,\alpha)}{\partial(z,\alpha)} = \begin{bmatrix} \frac{\partial \rho_{\mathbf{e}}(z)}{\partial z} & \frac{\partial \rho_{\mathbf{e}}(z)}{\partial \alpha} \\ \frac{\partial \Delta_v(z)}{\partial z} & \frac{\partial \Delta_v(z)}{\partial \alpha} \end{bmatrix} = \begin{bmatrix} \frac{\partial \rho_{\mathbf{e}}(z)}{\partial z} & 0 \\ \frac{\partial \Delta_v(z)}{\partial z} & 0 \end{bmatrix} \tag{8.8}$$

and notice that

$$\max \left| \text{eig} \left(\frac{\partial\, P^{\epsilon}_{\mathbf{e}}|_{\mathcal{Z}_{\mathbf{e}}}(z,\alpha)}{\partial(z,\alpha)} \right) \right| = \max \left| \text{eig} \left(\frac{\partial \rho_{\mathbf{e}}(z)}{\partial z} \right) \right|. \tag{8.9}$$

Stability implications of (8.8) and (8.9) will be investigated in the next section.

A major drawback of Theorem 8.2 is that the control designer must first find a satisfactory Δ_v before the theorem can be applied. Hypothesis H8.3-v gives a clear statement of the required

properties of Δ_v but provides no insight into its selection. The following proposition, stated without proof, describes conditions under which a satisfactory Δ_v is known to exist. As the result depends on the Implicit Function Theorem, the proposition asserts only existence of the parameter update function and does not provide its closed-form expression.

Proposition 8.5. *If there exists a periodic orbit $\mathcal{O}$ and a vector $\alpha = \alpha^*$ on which the output $h(x, \alpha)$ is identically zero, and the Jacobian*

$$\frac{\partial}{\partial \alpha} \begin{bmatrix} h(\xi,\alpha) \\ L_f h(\xi,\alpha) \\ \cdots \\ L_f^{k-1} h(\xi,\alpha). \end{bmatrix}_{\substack{\xi = \Delta(x^*) \\ \alpha = \alpha^*}} \tag{8.10}$$

has full row rank, then by the Implicit Function Theorem there exists a parameter update function $\Delta_v : \mathcal{S} \to \mathcal{A}$ such that $\forall x \in \mathcal{S} \cap \mathcal{Z}$, the values $\xi = \Delta(x)$, $\alpha = \Delta_v(x)$ result in

$$\begin{aligned} h(\xi,\alpha) &= 0 \\ L_f h(\xi,\alpha) &= 0 \\ &\cdots \\ L_f^{k-1} h(\xi,\alpha) &= 0. \end{aligned}$$

A different method for achieving hybrid invariant manifolds is presented in the following section. The result involves the use of deadbeat hybrid extensions, but outputs are chosen in such a way that leads to a closed-form expression of the required parameter update law.

8.3 Constructive Parameter Extensions for Hybrid Invariance

Theorem 8.6 (Impact Invariance by Construction). *Consider a smooth control system with impulse effects*[3] *$\Sigma = (\mathcal{X}, \mathcal{S}, \emptyset, \mathcal{U}, \Delta, f, g)$, with $\mathcal{U} \subset \mathbb{R}^m$. Assume there exists a periodic orbit $\mathcal{O}$ that is transversal to $\mathcal{S}$ and that in addition*

Hypotheses 8.7:

[3] Once again note that $\mathcal{V} = \emptyset$, indicating an absence of control authority over the impact map.

i) there exists a smooth output $h : \mathcal{X} \to \mathbb{R}^m$ such that h vanishes on the orbit and has uniform vector relative degree k in an open neighborhood of the orbit;

ii) the distribution $span\{g_1(x), \cdots, g_m(x)\}$ is involutive; and

iii) there exists a C^∞ real-valued function $\tau(x)$ such that

iii-a) $\tau(x)$ is strictly monotonically increasing[4] on $\mathcal{O}$;

iii-b) $L_g\tau(x) = \cdots = L_g L_f^{k-2}\tau(x) = 0$; and

iii-c) for $x^* = \bar{\mathcal{O}} \cap \mathcal{S}$, $\tau(x^*) = 1$ and $\tau(\Delta(x^*)) = 0$.

Then, starting from the original system Σ and output function $y = h(x)$, one can construct an open-loop deadbeat hybrid extension

$$\Sigma_{\mathbf{e}} = \left(\mathcal{X}_{\mathbf{e}}, \mathcal{S}_{\mathbf{e}}, \emptyset, \mathcal{U}, \bar{\Delta}_{\mathbf{e}}, f_{\mathbf{e}}, g_{\mathbf{e}}\right)$$

and a new output function $y = h_{\mathbf{e}}(x_{\mathbf{e}})$ such that all of the conditions of Corollary 7.8 are satisfied for $\Sigma_{\mathbf{e}}$ and $h_{\mathbf{e}}$. Moreover, the manifold $\mathcal{Z}_e$ defined as

$$\mathcal{Z}_{\mathbf{e}} = \{x_{\mathbf{e}} \in \mathcal{X}_{\mathbf{e}} \mid h_{\mathbf{e}}(x_{\mathbf{e}}) = 0, L_{f_{\mathbf{e}}} h_{\mathbf{e}}(x_{\mathbf{e}}) = 0, \cdots, L_{f_{\mathbf{e}}}^{k-1} h_{\mathbf{e}}(x_{\mathbf{e}}) = 0\},$$

is impact invariant w.r.t. $\Sigma_{\mathbf{e}}$ and contains $\mathcal{O}_{\mathbf{e}}$, the trivial lift of $\mathcal{O}$ into $\Sigma_{\mathbf{e}}$.

The parameter update law $\Delta_v : \mathcal{S} \to \mathcal{A}$ that provides impact invariance is unique only on the domain of $\mathcal{S} \cap \mathcal{Z}$. On the remainder of $\mathcal{S}$ the parameter update function can be arbitrarily defined, provided that Δ_v remains continuously differentiable on $\mathcal{S} \cap \mathcal{Z}$. Consider a parameter update function constructed as in the proof of Theorem 8.6 that is dependent[5] on a scalar λ. Assume that the parameter update law Δ_v^λ has the following properties:

Hypotheses 8.8:

i) For any $(x^-, \alpha^-) \in \mathcal{S}_{\mathbf{e}}$,

$$\begin{aligned} h_{\mathbf{e}}(x^+, \alpha^+) &= 0 \\ L_{f_{\mathbf{e}}} h_{\mathbf{e}}(x^+, \alpha^+) &= 0 \\ &\cdots \\ L_{f_{\mathbf{e}}}^{k-1} h_{\mathbf{e}}(x^+, \alpha^+) &= 0 \end{aligned} \tag{8.11}$$

where $(x^+, \alpha^+) = (\Delta(x^-), \Delta_v^\lambda(x^-))$ for $\lambda = 0$,

[4] In this context, a function $\tau(x)$ is strictly monotonically increasing if $L_f\tau(x) > 0$ for every point x in $\mathcal{O}$.

[5] Dependence of the parameter update law on λ will be emphasized using the notation $\Delta_v^\lambda(x^-)$.

ii) for any fixed $x_{\mathbf{e}}{}^- = (x^-, \alpha^-) \in \mathcal{S}_{\mathbf{e}}$, the value of $\Delta_v^\lambda(x^-)$ is continuous in λ; and

iii) for any fixed $x_{\mathbf{e}}{}^- = (x^-, \alpha^-) \in \mathcal{S}_{\mathbf{e}} \cap \mathcal{Z}_{\mathbf{e}}$, the value of $\Delta_v^\lambda(x^-)$ is independent of λ.

Stated without proof, the following theorem shows an elegant simplification that is possible when the parameter update law satisfies Hypotheses H8.8.

Proposition 8.9. *Consider the ϵ and λ dependant closed-loop deadbeat hybrid extension that is created as follows:*

1. *Begin with a control system with impulse effects $\Sigma = (\mathcal{X}, \mathcal{S}, \emptyset, \mathcal{U}, \Delta, f, g)$.*

2. *Apply Theorem 8.6 with a parameter update function satisfying Hypotheses H8.8 to create an open-loop deadbeat hybrid extension*

$$\Sigma_{\mathbf{e}}^\lambda = \left(\mathcal{X}_{\mathbf{e}}, \mathcal{S}_{\mathbf{e}}, \emptyset, \mathcal{U}, \bar{\Delta}_{\mathbf{e}}^\lambda, f_{\mathbf{e}}, g_{\mathbf{e}}\right).$$

3. *Apply Corollary 7.8 to the open-loop deadbeat hybrid extension to produce a closed-loop deadbeat hybrid extension*

$$\bar{\Sigma}_{\mathbf{e}}^{\epsilon,\lambda} = \left(\mathcal{X}_{\mathbf{e}}, \mathcal{S}_{\mathbf{e}}, \bar{\Delta}_{\mathbf{e}}^\lambda, \bar{f}_{\mathbf{e}}^\epsilon\right).$$

An autonomous system constructed in this way has a Poincaré return map that, when written in the coordinates of Theorem 7.4 and evaluated at a fixed point, will have a Jacobian linearization of

$$\mathcal{D}\hat{P}_{\mathbf{e}}^{\epsilon,\lambda}(z_{\mathbf{e}}{}^*, \eta_{\mathbf{e}}{}^*) = \left[\begin{array}{c|c|c} \mathcal{D}\rho_{\mathbf{e}}(z^*) & 0 & \star \\ \hline 0 & 0 & \star \\ \hline 0 & 0 & S_{\phi_{T_I \mathbf{e}}}^\epsilon(\bar{z_{\mathbf{e}}}{}^*, \bar{\eta_{\mathbf{e}}}{}^*) S_{\Delta_{\mathbf{e}}}^\lambda(z_{\mathbf{e}}{}^*, \eta_{\mathbf{e}}{}^*) \end{array}\right],$$

with $z_{\mathbf{e}}{}^* = (z^*, \alpha^*)$. As shown in the proof of Corollary 7.6,

$$\lim_{\epsilon \searrow 0} S_{\phi_{T_I \mathbf{e}}}^\epsilon(\bar{z_{\mathbf{e}}}{}^*, \bar{\eta_{\mathbf{e}}}{}^*) = 0,$$

and by Hypotheses H8.8,

$$\lim_{\lambda \to 0} S_{\Delta_{\mathbf{e}}}^\lambda(z_{\mathbf{e}}{}^*, \eta_{\mathbf{e}}{}^*) = 0.$$

The return map $P_{\mathbf{e}}^{\epsilon,\lambda}$ for the closed-loop deadbeat hybrid extension of Proposition 8.9 has a domain of $\mathcal{S} \times \mathcal{A}$. The Jacobian linearization of this map is square with $\dim(\mathcal{A}) + \dim(\mathcal{S})$ columns

and rows. To test the stability of this return map (without utilizing any of its special properties) would require checking the eigenvalues of a $(\dim(\mathcal{A}) + \dim(\mathcal{S})) \times (\dim(\mathcal{A}) + \dim(\mathcal{S}))$ matrix. In contrast, if a feedback controller were designed directly for the original control system with impulse effects considered in Proposition 8.9, the resulting autonomous system would not have an accompanying parameter space $\mathcal{A}$, and thus the Poincaré return map would have a domain of $\mathcal{S}$. To test the stability properties of this return map would require checking the eigenvalues of a $\dim(\mathcal{S}) \times \dim(\mathcal{S})$ matrix.

What then is the benefit of parameter augmentation? Proposition 8.9 shows that the Jacobian linearization of $P_{\mathbf{e}}^{\epsilon,\lambda}$, when evaluated at the fixed point and written in special coordinates, has a structure such that

$$\max |\mathcal{D}\hat{P}_{\mathbf{e}}^{\epsilon,\lambda}(z_{\mathbf{e}}{}^*, \eta_{\mathbf{e}}{}^*)| = \max |\text{eig}(\mathcal{D}\rho_{\mathbf{e}}(z^*))|,$$

for ϵ and λ constant and sufficiently close to zero. The stability of the return map $\mathcal{D}\hat{P}_{\mathbf{e}}^{\epsilon,\lambda}(z_{\mathbf{e}}{}^*, \eta_{\mathbf{e}}{}^*)$ is determined by the eigenvalues of the $(\dim(\mathcal{S} \cap \mathcal{Z})) \times (\dim(\mathcal{S} \cap \mathcal{Z}))$ Jacobian linearization of $\mathcal{D}\rho_{\mathbf{e}}(z^*)$, showing that parameter augmentation does not complicate the reduced dimensional stability tests of Chapter 7.

8.4 Discussion

Motivated by the problem of creating exponentially stable periodic orbits in bipedal robots with underactuation and actuator dynamics, Chapter 7 extended the hybrid zero dynamics (HZD) framework of [153] to nonlinear systems with impulse effects where the outputs have vector relative degree greater than two. Describing the required conditions of simultaneous invariance under the continuous dynamics and the impact map was straightforward.

The more challenging aspect of the extension is addressed in this chapter—how to meet the impact invariance condition when the relative degree is greater than two. The result on impact invariance in [153] could not be extended in a direct way. A novel embedding of the original system into a system with event-based parameter updates was therefore introduced. The additional dynamic elements in the larger system can be tailored to meet the boundary conditions associated with impact invariance. This result was formalized in Theorem 8.2, which gave a nonconstructive solution for the impact map yielding impact invariance. The proposed dynamic extension is deadbeat in that the

additional states are updated only at impacts, and their new values depend only on the states of the original system, not the previous values of the parameters.

Based strongly on spline-like transition functions, the constructive outputs proposed in Theorem 8.6 allow the use of a constructive parameter update law that leads to impact invariance. Although both improve upon previously published results, the constructive solution of Theorem 8.6 is a far more powerful solution than its nonconstructive counterpart, Theorem 8.2.

Overall this chapter demonstrates the important fact that impact invariance can be achieved under mild conditions by a deadbeat parameter update that introduces no additional dynamics to the original system with impulse effects. The proposed parameter updates are fully compatible with the stability tests derived in Chapter 7. Both parameter update schemes of this chapter are illustrated in Chapter 9, which is a case study of walking in a biped with series compliant actuation.

Notation Introduced in Chapter 8

Symbol	Meaning	Defined
$\Sigma_{\mathbf{e}}$	a parameterized system with impulse effects, or an open-loop deadbeat hybrid extension (depending on context)	Section 8.1
$\mathcal{A}$	the parameter space of a parameterized system with impulse effects	Section 8.1
Δ_v	the parameter update function of an open- or closed-loop deadbeat hybrid extension	Section 8.1
$\bar{\Sigma}_{\mathbf{e}}$	the closed-loop deadbeat hybrid extension of a system with impulse effects	Section 8.1
$\bar{\Sigma}_{\mathbf{e}}^{\epsilon}$	an ϵ-dependent family of closed-loop deadbeat hybrid extensions	Section 8.1
$\mathcal{Z}_{\mathbf{e}}$	a hybrid invariant manifold for $\Sigma_{\mathbf{e}}$ or $\Sigma_{\mathbf{e}}^{\epsilon}$	Section 8.2
$\bar{P}_{\mathbf{e}}{}^{\epsilon}$	the ϵ-dependent Poincaré return map of $\bar{\Sigma}_{\mathbf{e}}^{\epsilon}$	Section 8.2
$\tau(x)$	a function that is strictly monotonic on a periodic orbit $\mathcal{O}$	Section 8.3
$\Delta_v^{\lambda}(x)$	a λ-dependent parameter update function	Section 8.3
λ	a scalar determining the convergence properties of the impact map w.r.t. an impact invariant manifold	Section 8.3
$\bar{\Sigma}_{\mathbf{e}}^{\epsilon,\lambda}$	an ϵ and λ dependant closed-loop deadbeat hybrid extension	Section 8.3
$DP_{\mathbf{e}}^{\epsilon,\lambda}$	the Jacobian linearization of the Poincaré return map of $\bar{\Sigma}_{\mathbf{e}}^{\epsilon,\lambda}$	Section 8.3
$S^{\epsilon}_{\phi_{T_I}\mathbf{e}}$	the ϵ-dependant sensitivity of the transverse dynamics to the continuous flow of $\bar{\Sigma}_{\mathbf{e}}^{\epsilon,\lambda}$	Section 8.3
$S^{\lambda}_{\Delta_{\mathbf{e}}}$	the λ-dependant sensitivity of the transverse dynamics to the impact map of $\bar{\Sigma}_{\mathbf{e}}^{\epsilon,\lambda}$	Section 8.3

CHAPTER 9

Case Study: A Biped with Compliance Walking on Flat Ground

As an illustration of the stability tests of Chapter 7 and the parameter augmentation schemes of Chapter 8, this chapter provides an extended simulation study of a five-link planar biped with compliance walking on rigid flat ground. The model is similar to the anthropomorphic biped pictured in Figure 9.1. Parameter values for the model are listed in Table 9.1. This study illustrates the utility of the new theory, which provides provable stability on a model that was beyond the domain of application of previously published results on HZD controllers.

The remainder of this chapter is organized as follows: Section 9.1 motivates the use of series springs in walking robots and remarks on the additional degrees of freedom that they introduce. Section 9.2 derives a model of walking in a biped with compliance that is based on the model of a (rigid) biped without compliance. Key properties of the models are given in Section 9.3. Having derived an appropriate model and established its properties, Theorem 8.2 is used to achieve impact invariance for a class of outputs that has uniform vector relative degree four. The required parameter update function is derived by hand (with the lengthy derivation omitted). Theorem 8.6 is used to achieve impact invariance with a slightly different class of vector relative degree four output functions with a parameter update function that is easily derived. To compare the application of these theorems to the stabilization of walking gaits, both are used to stabilize the same steady-state walking gait having an average forward rate of 0.8 m/s.

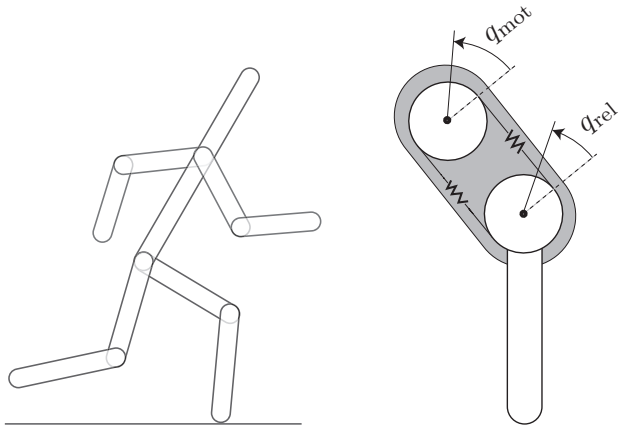

Figure 9.1: A class of compliant models. Left: A representative example, intentionally anthropomorphic, of the class of N-link biped robot models considered. Right: A schematic of a rotational joint with series compliant actuation.

Parameter	**Units**	**Value**
Length of each Link	m	0.5
Mass of the Torso	kg	27.5
Mass of each Femur and Tibia	kg	0.5
CoM Inertia of the Torso	$\text{kg} \cdot \text{m}^2$	0.5729
CoM Inertia of each Tibia	$\text{kg} \cdot \text{m}^2$	0.0104
CoM Inertia of each Femur	$\text{kg} \cdot \text{m}^2$	0.0391
Reflected Inertia of Rotors	$\text{kg} \cdot \text{m}^2$	0.03584
Transmission Ratio	(unitless)	$8:1$
Spring Constant	N/m	550

Table 9.1: Parameters of the five-link model with compliant actuation. All links have uniform mass distribution except the torso, whose COM is 0.15 m from the hip joint.

9.1 Benefits and Drawbacks of Compliance

In legged robots, the physical introduction of tuned springs into an otherwise rigid mechanism can significantly improve energy efficiency. The energetic benefits are twofold: within the strides of walking and running, springs can store and release some of the energy that would otherwise be lost as actuators do negative work [7]; and at foot touchdown events, springs isolate reflected motor inertias from the energy dissipating effects of rigid collisions. These and other uses of flexible elements have been demonstrated on *running* robots such as RHex [122], Scout [109], Sprawlita [26], Raibert's 2D and 3D hoppers [114], and the notably efficient ARL Monopod II [6]. And while the benefits of energy storage are most evident in running, in practice many robots must quite literally walk before they can run. In these cases compliance must be taken into account in the design and control of *walking* gaits, either explicitly by modeling or implicitly by treating nonrigid effects as disturbances to a fully rigid model.

Obtaining the energetic benefits of compliance is not without cost: delivering torque through compliant elements poses several challenges for control design. There is an obvious increase in the degrees of freedom of the robot model, and hence, the degree of underactuation. This is a widely recognized issue in robotics; see [129, 130, 10] and references therein. An additional challenge particular to legged robots arises from the impulsive effects occurring when the swing leg impacts the ground. When torque at a joint is generated by a motor and drivetrain in series with a spring (as in this chapter) the spring isolates the motor and drivetrain from the effects of an impact. Post-impact values of rotor position and velocity match their pre-impact values, and similar boundary conditions arise for joint torque. Seemingly benign, these additional post-impact boundary conditions alter the structure of the impact map and can significantly complicate controller design.

The method of hybrid zero dynamics, as presented in [153] for the control of planar walking, assumed that any actuator dynamics were sufficiently fast that they could be neglected in the controller design process. The novel element of Chapters 7 and 8 is the extension of the hybrid zero dynamics framework to address unique aspects of stabilizing walking motions using actuators with nontrivial series compliance. Treating actuator dynamics in this framework will lead to reduced dimensionality stability tests for closed-loop walking gaits despite the increased degrees of underactuation that accompany compliant actuation.

See Figure 9.1 for a description of the class of robots considered in this chapter, along with a schematic diagram of a flexible actuator. One example of the pictured compliant mechanism is the MIT Series Elastic Actuator, which uses stiff springs and an inner-loop feedback controller to achieve reliable force control [112, 111]. Another, the AMASC (Actuator with Mechanically Adjustable Series Compliance) designed by Hurst [76], consists of a drive motor connected in series with a pair of large, variable stiffness springs. Unlike the MIT Series Elastic Actuator, the AMASC is designed to mechanically store significant amounts of energy that would otherwise be wasted when the actuator does negative work.

9.2 A Biped with Uniform Series Compliant Actuation

Recall that the model of walking for a class of rigid robots was derived in Chapter 4. To distinguish this previously derived rigid model from a compliant model (to be derived shortly) the additional subscript "r" will be appended to each term of the rigid walking model of Chapter 4, and a subscript "c" will be appended to each term of the compliant walking model. The stance phase dynamics of the rigid walker are now written as

$$D_{\mathrm{s},r}(q_{\mathrm{s},r})\ddot{q}_{\mathrm{s},r} + C_{\mathrm{s},r}(q_{\mathrm{s},r},\dot{q}_{\mathrm{s},r})\dot{q}_{\mathrm{s},r} + G_{\mathrm{s},r}(q_{\mathrm{s},r}) = B_{\mathrm{s},r}u \tag{9.1}$$

where the configuration vector $q_{\mathrm{s},r} = (q_{\mathrm{b}}, q_N)$, where q_{b} is the vector of actuated body coordinates and q_N is the unactuated global coordinate. This stance model is combined with a rigid impact model and is written as a system with impulse effects

$$\Sigma_{\mathrm{s},r} : \begin{cases} \dot{x}_{\mathrm{s,r}} &= f_{\mathrm{s},r}(x_{\mathrm{s},r}) + g_{\mathrm{s},r}(x_{\mathrm{s},r})u & x_{\mathrm{s},r}^- \notin \mathcal{S}_{\mathrm{s},r} \\ x_{\mathrm{s},r}^+ &= \Delta_{\mathrm{s},r}(x_{\mathrm{s},r}^-) & x_{\mathrm{s},r}^- \in \mathcal{S}_{\mathrm{s},r}. \end{cases} \tag{9.2}$$

Alternatively, this system with impulse effects can be written compactly as

$$\Sigma_{\mathrm{s},r} = \left(\mathcal{X}_{\mathrm{s},r}, \mathcal{S}_{\mathrm{s},r}, \emptyset, I\!R^{(N-1)}, \Delta_{\mathrm{s},r}, f_{\mathrm{s},r}, g_{\mathrm{s},r}\right). \tag{9.3}$$

To investigate the effects of introducing springs at each actuated joint, a second simulation model is constructed that is identical to the rigid one above, except for the presence of series springs separating each independent actuator from its associated joint. In this case the compliant robot's

stance phase dynamics can be written as

$$\begin{aligned} D_{\mathrm{s},r}(q_{\mathrm{s},r})\ddot{q}_{\mathrm{s},r} + C_{\mathrm{s},r}(q_{\mathrm{s},r},\dot{q}_{\mathrm{s},r})\dot{q}_{\mathrm{s},r} + G_{\mathrm{s},r}(q_{\mathrm{s},r}) &= B_{\mathrm{s},r}K(q_m - q_{\mathrm{b}}) \\ J\ddot{q}_m + K(q_m - q_{\mathrm{b}}) &= u. \end{aligned}$$

where the configuration vector $q_{\mathrm{s},c} = (q_{\mathrm{s},r}, q_m) = (q_{\mathrm{b}}, q_N, q_m)$ where q_{b} is the vector of indirectly actuated body coordinates, q_N is the unactuated global coordinate, and q_m is the vector corresponding to the angular coordinates of the motor shafts that wind and unwind the series springs. The stance phase model of a robot with compliance can be written alternatively as

$$D_{\mathrm{s},c}(q_{\mathrm{s},c})\ddot{q}_{\mathrm{s},c} + C_{\mathrm{s},c}(q_{\mathrm{s},c},\dot{q}_{\mathrm{s},c})\dot{q}_{\mathrm{s},c} + G_{\mathrm{s},c}(q_{\mathrm{s},c}) = B_{\mathrm{s},c}u \tag{9.4}$$

where the inertia matrix $D_{\mathrm{s},c}$, Coriolis terms $C_{\mathrm{s},c}$, and potential forces $G_{\mathrm{s},c}$ are related to their rigid counterparts by

$$\begin{aligned} D_{\mathrm{s},c}(q_{\mathrm{s},c}) &= \begin{bmatrix} D_{\mathrm{s},r}(q_{\mathrm{s},r}) & 0 \\ 0 & J \end{bmatrix} \\ C_{\mathrm{s},c}(q_{\mathrm{s},c},\dot{q}_{\mathrm{s},c}) &= \begin{bmatrix} C_{\mathrm{s},r}(q_{\mathrm{s},r},\dot{q}_{\mathrm{s},r}) & 0 \\ 0 & 0 \end{bmatrix} \\ G_{\mathrm{s},c}(q_{\mathrm{s},c}) &= \begin{bmatrix} G_{\mathrm{s},r}(q_{\mathrm{s},r}) - B_{\mathrm{s},r}K(q_m - q_{\mathrm{b}}) \\ K(q_m - q_{\mathrm{b}}) \end{bmatrix}. \end{aligned}$$

The impact map for the motor coordinates q_m and $\dot{q}_m$ is trivial to derive. Series springs, whose relative tension or compression is unchanged by the impulsive torques, isolate the actuation subsystem by exerting constant nonimpulsive force during the impact event. Neglecting coordinate relabeling, the impact map of the actuation subsystem is simply the identity map

$$(q_m^+, \dot{q}_m^+) = (q_m^-, \dot{q}_m^-).$$

The model of walking in a compliant robot can now be written as

$$\Sigma_{\mathrm{s},c} : \begin{cases} \dot{x}_{\mathrm{s,c}} = f_{\mathrm{s},c}(x_{\mathrm{s},c}) + g_{\mathrm{s},c}(x_{\mathrm{s},c})u & x_{\mathrm{s},c}^- \notin \mathcal{S}_{\mathrm{s},c} \\ x_{\mathrm{s},c}^+ = \Delta_{\mathrm{s},c}(x_{\mathrm{s},c}^-) & x_{\mathrm{s},c}^- \in \mathcal{S}_{\mathrm{s},c}. \end{cases} \tag{9.5}$$

Alternatively, this system can be written more compactly as

$$\Sigma_{\mathrm{s},c} = \left(\mathcal{X}_{\mathrm{s},c}, \mathcal{S}_{\mathrm{s},c}, \emptyset, I\!R^{(N-1)}, \Delta_{\mathrm{s},c}, f_{\mathrm{s},c}, g_{\mathrm{s},c}\right). \tag{9.6}$$

Remark 9.1. *In the derivation of dimension reducing controllers of Chapters 7 and 8, we only required that the impact map be some continuously differentiable function of the pre-impact state. In the case of walking in a biped with springs, the isolation effects of series compliance are beneficial from a standpoint of energy efficiency, but by no means necessary to achieve dimension reduction. Similarly, partial linearity of the velocity impact map, employed heavily in [153], is a property that has not been used in the derivation of HZD the controllers of Chapters 7 and 8.*

9.3 Model Properties

The following propositions highlight properties of the rigid model (9.3) and the compliant model (9.6) that are useful for comparing the processes of designing stabilizing controllers for walking motions in each of the models. For the following propositions let the unactuated coordinate q_N be relabeled as θ, and recall that quantity σ is the angular momentum of the robot about the ground contact point.

Proposition 9.2. *The stance phase models of the rigid and compliant robots have the following properties:*

a) the inertia matrices $D_{\mathrm{s},r}$ and $D_{\mathrm{s},c}$ of (9.1) *and* (9.4) *are independent of θ;*

b) the stance phase model for the rigid robot is feedback equivalent to

$$\begin{aligned} \dot{\sigma} &= -\frac{\partial V}{\partial \theta}(q) \\ \dot{\theta} &= \frac{\sigma}{d_{NN}(q_{\mathrm{b}})} + R(q_{\mathrm{b}})\dot{q}_{\mathrm{b}} \\ \ddot{q}_{\mathrm{b}} &= w, \end{aligned}$$

where V is the potential energy of the robot model, $d_{i,j}$ are the individual elements of D

$$R(q_{\mathrm{b}}) = -\left[\frac{d_{N,1}(q_{\mathrm{b}})}{d_{N,N}(q_{\mathrm{b}})}, \cdots, \frac{d_{N,N-1}(q_{\mathrm{b}})}{d_{N,N}(q_{\mathrm{b}})}\right];$$

and

c) the stance phase model for the compliant robot is feedback equivalent to

$$\begin{aligned}\dot{\sigma} &= -\frac{\partial V}{\partial \theta}(q)\\ \dot{\theta} &= \frac{\sigma}{d_{NN}(q_{\rm b})} + R(q_{\rm b})\dot{q}_{\rm b}\\ q_{\rm b}^{(4)} &= w.\end{aligned}$$

The proof and the required feedback are given in [61] and are based on [135, 117].

By Proposition 9.2, the compliant model is a dynamic extension of the rigid model, and hence by [78], the problem of designing controllers to zero outputs having a uniform vector relative degree is, from a theoretical perspective, no more difficult for the compliant model than for the rigid model. In particular, parts (a) and (b) of Proposition 9.2 show that if an output function $h(q)$ for the rigid model $\Sigma_{{\rm s},r}$ satisfies H7.7-i, H7.7-ii, and H7.7-iii of Corollary 7.8, then the same output function when used with the compliant model $\Sigma_{{\rm s},c}$ will also satisfy H7.7-i, H7.7-ii, and H7.7-iii of Corollary 7.8. Creating a forward invariant manifold is straightforward in each case.

Proposition 9.3. *Include the same smooth output function $y = h(q)$ in the rigid model $\Sigma_{{\rm s},r}$ and the compliant model $\Sigma_{{\rm s},c}$. Then the following hold,*

a) h has uniform vector relative degree two for the continuous portion of the rigid stance model (9.2) *if, and only if, it has uniform vector relative degree four for the continuous portion of the compliant stance model* (9.5)*;*

b) the decoupling matrices depend only on q and they are equal, that is $L_{g_{{\rm s},r}}L_{f_{{\rm s},r}}h = L_{g_{{\rm s},c}}L^3_{f_{{\rm s},c}}h$;

c) for $h(q) = q_{\rm b} - h_d(\theta)$, $\det(L_gL_fh)(q) = 1 - R(q_{\rm b})\frac{\partial h_d(\theta)}{\partial \theta}$;

d) if the output function $h(q) = q_{\rm b} - h_d(\theta)$ has uniform vector relative degree two for the continuous portion of the rigid stance model, then the zero dynamics manifold for the rigid model is

$$\mathcal{Z}_{{\rm s},r} = \left\{ (q,\dot{q}) \in \mathcal{X}_{{\rm s},r} \;\middle|\; q_{\rm b} = h_d(\theta),\ \dot{q}_{\rm b} = \frac{\partial h_d(\theta)}{\partial \theta}\dot{\theta} \right\} \tag{9.7}$$

and in the coordinates (θ,σ), the continuous phase of the restriction dynamics $\Sigma_{{\rm s},r}|_{\mathcal{Z}_{{\rm s},r}}$ is

$$\dot{\sigma} = \left.\frac{-\partial V}{\partial \theta}\right|_{q_{\rm b}=h_d(\theta)} \tag{9.8}$$

$$\dot{\theta} = \frac{\sigma}{\tilde{d}_{N,N}(\theta)}\left(1 - \tilde{R}(\theta)\frac{\partial h_d(\theta)}{\partial \theta}\right)^{-1}, \tag{9.9}$$

where, $\tilde{d}_{N,N}(\theta) = d_{N,N}|_{q_{\rm b}=h_d(\theta)}$ *and* $\tilde{R}(\theta) = R|_{q_{\rm b}=h_d(\theta)}$*;*

e) the zero dynamics manifold of the rigid stance phase model will be diffeomorphic to the zero dynamics manifold of the compliant stance phase model; and

f) when well-defined, the restriction dynamics of rigid stance phase model will be diffeomorphic to a well-defined restriction dynamics of the compliant stance phase model.

All parts of the above follow directly from Proposition 9.2 with the exception of part c) whose derivation requires the Sherman-Morrison-Woodbury formula [15].

9.4 An Application of Theorem 8.2 on Nonconstructive Extensions

The following procedure will be used to derive dimension reducing HZD controllers for the model of walking in a compliant robot:

1. Begin with the model of walking in a robot with compliance

$$\Sigma_{{\rm s},c} = \left(\mathcal{X}_{{\rm s},c}, \mathcal{S}_{{\rm s},c}, \emptyset, I\!R^{(N-1)}, \Delta_{{\rm s},c}, f_{{\rm s},c}, g_{{\rm s},c} \right).$$

2. Select an output function $h : \mathcal{X}_{{\rm s},c} \times \mathcal{A} \to I\!R^m$ and a parameter update function $\Delta_v : \mathcal{S}_{{\rm s},c} \to \mathcal{A}$ satisfying Hypotheses H8.3.

3. Form the open-loop and closed-loop deadbeat hybrid extensions of Theorem 8.2.

Motivated by Proposition 9.3 and [153], the output is selected as

$$y = h(q, \alpha) = q_{\rm b} - h_d \left(\frac{\theta - \theta_i}{\theta_f - \theta_i}, \alpha \right) \tag{9.10}$$

where $h_d : I\!R \times \mathcal{A} \to I\!R^4$ is a 4×1 vector of Bézier polynomials of degree seven.[1] The terms θ_i and θ_f are constants, equal to the values of θ at the beginning and end, respectively, of a steady state gait. For any choice[2] of $\alpha = (\alpha_0, \alpha_1, \alpha_2, \alpha_3) \in \mathcal{A} = I\!R^{4\times 4}$, the set of outputs (9.10) is relative

[1] Seventh degree Bézier polynomials have eight independent parameters. This can be shown to be the minimum number of free parameters needed to design the parameter update law and guarantee that $\mathcal{S}_e \cap \mathcal{Z}_{e,\alpha}$ is independent of α.

[2] Note that although the Bézier polynomials of $h(q, \alpha)$ each have 8 coefficients, only the first four components are treated by the parameter update function. The last four must remain constant—after the computation of a periodic orbit—so that $\mathcal{S}_e \cap \mathcal{Z}_{e,\alpha}$ is independent of α.

degree two with respect to the biped model without actuator dynamics, and so by Proposition 9.3 (a) is relative degree four with respect to the biped model with compliant actuation.

With $h_d(\theta, \alpha)$ selected as a Bézier polynomial, it can be shown that $\forall \alpha \in \mathcal{A}$, $\forall x_{\mathbf{e}} \in \Delta_{\mathbf{e}}(\mathcal{S}_{\mathbf{e}} \cap \mathcal{Z}_{\mathbf{e}})$,

$$\begin{aligned} h(x_e, \alpha) &= A_0(x_e)\alpha_0 + B_0(x_e) \\ L_f h(x_e, \alpha) &= A_1(x_e)\alpha_1 + B_1(x_e, \alpha_0) \\ L_f^2 h(x_e, \alpha) &= A_2(x_e)\alpha_2 + B_2(x_e, \alpha_0, \alpha_1) \\ L_f^3 h(x_e, \alpha) &= A_3(x_e)\alpha_3 + B_3(x_e, \alpha_0, \alpha_1, \alpha_2) \end{aligned} \tag{9.11}$$

with A_i's invertible. This property guarantees that there exists an impact update law Δ_v satisfying Hypothesis H8.3-v of Theorem 8.2. Hypotheses H8.3-iii and H8.3-iv are satisfied by noting that for a five-link biped without impact updated parameters or actuator dynamics, $\mathcal{S} \cap \mathcal{Z}$ is smooth and has dimension one less than $\mathcal{Z}$ [153], and that the same derivation applies as long as $\mathcal{S} \cap \mathcal{Z}_\alpha$ is independent of α. (Such independence has been established earlier by specifying that the last four coefficients of each Bézier polynomial are unaffected by the update law.) Hypothesis H8.3-i and H8.3-ii have already been established by Proposition 9.3. Thus, the conditions of Theorem 8.2 are met. To apply the theorem, form an open-loop deadbeat hybrid extension of the model with compliant actuation as

$$\Sigma_{\mathbf{e}} : \begin{cases} \dot{x}_{\mathbf{e}} = f_{\mathbf{e}}(x_{\mathbf{e}}) + g_{\mathbf{e}}(x_{\mathbf{e}})u & x_{\mathbf{e}}^- \notin \mathcal{S}_{\mathbf{e}} \\ x_{\mathbf{e}}^+ = \bar{\Delta}_{\mathbf{e}}(x_{\mathbf{e}}^-) & x_{\mathbf{e}}^- \in \mathcal{S}_{\mathbf{e}}, \end{cases} \tag{9.12}$$

with an output of

$$y = h_{\mathbf{e}}(x_{\mathbf{e}}) = q_{\mathrm{b}} - h_d\left(\frac{\theta - \theta_i}{\theta_f - \theta_i}, \alpha\right),$$

where (for Δ_v as implicitly defined above), $x_{\mathbf{e}} = (x_{\mathrm{s},c}, \alpha)$, $\mathcal{X}_{\mathbf{e}} = \mathcal{X}_{\mathrm{s},c} \times \mathcal{A}$, $\mathcal{S}_{\mathbf{e}} = \mathcal{S}_{\mathrm{s},c} \times \mathcal{A}$,

$$\begin{aligned} f_{\mathbf{e}}(x_{\mathbf{e}}) &= \begin{bmatrix} f_{\mathrm{s},c}(x_{\mathrm{s},c}) \\ 0 \end{bmatrix}, \\ g_{\mathbf{e}}(x_{\mathbf{e}}) &= \begin{bmatrix} g_{\mathrm{s},c}(x_{\mathrm{s},c}) \\ 0 \end{bmatrix}, \\ \bar{\Delta}_{\mathbf{e}}(x_{\mathbf{e}}^-) &= \begin{bmatrix} \Delta_{\mathrm{s},c}(x_{\mathrm{s},c}^-) \\ \Delta_v(x_{\mathrm{s},c}^-) \end{bmatrix}. \end{aligned}$$

In the context of this extended model, differentiating the output four times yields

$$y^{(4)} = L_{f_\mathbf{e}}^4 h_\mathbf{e}(x_\mathbf{e}) + L_{g_\mathbf{e}} L_{f_\mathbf{e}}^3 h_\mathbf{e}(x_\mathbf{e}) u,$$

where the domain of invertibility of the decoupling matrix, $L_{g_\mathbf{e}} L_{f_\mathbf{e}}^3 h_\mathbf{e}(x_\mathbf{e})$ is computable using Proposition 9.3 parts (b) and (c). The zero dynamics manifold associated with this output is

$$\mathcal{Z}_\mathbf{e} = \left\{ x_\mathbf{e} \in \mathcal{X}_\mathbf{e} \;\middle|\; \begin{array}{ll} h_\mathbf{e}(x_\mathbf{e}) = 0, & L_{f_\mathbf{e}} h_\mathbf{e}(x_\mathbf{e}) = 0, \\ L_{f_\mathbf{e}}^2 h_\mathbf{e}(x_\mathbf{e}) = 0, & L_{f_\mathbf{e}}^3 h_\mathbf{e}(x_\mathbf{e}) = 0 \end{array} \right\},$$

and is diffeomorphic to the zero dynamics manifold (9.7). The feedback

$$u^\epsilon(x_\mathbf{e}) = -\left(L_{g_\mathbf{e}} L_{f_\mathbf{e}}^{k-1} h_\mathbf{e}(x_\mathbf{e}) \right)^{-1} \left(\; L_{f_\mathbf{e}}^k h_\mathbf{e}(x_\mathbf{e}) + \textstyle\sum_{i=0}^{k-1} \frac{1}{\epsilon^{k-i}} K_i L_{f_\mathbf{e}}^i h_\mathbf{e}(x_\mathbf{e}) \; \right), \tag{9.13}$$

modified from (7.12) will render $\mathcal{Z}_\mathbf{e}$ invariant and exponentially attractive in the continuous phase of the closed-loop system. Note that this feedback is defined using a constant $\epsilon > 0$ that is tuned so that $\mathcal{Z}_\mathbf{e}$ can be made exponentially attractive with arbitrarily fast convergence. Applying the feedback (9.13) to the open-loop deadbeat hybrid extension (9.12) results in a closed-loop deadbeat hybrid extension

$$\bar{\Sigma}_\mathbf{e}^\epsilon : \left\{ \begin{array}{rcll} \dot{x}_\mathbf{e} & = & \bar{f}_\mathbf{e}^\epsilon(x_\mathbf{e}) & x_\mathbf{e}^- \notin \mathcal{S}_\mathbf{e} \\ x_\mathbf{e}^+ & = & \bar{\Delta}_\mathbf{e}(x_\mathbf{e}^-) & x_\mathbf{e}^- \in \mathcal{S}_\mathbf{e}, \end{array} \right. \tag{9.14}$$

denoted alternatively as

$$\bar{\Sigma}_\mathbf{e}^\epsilon = \left(\mathcal{X}_\mathbf{e}, \mathcal{S}_\mathbf{e}, \bar{\Delta}_\mathbf{e}, \bar{f}_\mathbf{e}^\epsilon \right).$$

To apply the stability test of Corollary 7.6 to the closed-loop deadbeat hybrid extension of (9.14), all that remains is to find a periodic orbit and a constant parameter vector for which the output function (9.10) is zeroed at every point of the orbit. This can be done quite efficiently on the basis of the HZD using an optimization technique developed in [151] for finding periodic orbits in the HZD subject to constraints on stability, torque, energy efficiency, ground friction, etc. Using this method, a gait was designed using MATLAB's `fmincon` function to achieve a forward progression rate of 0.8 m/s and to minimize an approximation of motor electrical energy consumed per distance traveled.

Figure 9.2 gives a stick animation of the sample gait. Values of θ below each frame show that θ is monotonically increasing within a stride. The percentage value indicates the amount of total

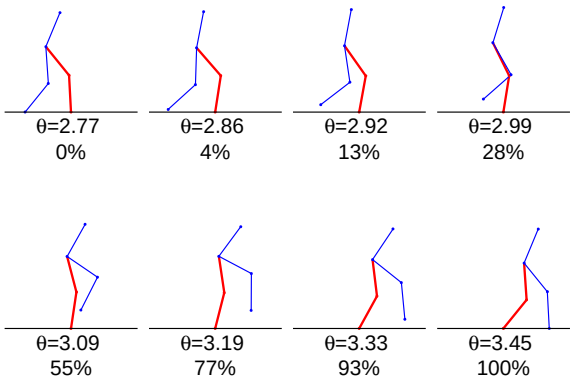

Figure 9.2: Stick figure of walking in a biped with compliance at 0.8 m/s. Values of θ are monotonically increasing.

step time elapsed, which has a nonlinear relationship with θ. Rotor angles for the sample motion are shown in Figure 9.3. As required by the impact model, values of rotor position and velocity are constant across the impact event, up to joint relabeling. Figure 9.4 illustrates one interpretation of Corollary 7.8, namely that while the feedback law of (9.13) will render $\mathcal{Z}_{\mathbf{e}}$ forward invariant and continuous phase exponentially attractive for any value of $\epsilon > 0$, only for ϵ sufficiently small does it render the manifold exponentially attractive in a hybrid sense. The reason is that for state values outside the zero dynamics manifold, application of the impact map will tend to push the state further away—an effect that can be overcome by sufficiently fast convergence in the continuous phase. This conclusion is reinforced in Figure 9.5, where the spectral radius of the Poincaré return map of the closed-loop system is plotted along with the eigenvalue of the return map associated with the HZD. Figure 9.6 then shows that the trajectories of the HZD converge to a periodic orbit.

9.5 An Application of Theorem 8.6 on Constructive Extensions

A numerical example is provided here to illustrate the application Theorem 8.6 to the task of stabilizing the same walking gait that was considered in the last section, the gait pictured in Figure 9.2. The procedure of Proposition 8.9 gives an explicit set of steps for constructing a closed-loop deadbeat hybrid extension having a Poincaré return map with favorable stability properties, allowing

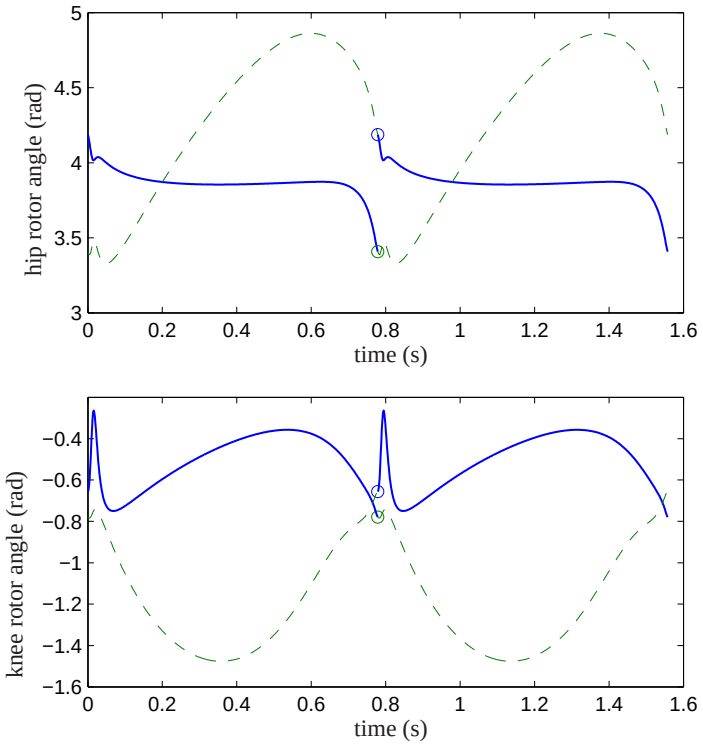

Figure 9.3: Values of the motor angles q_m along two cycles of the periodic orbit. Stance knee and hip rotors are plotted with a solid line, swing knee and hip rotors with a dashed line. Moments of impact are noted with a circle. Consistent with the impact model, rotor positions and velocities are continuous across the impact.

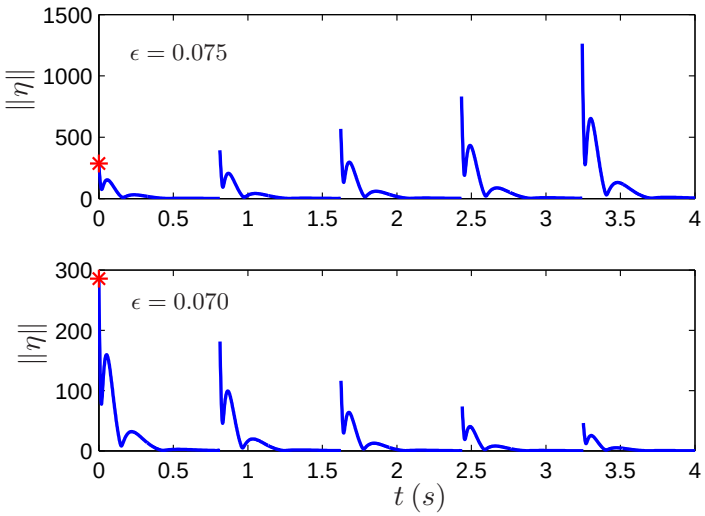

Figure 9.4: Behavior of the transverse dynamics for two values of ϵ. Under the feedback (7.12), for the choice of gains $K_0 = 1$, $K_1 = 4$, $K_2 = 6$, $K_3 = 4$, the zero dynamics manifold is attractive for $\epsilon = 0.070$ but not for $\epsilon = 0.075$. Plotted on the vertical axis is the euclidian norm of $\eta_{\mathbf{e}} = (h_{\mathbf{e}}(x_{\mathbf{e}}); L_{f_{\mathbf{e}}} h_{\mathbf{e}}(x_{\mathbf{e}}); L^2_{f_{\mathbf{e}}} h_{\mathbf{e}}(x_{\mathbf{e}}); L^3_{f_{\mathbf{e}}} h_{\mathbf{e}}(x_{\mathbf{e}}))$. The horizontal axis is time. The observed behavior is consistent with Corollary 7.8, where the zero dynamics manifold $\mathcal{Z}_{\mathbf{e}}$ is made exponentially attractive for sufficiently small ϵ with the feedback (7.12). Initial conditions for the two plots are the same and indicated by an asterisk.

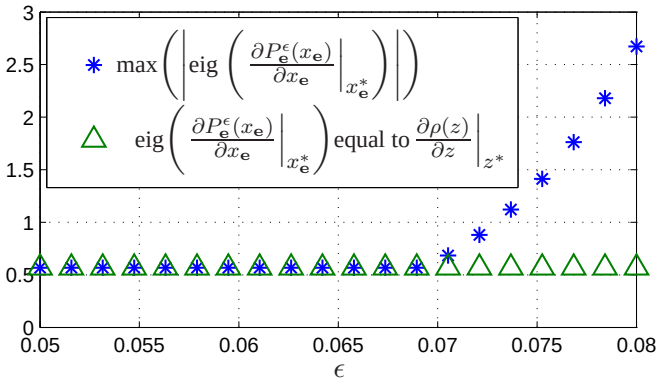

Figure 9.5: The dependence of closed-loop eigenvalues on the parameter ϵ. As ϵ approaches zero, one eigenvalue remains constant, equal to the eigenvalue of the hybrid zero dynamics $\partial\rho(z)/\partial z$, while all other eigenvalues go to zero. The eigenvalue associated with the 1 DOF HZD is 0.567.

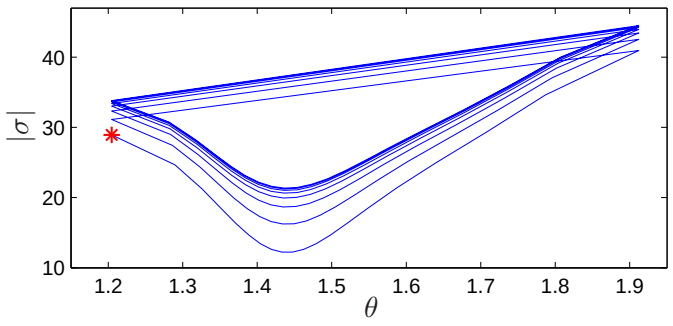

Figure 9.6: System response from a perturbation in initial condition. The initial condition (noted with an asterisk) lies within the hybrid zero dynamics but not on the periodic orbit. The state converges exponentially quickly back to the periodic orbit.

the stability test of Theorem 7.4 to be carried out on an orbit that is a trivial lift[3] of the original. For completeness, the steps are copied here with notation appropriate for the task of stabilizing walking in a compliant robot.

1. Begin with the open-loop model $\Sigma_{\mathrm{s},c} = \left(\mathcal{X}_{\mathrm{s},c}, \mathcal{S}_{\mathrm{s},c}, \emptyset, I\!R^{(N-1)}, \Delta_{\mathrm{s},c}, f_{\mathrm{s},c}, g_{\mathrm{s},c}\right)$.

2. Apply Theorem 8.6 with a parameter update function satisfying Hypotheses H8.8 to create an open-loop deadbeat hybrid extension

$$\Sigma_{\mathbf{e}}^{\lambda} = \left(\mathcal{X}_{\mathbf{e}}, \mathcal{S}_{\mathbf{e}}, \emptyset, \mathcal{U}, \bar{\Delta}_{\mathbf{e}}^{\lambda}, f_{\mathbf{e}}, g_{\mathbf{e}}\right).$$

3. Apply Corollary 7.8 to the open-loop deadbeat hybrid extension to produce a closed-loop deadbeat hybrid extension

$$\bar{\Sigma}_{\mathbf{e}}^{\epsilon,\lambda} = \left(\mathcal{X}_{\mathbf{e}}, \mathcal{S}_{\mathbf{e}}, \bar{\Delta}_{\mathbf{e}}^{\lambda}, \bar{f}_{\mathbf{e}}^{\epsilon}\right).$$

To prepare for the application of Theorem 8.6, choose the output

$$y = h(q, \beta) = q_{\mathrm{b}} - h_d(\theta, \beta),$$

where h_d is, as in the previous section, a 4×1 vector of seventh degree Bézier polynomials. With the polynomial coefficients β^*, the initial condition $x_0 \in \mathcal{X}_c$ and gait progression function

$$\tau(x) = \frac{\theta - \theta_i}{\theta_f - \theta_i}$$

[3] See Remark 8.4 for a definition of the trivial lift of an orbit.

satisfy the properties that

i) x_0 lies in a periodic orbit $\mathcal{O}$ of the system

$$\bar{\Sigma}_{\mathrm{s,c}} : \begin{cases} \dot{x}_{\mathrm{s,c}} &= f_{\mathrm{s},c}(x_{\mathrm{s},c}) + g_{\mathrm{s},c}(x_{\mathrm{s},c})u(x_{\mathrm{s},c}) & x_{\mathrm{s},c}^- \notin \mathcal{S}_{\mathrm{s},c} \\ x_{\mathrm{s},c}^+ &= \Delta_{\mathrm{s},c}(x_{\mathrm{s},c}^-) & x_{\mathrm{s},c}^- \in \mathcal{S}_{\mathrm{s},c}, \end{cases}$$

where

$$u(x_{\mathrm{s},c}) = -\left(L_{g_{\mathrm{s},c}} L_{f_{\mathrm{s},c}}^{k-1} h(x_{\mathrm{s},c}, \beta^*)\right)^{-1} \left(L_{f_{\mathrm{s},c}}^{k} h(x_{\mathrm{s},c}, \beta^*)\right);$$

ii) the outputs $y = q_{\mathrm{b}} - h_d(\tau(x), \beta^*)$ vanish on the orbit $\mathcal{O}$ and have uniform vector relative degree four in an open neighborhood of $\mathcal{O}$; and

iii) the function $\tau(x)$ is strictly monotonic on the orbit.

Thus, the orbit and output function satisfy Hypotheses H8.7. Apply Theorem 8.6 with a parameter update function satisfying Hypotheses H8.8 to create an open-loop deadbeat hybrid extension with an output

$$\Sigma_{\mathbf{e}}^{\lambda} : \begin{cases} \dot{x}_{\mathbf{e}} &= f_{\mathbf{e}}(x_{\mathbf{e}}) + g_{\mathbf{e}}(x_{\mathbf{e}})u & x_{\mathbf{e}}^- \notin \mathcal{S}_{\mathbf{e}} \\ x_{\mathbf{e}}^+ &= \bar{\Delta}_{\mathbf{e}}^{\lambda}(x_{\mathbf{e}}) & x_{\mathbf{e}}^- \in \mathcal{S}_{\mathbf{e}} \end{cases} \tag{9.15}$$

denoted alternatively as

$$\Sigma_{\mathbf{e}}^{\lambda} = \left(\mathcal{X}_{\mathbf{e}}, \mathcal{S}_{\mathbf{e}}, \emptyset, \mathcal{U}, \bar{\Delta}_{\mathbf{e}}^{\lambda}, f_{\mathbf{e}}, g_{\mathbf{e}}\right)$$

where $x_{\mathbf{e}} = (x_{\mathrm{s},c}, \alpha)$, $\mathcal{X}_{\mathbf{e}} = \mathcal{X}_{\mathrm{s},c} \times \mathcal{A}$, $\mathcal{S}_{\mathbf{e}} = \mathcal{S}_{\mathrm{s},c} \times \mathcal{A}$,

$$f_{\mathbf{e}}(x_{\mathbf{e}}) = \begin{bmatrix} f_{\mathrm{s},c}(x_{\mathrm{s},c}) \\ 0 \end{bmatrix},$$

$$g_{\mathbf{e}}(x_{\mathbf{e}}) = \begin{bmatrix} g_{\mathrm{s},c}(x_{\mathrm{s},c}) \\ 0 \end{bmatrix},$$

$$\bar{\Delta}_{\mathbf{e}}^{\lambda}(x_{\mathbf{e}}^-) = \begin{bmatrix} \Delta_{\mathrm{s},c}(x_{\mathrm{s},c}^-) \\ \Delta_{v}^{\lambda}(x_{\mathrm{s},c}^-) \end{bmatrix},$$

and where the parameter space $\mathcal{A}$ and a new output function $y = h_{\mathbf{e}}(x_{\mathbf{e}})$ are as defined in the proof of Theorem 8.6. As noted in the statement of Theorem 8.6, system (9.15) satisfies Hypotheses H7.7

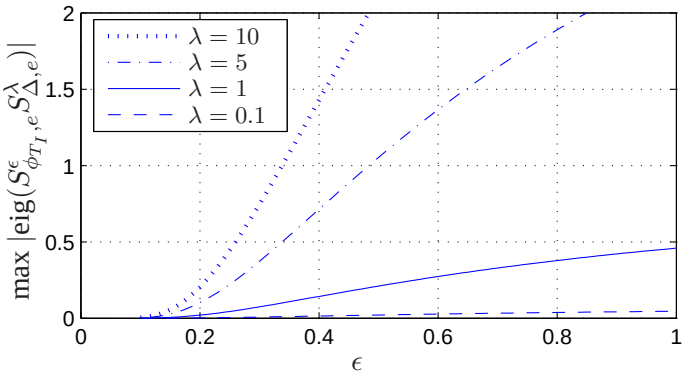

Figure 9.7: Effects of the controller parameters ϵ and λ on the transverse sensitivity matrices. As λ is held fixed and ϵ decreases to zero, the eigenvalues of the matrix product converge to zero. Similarly, as ϵ is held fixed and λ approaches zero, the eigenvalues converge to zero.

of Corollary 7.8. Using Corollary 7.8, form the autonomous system

$$\bar{\Sigma}^{\epsilon,\lambda}_{\mathbf{e}} : \begin{cases} \dot{x_{\mathbf{e}}} & = & \bar{f}^{\epsilon}_{\mathbf{e}}(x_{\mathbf{e}}) & x^{-}_{\mathbf{e}} \notin \mathcal{S}_{\mathbf{e}} \\ x^{+}_{\mathbf{e}} & = & \bar{\Delta}^{\lambda}_{\mathbf{e}}(x_{\mathbf{e}}{}^{-}) & x^{-}_{\mathbf{e}} \in \mathcal{S}_{\mathbf{e}} \end{cases} \tag{9.16}$$

where

$$\bar{f}_{\mathbf{e}}{}^{\epsilon}(x_{\mathbf{e}}) = f_{\mathbf{e}}(x_{\mathbf{e}}) + g_{\mathbf{e}}(x_{\mathbf{e}}) u^{\epsilon}(x_{\mathbf{e}}) \tag{9.17}$$

by applying the feedback

$$u^{\epsilon}(x_{\mathbf{e}}) = -\left(L_{g_{\mathbf{e}}} L^{k-1}_{f_{\mathbf{e}}} h_{\mathbf{e}}(x_{\mathbf{e}})\right)^{-1} \left(\begin{array}{l} L^{k}_{f_{\mathbf{e}}} h_{\mathbf{e}}(x_{\mathbf{e}}) + \sum_{i=0}^{k-1} \frac{1}{\epsilon^{k-i}} K_i L^{i}_{f_{\mathbf{e}}} h_{\mathbf{e}}(x_{\mathbf{e}}) \end{array} \right),$$

with $K_0 = 1$, $K_1 = 4$, $K_2 = 6$, $K_3 = 4$, to the open-loop deadbeat hybrid extension (9.16).

Figure 9.7 compares eigenvalues of the transverse sensitivity matrix

$$S^{\epsilon}_{\phi_{T_I},e}(\bar{z_{\mathbf{e}}}^{*}, \bar{\eta_{\mathbf{e}}}^{*}) S^{\lambda}_{\Delta,e}(z_{\mathbf{e}}{}^{*}, \eta_{\mathbf{e}}{}^{*})$$

of the closed-loop deadbeat hybrid extension at various values of ϵ and λ. As either ϵ or λ is held constant and the other approaches zero, the eigenvalues of the transverse sensitivity matrix converge to zero.[4] Once $\max |\text{eig}(S^{\epsilon}_{\phi_{T_I},e}(\bar{z_{\mathbf{e}}}^{*}, \bar{\eta_{\mathbf{e}}}^{*}) S^{\lambda}_{\Delta,e}(z_{\mathbf{e}}{}^{*}, \eta_{\mathbf{e}}{}^{*}))| < 1$, the stability of the periodic orbit is determined solely by the partial map $\rho_{\mathbf{e}}$ of (8.7), whose eigenvalues are unaffected by either ϵ or λ. For this example, the eigenvalues of the transverse sensitivity matrix are known in closed-form as

[4]Theory predicts that as long as $\lambda = 0$, stability of the transverse dynamics can be obtained any value of $\epsilon > 0$. Our simulations indicated that the region of attraction of the controller becomes vanishingly small when ϵ is large.

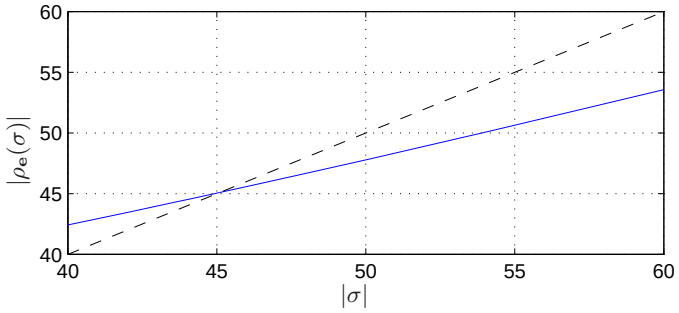

Figure 9.8: The restricted return map $\rho_{\mathbf{e}}$. The fixed point is located at the point where $\sigma = \rho_{\mathbf{e}}(\sigma)$, at approximately $|\sigma| = 45$ kg m^2/s. The slope at the fixed point is approximately 0.55, indicating that the discrete time system $\sigma_{k+1} = \rho_{\mathbf{e}}(\sigma_k)$ is locally exponentially stable. The dashed line is the identity map.

$S^{\epsilon}_{\phi_{T_I},e}(\bar{z_{\mathbf{e}}}^*, \bar{\eta_{\mathbf{e}}}^*) S^{\lambda}_{\Delta,e}(z_{\mathbf{e}}{}^*, \eta_{\mathbf{e}}{}^*) = \lambda e^{At^*/\epsilon}$, for t^* equaling the period of the orbit and the constant matrix

$$A = \begin{bmatrix} 0_{4\times4} & I_{4\times4} & 0_{4\times4} & 0_{4\times4} \\ 0_{4\times4} & 0_{4\times4} & I_{4\times4} & 0_{4\times4} \\ 0_{4\times4} & 0_{4\times4} & 0_{4\times4} & I_{4\times4} \\ -1\cdot I_{4\times4} & -4\cdot I_{4\times4} & -6\cdot I_{4\times4} & -4\cdot I_{4\times4} \end{bmatrix}. \tag{9.18}$$

The one nonzero eigenvalue unaffected by either ϵ or λ can be found as slope of $\rho_{\mathbf{e}}$ at the fixed point; see Figure 9.8.

For parameter choices of $\epsilon = 0.07$ and $\lambda = 1$, the magnitudes of the eigenvalues of the transverse sensitivity matrix are well below zero, the eigenvalues associated with parameter updates are identically zero (see (8.7)), and the eigenvalue of the partial map $\rho_{\mathbf{e}}$ is approximately equal to 0.55—indicating that the trivial lift $\mathcal{O}_{\mathbf{e}}$ is a stable periodic orbit in the closed-loop deadbeat hybrid extension $\bar{\Sigma}^{\epsilon,\lambda}_{\mathbf{e}}$. A visualization of convergence is given in Figure 9.9. The most important feature of this plot is that the parameters (i.e., α coordinates) are indeed constant within a stride, and stride-to-stride they converge to zero. In the figure, the initial condition is marked with an asterisk and the solution progresses from stride-to-stride in the direction of the arrow.

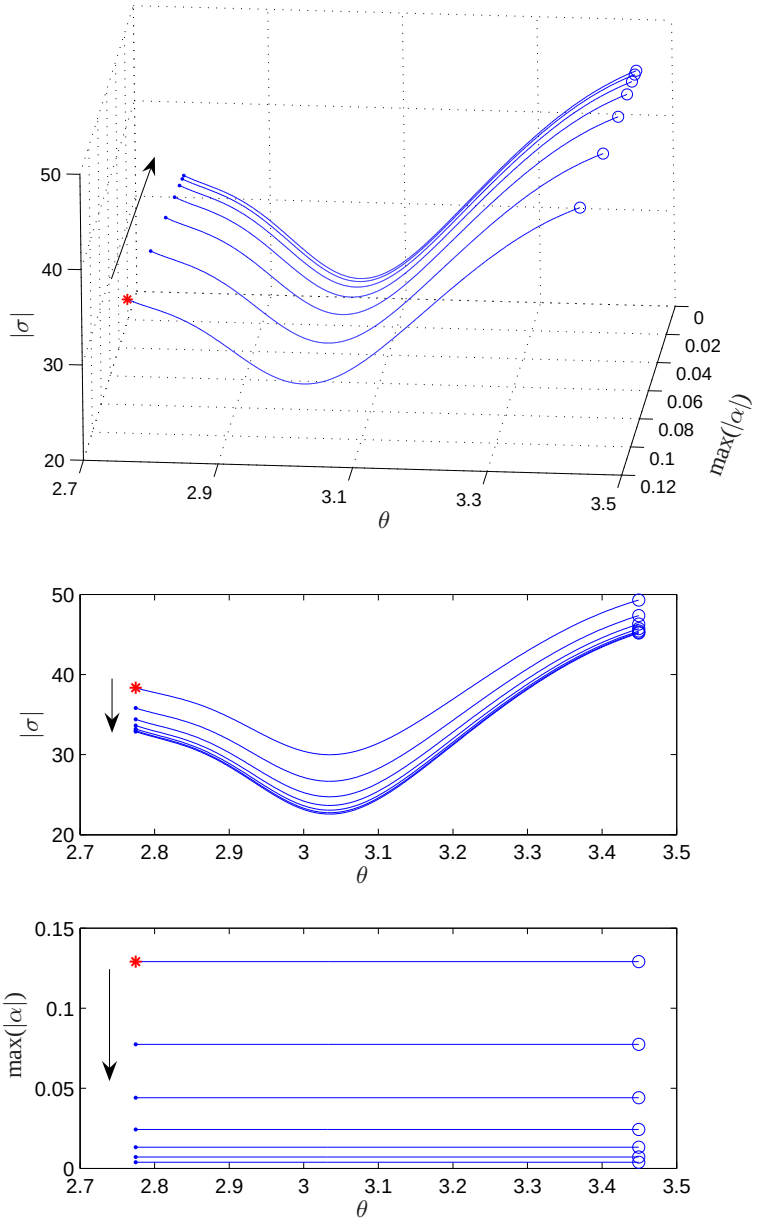

Figure 9.9: Projections of a solution converging back to the periodic orbit. Plots correspond to parameter values of $\epsilon = 0.07$ and $\lambda = 1$. The initial condition is marked with an asterisk. Within a given stride, values of α are constant and converge from step to step to $\alpha = 0$. The initial condition is marked as an asterisk in the different projections. The solution progresses stride-to-stride in the direction of the arrows.

9.6 Discussion

In an application of the results of previous chapters, this chapter carried out an extended simulation study on the use of smooth continuous phase controllers (of Chapter 7) and discrete parameter update schemes (of Chapter 8) to design an exponentially stabilizing controller for a periodic walking gait in a robot with series compliant actuation. Section 9.4 presented a set of steps demonstrating the use of Theorem 8.2 in the derivation of a nonconstructive deadbeat hybrid extension for achieving impact invariance, and Section 9.5 presented a second set of steps demonstrating the use of Theorem 8.6 in the constructive assembly of a deadbeat hybrid extension, also for the purpose of meeting impact invariance conditions. In order to carefully compare the uses of the theorems, the same gait was stabilized using both constructive and nonconstructive techniques.

Because the constructive technique of achieving impact invariance involves modification of the output function provided by the control designer, the controllers of Section 9.4 and Section 9.5 result in different zero dynamics manifolds and different hybrid zero dynamics. In the chosen example, the controller of Section 9.4 results in a 1 DOF hybrid zero dynamics with a Poincaré map having an eigenvalue of 0.567 while the controller of Section 9.5 results in a 1 DOF hybrid zero dynamics with a Poincaré map having an eigenvalue of 0.55. Similarly, different values of ϵ are required to stabilize the transverse dynamics, even when the nominal continuous phase gain matrix (9.18) is the same for both controllers. For the controller of Section 9.4, a value of $\epsilon = 0.075$ is insufficient to stabilize the transverse dynamics (in a hybrid sense). To contrast, for the controller of Section 9.5, the nominal values of $\lambda = 1$ and $\epsilon = 1$ result in a stable transverse dynamics. In order to provide more robustness to external disturbances, the constructive controller of Figure 9.9 is chosen to have $\epsilon = 0.07$.

In the general case, any modification of the output functions, either by Theorem 8.6 or otherwise, will result in changes in the stability properties of the hybrid zero dynamics. It has been observed that for planar walkers with a 1 DOF hybrid zero dynamics, the configuration at impact is by far the most dominant property affecting the eigenvalue of the resulting Poincaré map. This means that while changing the parameter update scheme used to achieve impact invariance may have some effect on the stability properties of the hybrid zero dynamics, as long as the configuration at impact remains the same, the effect will be minimal.

While this chapter has demonstrated the use of the theory of previous chapters in the design of stabilizing controllers for robots with compliant actuation, no investigation (either theoretical or computational) was made into the relative control effort of stabilization as compared to that of a robot without springs. It's known that in each case, decreasing the convergence parameter ϵ (equivalently, increasing the control gains to reject errors ever more aggressively) will result in transverse dynamics that are stable in the hybrid sense. In all likelihood, the introduction of springs could necessitate the need for higher gains (lower values of ϵ) to stabilize the resulting transverse dynamics. This could be seen as an acceptable tradeoff if the introduction of springs allowed significantly more efficient steady-state gaits to be found.

What is still unclear is the role that parameter augmentation could play in reducing the magnitude of the continuous phase control gains required to provide stability. As noted in Section 9.5, for the proposed parameter update scheme, when $\lambda = 0$ the value of ϵ can be arbitrarily large (equivalently, controller gains can be arbitrarily small) and the closed-loop system will still have transverse dynamics that are exponentially stable in the hybrid sense. In this case, the role of the controller gains could be similar to that proposed by Morris, Westervelt, and Farrell in [154], where control of the transverse dynamics is done *only* to increase the size of the basin of attraction and not to provide stability. Ultimately, the wisdom of including springs in a biped robot will be demonstrated or refuted in experiment, where electrical noise, signal delay, quantization, saturation, modeling error, and parameter mismatch will be the true test of a controller's stabilizing properties.

CHAPTER 10

Concluding Remarks

10.1 Summary of New Contributions

In light of experiments on RABBIT and in preparation for the new robot MABEL, this thesis has developed extensive new design tools that address the performance limiting aspects of previous HZD controllers. Such limitations included the requirement of "configuration determinism" at the landing event of running [31], the dependence of previous reduced-dimensionality stability tests on finite-time converging transverse dynamics [60, 153], and the potentially restrictive gait design procedure of [151] that prevented HZD control from being applied to gaits designed using other procedures—existing HZD techniques could do no better than to project the motion onto the closest member of a parameterized family of constraints. The use of transition functions[1], and a general trend toward the relaxation of previous controller hypotheses are features of this thesis that tie together the original contributions of Chapters 5 through 9.

As noted in Chapter 5, the property of "configuration determinism" at landing required by the HZD running controllers of [31] could not be met in the time alloted for experiments. The proposed solution was to use transition-on-landing controllers, also given in Chapter 5, to bring about stability under a similar dimension-reducing control scheme.

A key application of the new tools of Chapter 6 is the design of HZD controllers that render a passive bipedal gait robust to disturbances, without the use of full actuation, and while still requiring zero control effort at steady-state. The new tools can also be used to design controllers for gaits

[1]The transition functions of previous chapters are similar to those proposed by Westervelt et al in [152].

having an arbitrary steady-state torque profile. Other results of this chapter include the analysis of walking on a slope and the analysis of dynamic (decoupling matrix) singularities. Five examples are given showing how these new results support each other and extend the framework of hybrid zero dynamics.

Chapter 7 presents two new sets of hypotheses for autonomous systems with impulse effects, both of which lead to reduced dimensionality stability tests for periodic orbits lying in invariant manifolds with smooth transverse dynamics. The first set of hypotheses describes a special set of coordinates for which the linearization of the return map has a special upper triangular structure. With sufficiently rapid convergence of the transverse dynamics, all eigenvalues of the linearized return map are shown to converge to zero except those of the hybrid zero dynamics. The existence of a special set of coordinates simplifies the representation of the transverse dynamics and allows for a more direct computation of the linearization of the Poincaré map. The second set of hypotheses is a coordinate-free description of conditions that lead to the same upper triangular form. In practice, these coordinate-free hypotheses are easier to verify than their coordinate-specific counterparts.

The design of output functions that lead to invariance under the impact map is the topic of Chapter 8, where the novel use of parameter extensions allows the satisfaction of impact invariance hypotheses. The proposed parameter extensions are deadbeat, introducing no additional dynamic modes to the system, either discrete or continuous, stable or unstable. Two new theorems are given that rigorously describe the use of deadbeat hybrid extensions in achieving impact invariance. The method of the first theorem is nonconstructive and can be difficult to carry out in practice. Involving the use of spline-like transition functions, the method of the second theorem is constructive and should be significantly more straightforward to implement.

A capstone example showing a biped with uniform compliant actuation walking on flat ground ties together many of the new contributions of this thesis: the need for springs as motivated by Chapter 5, the transition polynomials of Chapter 6, the stability tests of Chapter 7, and the parameter augmentation of Chapter 8.

10.2 Perspectives on Future Work

Following the experimental and theoretical investigations reported in this thesis, two directions of future research are readily apparent: the opportunity for testing model-based controllers on the newly completed biped MABEL, and an opportunity to address problematic issues of computational complexity currently associated with gait design, symbolic controller derivation, and numeric controller deployment.

Construction of the mechanical portion of the five-link planar bipedal robot MABEL was recently completed by Jonathan Hurst of Carnegie Mellon University, under the supervision of Matt Mason and Al Rizzi. With final wiring yet to be performed, a significant amount of work will soon be put into developing and testing safety systems, calibrating sensors and actuators, and performing system identification experiments. Only after these steps are completed can meaningful model-based controllers be tested. Remaining hardware issues yet to be addressed include determining the working limits of motor and software performance; deriving model-based observers to estimate link velocities from encoder data; modeling and attenuating boom dynamics; and tuning the series springs to enhance dynamic performance. To successfully address these issues will require both mechanical insight and the support of computer simulations.

In the near future, problems of numerical conditioning and computational complexity could create a bottleneck in the process of SQP optimization that is currently used to design candidate walking and running gaits for stabilization by HZD controllers. This effect will become most pronounced when the nonuniform actuation of MABEL's joints are rigorously addressed in a theoretical framework. The decoupling matrix associated with imposing virtual constraints on MABEL could easily be an order of magnitude more complex than the equivalent decoupling matrix for RABBIT. Already, the decoupling matrix for the compliant model of Chapter 9 in its standard form of $L_g L_f^3 h(x)$ is far too complex to be computed in MATLAB's symbolic toolbox. Intermediate terms of this matrix, when output to a text file, can fill 10 to 100 megabytes of disk space. Numerical bottlenecks such as these must be addressed, whether in the authorship of more efficient software for symbolic derivation, or in a complexity-conscious revisitation of the theoretical foundations of hybrid zero dynamics.

As a theoretical framework, the paradigm of hybrid zero dynamics offers unparalleled versatility, mathematical rigor, and breadth of potential use. With this thesis containing the theoretical extensions necessary for encompassing walking in bipeds with compliance, attention can be turned toward the more physically motivated issues of experimentation on hardware and the development of efficient software. Research in these extensions will not be easy, but when completed could pay large dividends in the form of providing a clear path from the derivation of model-based controllers to their computationally efficient, low complexity, realtime implementation on the hardware of the newly constructed biped MABEL.

APPENDIX

APPENDIX A

Proofs

A.1 Proof of Theorem 3.1:

Method of Poincaré Sections for Systems with Impulse Effects

The equivalences for stability in the sense of Lyapunov and asymptotic stability are proven in [60, 103]. The equivalence for exponential stability is proven here. For a C^1 autonomous system with impulse effects having an orbit that is transversal to the impact surface, the function $T_I \circ \Delta$ is continuous in a neighborhood of x^* [60, App. B]. By the assumption that $\mathcal{S} \cap \Delta(\mathcal{S}) = \emptyset$, the post-impact time-to-next-impact function is strictly positive on all of $\mathcal{S}$, that is $T_I \circ \Delta(x) > 0$ for all $x \in \mathcal{S}$. By continuous differentiability of f it follows that there exists an open ball $\mathcal{B}_r(x^*),\ r > 0$, and strictly positive scalars T_* and T^* such that for every $x_0 \in \mathcal{B}_r(x^*) \cap \mathcal{S}$, $0 < T_* \leq T_I \circ \Delta(x_0) \leq T^* < \infty$, and $\forall x \in \Delta(\mathcal{B}_r(x^*))$, a solution to the autonomous system $\dot{x} = f(x)$ exists on $[0, T^*]$.

To show that ii) implies i) assume that $\mathcal{O}$ is an exponentially stable periodic orbit. If necessary, shrink $\delta > 0$ such that $Ne^{-\gamma T_*}\delta < r$ so that the return map will be well defined for all $x_0 \in \mathcal{B}_\delta(x^*) \cap \mathcal{S}$. Let $x_{k+1} = P(x_k),\ k \geq 0$. Then by induction $\|x_k - x^*\| \leq Ne^{-k\gamma T_*}\|x_0 - x^*\|$.

To show that i) implies ii) assume that x^* is an exponentially stable fixed point of P. Exponential stability of x^* implies stability i.s.L. of x^*, and the Method of Poincaré Sections for the case of stability i.s.L [60] further implies that $\mathcal{O}$ is stable i.s.L. Hence, there exists $\delta > 0$ such that dist$(x_0, \mathcal{O}) < \delta$ implies dist$(\varphi(t, x_0), \mathcal{O}) \leq r,\ t \geq 0$. Let $\mathcal{K} = \{x \in \mathcal{X} \mid \text{dist}(x, \bar{\mathcal{O}}) \leq r\}$. Since $\mathcal{K}$ is compact and f and Δ are differentiable, there exists a constant $\bar{L} < \infty$ such that $\|f(x) - f(\bar{x})\| \leq \bar{L}\|x - \bar{x}\|$, for all $x, \bar{x} \in \mathcal{K}$. And, $\|\Delta(x) - \Delta(\bar{x})\| \leq \bar{L}\|x - \bar{x}\|$, for all

$x, \bar{x} \in \mathcal{K} \cap \mathcal{S}$. Let $L = \bar{L}e^{\bar{L}T^*}$. Then, using standard bounds for the Lipschitz dependence of the solution of the autonomous system $\dot{x} = f(x)$ w.r.t. its initial condition [87, pp. 79], it follows that for $x \in \mathcal{B}_\delta(x^*) \cap \mathcal{S}$,

$$\sup_{0 \le t \le T_I \circ \Delta(x)} \text{dist}(\phi(t, \Delta(x)), \mathcal{O}) \le \sup_{0 \le t \le T^*} \|\phi(t, \Delta(x)) - \phi(t, \Delta(x^*))\| \le L\|x - x^*\|.$$

From this inequality, it follows easily that when x^* is an exponentially stable fixed point of P, the corresponding orbit $\mathcal{O}$ is exponentially stable.

A.2 Proof of Theorem 7.2

(Coordinate Dependent Reduced Dimensional Stability Test)

In the coordinates $x = (z, \eta)$, H7.1-iv implies that $x^* = (z^*, 0)$. Since $\bar{f}^\epsilon_{k+1:n}(0) = 0$, H7.1-v is equivalent to $\frac{\partial H}{\partial z}(z^*, 0)\bar{f}_{1:k}(z^*, 0) \neq 0$, which, writing $z = (z_1, \cdots, z_k)$, is equivalent to $\sum_{i=1}^k \frac{\partial H}{\partial z_i}(z^*, 0)\bar{f}_i(z^*, 0) \neq 0$. If necessary, the components of z can always be re-ordered so that

$$\frac{\partial H}{\partial z_1}(z^*, 0)\bar{f}_1(z^*, 0) \neq 0; \tag{A.1}$$

this will allow $(z_{2:k}, \eta)$, where $z_{2:k} = (z_2, \cdots, z_k)$, to be used as coordinates for $\mathcal{S}$. Indeed, (A.1) implies that $\frac{\partial H}{\partial z_1}(z^*, 0) \neq 0$, and hence by the Implicit Function Theorem, there exists a continuously differentiable scalar function Γ on an open neighborhood of x^* such that

$$(z_1, z_{2:k}, \eta) \in \mathcal{S} \Leftrightarrow z_1 = \Gamma(z_{2:k}, \eta).$$

It follows that

$$(z_1, z_{2:k}, \eta) \in \mathcal{S} \cap \mathcal{Z} \Leftrightarrow z_1 = \Gamma(z_{2:k}, 0) \text{ and } \eta = 0.$$

Letting $\hat{\Delta}$ be the representation of Δ in local coordinates on $\mathcal{S}$ gives

$$\hat{\Delta}(z_{2:k}, \eta) = \Delta(\Gamma(z_{2:k}, \eta), z_{2:k}, \eta).$$

Defining the projection π by

$$\pi(z_1, z_{2:k}, \eta) = (z_{2:k}, \eta), \tag{A.2}$$

then allows P^ϵ to be expressed in local coordinates $(z_{2:k}, \eta)$ on $\mathcal{S}$ by

$$\hat{P}^\epsilon(z_{2:k}, \eta) = \pi \circ \phi^\epsilon \left(T_I^\epsilon \circ \hat{\Delta}(z_{2:k}, \eta), \hat{\Delta}(z_{2:k}, \eta) \right).$$

Similarly, the restricted Poincaré map in local coordinates $z_{2:k}$ on $\mathcal{S} \cap \mathcal{Z}$ is given by

$$\hat{\rho}\left(z_{2:k}\right) = \pi_2 \circ \hat{P}^{\epsilon} \circ \mathcal{I}\left(z_{2:k}\right),$$

where

$$\pi_2(z_{2:k}, \eta) = z_{2:k}, \text{ and } \mathcal{I}\left(z_{2:k}\right) = (z_{2:k}, 0).$$

The remainder of the proof is broken down into three lemmas which together prove Theorem 7.2. The first involves the *trajectory sensitivity matrix* of $\dot{x} = \bar{f}^{\epsilon}(x)$, which is defined by[1]

$$\Phi^{\epsilon}(t, x_0) = \mathcal{D}_2 \phi^{\epsilon}(t, x_0)$$

for t in the maximal domain of existence of $\phi^{\epsilon}(t, x_0)$. Partition $\Phi^{\epsilon}(t, x_0)$ compatible with $(z_1, z_{2:k}, \eta)$, viz

$$\Phi^{\epsilon}(t, x_0) = \begin{bmatrix} \Phi^{\epsilon}_{11}(t, x_0) & \Phi^{\epsilon}_{12}(t, x_0) & \Phi^{\epsilon}_{13}(t, x_0) \\ \Phi^{\epsilon}_{21}(t, x_0) & \Phi^{\epsilon}_{22}(t, x_0) & \Phi^{\epsilon}_{23}(t, x_0) \\ \Phi^{\epsilon}_{31}(t, x_0) & \Phi^{\epsilon}_{32}(t, x_0) & \Phi^{\epsilon}_{33}(t, x_0) \end{bmatrix}.$$

Lemma A.1. *For all $x_0 \in \mathcal{Z}$, the entries of the sensitivity matrix $\Phi^{\epsilon}(t, x_0)$ satisfy:*

i) $\Phi^{\epsilon}_{31}(t, x_0) = \Phi^{\epsilon}_{32}(t, x_0) = 0$*;*

ii) $\Phi^{\epsilon}_{11}(t, x_0)$, $\Phi^{\epsilon}_{21}(t, x_0)$, $\Phi^{\epsilon}_{12}(t, x_0)$, *and* $\Phi^{\epsilon}_{22}(t, x_0)$ *are independent of* ϵ*; and*

iii) $\Phi^{\epsilon}_{33}(t, x_0) = e^{A(\epsilon)t}$.

Proof. The trajectory sensitivity matrix can be calculated as follows [106]:

$$\begin{Bmatrix} \dot{x} \\ \dot{\Phi} \end{Bmatrix} = \begin{Bmatrix} \bar{f}^{\epsilon}(x) \\ \mathcal{D}\bar{f}^{\epsilon}(x)\Phi \end{Bmatrix} \text{ with i.c. } \begin{Bmatrix} x_0 \\ I \end{Bmatrix}.$$

Hypothesis H7.1-i implies that for $i \in \{1, 2, 3\}$, $\mathcal{D}_i \bar{f}^{\epsilon}_{1:k}(z_1, z_{2:k}, \eta)$ is independent of ϵ and that $\mathcal{D}_1 \bar{f}^{\epsilon}_{k+1:n}(z_1, z_{2:k}, \eta) = 0$, $\mathcal{D}_2 \bar{f}^{\epsilon}_{k+1:n}(z_1, z_{2:k}, \eta) = 0$, and $\mathcal{D}_3 \bar{f}^{\epsilon}_{k+1:n}(z_1, z_{2:k}, \eta) = A(\epsilon)$. By the

[1] For a differentiable function $g(x_1, x_2, ..., x_p)$, the notation $\mathcal{D}_i g(y_1, y_2, ..., y_p)$ refers to $\partial g / \partial x_i$ evaluated at $(x_1, x_2, ..., x_p) = (y_1, y_2, ..., y_p)$. The argument x_i can be a vector. $\mathcal{D}g(y_1, ..., y_p)$ is $(\partial g/\partial x_1, \ldots, \partial g/\partial x_p)$ evaluated at $(x_1, ..., x_p) = (y_1, ..., y_p)$.

Peano-Baker formula, the trajectory sensitivity matrix satisfies

$$\Phi^\epsilon(t,x_0) = I + \int_0^t K^\epsilon(\tau_1,x_0)\,d\tau_1 +$$
$$\int_0^t \int_0^{\tau_1} K^\epsilon(\tau_1,x_0)K^\epsilon(\tau_2,x_0)\,d\tau_2 d\tau_1 +$$
$$\int_0^t \int_0^{\tau_1} \int_0^{\tau_2} K^\epsilon(\tau_1,x_0)K^\epsilon(\tau_2,x_0)K^\epsilon(\tau_3,x_0)\,d\tau_3 d\tau_2 d\tau_1 +$$
$$\cdots$$

where, since $x_0 \in \mathcal{Z}$, and $\mathcal{Z}$ is invariant under the solution of $\dot{x} = f^\epsilon(x)$,

$$K^\epsilon(t,x_0) = \mathcal{D}\bar{f}^\epsilon(x)|_{x=\phi_{\mathcal{Z}}(t,x_0)}.$$

Evaluating the expansion term-by-term then verifies the lemma. □

Lemma A.2. *Let $(z_1^*, z_{2:k}^*, \eta^*) = x^*$ represent the fixed point and $t^* = T_I^\epsilon \circ \hat{\Delta}(z_{2:k}^*, \eta^*)$ be the fundamental period of the periodic orbit $\mathcal{O}$. Then,*

$$\mathcal{D}\hat{P}^\epsilon(z_{2:k}^*, \eta^*) = \mathrm{C}(\mathrm{F}\mathrm{T} + \mathrm{Q})\mathrm{R}. \tag{A.3}$$

When partitioned compatibly with $(z_1, z_{2:k}, \eta)$, these matrices have the indicated structure[2]*:*

$$\mathrm{C} = \mathcal{D}\pi(z_1^*, z_{2:k}^*, \eta^*) = \begin{bmatrix} 0 & I & 0 \\ 0 & 0 & I \end{bmatrix} \tag{A.4a}$$

$$\mathrm{F} = \mathcal{D}_1\phi^\epsilon(t^*, \hat{\Delta}(z_{2:k}^*, \eta^*)) = \begin{bmatrix} \mathrm{F}_1 \\ \mathrm{F}_2 \\ 0 \end{bmatrix} \tag{A.4b}$$

$$\mathrm{T} = \mathcal{D}T_I^\epsilon(\hat{\Delta}(z_{2:k}^*, \eta^*)) = \begin{bmatrix} \mathrm{T}_1 & \mathrm{T}_2 & \mathrm{T}_3^\epsilon \end{bmatrix} \tag{A.4c}$$

$$\mathrm{Q} = \Phi^\epsilon(t^*, \hat{\Delta}(z_{2:k}^*, \eta^*)) = \begin{bmatrix} \mathrm{Q}_{11} & \mathrm{Q}_{12} & \mathrm{Q}_{13}^\epsilon \\ \mathrm{Q}_{21} & \mathrm{Q}_{22} & \mathrm{Q}_{23}^\epsilon \\ 0 & 0 & e^{A(\epsilon)t^*} \end{bmatrix} \tag{A.4d}$$

[2] For a related decomposition, using a slightly different structure, see [36].

$$\mathrm{R} = \mathcal{D}\hat{\Delta}(z^*_{2:k}, \eta^*) = \begin{bmatrix} \mathrm{R}_{11} & \mathrm{R}_{12} \\ \mathrm{R}_{21} & \mathrm{R}_{22} \\ 0 & \mathrm{R}_{32} \end{bmatrix}. \tag{A.4e}$$

Proof. Equation (A.3) follows from the chain rule, using

$$\begin{aligned}
(z^*_1, z^*_{2:k}, \eta^*) &= \phi^\epsilon(T^\epsilon_I \circ \hat{\Delta}(z^*_{2:k}, \eta^*), \hat{\Delta}(z^*_{2:k}, \eta^*)) \\
&= \phi_{\mathcal{Z}}(T_{I,\mathcal{Z}} \circ \hat{\Delta}(z^*_{2:k}, \eta^*), \hat{\Delta}(z^*_{2:k}, \eta^*)), \\
t^* &= T^\epsilon_I \circ \hat{\Delta}(z^*_{2:k}, \eta^*) \\
&= T_{I,\mathcal{Z}} \circ \hat{\Delta}(z^*_{2:k}, \eta^*), \\
\Phi^\epsilon(t^*, \hat{\Delta}(z^*_{2:k}, \eta^*)) &= \mathcal{D}_2\phi^\epsilon\left(t^*, \hat{\Delta}(z^*_{2:k}, \eta^*)\right).
\end{aligned}$$

The structure of C is immediate from the definition of π in (A.2). From [106, App. D], $F = \bar{f}^\epsilon(z^*_1, z^*_{2:k}, \eta^*)$, leading to $F_3 = 0$ because $\eta^* = 0$. Also from [106, App. D], T^ϵ_I is differentiable due to the transversality condition H7.1-v with

$$\mathcal{D}T^\epsilon_I(\hat{\Delta}(z^*_{2:k}, \eta^*)) = -(L_{\bar{f}^\epsilon}H(x^*))^{-1}\left(\frac{\partial H}{\partial x}(x^*)\right)^T \Phi^\epsilon(t^*, \hat{\Delta}(z^*_{2:k}, \eta^*)).$$

The structure of Q is given by Lemma A.1, and the form of R follows from H7.1-ii, namely, (7.2).

□

Lemma A.3. *At the fixed point x^*, the linearization of the Poincaré map is*

$$\mathcal{D}\hat{P}^\epsilon(z^*_{2:k}, \eta^*) = \begin{bmatrix} M_{11} & M^\epsilon_{12} \\ 0 & M^\epsilon_{22} \end{bmatrix}, \tag{A.5}$$

and the linearization of the restricted Poincaré map is

$$\mathcal{D}\hat{\rho}(z^*_{2:k}) = M_{11}, \tag{A.6}$$

where

$$\begin{aligned}
M_{11} &= (\mathrm{F}_2\mathrm{T}_1 + \mathrm{Q}_{21})\mathrm{R}_{11} + (\mathrm{F}_2\mathrm{T}_2 + \mathrm{Q}_{22})\mathrm{R}_{21}, \\
M^\epsilon_{12} &= (\mathrm{F}_2\mathrm{T}_1 + \mathrm{Q}_{21})\mathrm{R}_{12} + (\mathrm{F}_2\mathrm{T}_2 + \mathrm{Q}_{22})\mathrm{R}_{22} \\
&\quad + (\mathrm{F}_2\mathrm{T}^\epsilon_3 + \mathrm{Q}^\epsilon_{23})\mathrm{R}_{32}, \\
M^\epsilon_{22} &= e^{A(\epsilon)t^*}\mathrm{R}_{32}.
\end{aligned} \tag{A.7}$$

Proof. Multiplying out (A.3) using the structure in (A.4) proves (A.5). The second part follows because the Poincaré map leaves $\mathcal{S} \cap \mathcal{Z}$ invariant. In local coordinates, direct calculation yields

$$\begin{aligned} \mathcal{D}\hat{\rho}(z^*_{2:k}) &= \mathcal{D}\pi_2(z^*_{2:k}, \eta^*)\, \mathcal{D}\hat{P}^\epsilon(z^*_{2:k}, \eta^*)\, \mathcal{D}\mathcal{I}(z^*_{2:k}) \\ &= \begin{bmatrix} I & 0 \end{bmatrix} \begin{bmatrix} M_{11} & M^\epsilon_{12} \\ 0 & M^\epsilon_{22} \end{bmatrix} \begin{bmatrix} I \\ 0 \end{bmatrix} \\ &= M_{11}. \end{aligned}$$

□

The completion of the proof of Theorem 7.2 is as follows: Suppose that x^* is an exponentially stable fixed point of ρ. Then by (A.6), the eigenvalues of M_{11} have magnitude less than one. By H7.1-vi and (A.7), $\lim_{\epsilon \searrow 0} M^\epsilon_{22} = \lim_{\epsilon \searrow 0} e^{A(\epsilon)t^*} \mathrm{R}_{32} = 0$, and therefore, because eigenvalues depend continuously on the entries of the matrix, there exists $\bar{\epsilon} > 0$ such that for $0 < \epsilon < \bar{\epsilon}$, the eigenvalues of M^ϵ_{22} all have magnitude less than one, and hence, x^* is an exponentially stable fixed point of P^ϵ. The other direction of the proof is trivial.

A.3 Proof of Theorem 7.4 (Structure of the Linearized Return Map)

The (local) coordinate transform Γ represents elements of the submanifold $\mathcal{S} \cap \mathcal{Z}$ in *preferred coordinates*, so that[3] i) for any point[4] $x \in \mathcal{S} \cap \mathcal{Z} \cap U$, $\Gamma_2(x) = 0$, and ii) for any point $x \in \mathcal{S} \cap U$, $\Gamma^{-1}(\Gamma_1(x), 0) \in \mathcal{S} \cap \mathcal{Z} \cap U$. Similarly, the coordinate transform Ψ represents elements of $\mathcal{Z}$ in preferred coordinates: i) for any $x \in \mathcal{Z} \cap V$, $\Psi_2(x) = 0$, and ii) for any point $x \in V$, $\Psi^{-1}(\Psi_1(x), 0) \in \mathcal{Z} \cap V$. The coordinate transforms Γ and Ψ must exist by virtue of the fact that $\mathcal{S} \cap \mathcal{Z}$ and $\mathcal{Z}$ are embedded submanifolds. Conditions H7.3-ii and the transversality portion of H7.3-iii are sufficient conditions under which the return map is differentiable at the point x^*. Let $\hat{P}_1(z, \eta) = \Gamma_1 \circ P \circ \Gamma^{-1}(z, \eta)$ and $\hat{P}_2(z, \eta) = \Gamma_2 \circ P \circ \Gamma^{-1}(z, \eta)$ so that the Jacobian of the return

[3] Facts i) and ii) are properties easily derived from the definition of *preferred coordinates* in [20, p. 76].

[4] By definition, the domain U of Γ is a subset of $\mathcal{S}$ and thus $(U \cap \mathcal{S}) = U$. To emphasize this fact, we prefer to designate the domain of Γ as $(U \cap \mathcal{S})$.

map can be written as

$$\mathcal{D}\hat{P}(z,\eta) = \begin{bmatrix} \mathcal{D}_1\hat{P}_1(z,\eta) & \mathcal{D}_2\hat{P}_1(z,\eta) \\ \mathcal{D}_1\hat{P}_2(z,\eta) & \mathcal{D}_2\hat{P}_2(z,\eta) \end{bmatrix},$$

which, when evaluated at $(z^*,\eta^*) = \Gamma(x^*)$, reduces to (7.9). By H7.3-iii, the fixed point x^* lies within $\mathcal{Z}$, and as a consequence of property i) of Γ, $\eta^* = \Gamma_2(x^*) = 0$. By the definition of $\hat{P}_1$ above and ρ in (7.7), $\hat{P}_1(z,0) \equiv \rho(z)$, implying that $\mathcal{D}_1\hat{P}_1(z^*,\eta^*) = \mathcal{D}\rho(z^*)$ and proving the form of the upper left block of (7.9). The hypothesis on hybrid invariance, H7.3-i, is a sufficient condition for (7.4) and (by property i) of Γ) implies that $\hat{P}_2(z,0) = 0$ at all points $(z,0)$ of its domain. Differentiation with respect to the z coordinates gives $\mathcal{D}_1\hat{P}_2(z^*,\eta^*) = 0$, which is the lower left block of (7.9). Applying the chain rule[5] to the alternative form of the return map gives

$$\begin{aligned}
\mathcal{D}_2\hat{P}_2(z^*,\eta^*) &= \mathcal{D}_2(\Gamma_2 \circ \phi_{T_I} \circ \Delta \circ \Gamma^{-1})(z^*,\eta^*) \\
&= \mathcal{D}_2\left((\Gamma_2 \circ \phi_{T_I} \circ \Psi^{-1}) \circ (\Psi \circ \Delta \circ \Gamma^{-1})\right)(z^*,\eta^*) \\
&= \mathcal{D}_1(\Gamma_2 \circ \phi_{T_I} \circ \Psi^{-1})(\bar{z}^*,\bar{\eta}^*)\, \mathcal{D}_2(\Psi_1 \circ \Delta \circ \Gamma^{-1})(z^*,\eta^*) \\
&\qquad + \mathcal{D}_2(\Gamma_2 \circ \phi_{T_I} \circ \Psi^{-1})(\bar{z}^*,\bar{\eta}^*)\, \mathcal{D}_2(\Psi_2 \circ \Delta \circ \Gamma^{-1})(z^*,\eta^*).
\end{aligned}$$

Forward invariance of $\mathcal{Z}$ implies that $\mathcal{D}_1(\Gamma_2 \circ \phi_{T_I} \circ \Psi^{-1})(\bar{z}^*,\bar{\eta}^*) = 0$, leading to the expression $\mathcal{D}_2\hat{P}_2(z^*,\eta^*) = S_{\phi_{T_I}}(\bar{z}^*,\bar{\eta}^*)S_\Delta(z^*,\eta^*)$, which completes the derivation of the form (7.9).

Lemma A.4. *Suppose that for some $r > 0$, $F : B_r(0) \to \mathbb{R}^n$ satisfies*

i) $\exists L < \infty$ such that $\forall x \in B_r(0),\ \|F(x)\| \le L\|x\|$; and

ii) F is continuously differentiable at every point in $B_r(0)$.

Then, $\|\partial F(0)/\partial x\|_i \le L$ where $\|\cdot\|_i$ is the induced norm.

Proof. By ii) and Taylor's theorem, $F(x) = F(0) + (\partial F(0)/\partial x)x + R(x)$ where $\lim_{x\to 0} \|R(x)\|/\|x\| = 0$. By i), $F(0) = 0$ and $\|(\partial F(0)\partial x)\ x + R(x)\| = \|F(x)\| \le L\|x\|$. By compactness of closed unit balls in $\mathbb{R}^n$, there exists $\bar{x}$ such that $\|(\partial F(0)/\partial x)\ \bar{x}\| = \|(\partial F(0)/\partial x)\|_i$ and $\|\bar{x}\| = 1$. Letting $x = \delta\bar{x}$, for any value of $\delta > 0$, $\|\,(\partial F(0)/\partial x)\,(\delta\bar{x}/\|\delta\bar{x}\|)$ $+ (R(\delta\bar{x})/\|\delta\bar{x}\|)\,\| = \|(\partial F(0)/\partial x)\ \bar{x} + (R(\delta\bar{x})/\|\delta\bar{x}\|)\| \le L$. It follows that $\lim_{\delta\searrow 0} \|(\partial F(0)/\partial x)\,\bar{x} + (R(\delta\bar{x})/\|\delta\bar{x}\|)\| = \|(\partial F(0)/\partial x)\|_i$ and hence $\|(\partial F(0)/\partial x)\|_i \le L$. □

[5]For any differentiable functions $F_1 : \mathbb{R}^m \times \mathbb{R}^n \to \mathbb{R}^u$, $F_2 : \mathbb{R}^m \times \mathbb{R}^n \to \mathbb{R}^v$, $F(x_1,x_2) = (F_1(x_1,x_2), F_2(x_1,x_2))$, and $G : \mathbb{R}^u \times \mathbb{R}^v \to \mathbb{R}^p$, application of the chain rule shows that $\mathcal{D}_2(G \circ F)(x_1,x_2) = \mathcal{D}_1G \cdot \mathcal{D}_2F_1 + \mathcal{D}_2G \cdot \mathcal{D}_2F_2$.

Remark A.5. *Any parameterized function* $F^\epsilon : B_{r(\epsilon)}(0) \to I\!R^n,\ \ r(\epsilon) > 0$ *that satisfies*

i) for each $\epsilon > 0$, $F^\epsilon(0) = 0$*;*

ii) for each $\epsilon > 0$*, there exists* $\delta(\epsilon) > 0$ *such that* $F^\epsilon(x)$ *is continuously differentiable on* $B_{\delta(\epsilon)}(0)$*; and*

iii) $\|F^\epsilon(x)\| \leq L(\epsilon)\|x\|$ *with* $\lim_{\epsilon \searrow 0} L(\epsilon) = 0$*,*

must (by Lemma A.4) have the property that $\lim_{\epsilon \searrow 0} \left\| \frac{\partial F^\epsilon}{\partial x}(0) \right\|_i = 0.$

A.4 Proof of Corollary 7.8

(Coordinate Independent Reduced Dimensional Stability Test)

The first claim of the corollary is trivial to prove: the system $\bar{\Sigma}^\epsilon$ restricted to the hybrid invariant manifold $\mathcal{Z}$ is independent of ϵ. By H7.5-i and H7.5-ii, the manifold $\mathcal{Z}$ is independent of ϵ and so is the vector field $\bar{f}^\epsilon|_{\mathcal{Z}}$. For the second claim of the corollary, the Method of Poincaré Sections is used to establish a relationship between the eigenvalues of the Jacobian of a Poincaré map and the stability of the underlying orbit. Because they are unaffected by coordinate transforms, the eigenvalues of $\mathcal{D}P^\epsilon(x^*)$ are equal to the eigenvalues of $\mathcal{D}\hat{P}^\epsilon(z^*, \eta^*)$. As shown in Theorem 7.4, the matrix $\mathcal{D}\hat{P}^\epsilon(z^*, \eta^*)$ is block upper triangular for all values of ϵ, and therefore

$$\text{eig}(DP^\epsilon(x^*)) = \text{eig}(\mathcal{D}\rho(z^*)) \cup \text{eig}(S^\epsilon_{\phi_{T_I}}(\bar{z}^*, \bar{\eta}^*) S_\Delta(z^*, \eta^*)).$$

Assume that $\lim_{\epsilon \searrow 0} S^\epsilon_{\phi_{T_I}}(\bar{z}^*, \bar{\eta}^*) = 0$ (a fact to be proven below). In this case, for ϵ sufficiently small, the maximum eigenvalue of $\mathcal{D}P^\epsilon(x^*)$ is equal to the maximum eigenvalue of $\mathcal{D}\rho(z^*)$, and by the Method of Poincaré Sections, the orbit $\mathcal{O}$ is exponentially stable in the full system $\bar{\Sigma}^\epsilon$ if and only if the same orbit is exponentially stable in the restricted system $\bar{\Sigma}_{\mathcal{Z}}$.

To show that $\lim_{\epsilon \searrow 0} S^\epsilon_{\phi_{T_I}}(\bar{z}^*, \bar{\eta}^*) = 0$, invoke the convergence property of H7.5-iii in the application of Taylor's theorem in Lemma A.4. To start, note that the function Γ is differentiable and therefore locally Lipschitz continuous. That is, there exists $L_\Gamma > 0$ such that for all x in an open neighborhood of $U \cap \mathcal{S}$ containing the point x^*,

$$\begin{aligned} \text{dist}(x, \mathcal{Z}) = \inf_{y \in \mathcal{Z}} \|x - y\| &\geq \inf_{y \in \mathcal{Z}} \tfrac{1}{L_\Gamma} \|\Gamma(x) - \Gamma(y)\| \\ &= \inf_{y \in \mathcal{Z}} \tfrac{1}{L_\Gamma} \|(\Gamma_1(x), \Gamma_2(x)) - (\Gamma_1(y), 0)\|. \end{aligned} \tag{A.8}$$

The last line in the above is obtained using property i) of the preferred coordinates given by Γ (as used in the proof of Theorem 7.4). By property ii) of Γ, $\forall x \in U \cap \mathcal{S}, \Gamma^{-1}(\Gamma_1(x), 0) \in U \cap \mathcal{S} \cap \mathcal{Z}$. Stated differently, $\forall x \in U \cap \mathcal{S}, \exists\, y \in U \cap \mathcal{S} \cap Z$ such that $\Gamma_1(x) = \Gamma_1(y)$. Applying this to the last line of (A.8) shows that

$$\text{dist}(x, \mathcal{Z}) \geq \tfrac{1}{L_\Gamma} \|(\Gamma_1(x), \Gamma_2(x)) - (\Gamma_1(x), 0)\| = \tfrac{1}{L_\Gamma} \|\Gamma_2(x)\|. \tag{A.9}$$

Next, by the triangle inequality, for any x_0 in an open neighborhood of V containing $\Delta(x^*)$,

$$\text{dist}(x_0, \mathcal{Z}) \leq \|x_0 - \Psi^{-1}(\Psi_1(x_0), 0)\|.$$

Writing x_0 as the identity $x_0 = \Psi^{-1}(\Psi_1(x_0), \Psi_2(x_0))$ gives

$$\begin{aligned} \text{dist}(x_0, \mathcal{Z}) &\leq \|\Psi^{-1}(\Psi_1(x_0), \Psi_2(x_0)) - \Psi^{-1}(\Psi_1(x_0), 0)\| \\ &\leq L_{\Psi^{-1}} \|(\Psi_1(x_0), \Psi_2(x_0)) - (\Psi_1(x_0), 0)\| = L_{\Psi^{-1}} \|\Psi_2(x_0)\|, \end{aligned} \tag{A.10}$$

for some finite $L_{\Psi^{-1}} > 0$ (as Ψ^{-1} is also locally Lipschitz).

Recall the following facts: $\Delta(x^*)$ lies within the open set V; for every $\epsilon > 0$, $\phi_{T_I}^\epsilon(\Delta(x^*)) = x^*$ lies within the open set $U \cap S$; and for every $\epsilon > 0$, $\Delta(x^*)$ lies within the open set $B_\delta(\Delta(x^*))$ for δ from H7.5-iii. The function Δ is continuous, as is $\phi_{T_I}^\epsilon$ for each value of $\epsilon > 0$. Thus, for every $\epsilon > 0$ there exists $\mu > 0$ such that $B_\mu(\Delta(x^*)) \subset V$, $\phi_{T_I}^\epsilon(B_\mu(\Delta(x^*))) \subset (U \cap \mathcal{S})$, and $\mu < \delta$. Together, (A.9), (A.10), and H7.5-iii imply that $\forall x_0 \in B_\mu(\Delta(x^*))$

$$\tfrac{1}{L_\Gamma} \|\Gamma_2 \circ \phi_{T_I}^\epsilon(x_0)\| \leq \text{dist}(\phi_{T_I}^\epsilon(x_0), \mathcal{Z}) \leq K(\epsilon)\, \text{dist}(x_0, \mathcal{Z}) \leq K(\epsilon)\, L_{\Psi^{-1}} \|\Psi_2(x_0)\|.$$

Setting $(\bar{z}, \bar{\eta}) = \Psi(x_0)$ leads to $\|\Gamma_2 \circ \phi_{T_I}^\epsilon \circ \Psi^{-1}(\bar{z}, \bar{\eta})\| \leq L_\Gamma L_{\Psi^{-1}} K(\epsilon) \|\bar{\eta}\|$. The periodic orbit $\mathcal{O}$ is contained in $\mathcal{Z}$ and thus for all $\epsilon > 0$, $\eta^* = (\Gamma_2 \circ \phi_{T_I}^\epsilon \circ \Psi^{-1})(\bar{z}^*, \bar{\eta}^*) = 0$. Thus, the function $(\Gamma_2 \circ \phi_{T_I}^\epsilon \circ \Psi^{-1})(\bar{z}^*, \bar{\eta}^*)$ meets the criteria of Lemma A.4 and Remark A.5, which imply that $\lim_{\epsilon \searrow 0} \mathcal{D}_2(\Gamma_2 \circ \phi_{T_I}^\epsilon \circ \Psi^{-1})(\bar{z}^*, \bar{\eta}^*) = 0$, or, equivalently $\lim_{\epsilon \searrow 0} S_{\phi_{T_I}}^\epsilon(\bar{z}^*, \bar{\eta}^*) = 0$, which was to be shown.

A.5 Proof of Corollary 7.8

(Feedback Design for Reduced Dimension Stability Testing)

Forward invariance and the submanifold property of $\mathcal{Z}$ follow from applying the general results of [78, Ch.5] to the drift and control vector fields of Σ. Condition H7.5-i of Corollary 7.6 is trivially

satisfied because ϵ does not participate in the definition of $\mathcal{Z}$. Similarly, the feedback (7.12) is independent of ϵ on the manifold $\mathcal{Z}$ and therefore the closed-loop flow $f(x) + g(x)u^\epsilon(x)$ when restricted to $\mathcal{Z}$ is independent of ϵ.

Under the feedback (7.12), the manifold $\mathcal{Z}$ is exponentially attractive with ϵ-dependant convergence parameters c and γ satisfying[6] $\forall\, 0 \le t < T_I^\epsilon(x_0)$ dist$(\phi^\epsilon(t, x_0), \mathcal{Z}) \le c(\epsilon)e^{-\gamma(\epsilon)t}$dist$(x_0, \mathcal{Z})$ and $\lim_{\epsilon \searrow 0} c(\epsilon)e^{-\gamma(\epsilon)} = 0$. For a given $\epsilon > 0$, choose $\delta > 0$ such that ${\phi_{T_I}}^\epsilon(x_0)$ exists for all x_0 in the *closed* ball $\bar{B}_\delta(\Delta(x^*))$. On this compact set, the differentiable function $T_I^\epsilon(x)$ achieves a minimum value. If necessary, further restrict δ so that this minimum value is strictly greater than one half of the period t^* of the orbit $\mathcal{O}$. Then for the chosen ϵ and corresponding δ, each x_0 in the *open* ball $B_\delta(\Delta(x^*))$ satisfies dist$({\phi_{T_I}}^\epsilon(x_0), \mathcal{Z}) \le c(\epsilon)e^{-\gamma(\epsilon)T_I^\epsilon(x_0)}$dist$(x_0, \mathcal{Z}) \le c(\epsilon)e^{-\gamma(\epsilon)\frac{1}{2}t^*}$dist$(x_0, \mathcal{Z})$. Define $K(\epsilon) = c(\epsilon)e^{-\gamma(\epsilon)\frac{1}{2}t^*}$. Then for each value of $\epsilon > 0$ there exists $\delta > 0$ such that for all $x_0 \in B_\delta(\Delta(x^*))$, dist$(\phi_{T_I}^\epsilon(x_0), \mathcal{Z}) \le K(\epsilon)$ dist$(x_0, \mathcal{Z})$, with $\lim_{\epsilon \searrow 0} K(\epsilon) = 0$. Thus Hypothesis H7.5-iii of Corollary 7.6 is satisfied, completing the proof of Corollary 7.8.

A.6 Proof of Theorem 8.2

(Invariance by Nonconstructive Deadbeat Hybrid Extension)

Hypotheses H8.3-i and H8.3-ii imply two things: that $\forall \alpha \in \mathcal{A}$ the continuous part of (8.4) has a well-defined, zero dynamics manifold[7] $\mathcal{Z}_\alpha$, and that the continuous portion of (8.5) has a well-defined zero dynamics manifold, denoted temporarily by $\tilde{\mathcal{Z}}$. Again using H8.3-ii, it follows that $\tilde{\mathcal{Z}} = \cup_{\alpha \in \mathcal{A}}(\mathcal{Z}_\alpha, \alpha)$, and hence the set $\tilde{\mathcal{Z}} = \mathcal{Z}_{\mathbf{e}}$ is a zero dynamics manifold of the continuous portion of (8.5). Next, note that by Hypothesis H8.3-iii,

$$\begin{aligned}
\mathcal{Z}_{\mathbf{e}} \cap (\mathcal{S} \times \mathcal{A}) &= (\cup_{\alpha \in \mathcal{A}}(\mathcal{Z}_\alpha, \alpha)) \cap (\cup_{\alpha \in \mathcal{A}}(\mathcal{S}, \alpha)) \\
&= \cup_{\alpha \in \mathcal{A}} (\mathcal{S} \cap \mathcal{Z}_\alpha, \alpha) \\
&= \cup_{\alpha \in \mathcal{A}} (\mathcal{S} \cap \mathcal{Z}, \alpha) \\
&= (\mathcal{S} \cap \mathcal{Z}) \times \mathcal{A},
\end{aligned}$$

[6] As specified earlier, the initialization time for $\phi(t, x_0)$ is always assumed to be $t_0 = 0$.

[7] This does not imply that there exists a value of α for which $\mathcal{Z}_\alpha$ is a hybrid zero dynamics manifold of (8.4). No such value for α need exist.

establishing part b) of the theorem. This and Hypothesis H8.3-iv imply that $\mathcal{Z}_{\mathbf{e}} \cap (\mathcal{S} \times \mathcal{A})$ is a C^∞ submanifold of $\mathcal{X} \times \mathcal{A}$, and has dimension one less than $\mathcal{Z}_{\mathbf{e}}$. By Hypothesis H8.3-v, $\mathcal{Z}_{\mathbf{e}} \cap (\mathcal{S} \times \mathcal{A})$ is invariant under the impact map of (8.5). It follows that (8.5) has an HZD with zero dynamics manifold $\mathcal{Z}_{\mathbf{e}}$, proving part a) of the theorem. The corresponding restriction dynamics of (8.5) is

$$\bar{\Sigma}\big|_{\mathcal{Z}_{\mathbf{e}}} : \begin{cases} (\dot{z}, \dot{\alpha}) &= (\bar{f}|_{\mathcal{Z}_{\mathbf{e}}}(z, \alpha), 0) & (z^-, \alpha^-) \notin (\mathcal{S} \cap \mathcal{Z}) \times \mathcal{A} \\ (z^+, \alpha^+) &= (\Delta|_{\mathcal{S} \cap \mathcal{Z}}(z^-), \Delta_1|_{\mathcal{S} \cap \mathcal{Z}}(z^-)) & (z^-, \alpha^-) \in (\mathcal{S} \cap \mathcal{Z}) \times \mathcal{A} \end{cases}$$

from which the form of the Poincaré map is immediate, thus proving part c).

A.7 Proof of Theorem 8.6

(Impact Invariance by Construction)

This section constructs the open-loop deadbeat hybrid extension

$$\Sigma_{\mathbf{e}}{}^{\lambda} = \left(\mathcal{X}_{\mathbf{e}}, \mathcal{S}_{\mathbf{e}}, \emptyset, \mathcal{U}, \bar{\Delta}_{\mathbf{e}}^{\lambda}, f_{\mathbf{e}}, g_{\mathbf{e}}\right)$$

and output function $y_{\mathbf{e}} = h_{\mathbf{e}}(x_{\mathbf{e}})$ used in the proof of Theorem 8.6. A proof of the theorem is then given. To begin the construction of $y_{\mathbf{e}} = h_{\mathbf{e}}(x_{\mathbf{e}})$, choose any function $B : \mathbb{R} \times \mathbb{R}^{mk} \to \mathbb{R}^m$ satisfying the properties[8]

i) for any $b = (b_0, \ldots, b_{k-1})$, $b_0, \ldots, b_{k-1} \in \mathbb{R}^m$

$$B(s,b)|_{s=0} = b_0, \tfrac{\partial}{\partial s}B(s,b)|_{s=0} = b_1, \ldots, \tfrac{\partial^{k-1}}{\partial s^{k-1}}B(s,b)|_{s=0} = b_{k-1};$$

ii) for any $b = (b_0, \ldots, b_{k-1})$, $b_0, \ldots, b_{k-1} \in \mathbb{R}^m$

$$B(s,b)|_{s=1} = 0, \tfrac{\partial}{\partial s}B(s,b)|_{s=1} = 0, \ldots, \tfrac{\partial^{k}}{\partial s^{k}}B(s,b)|_{s=1} = 0;$$

iii) $\forall s \in \mathbb{R}, B(s,0) \equiv 0$;

iv) $\forall b \in \mathbb{R}^{mk}$, the function $B(s,b)$ is C^{k+1} in s; and

v) $\forall s \in \mathbb{R}$, each of the functions $B(s,b), \frac{\partial}{\partial s}B(s,b), \ldots, \frac{\partial^k}{\partial s^k}B(s,b)$ is continuous in b.

[8] That is, B is a vector-valued C^{k+1} spline.

Continuing, define a function $s : \mathcal{X} \times I\!R \to I\!R$ as $s(x, s_0) = 2\tau(x) + s_0$, and note that by monotonicity of $\tau(x)$ (Hypothesis H8.7-iii $s(x, s_0)$ will be strictly monotonically increasing (that is, $L_f s(x, s_0) = 2L_f(x)\tau > 0$ on $\mathcal{O}$) for any choice of s_0. Define the parameter vector $\alpha = (b, s_0) \in I\!R^{mk+1}$ for $b \in I\!R^{mk}$ and $s_0 \in I\!R$, and designate an extended state vector as $x_{\mathbf{e}} = (x, \alpha)$. With this notation, the constructed output function is written as

$$h_{\mathbf{e}}(x_{\mathbf{e}}) = \begin{cases} h(x) + B(s(x, s_0), b) & \text{for } s(x, s_0) < 1 \\ h(x) & \text{otherwise.} \end{cases} \tag{A.11}$$

Motivated by the parameter vector of the constructed output (A.11), let $\mathcal{A} = I\!R^{mk+1}$. In general, there are uncountably many parameter update functions that could be constructed to satisfy Theorem 8.6. One family of such updates is indexed by a scalar $\lambda \in I\!R$ with

$$v^\lambda(x^-) = (b_0^\lambda(x^-), \ldots, b_{k-1}^\lambda(x^-), s_0(x^-))$$

where $s_0(x^-) = -2\tau(x^+)$, $b_0^\lambda(x^-) = \lambda h(x^-) - h(x^+)$, and

$$b_n^\lambda(x^-) = (2L_f\tau(x^+))^{-n}\left(-L_f^n h(x^+) + \lambda L_f^n h(x^-) - \mathcal{R}_n^{(1)}(x^+, b_0(x^-), \ldots, b_{n-1}(x^-))\right) \tag{A.12}$$

for $x^- \in \mathcal{S}$, $x^+ = \Delta(x^-)$, and $1 \leq n \leq k-1$. The term $\mathcal{R}_n^{(1)}(x^+, b_0, \ldots, b_{n-1})$ will be defined shortly, following Remark A.6. Letting $\mathcal{X}_{\mathbf{e}} = \mathcal{X} \times \mathcal{A}$, $\mathcal{S}_{\mathbf{e}} = \mathcal{S} \times \mathcal{A}$, $\bar{\Delta}\lambda_e(x_{\mathbf{e}}) = \big(\Delta(x), v^\lambda(x)\big)$, $x_{\mathbf{e}} = (x, \alpha)$, $f_{\mathbf{e}}(x_{\mathbf{e}}) = (f(x), 0)$, and $g_{\mathbf{e}}(x_{\mathbf{e}}) = (g(x), 0)$ leads to the final construction of the open-loop deadbeat hybrid extension, ${\Sigma_{\mathbf{e}}}^\lambda = \big(\mathcal{X}_{\mathbf{e}}, \mathcal{S}_{\mathbf{e}}, \emptyset, \mathcal{U}, \bar{\Delta}_{\mathbf{e}}^\lambda, f_{\mathbf{e}}, g_{\mathbf{e}}\big)$.

Remark A.6. *For the composition $B(s(x, s_0), b)$, Faá di Bruno's formula [80] for the n^{th} partial derivative generalizes*[9] *to a formula for the n^{th} Lie derivative*

$$L_f^n B(s(x, s_0), b) = \sum_{\mathcal{J}_n} \frac{n!}{j_1!\, j_2!\, \ldots\, j_n!} \frac{\partial^j B(s(x, s_0), b)}{\partial s^j} \prod_{i=1}^{n} \left(\frac{L_f^i s(x, s_0)}{i!}\right)^{j_i}, \tag{A.13}$$

where $j = j_1 + \cdots + j_n$ and the summation is over the set $\mathcal{J}_n$ of all n-tuples of nonnegative integer values $(j_1, \ldots, j_n)$ satisfying $j_1 + 2j_2 + \cdots + nj_n = n$.

For use in (A.12), let $\mathcal{R}_n^{(1)}(x, \alpha)$ represent the summation of (A.13) over the index set $\mathcal{J}_n^{(1)} = \mathcal{J}_n \setminus \{(n, 0, \ldots, 0\}$, so that with $\alpha = (b, s_0)$ and $x_{\mathbf{e}} = (x, \alpha)$,

$$L_{f_{\mathbf{e}}}^n h_{\mathbf{e}}(x_{\mathbf{e}}) = L_f^n h(x) + \mathcal{R}_n^{(1)}(x, \alpha) + \frac{\partial^n B(s(x, s_0), b)}{\partial s^n}(L_f s(x, s_0))^n. \tag{A.14}$$

[9] This generalization is only possible because the function s is scalar-valued.

By property i) of B, when x and s_0 are such that $s(x, s_0) = 0$, the value of $\mathcal{R}_n^{(1)}(x, \alpha)$ is dependent only on x and the parameters $b_0, \ldots, b_{n-1}$, and the notation $\mathcal{R}_n^{(1)}(x, b_0, \ldots, b_{n-1})$ becomes appropriate. For use in the proof of Lemma A.7, let $\mathcal{R}_n^{(2)}(x, \alpha)$ represent the summation of (A.13) over the index set $\mathcal{J}_n^{(2)} = \mathcal{J}_n \setminus \{(0, \ldots, 0, 1)\}$, so that with $\alpha = (b, s_0)$ and $x_{\mathbf{e}} = (x, \alpha)$,

$$L_{f_{\mathbf{e}}}^n h_{\mathbf{e}}(x_{\mathbf{e}}) = L_f^n h(x) + \mathcal{R}_n^{(2)}(x, \alpha) + \frac{\partial B(s(x, s_0), b)}{\partial s} L_f^n s(x, s_0). \tag{A.15}$$

Lemma A.7. *The output $h_{\mathbf{e}}(x_{\mathbf{e}})$ of* (A.11) *has uniform vector relative degree k for all $x_{\mathbf{e}}$ in an open neighborhood of the $\mathcal{O}_{\mathbf{e}}$, which is the trivial lift of $\mathcal{O}$ into $\Sigma_{\mathbf{e}}$.*

Proof. For all $x_{\mathbf{e}} \in \mathcal{X}_{\mathbf{e}}$, $0 \leq n \leq k-1$

$$L_{f_{\mathbf{e}}}^n h_{\mathbf{e}}(x_{\mathbf{e}}) = \begin{cases} L_f^n h(x) + L_f^n B(s(x, s_0), b) & \text{for } s(x, s_0) < 1 \\ L_f^n h(x) & \text{otherwise.} \end{cases} \tag{A.16}$$

By H8.7-i, the claim of the Lemma is trivial for all $x_{\mathbf{e}} \in \mathcal{X}_{\mathbf{e}}$ for which $s(x, s_0) > 1$. Using the term $\mathcal{R}_n^{(2)}(x, \alpha)$ developed after Remark A.6, expand the first line of (A.16) to obtain that for all $x_{\mathbf{e}} = (x, \alpha) \in \mathcal{X}_{\mathbf{e}}$ such that $s(x, s_0) < 1$, for $0 \leq n \leq k-1$,

$$L_{f_{\mathbf{e}}}^n h_{\mathbf{e}}(x_{\mathbf{e}}) = L_f^n h(x) + \mathcal{R}_n^{(2)}(x, \alpha) + \frac{\partial B(s(x, s_0), b)}{\partial s} L_f^n s(x, s_0), \tag{A.17}$$

which is (A.15). Each additive term of $\mathcal{R}_n^{(2)}(x, \alpha)$ contains $L_f^i s(x, s_0)$ for some $0 \leq i \leq n-1$. From its definition, the function $s(x, s_0)$ satisfies the property that $\forall x \in \mathcal{X}$, $\forall s_0 \in I\!R$ and $0 \leq n \leq k-1$, $L_g L_f^n s(x, s_0) = 2 L_g L_f^n \tau(x)$. And, by H8.7-iii, $L_g L_f^n \tau(x) = 0$ for $0 \leq n \leq k-2$. With omitted chain-rule calculations left to the reader, this further implies that for all $x_{\mathbf{e}} = (x, \alpha) = (x, b, s_0) \in \mathcal{X}_{\mathbf{e}}$ such that $s(x, s_0) < 1$, $0 \leq n \leq k-2$, it holds that $L_g \mathcal{R}_n^{(2)}(x, b, s_0) = 0$. Accordingly, for all $x_{\mathbf{e}} = (x, \alpha) \in \mathcal{X}_{\mathbf{e}}$ such that $s(x, s_0) < 1$, for $0 \leq n \leq k-2$, $L_{g_{\mathbf{e}}} L_{f_{\mathbf{e}}}^n h_{\mathbf{e}}(x_{\mathbf{e}}) = 0$, which is part of the definition uniform vector relative degree (3.2). In the case of $n = k-1$, (A.17) simplifies to

$$L_{g_{\mathbf{e}}} L_{f_{\mathbf{e}}}^{k-1} h_{\mathbf{e}}(x_{\mathbf{e}}) = L_g L_f^{k-1} h(x) + L_g \left(\frac{\partial B(s(x, s_0), b)}{\partial s} L_f^{k-1} s(x, s_0) \right)$$

giving the decoupling matrix as

$$L_{g_{\mathbf{e}}} L_{f_{\mathbf{e}}}^{k-1} h_{\mathbf{e}}(x_{\mathbf{e}}) = L_g L_f^{k-1} h(x) + \frac{\partial B(s(x, s_0), b)}{\partial s} L_g L_f^{k-1} s(x, s_0).$$

Applying the Sherman-Morrison-Woodbury formula [15], the decoupling matrix is invertible at each point $x_{\mathbf{e}} = (x, b, s_0) \in \mathcal{X}_{\mathbf{e}}$ where the continuous scalar function

$$1 + L_g L_f^{k-1} s(x, s_0) \left(L_g L_f^{k-1} h(x) \right)^{-1} \frac{\partial B(s(x, s_0), b)}{\partial s} \tag{A.18}$$

is nonzero. Along $\mathcal{O}_{\mathbf{e}}$, the trivial lift of $\mathcal{O}$, the parameter b takes a value of $0 \in I\!R^{mk}$ and thus by property iii) of B, for all $(x, b, s_0) \in \mathcal{O}_{\mathbf{e}}$, $\partial B(s(x, s_0), b)/\partial s = 0$. As a result, the function in (A.18) has a constant value of 1 on the orbit $\mathcal{O}_{\mathbf{e}}$. Because (A.18) is continuous and nonzero on $\mathcal{O}_{\mathbf{e}}$, it must be nonzero in an open neighborhood of $\mathcal{O}_{\mathbf{e}}$. Equivalently, the decoupling matrix $L_{g_{\mathbf{e}}} L_{f_{\mathbf{e}}}^{k-1} h_{\mathbf{e}}(x_{\mathbf{e}})$ is invertible in an open neighborhood of $\mathcal{O}_{\mathbf{e}}$, which fulfills the invertibility portion of the definition of uniform vector relative degree (3.2). □

The proof of Theorem 8.6 is as follows: By Lemma A.7, the parameterized extension, $\Sigma_{\mathbf{e}}^{\lambda}$ and output function $h_{\mathbf{e}}$ together fulfill H7.7-i of Corollary 7.8. Hypothesis H8.7-i of Theorem 8.6 implies that H7.7-ii of Corollary 7.8 is true—indeed every point on the trivial lift $\mathcal{O}_{\mathbf{e}}$ meets this condition. Hypothesis H8.7-ii of Theorem 8.6 implies that the open-loop deadbeat hybrid extension meets H7.7-iii. The manifold $\mathcal{Z}_{\mathbf{e}}$ is impact invariant if and only for all $x_{\mathbf{e}}{}^- = (x^-, \alpha^-) \in \mathcal{S}_{\mathbf{e}} \cap \mathcal{Z}_{\mathbf{e}}$,

$$h_{\mathbf{e}}(x^+, \alpha^+) = 0, L_{f_{\mathbf{e}}} h_{\mathbf{e}}(x^+, \alpha^+) = 0, \ldots, L_{f_{\mathbf{e}}}^{k-1} h_{\mathbf{e}}(x^+, \alpha^+) = 0$$

with $x^+ = \Delta(x^-)$ and $\alpha^+ = v^{\lambda}(x^-)$. The above Lie derivatives can be expanded as in (A.14); $\forall x^- \in \mathcal{S}$ with $x^+ = \Delta(x^-)$ and $0 \leq n \leq k-1$,

$$L_{f_{\mathbf{e}}}^n h_{\mathbf{e}}(x^+, \alpha) = L_f^n h(x^+) + \mathcal{R}_n^{(1)}(x^+, \alpha) + \frac{\partial^n B(s(x^+, s_0), b)}{\partial s^n} (L_f s(x^+, s_0))^n, \tag{A.19}$$

for any $\alpha \in \mathcal{A}$. By the construction of s, $L_f s(x, s_0) = 2 L_f \tau(x)$ (independent of the value of s_0). After the update of $s_0 = -2\tau(x^+)$, the value of $s(x^+, s_0)$ is necessarily zero. Using property i) of B, the $n = 0$ case of (A.19) is simplified to $h_{\mathbf{e}}(x^+, b, s_0) = h(x^+) + b_0$, and for $1 \leq n \leq k-1$, $L_{f_{\mathbf{e}}}^n h_{\mathbf{e}}(x^+, b, s_0) = L_f^n h(x^+) + b_n (2 L_f \tau(x^+))^n + \mathcal{R}_n^{(1)}(x^+, b_0, \ldots, b_{n-1})$. The parameter updates of (A.12) are derived by setting $L_{f_{\mathbf{e}}}^n h_{\mathbf{e}}(x^+, b, s_0) = \lambda L_f^n h(x^-)$ and solving for b_n. In this way, impact invariance of $\mathcal{Z}_{\mathbf{e}}$ is achieved by construction. Lastly, Hypothesis H8.7-i and property iii) of B imply that the orbit $\mathcal{O}_{\mathbf{e}}$ is in $\mathcal{Z}_{\mathbf{e}}$, which is the final claim of the theorem.

BIBLIOGRAPHY

BIBLIOGRAPHY

[1] Japan's humanoid robots: Better than people. *The Economist*, December 2005.

[2] Boston dynamics web site. http://www.bostondynamics.com/, December 2007.

[3] Yobotics web site. http://www.yobotics.com/, December 2007.

[4] G. Abba and N. Chaillet. Robot dynamic modeling using a power flow approach with application to biped locomotion. *Autonomous Robots*, 6(1):39–52, 1999.

[5] J. A. Acosta, R. Ortega, A. Astolfi, and A. D. Mahindrakar. Interconnection and damping assignment passivity-based control of mechanical systems with underactuation degree one. *IEEE Transactions on Automatic Control*, 50(12):1936–1955, December 2005.

[6] M. Ahmadi and M. Buehler. The ARL Monopod II running robot: Control and energetics. In *IEEE International Conference on Robotics and Automation*, pages 1689–1694, May 1999.

[7] R. McN. Alexander. Three uses for springs in legged locomotion. *International Journal of Robotics Research*, 9(2):53–61, 1990.

[8] A. D. Ames and R. D. Gregg. Stably extending two-dimensional bipedal walking to three. In *Proc. of the 2007 American Control Conference, New York, NY*, 2007.

[9] F. Asano, M. Yamakita, N. Kamamichi, and Z.W. Luo. A novel gait generation for biped walking robots based on mechanical energy constraint. *IEEE Transactions on Robotics and Automation*, 20(3):565–73, 2004.

[10] A. Astolfi and R Ortega. Immersion and invariance: A new tool for stabilization and adaptive control of nonlinear systems. *IEEE Transactions on Automatic Control*, 48(4):590–606, 2003.

[11] K.J. Åström. Åström's homepage. http://www.control.lth.se/~kja/, 2007.

[12] D.D. Bainov and P.S. Simeonov. *Systems with Impulse Effects : Stability, Theory and Applications*. Ellis Horwood Limited, Chichester, 1989.

[13] BBC News / Health. Bear robot rescues wounded troops. http://news.bbc.co.uk/2/low/health/6729745.stm, June 2007.

[14] K. Berns. The Walking Machine Catalogue. http://www.walking-machines.org/, 2007.

[15] Dennis S. Bernstein. *Matrix mathematics : theory, facts, and formulas with application to linear systems theory*. Princeton, N.J. : Princeton University Press, 2005.

[16] S. P. Bhat and D. S. Bernstein. Continuous finite-time stabilization of the translational and rotational double integrators. *IEEE Transactions on Automatic Control*, 43(5):678–682, 1998.

[17] S. P. Bhat and D. S. Bernstein. Finite-time stability of continuous autonomous systems. *SIAM Journal on Control and Optimization*, 38:751–766, 2000.

[18] B.Hindle and S. Lubar. *Engines of Change: The American Industrial Revolution, 1790-1860*. Smithsonian Institution Press, 1986.

[19] R. Bockbrader. Design of a five-link planar bipedal running mechanism. Master's thesis, The Ohio State University, 2006.

[20] W. M. Boothby. *An Introduction to Differentiable Manifolds and Riemannian Geometry*. Academic Press, New York, 1975.

[21] B. Brogliato. *Nonsmooth Impact Dynamics: Models, Dynamics and Control*, volume 220 of *Lecture Notes in Control and Information Sciences*. Springer, London, 1996.

[22] M. Bühler, D. E. Koditschek, and P. J. Kindlmann. Planning and control of a juggling robot. *International Journal of Robotics Research*, 13(2):101–18, 1994.

[23] C. Byrnes and A. Isidori. Asymptotic stabilization of nonlinear minimum phase systems. *IEEE Transactions on Automatic Control*, 376:1122–37, 1991.

[24] Rony Caballero, Manuel A. Armada, and Pedro Alarcón. Methodology for zero-moment point experimental modeling in the frequency domain. *Journal of Vibration and Control*, 12(12):1385–1406, 2006.

[25] C. Canudas. On the concept of virtual constraints as a tool for walking robot control and balancing. *Annual Reviews in Control*, 28:157–66, 2004.

[26] J. G. Cham, S. A. Bailey, J. E. Clark, R. J. Full, and M. R. Cutkosky. Fast and robust: Hexapedal robots via shape deposition manufacturing. *International Journal of Robotics Research*, 21(10-11):869–882, 2002.

[27] V. Chellaboina, S. P. Bhat, and W. M. Haddad. An invariance principle for nonlinear hybrid and impulsive dynamical systems. *Nonlinear Analysis*, 53:527–50, 2003.

[28] C. Chevallereau. Time-scaling control for an underactuated biped robot. *IEEE Transactions on Robotics and Automation*, 19(2):362–368, 2003.

[29] C. Chevallereau, G. Abba, Y. Aoustin, F. Plestan, E. R. Westervelt, C. Canudas, and J. W. Grizzle. RABBIT: a testbed for advanced control theory. *IEEE Control Systems Magazine*, 23(5):57–79, October 2003.

[30] C. Chevallereau and Y. Aoustin. Optimal reference trajectories for walking and running of a biped robot. *Robotica*, 19(5):557–69, September 2001.

[31] C. Chevallereau, E. R. Westervelt, and J. W. Grizzle. Asymptotically stable running for a five-link, four-actuator, planar bipedal robot. *International Journal of Robotics Research*, 24:431–64, 2005.

[32] J. H. Choi. *Model-based Control and Analysis of Anthropomorphic Walking*. PhD thesis, University of Michigan, 2005.

[33] J. H. Choi and J. W. Grizzle. Feedback control of an underactuated planar bipedal robot with impulsive foot action. *Robotica*, 23:567–80, September 2005.

[34] J. H. Choi and J. W. Grizzle. Planar bipedal walking with foot rotation. In *Proc. of the 2005 American Control Conference, Portland, OR*, pages 4909–16, 2005.

[35] D. B. Cleveland. *The Role of Services in the Modern U.S. Economy*. U.S Department of Commerce, International Trade Administration, Office of Service Industries, January 1999.

[36] M. J. Colemen, A. Chatterjee, and A. Ruina. Motions of a rimless spoked wheel: a simple 3D system with impacts. In *Dynamics and Stability of Systems*, volume 12, pages 139–60, 1997.

[37] S. H. Collins and A. Ruina. A bipedal walking robot with efficient and human-like gait. In *Proc. of the 2005 IEEE International Conference on Robotics and Automation, Barcelona, Spain*, pages 1983–8, 2005.

[38] S. H. Collins, A. Ruina, R. Tedrake, and M. Wisse. Efficient bipedal robots based on passive-dynamic walkers. *Science*, 307:1082–85, 2005.

[39] S. H. Collins, M. Wisse, and A. Ruina. A three-dimensional passive-dynamic walking robot with two legs and knees. *International Journal of Robotics Research*, 20(7):607–15, July 2001.

[40] C. De Boor. *A Practical Guide to Splines*. Springer-Verlag, 1978.

[41] D. Djoudi and C. Chevallereau. *Fast motions in Biomechanics and Robotics*, chapter Stability analysis of bipedal walking with control or monitoring of the center of pressure, pages 95–120. Lecture Notes in Control and Information Sciences. Springer, Heidelberg, Germany, 2006.

[42] V. Duindam. *Port-Based Modeling and Control for Efficient Bipedal Walking Robots*. PhD thesis, University of Twente, March 2006.

[43] G. Endo, J. Nakanishi, J. Morimoto, and G. Cheng. Experimental studies of a neural oscillator for biped locomotion with qrio. In *Proceedings of the IEEE International Conference on Robotics and Automation*, April 2005.

[44] K. Erbatur, A. Okazaki, K. Obiya, T. Takahashi, and A. Kawamura. A study on the zero moment point measurement for biped walking robots. In *Proc. of the 2002 IEEE International Workshop on Advanced Motion Control, Maribor, Slovenia*, pages 431–6, 2002.

[45] B. Espiau and A. Goswani. Compass gait revisited. In *Proc. of the IFAC Symposium on Robot Control, Capri, Italy*, pages 839–846, September 1994.

[46] R. Featherstone. The calculation of robot dynamics using articulated-body inertias. *International Journal of Robotics Research*, 2(1):13–30, 1983.

[47] C. Francois and C. Samson. A new approach to the control of the planar one-legged hopper. *International Journal of Robotics Research*, 17(11):1150–66, 1998.

[48] M. Garcia. *Stability, Scaling, and Chaos in Passive-Dynamic Gait Models*. PhD thesis, Cornell University, 1999.

[49] M. Garcia, A. Chatterjee, and A. Ruina. Efficiency, speed, and scaling of two-dimensional passive-dynamic walking. *Dynamics and Stability of Systems*, 15(2):75–99, June 2000.

[50] M. Garcia, A. Chatterjee, A. Ruina, and M. Coleman. The simplest walking model: Stability, complexity, and scaling. *ASME Journal of Biomechanical Engineering*, 120(2):281–8, April 1998.

[51] L. Geppert. Qrio, the robot that could. *Spectrum, IEEE*, 41:34 – 37, May 2004. Rank1.

[52] M. Gienger, K. Löffler, and F. Pfeiffer. A biped robot that jogs. In *Proc. of the 2000 IEEE International Conference on Robotics and Automation, San Francisco, CA*, pages 3334–9, 2000.

[53] J. M. Goncalves, A. Megretski, and M. A. Dahleh. Global stability of relay feedback systems. *IEEE Transactions on Automatic Control*, 46(4):550–62, April 2001.

[54] A. Goswami. Postural stability of biped robots and the foot-rotation indicator (FRI) point. *International Journal of Robotics Research*, 18(6):523–33, June 1999.

[55] A. Goswami, B. Espiau, and A. Keramane. Limit cycles and their stability in a passive bipedal gait. In *Proc. of the 1996 IEEE International Conference on Robotics and Automation, Minneapolis, MN*, pages 246–51, 1996.

[56] A. Goswami, B. Espiau, and A. Keramane. Limit cycles in a passive compass gait biped and passivity-mimicking control laws. *Autonomous Robots*, 4(3):273–86, 1997.

[57] A. Goswami, B. Thuilot, and B. Espiau. A study of the passive gait of a compass-like biped robot: Symmetry and chaos. *International Journal of Robotics Research*, 17(12):1282–301, 1998.

[58] A. A. Grishin, A. M. Formal'sky, A. V. Lensky, and S. V. Zhitomirsky. Dynamical walking of a vehicle with two telescopic legs controlled by two drives. *International Journal of Robotics Research*, 13(2):137–47, 1994.

[59] J. W. Grizzle. Jessy Grizzle's publications. http://www.eecs.umich.edu/~grizzle/papers/robotics.html, 2007.

[60] J. W. Grizzle, G. Abba, and F. Plestan. Asymptotically stable walking for biped robots: Analysis via systems with impulse effects. *IEEE Transactions on Automatic Control*, 46:51–64, January 2001.

[61] J. W. Grizzle, C. H. Moog, and C. Chevallereau. Nonlinear control of mechanical systems with an unactuated cyclic variable. *IEEE Transactions on Automatic Control*, 30(5):559–576, May 2005.

[62] J. Guckenheimer and P. Holmes. *Nonlinear Oscillations, Dynamical Systems, and Bifurcations of Vector Fields*, volume 42 of *Applied Mathematical Sciences*. Springer-Verlag, New York, 1996.

[63] J. Guckenheimer and S. Johnson. Planar hybrid systems. In *Hybrid Systems II, Lecture Notes in Computer Science*, pages 203–25. Springer-Verlag, 1995.

[64] W. M. Haddad, S. G. Nersesova, and V. Chellaboina. Energy-based control for hybrid port-controlled Hamiltonian systems. *Automatica*, 39:1425–35, 2003.

[65] K. Hirai. Current and future perspective of Honda humanoid robot. In *IEEE/RSJ International Conference on Intelligent Robots and Systems*, volume 2, pages 500–508, 1997.

[66] K. Hirai. The Honda humanoid robot: development and future perspective. *Industrial Robot*, 26(4):260–6, 1999.

[67] K. Hirai, M. Hirose, Y. Haikawa, and T. Takenake. The development of Honda humanoid robot. In *Proc. of the 1998 IEEE International Conference on Robotics and Automation, Leuven, Belgium*, pages 1321–26, 1998.

[68] H. Hirukawa, F. Kanehiro, K. Kaneko, S. Kajita, K. Fujiwara, Y. Kawai, F. Tomita, S. Hirai, K. Tanie, T. Isozumi, K. Akachi, T. Kawasaki, S. Ota, K. Yokoyama, H. Handa, Y. Fukase, J. Maeda, Y. Nakamura, S. Tachi, and H. Inoue. Humanoid robotics platforms developed in hrp. *Robotics and Autonomous Systems*, 48(4):165–75, 2004.

[69] I. A. Hiskens. Stability of hybrid system limit cycles: application to the compass gait biped robot. In *Proc. of the 2001 IEEE International Conference on Decision and Control, Orlando, FL*, pages 774–9, 2001.

[70] I. A. Hiskens. Stability of limit cycles in hybrid systems. In *Proc. of the 34th Annual Hawaii International Conference on System Sciences*, pages 756–61, 2001.

[71] Honda Corporation. ASIMO: Frequently Asked Questions. http://asimo.honda.com/downloads/pdf/asimo-technical-faq.pdf, 2007.

[72] Honda Corporation. ASIMO's Homepage. http://world.honda.com/ASIMO/, 2007.

[73] Y. Hürmüzlü, F. Génot, and B. Brogliato. Modeling, stability and control of biped robots - a general framework. *Automatica*, 40(10):1647–1664, 2004.

[74] Y. Hürmüzlü and D. B. Marghitu. Rigid body collisions of planar kinematic chains with multiple contact points. *International Journal of Robotics Research*, 13(1):82–92, 1994.

[75] Y. Hürmüzlü and D. Moskowitz. The role of impact in the stability of bipedal locomotion. *Dynamics and Stability of Systems*, 1(3):217–34, 1986.

[76] J. W. Hurst, J. E. Chestnutt, and A. A. Rizzi. An actuator with physically variable stiffness for highly dynamic legged locomotion. In *Proc. of the 2004 IEEE International Conference on Robotics and Automation, New Orleans, LA*, pages 4662–7, 2004.

[77] A. Isidori. *Nonlinear Control Systems: An Introduction*. Springer-Verlag, Berlin, 2nd edition, 1989.

[78] A. Isidori. *Nonlinear Control Systems*. Springer-Verlag, Berlin, third edition, 1995.

[79] Japanese Robot Association. Summary report on technology strategy for creating a robot society in the 21st century. http://www.jara.jp/e/index.html, 2001.

[80] W. P. Johnson. The curious history of faá di bruno's formula. *American Mathematical Monthly*, 109:217–234, March 2002.

[81] S. Kajita, F. Kanehiro, K. Kaneko, K. Fujiwara, K. Yokoi, and H. Hirukawa. A realtime pattern generator for biped walking. In *Proc. of the 2002 IEEE International Conference on Robotics and Automation, Washington, D.C.*, pages 31–7, 2002.

[82] S. Kajita, T. Nagasaki, K. Kaneko, K. Yokoi, and K. Tanie. A hop towards running humanoid biped. In *Proc. of the 2004 IEEE International Conference on Robotics and Automation, New Orleans, LA*, pages 629–35, 2004.

[83] N. Kanehira, T.U. Kawasaki, S. Ohta, T. Ismumi, T. Kawada, F. Kanehiro, S. Kajita, and K. Kaneko. Design and experiments of advanced leg module (HRP-2L) for humanoid robot (HRP-2) development. In *Proc. of the 2002 IEEE/RSJ International Conference on Intelligent Robots and Systems, Lausanne, Switzerland*, pages 2455–60, 2002.

[84] K. Kaneko, F. Kanehiro, S. Kajita, K. Yokoyama, K. Akachi, T. Kawasaki, S. Ota, and T. Isozumi. Design of prototype humanoid robotics platform for HRP. In *Proc. of the 2002 IEEE/RSJ International Conference on Intelligent Robots and Systems, Lausanne, Switzerland*, pages 2431–6, 2002.

[85] K. Kasaoka and Y. Sankai. Predictive control estimating operator's intention for stepping-up motion by exo-skeleton type power assist system HAL. In *In IEEE/RSJ International Conference on Intelligent Robots and Systems*, pages 1578–1583, 2001.

[86] H. Kazerooni, R. Steger, and L. Huang. Hybrid control of the berkeley lower extremity exoskeleton (bleex). *International Journal of Robotics Research*, 25(5-6):561 – 573, May-June 2006.

[87] H. K. Khalil. *Nonlinear Systems - 2nd Edition*. Prentice Hall, Upper Saddle River, 1996.

[88] D. E. Koditschek and M. Bühler. Analysis of a simplified hopping robot. *International Journal of Robotics Research*, 10(6):587–605, 1991.

[89] V.R. Kumar and K.J. Waldron. A review of research on walking vehicles. In O. Khatib, J.J. Craig, and T. Lozano-Pérez, editors, *The robotics review 1*, pages 243–66. MIT Press, Cambridge, MA, 1989.

[90] A. D. Kuo. Stabilization of lateral motion in passive dynamic walking. *International Journal of Robotics Research*, 18(9):917–30, 1999.

[91] A. D. Kuo. Energetics of actively powered locomotion using the simplest walking model. *Journal of Biomechanical Engineering*, 124(1):113–20, 2002.

[92] A.D. Kuo. Choosing your steps carefully. *Robotics & Automation Magazine, IEEE*, 14(2):18–29, 2007.

[93] A.D Kuo, J. M. Donelan, and A. Ruina. Energetic consequences of walking like an inverted pendulum: Step-to-step transitions. *Exercise and Sport Sciences Reviews*, 33:88–97, 2005.

[94] K. Loffler, M. Gienger, F. Pfeiffer, and H. Ulbrich. Sensors and control concept of a biped robot. *IEEE Transactions on Industrial Electronics*, 51(5):972–80, 2004.

[95] T. McGeer. Passive bipedal running. *Proceedings of the Royal Society of London*, 240(1297):107–34, May 1990.

[96] T. McGeer. Passive dynamic walking. *International Journal of Robotics Research*, 9(2):62–82, April 1990.

[97] T. A. McMahon, G. Valiant, and E. C. Frederick. Groucho running. *Journal of Applied Physiology*, 62(6):2326–37, June 1987.

[98] P. Michel, J. Chestnutt, J. Kuffner, and T. Kanade. Vision-guided humanoid footstep planning for dynamic environments. In *IEEE-RAS International Conference on Humanoid Robots*, pages 13–18, 2005.

[99] K. D. Mombaur, R. W. Longman, H. G. Bock, and J. P. Schloder. Open-loop stable running. *Robotica*, 23:21–33, 2005.

[100] B. Morris and J. W. Grizzle. A restricted Poincaré map for determining exponentially stable periodic orbits in systems with impulse effects: Application to bipedal robots. In *Proc. of the 2005 IEEE International Conference on Decision and Control / European Control Conference, Seville, Spain*, pages 4199–206, 2005.

[101] B. Morris, E. R. Westervelt, C. Chevallereau, G. Buche, and J. W. Grizzle. *Fast Motions Symposium on Biomechanics and Robotics*, chapter Achieving Bipedal Running with RABBIT: Six Steps toward Infinity, pages 277–97. Lecture Notes in Control and Information Sciences. Springer-Verlag, Heidelberg, Germany, 2006.

[102] R. M. Murray, Z. Li, and S. Sastry. *A Mathematical Introduction to Robotic Manipulation*. CRC Press, 1994.

[103] S. G. Nersesov, V. Chellaboina, and W. M. Haddad. A generalization of Poincaré's theorem to hybrid and impulsive dynamical systems. *International Journal of Hybrid Systems*, 2:39–55, 2002.

[104] M.W. Ortega, R.and Spong and F Gomez-Estern. Stabilization of underactuated mechanical systems via interconnection and damping assignment. *IEEE Trans. Aut. Control*, 47, 2002.

[105] E. Papadopoulos and S. Dubowsky. Dynamic singularities in free-floating space manipulators. *Journal of Dynamic Systems Measurement and Control-Transactions of the ASME*, 115(1):44–52, March 1993.

[106] T. S. Parker and L. O. Chua. *Practical Numerical Algorithms for Chaotic Systems*. Springer-Verlag, New York, 1989.

[107] F. Pfeiffer, K. Löffler, and M. Gienger. The concept of Jogging JOHNNIE. In *Proc. of the 2002 IEEE International Conference on Robotics and Automation, Washington, D.C.*, pages 3129–35, 2002.

[108] F. Plestan, J. W. Grizzle, E. R. Westervelt, and G. Abba. Stable walking of a 7-DOF biped robot. *IEEE Transactions on Robotics and Automation*, 19(4):653–68, August 2003.

[109] I. Poulakakis, J. A. Smith, and M. Buehler. Modeling and experiments of untethered quadrupedal running with a bounding gait: The Scout II robot. *International Journal of Robotics Research*, 24(4):239–256, 2005.

[110] G.A Pratt. Legged robots at MIT: What's new since Raibert. *IEEE Robotics and Automation Magazine*, 7(3):15–19, 2000.

[111] J. Pratt, B. Krupp, and C. Morse. Series elastic actuators for high fidelity force control. *Industrial Robot Journal*, 29(3):234–241, 2002.

[112] J. E. Pratt and B. T. Krupp. Series elastic actuators for legged robots. *SPIE, Unmanned Ground Vehicle Technology VI*, 5422(1):135–144, 2004.

[113] M. Buehler R. Playter and M. Raibert. Bigdog. In *Proc. SPIE Defense&Security Symposium, Unmanned Systems Technology*, Orlando, FL, April 2006.

[114] M. H. Raibert. *Legged Robots that Balance*. MIT Press, Cambridge, MA, 1986.

[115] M. H. Raibert, S. Tzafestas, and C. Tzafestas. Comparative simulation study of three control techniques applied to a biped robot. In *Proc. of the IEEE International Conference on Systems, Man and Cybernetics Systems Engineering in the Service of Humans, Le Touquet, France*, pages 494–502, October 1993.

[116] J.R. Rebula, P.D. Neuhaus, B.V. Bonnlander, M.J. Johnson, and J.E. Pratt. A controller for the littledog quadruped walking on rough terrain. In *Proceedings of the 2007 IEEE International Conference on Robotics and Automation*, April 2007.

[117] M. Reyhanoglu, A. van der Schaft, N.H. McClamroch, and I. Kolmanovsky. Dynamics and control of a class of underactuated mechanical systems. *IEEE Transactions on Automatic Control*, 44(9):1663–71, 1999.

[118] ROBEA: Robotics and Artificial Entities. http://robot-rabbit.lag.ensieg.inpg.fr/English/. 2007.

[119] M. E. Rosheim. *Robot Evolution: The Development of Anthrobotics*. Wiley, New York, 1994.

[120] A. V. Roup, D. S. Bernstein, S. G. Nersesov, W. M. Haddad, and V. Chellaboina. Limit cycle analysis of the verge and foliot clock escapement using impulsive differential equations and Poincaré maps. *International Journal of Control*, 76(17):1685–98, 2003.

[121] Y. Sakagami, R. Watanabe, C. Aoyama, S. Matsunaga, N. Higaki, and K. Fujimura. The intelligent ASIMO: system overview and integration. In *Proc. of the 2002 IEEE/RSJ International Conference on Intelligent Robots and Systems, Lausanne, Switzerland*, pages 2478–83, 2002.

[122] U. Saranli, M. Bühler, and D. E. Koditschek. RHex: A simple and highly mobile hexapod robot. *International Journal of Robotics Research*, 20(7):616–31, July 2001.

[123] U. Saranli, W. Schwind, and D. E. Koditschek. Toward the control of a multi-jointed, monoped runner. In *Proc. of the 1998 IEEE International Conference on Robotics and Automation, Leuven, Belgium*, pages 2676–82, 1998.

[124] P. Sardain and G. Bessonnet. Forces acting on a biped robot. Center of pressure-zero moment point. *IEEE Transactions on Systems, Man and Cybernetics, Part A*, 34:630 – 637, September 2004.

[125] A. Saunders, D. I. Goldman, R. J. Full, and M. Buehler. The rise climbing robot: Body and leg design. In *Proc. SPIE Defense&Security Symposium, Unmanned Systems Technology*, Orlando, FL, April 2006.

[126] J. P. Schmiedeler, E. R. Westervelt, and A. R. Dunki-Jacobs. Integrated design and control of a biped robot. In *Proceedings of the 2005 ASME International Design Engineering Technical Conference*, Long Beach, CA, 2005.

[127] E. Sofge. Nerves of steel. *Popular Mechanics*, April 2006.

[128] G. Song and M. Zefran. Stabilization of hybrid periodic orbits with application to bipedal walking. In *Proc. of the 2006 American Control Conference, Minneapolis, MN*, pages 2504–9, 2006.

[129] M. W. Spong. Modeling and control of elastic joint robots. *Journal of Dynamic Systems, Measurement, and Control*, 109:310–9, December 1987.

[130] M. W. Spong. Adaptive control of flexible joint manipulators. *Systems & Control Letters*, 13:15–21, 1989.

[131] M. W. Spong. Partial feedback linearization of underactuated mechanical systems. In *Proc. of the 1994 IEEE/RSJ International Conference on Intelligent Robots and Systems, Munich, Germany*, pages 314–21, September 1994.

[132] M. W. Spong. The swing up control problem for the Acrobot. *IEEE Control Systems Magazine*, 15(1):49–55, February 1995.

[133] M. W. Spong and F. Bullo. Controlled symmetries and passive walking. *Automatic Control, IEEE Transactions on*, 50(7):1025–31, 2005.

[134] M. W. Spong, S. Hutchinson, and M. Vidyasagar. *Robot Modeling and Control*. John Wiley & Sons, 2005.

[135] M.W. Spong. Energy based control of a class of underactuated mechanical systems. In *Proc. of IFAC World Congress, San Francisco, CA*, pages 431–5, 1996.

[136] M.W. Spong and F. Bullo. Controlled symetries and passive walking. *IEEE Transactions on Automatic Control*, 2003.

[137] S. Suzuki, K. Furuta, Y. Pan, and S. Hatakeyama. Biped walking robot control with passive walker model by new vsc. In *Proc. of the 2001 American Control Conference, Arlington, VA*, volume 1, pages 107–12, 2001.

[138] F. W. Taylor. *The Principles of Scientific Management*. W. W. Norton & Company, 1967.

[139] R. Tedrake. *Applied Optimal Control for Dynamically Stable Legged Locomotion*. PhD thesis, Massachusetts Institute of Technology, 2004.

[140] R. Tedrake, T. W. Zhang, and H. S. Seung. Stochastic policy gradient reinforcement learning on a simple 3D biped. In *Proc. of the 2004 IEEE/RSJ International Conference on Intelligent Robots and Systems*, volume 3, pages 2849–54, 2004.

[141] B. Thuilot, A. Goswami, and B. Espiau. Bifurcation and chaos in a simple passive bipedal gait. In *Proc. of the 1997 IEEE International Conference on Robotics and Automation, Albuquerque, NM*, pages 792–8, 1997.

[142] D. J. Todd. *Walking Machines: An Introduction to Legged Robotics*. Chapman & Hall, 1985.

[143] S. Tzafestas, M. Raibert, and C. Tzafestas. Robust sliding-mode control applied to a 5-link biped robot. *Journal of Intelligent and Robotic Systems: Theory & Applications*, 15(1):67–133, 1996.

[144] R.Q. van der Linde. Design, analysis, and control of a low power joint for walking robots, by phasic activation of mckibben muscles. *IEEE Transactions on Robotics and Automation*, 15(4):599–604, August 1999.

[145] B. Verrelst, O. Stasse, K. Yokoi, and B. Vanderborght. Dynamically stepping over obstacles by the humanoid robot hrp-2. In *IEEE-RAS International Conference on Humanoid Robots*, pages 117–123, December 2006.

[146] M. Vukobratović and B. Borovac. Zero-moment point—thirty five years of its life. *International Journal of Humanoid Robotics*, 1(1):157–73, 2004.

[147] M. Vukobratović, B. Borovac, and V. Potkonjak. ZMP: A review of some basic misunderstandings. *International Journal of Humanoid Robotics*, 3(2):153–75, June 2006.

[148] M. Vukobratović, B. Borovac, D. Surla, and D. Stokic. *Biped Locomotion*. Springer-Verlag, Berlin, 1990.

[149] E. R. Westervelt, G. Buche, and J. W. Grizzle. Experimental validation of a framework for the design of controllers that induce stable walking in planar bipeds. *International Journal of Robotics Research*, 23(6):559–82, 2004.

[150] E. R. Westervelt, G. Buche, and J. W. Grizzle. Inducing dynamically stable walking in an underactuated prototype planar biped. In *Proc. of the 2004 IEEE International Conference on Robotics and Automation, New Orleans, LA*, pages 4234 –9, 2004.

[151] E. R. Westervelt and J. W. Grizzle. Design of asymptotically stable walking for a 5-link planar biped walker via optimization. In *Proc. of the 2002 IEEE International Conference on Robotics and Automation, Washington, D.C.*, pages 3117–22, 2002.

[152] E. R. Westervelt, J. W. Grizzle, and C. Canudas. Switching and PI control of walking motions of planar biped walkers. *IEEE Transactions on Automatic Control*, 48(2):308–12, February 2003.

[153] E. R. Westervelt, J. W. Grizzle, and D. E. Koditschek. Hybrid zero dynamics of planar biped walkers. *IEEE Transactions on Automatic Control*, 48(1):42–56, January 2003.

[154] E. R. Westervelt, B. Morris, and K. D. Farrell. Analysis results and tools for the control of planar bipedal gaits using hybrid zero dynamics. *Autonomous Robots*, 23:131–45, 2007.

[155] M. Wisse. *Essentials of Dynamic Walking: Analysis and design of two-legged robots*. PhD thesis, TU Delft, 2004.

[156] M. Wisse, A. L. Schwab, R. Q. van der Linde, and F. C. T. van der Helm. How to keep from falling forward: Elementary swing leg action for passive dynamic walkers. *IEEE Transactions on Robotics*, 21(3):393–401, 2005.

[157] M. Wisse, A.L. Schwab, and R.Q. van der Linde. A 3D passive dynamic biped with yaw and roll compensation. *Robotica*, 19(3):275–84, 2001.

[158] F. Xi and R.G. Fenton. On the inverse kinematics of space manipulators for avoiding dynamic singularities. In *Proc. of the 1994 IEEE International Conference on Robotics and Automation, San Diego, CA*, volume 4, pages 3460–5, 1994.

[159] T. Yang, E. R. Westervelt, and A. Serrani. A framework for the control of stable aperiodic walking in underactuated planar bipeds. In *Proc. of the 2007 IEEE International Conference on Robotics and Automation, Rome, Italy*, pages 4661–6, 2007.

[160] H. Ye, A. N. Michel, and L. Hou. Stability theory for hybrid dynamical systems. *IEEE Transactions on Automatic Control*, 43(4):461–74, April 1998.

[161] K. Yokoi, F. Kanehiro, K. Kaneko, S. Kajita, K. Fujiwara, and H. Hirukawa. Experimental study of humanoid robot HRP-1S. *International Journal of Robotics Research*, 23(4-5):351–362, 2004.

[162] E. Yoshida, C. Esteves, T. Sakaguchi, J.P. Laumond, and K. Yokoi. Smooth collision avoidance: Practical issues in dynamic humanoid motion. In *IEEE/RSJ International Conference on Intelligent Robots and Systems*, pages 827–832, 2006.